HYDROTHERMAL CRYSTALLIZATION OF ZEOLITE CATALYSTS USING KAOLIN AND VOLCANIC ASH MATERIALS FOR BIODIESEL SYNTHESIS FROM *Jatropha curcas* AND WASTE COOKING OILS

BY

STEPHEN OCHIENG OTIENO

A THESIS SUBMITTED IN FULFILMENT OF THE REQUIREMENTS FOR THE DEGREEE OF DOCTOR OF PHILOSOPHY IN CHEMISTRY

SCHOOL OF BIOLOGICAL AND PHYSICAL SCIENCES

MASENO UNIVERSITY

©2022

DECLARATIONS

Declaration by the Candidate

I certify that this thesis has not been previously presented for a degree award of Maseno University or in any other university. This thesis is my original work and all sources of information herein have been supported by relevant references.

Signature: ……………………………………. Date: ……30/04/2022………

Stephen Ochieng Otieno

PHD/SC/00056/2014

Declaration by the Supervisors

This thesis has been submitted for examination with our approval as the University supervisors.

Supervisors
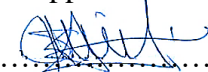
1. Prof. Chripin Kowenje

   Maseno University

   Department of Chemistry, Kenya

   Signature: …………………………………… Date: ……30/04/2022………

2. Prof. Fredrick Kengara

   Bomet University College

   School of Pure and Applied Sciences, Kenya

   Signature: …………………………………… Date: ……30/04/2022………

3. Prof. Robert Mokaya

   School of Chemistry

   University of Nottingham, United Kingdom

   Signature: …………………………………. Date: ……30/04/2022……

ACKNOWLEDGEMENT

DEDICATION

To my parents and family…………...

ABSTRACT

Although biodiesel is a promising alternative source of energy, the cost of its production remains high because of the use of expensive feedstocks and catalysts. Zeolites derived from clay and volcanic ash as alternative sources of aluminosilicates are promising catalysts for the biodiesel synthesis from non-edible plant oils. The aim of this study was to develop zeolite catalysts for transesterification of *Jatropha curcas* and waste cooking oils. For sustainability and cost reduction, the zeolites were hydrothermally crystallized at 100 °C using kaolin and volcanic ash natural materials through metakaolinite and fused-metakaolinite methods. Kaolin was supplied by the department of Inorganic Chemistry, University of Yaoundé 1 (Cameroon) while volcanic ash was obtained from the slopes of Mt. Eburu, Nakuru County (Kenya). In the fused-metakaolinite method, besides the partial versus full fusion, pre-treatment of clay by wet or dry mixing with NaOH activator before fusion were also studied. The zeolite catalysts were prepared by wet ion impregnation method using CH_3COONa salt. The catalysts were tested in the batch transesterification of *Jatropha curcas* and waste cooking oils. Transesterification factors were optimized using $L_{16}(4^4)$ Taguchi approach. Materials used, resulting zeolites and biodiesel products were characterized using XRD (crystallinity), SEM (morphology), EDX (elemental), ICP-OES (elemental), TGA (thermal stability), BET (surface area and porosity), FT-IR (functional groups) and GC-FID (qualitative and quantitative analysis). Obtained data was analysed and organized using Minitab 18.1.0.0, OriginLab 9.80.200 and ImageJ software. Analysis of raw materials showed that clay material was a kaolin type with high quartz impurity at 21.03 %. Volcanic ash, on the other hand, was majorly CaO at 47.09 % and SiO_2 at 18.38 %. In zeolites syntheses using kaolin, zeolites Na-A and Na-X were obtained within 8 h in the metakaolinite and fused-metakaolinite methods, respectively. High hydrogel SiO_2/Al_2O_3 molar ratio resulted in a mixture of products and zeolite Na-Y in the metakaolinite and fused-metakaolinite methods, respectively. In the partial versus full fusion, Na-Y with low surface area and Na-X with high surface area were obtained from partial and full fusion methods, respectively. In the full fusion, pre-treatment of kaolin by dry mixing before dry fusion resulted in Na-X alongside Na-A impurity. The Na-X with high porosity comparable to that of commercial zeolite 13X was obtained in the wet mixing before dry fusion. Wet mixing with subsequent wet fusion resulted in poor crystallinity Na-X alongside hydroxysodalite impurity. In zeolites syntheses using volcanic ash, zeolites Na-X, Na-P and hydroxysodalite were obtained depending on SiO_2 and Na_2O contents of the synthesis hydrogel. For the biodiesel synthesis, optimal conditions for the oil conversion were methanol:oil molar ratio of 10:1, catalyst loading of 8 %, reaction temperature of 70 °C and reaction time of 5 hours. In addition, based on ANOVA, the contribution of the catalyst loading was the most significant at 93.79 %. The maximum FAME yield under these conditions were 93.94 % and 95.54 % for synthesized zeolite Na-X and natural clinoptilolite zeolite, respectively. This study has therefore shown the importance of performing metakaolinization versus fused-metakaolinization as well as the crucial role of NaOH content in the fusion of kaolin in zeolite synthesis. In addition, a variety of high-quality zeolites are achievable via choice of pre-treatment protocols. Both industrial production of zeolites, for various applications, as well as biodiesel production, in the energy sector, are therefore expected to greatly benefit from the findings of this study.

TABLE OF CONTENTS

ABBREVIATIONS

General abbreviations

Code/ symbol	Description
%SS	Percent sum of squares
$A_{(BET)}$	BET surface area,
Adj MS,	Adjusted mean squares
Adj SS	Adjusted sum of squares
ANOVA	Analysis of variance
A_P	Peak area
B10	Fuel blend consisting of 10 % (wt. %) biodiesel and 90 % (wt. %) petro-diesel
B100	Fuel consisting of 100 % biodiesel
B20	Fuel blend consisting of 20 % (wt. %) biodiesel and 80 % (wt. %) petro-diesel
BET	Brunauer-Emmett-Teller
C18:1Me	Methyl oleate
C18:2Me	Methyl linoleate
C18:3Me	Methyl linolenate
D4R	Doble 4-membered ring
D6R	Doble 6-membered ring
DCC	Double crankshaft chain
DF	Degrees of freedom,

DG	Diglyceride
DOE	Design of experiments
DSC	Differential scanning calorimetry
DTA	Differential thermogravimetric analysis
FAME	Fatty acid methyl ester
FAO	Food and Agriculture Organization
FAU	Faujasite
FFA	Free fatty acid
FID	Flame ionization detector
F-test	Fischer's test value
FTIR	Fourier transform infrared
GC	Gas chromatography
GIS	Gismondine
GLC-10	Supelco multicomponent consisting of 5 reference standards
HEU	Heulandite
HS	Hydroxysodalite
i.s	Internal standard
ICP-OES	Inductively Coupled Plasma fitted with Optical Emission Spectroscopy detector
IZA	International Zeolite Association
JCO	*Jatropha curcas* oil

Kao	Kaolin
LOI	Loss on ignition
LTA	Linde type A
MG	Monoglyceride
NREL	National Renewable Energy Laboratory
OECD	Organization for Economic Co-operation and Development
PBU	Primary building unit
PBU	Primary building unit
PET	Polyethylene terephthalate
P-test	Probability value
PTFE	Polytetrafluoroethylene
rds.	Reference standard
RF	Response factor
S/N	Signal to noise ratio
S4R	Single 4-membered ring
S6R	Single 6-membered ring
SBU	Secondary building unit
SBU	Secondary building unit
SDA	Structure-directing agent
SEM	Scanning electron microscope

SEM-EDX	Scanning electron microscope fitted with energy dispersive spectrometer
Seq SS	Sequential sum of squares
SOD	Sodalite
TG	Triglyceride
TGA	Thermogravimetric Analysis
TO_4	Tetrahedral $(AlO_4)^{5-}$/ $(SiO_4)^{4-}$
$V_{(Micro)}$	Micropore volume
WCO	Waste cooking oil
XRD	X-ray diffraction spectrophotometer

Nomenclature, abbreviation of products codes and words used for inorganic raw materials and zeolite products

Symbol/ code	Description
a	Product obtained from dry mixing of kaolin with NaOH before dry fusion
b	Product obtained from wet mixing of kaolin with NaOH before wet fusion
c	Product obtained from wet mixing of kaolin with NaOH then drying out water solvent before dry fusion
FF	Full fusion product
FM	Fused-metakaolinite product
F-MK	Fused-metakaolinite (fused kaolin with NaOH at 750 °C for 8h)
FSX	Synthesized zeolite X from F-MK hydrogel modified with additional fumed silica

FSY	Synthesized zeolite Y from MK or F-MK hydrogel modified with additional fumed silica
FSY-a-FM	Zeolite Na-Y synthesized from the F-MK modified with fumed silica (dry fusion of a dry mixture)
FSY-MK	Zeolite Na-Y synthesized from the MK modified with fumed silica
Full fusion	Calcining kaolin in the presence of larger quantity of NaOH
FVA	Fused volcanic ash
KaVo	Mixture of zeolite X & P from fused KVA-10%A-750C & kaolin with NaOH hydrogel
KaVo-c-FM	Mixture of zeolite X and P synthesized from full fusion of dried out wet mixture of KVA-10%A-750C & kaolin with NaOH (dry fusion of wet mixture)
KVA-10%A	Kenyan volcanic ash washed with 10 % HCl solution
KVA-10%A-750C	Kenyan volcanic ash washed with 10 % HCl then calcined at 750 °C for 8h
KVA-Raw	Raw Kenyan volcanic ash
MK	Metakaolinite product
MSX-a-FM/FF	Zeolite X synthesized from full fusion of dry mixture of kaolin with NaOH (dry fusion of a dry mixture)
MSX-b-FM/FF	Zeolite X synthesized from full fusion of wet mixture of kaolin with NaOH (wet fusion of wet mixture)
MSX-c-FM/FF	Zeolite X synthesized from full fusion of dried out wet mixture of kaolin with NaOH (dry fusion of a wet mixture)
MSY-a-FM/PF	Zeolite Na-Y synthesized from partial fusion of dry mixture of kaolin with NaOH (dry fusion of a dry mixture)

MSY-b-FM/PF	Zeolite Y synthesized from partial fusion of wet mixture of kaolin with NaOH (wet fusion of a wet mixture)
Nat-SA-10%A	Natural zeolite washed with 10% HCl solution
Nat-SA-Pristine	Pristine Natural zeolite
Partial fusion	Calcining kaolin in the presence of smaller quantity of NaOH compared to full fusion
PF	Partial fusion product
S1	Synthesized zeolite X from fused KVA-10%A-750C & sodium aluminate with NaOH hydrogel
S2	Mixture of zeolite X & P from fused KVA-10%A-750C & sodium aluminate with NaOH hydrogel
S3	Synthesized zeolite HS from fused KVA-10%A-750C & sodium aluminate with NaOH hydrogel
SA	Synthesized zeolite A from un modified MK hydrogel
SA-MK	Zeolite Na-A synthesized from the unmodified MK hydrogel
SMX	Synthesized zeolite X from F-MK hydrogel modified with additional sodium metasilicate
SX	Synthesized zeolite X from un modified F-MK hydrogel
SX-a-FM	Zeolite Na-X synthesized from the unmodified F-MK (dry fusion of a dry mixture)
SZ1-c-FVA	Zeolite X synthesized from full fusion of dried out wet mixture of KVA-10%A-750C & sodium aluminate with NaOH (dry fusion of wet mixture)

SZ2-c-FVA   Mixture of zeolite X and P synthesized from full fusion of dried out wet mixture of KVA-10%A-750C & sodium aluminate with NaOH (dry fusion of wet mixture)

SZ3-c-FVA   Zeolite HS synthesized from full fusion of dried out wet mixture of KVA-10%A-750C & sodium aluminate with NaOH (dry fusion of wet mixture)

Washed F-MK   Fused-metakaolinite washed with deionized water

LIST OF FIGURES

LIST OF TABLES

CHAPTER 1

INTRODUCTION

1.1   Background of the study

The world's demand for energy has increased in the past few years due to the increase in human population (OECD, 2011). This has necessitated the need for advancements in technology and industrial developments in order to maintain and improve on the supply of food and other goods and services. According to the (*BP Statistical Review of World Energy*, 2019), about 80 % of the current energy usage is sourced from natural gas, coal and oil which are non-renewable fossil fuels. Fossil fuels have adverse impacts to the environment and has led to an increase in the global total excess mortality rate and a decrease in the mean life expectancy arising from chronic diseases attributed to the emissions during utilization (Lelieveld et al., 2019). Besides, there has been an upward trend in the prices of crude oil in the recent past due to civil strife, geopolitical and economic events especially in the regions known to produce oil in bulk (U.S. Energy Information Administration, 2022). The upward changes in market oil prices are often quickly reflected in prices faced by consumers and can therefore have adverse effects on holding down the global growth. The shifts in both the demand and the cost together with the adverse effects of fossil fuels on the environment and living organisms have necessitated the need for alternative sources of green and sustainable energy.

Although research on renewable energy has tremendously increased in the recent years (Lelieveld et al., 2019; Perego & Bosetti, 2010), it is only in the past few years that the production and consumption of renewable energy have become significant. For example, renewable sources of energy made up 7 % of the United Kingdom's primary energy in 2018 compared to just 1 % about 10 years ago (*BP Statistical Review of World Energy*, 2019). However, in comparison to other energy sources, the current world production and

consumption of renewable energy is still too low (*BP Energy Outlook*, 2018). In addition, according to the (*BP Statistical Review of World Energy*, 2019), the African continent has the least growth in both production and consumption of renewable energy. However, the worldwide production and consumption of renewables are anticipated to increase in the coming years (*BP Energy Outlook*, 2018) as significant technological improvement in the current production methods are realized.

Biofuels are some of the promising renewable energy sources. Among the biofuels, biodiesel is a promising alternative source of renewable energy for petro-diesel engines. Biodiesel is a mixture of fatty acid alkyl esters (FAAEs) derived from a fatty acid chain and a low molecular weight alcohol, usually methanol. Biodiesel was first evaluated in the late 1970s, but it is only in the recent years that it has received a great deal of interest (Maryam et al., 2014; Okoronkwo et al., 2012). The current industrial production of biodiesel is expensive as it involves the use of environmentally unclean homogeneous basic catalysts and edible oils. It is estimated that >12 % of all the edible oils currently produced is used in the production of biodiesel (OECD/FAO, 2019). And of all the worldwide biodiesel production, about 77 % is based on vegetable oils (i.e., 37 % rapeseed oil, 27 % soybean oil, 9 % palm oil and 4 % others) or used cooking oils (23 %) (OECD/FAO, 2020). The use of edible oils has led to high prices of biodiesel where the estimated overall cost of the feedstock takes >70 % of the total cost of the biodiesel product.

Substitution of the current edible oils with sustainable non-edible oils which has low commercial value to humans and the use of heterogeneous catalysts in the production process will therefore drastically reduce the cost of production and subsequently the cost of the produced biodiesel fuels. *Jatropha curcas* seed oil (JCO) and waste cooking oils (WCO) are both non-edible oils and are therefore of low value to humans. They are therefore suitable

alternative feedstock for biodiesel production. *Jatropha curcas* is a deciduous hardy shrub with a productive life span of over 40 years but having a short gestation period and can grow on poor soils and areas of low rainfall (Anil et al., 2011; Shambhu et al., 2013). Waste cooking oil (WCO), on the other hand, is a municipal waste which if not well disposed of ends up increasing the operating cost of sewer water treatment in addition to the risks of ground water contamination and the subsequent greenhouse gases emission (Tsoutsos et al., 2019). Using WCO for biodiesel production will therefore not only lower the cost of biodiesel production but also help in minimizing the negative environmental impacts by converting these wastes into sustainable green energy resources.

Heterogeneous catalysts derived from materials such as alkaline earth metals, calcium oxide, kaolinite, bio-char as well as industrial and biological wastes have been studied as possible substitutes for the current homogenous catalysts (Abukhadra & Sayed, 2018; Chellappan et al., 2018; Marwaha et al., 2018; Thangaraj et al., 2019). However, limitations to catalyst sustainability, active sites, mass transfer and catalyst stability and regeneration are still some of the challenges facing heterogeneous catalysts in the transesterification reactions. Consequently, zeolites are viewed as panaceas to the limitations cited above.

Zeolites have been used in several areas including catalysis (Sousa-Aguiar, 2016), water purification (Margeta et al., 2013) as well as soil enhancers in agriculture (Climent et al., 2010; Weitkamp & Puppe, 1999). Because of their unique structure and properties, zeolites are promising substitutes for use as heterogeneous catalysts in the transesterification reactions of oils in place of conventional homogeneous catalysts. The aluminium atoms and ions in the zeolite skeleton and porosity of zeolites supply active catalytic sites (Schwanke & Pergher, 2018) thus providing highly reactive centres for numerous acid and base-catalysed reactions. Besides, the zeolite pore structures increase their surface area as well as making it possible for

the occlusion of guest atoms and compounds to further enhance the catalytic activities by modifying their acidic or basic properties. Refinement of zeolite's crystallinity, pore size as well as the amount and composition of the guest atoms can therefore lead to catalysts with superior quality for the desired reactions (Baroi et al., 2014; Carrero et al., 2011; Shu et al., 2009).

Natural zeolites occur naturally in the earth's crust where they are formed at alteration of volcanic and other feldspathic rocks at temperatures lower than 200 °C (Alderton, 2021). The zeolite mineral deposits may constitute important components of tuffs or clay which are easily mined by the opencast method (Król, 2020). Synthetic zeolites on the other hand are man-made and are produced from aluminosilicate starting raw materials. Synthesis of zeolites is however known to be influenced by several variables. Key synthesis variables such as hydrogel aluminosilicate composition, concentration of alkaline activator as well as crystallization time and temperature influence the zeolite structure type, chemical composition, crystallinity and porosity of the resulting zeolites (Abdullahi et al., 2017; Foroughi et al., 2021; Johnson & Arshad, 2014). The multiplicity of the variables means that the synthesis of zeolites can be a complex process.

The current synthesis methods for zeolites utilize costly high purity commercial synthetic silica and alumina sources. In order to lower the cost of production, research is ongoing to synthesize zeolites from alternative materials like natural materials as well as agricultural and industrial wastes, (such as rice husk, fly ash and sewage sludge) (Cheng et al., 2012; Musyoka et al., 2014; Ríos et al., 2012; Volli & Purkait, 2015; Zhang et al., 2018) which are rich in aluminosilicates.

The challenge faced in using natural clays is that they are heterogeneous in composition and purity because of their diverse sources in the earth crust. Some of the impurities such as quartz

and muscovite mica are very stable even at high temperature. Before the hydrothermal synthesis of zeolites, crystalline kaolin is usually converted to amorphous phases by high temperature pre-treatment via either calcination to form metakaolinite (MK) or fusing with an alkaline activator to form fused-metakaolinite (F-MK). Using F-MK method over MK method in the pre-treatment of kaolin is advantageous because it enables complete breakdown of the kaolinite structure (Ayele et al., 2016).

Even though fusion is considered effective in the conversion of aluminosilicates to zeolite structural building units, faujasite zeolites and hydroxysodalite (HS) alongside other impurities such as zeolite A and quartz have been reported (Anderson et al., 2017; Ayele et al., 2016; Belviso et al., 2013; Castro et al., 2019; Djeffal et al., 2017; Doyle et al., 2016; Ma et al., 2014; Mezni et al., 2011; Musyoka et al., 2014; Ríos et al., 2012; Zayed et al., 2017). These studies strongly suggest that current practice, which involves pre-treatment of clays via F-MK, may be ineffective because there is no consistency in the properties of reported zeolite structures synthesized from kaolin. The structure types and properties varied from one study to another. The manner and steps via which F-MK is carried out and the post modifications carried out on the synthesis hydrogels therefore play a role in determining the resulting zeolite structure types and their properties. Despite the attraction and huge potential of kaolinite rich clays and related materials as a sustainable alternative source of aluminosilicates in zeolite synthesis, the apparent differences and inconsistency in the products generated and their properties are still an on-going challenge. It is therefore important to fully explore the conversion of aluminosilicates in kaolin, into a form that ensures subsequent complete dissolution to a homogeneous synthesis hydrogel.

In this study, heterogeneous zeolite catalysts have been synthesized from kaolin and Kenyan volcanic ash, via MK and F-MK methods. The effects of NaOH concentration in the alkaline

fusion step was investigated by performing partial fusion versus full fusion of kaolin before hydrothermal crystallization. Besides, various pre-treatment methods for kaolin with alkaline activator prior to the fusion step were explored by subjecting the raw clay to two regimes, namely; dry mixing with NaOH followed by dry fusion, or wet mixing with NaOH followed by either wet or dry fusion. Both natural and synthesized zeolites were modified by the wet impregnation method using sodium acetate salt before activation by heat. Prepared zeolite catalysts were then tested in batch transesterification reactions of JCO and WCO. The findings of this study could inform on the best zeolite synthesis method for use when using natural aluminosilicates as starting raw materials. It was also to inform on the choice of pre-treatment processes that may be applied to clay materials before fusion and hydrothermal synthesis of zeolite

1.2   Statement of the problem

There is continued rise in selling price of conventional fossil fuels in the market and this points to the need for search for cheap alternative fuels. In addition, with the continued depletion and the uncertainty in sustainability of conventional fossil fuel reserves, biofuels stand to be one of the best alternative sources of fuel. Biodiesel is a promising alternative energy source due to its advantages over petro-diesel fuel. However, the current production methods using feedstock materials which are also competitively used for human food production and the use of homogeneous catalysts increase the costs of biodiesel production.

Although zeolites are promising alternative catalysts, their current production method using commercial sources of aluminosilicate raw materials is still expensive. Natural zeolites and synthetic zeolites, obtained from natural resources such as clay minerals and volcanic ash, are suitable alternatives. However, the resulting zeolite types, quality and crystallinity reported in the literature using clays and other natural materials from different sources varies even when

the same formulation and synthesis conditions are used. There is therefore need for research on suitable methods of converting the aluminosilicates to suitable forms prior to zeolite synthesis. Besides, to cut on the costs, there is need for research on the optimized production of biodiesel using non-edible oils (such as JCO and WCO), natural zeolites as well as zeolites synthesized from natural materials. The characteristics of raw materials, modified materials as well as synthesized products also need to be investigated to identify the phases, compositions, purities of raw materials as well as yields and the derived products.

1.3 Objectives of the study

1.3.1 General objective

The aim of this study was to synthesize and characterize zeolites using clay and volcanic ash natural materials through metakaolinite (MK) and fused-metakaolinite (F-MK) methods in the hydrothermal crystallization at 100 °C. Both natural and synthesized zeolites were modified before use in optimized batch catalytic transesterification reactions of *Jatropha curcas* oil and waste cooking oils with methanol.

1.3.2 Specific objectives

1. Synthesize zeolites through hydrothermal reaction using kaolin, additional silica and volcanic ash as sources of aluminosilicates.
2. Determine the optimum conditions in the pre-treatment of kaolin for the conversion of kaolin's crystalline aluminosilicates to free ions to achieve high quality zeolites.
3. Determine the effects of functionalization of both the natural and synthesized zeolites, through occlusion of Na^+ cations, on the catalytic activity of zeolites.
4. Determine the optimized conditions for biodiesel synthesis regarding catalyst load, alcohol to oil molar ratio, reaction temperature and time.

5. Determine the catalytic activity of the prepared zeolite catalysts by batch transesterification of *Jatropha curcas* and waste cooking oils.

1.4   Research questions

1. What are the qualities of zeolites obtained using kaolin and Kenyan volcanic ash as sources of aluminosilicates in the hydrothermal reaction process?

2. What is the optimized pre-treatment condition for kaolin that will lead to full conversion of the crystalline aluminosilicates of kaolin to ions?

3. What are the kaolin and Kenyan volcanic ash derived zeolites together with natural zeolites functionalized by occlusion of Na^+ ions?

4. What are the optimized conditions for the transesterification of JCO and WCO using kaolin and volcanic ash derived zeolite catalysts?

5. What are the similarities or difference in the catalytic activities exhibited by various zeolites prepared under different conditions towards transesterification of JCO and WCO?

1.5   Justification of the study

Biodiesel is a renewable, biodegradable, non-toxic and carbon neutral fuel with good engine lubricity. Using biodiesel contributes to the reduction of CO, hydrocarbons (HC) and carbon granules (smoke) emissions. *Jatropha curcas* and waste cooking oils are non-edible feedstocks thus are currently of low value to humans. On the other hand, the use of zeolites is promising because of their high surface area due to their porosity which also makes them tunable to increase their acidity or basicity.

Using natural materials for the production of zeolite catalysts is a sustainable and cost-effective method considering that they are easily obtained from the environment and that clay is the most

abundant mineral in the earth's crust. Efficient conversion of the clay mineral to free silicates and aluminates in the pre-treatment step will eliminate the current challenges with the products obtained using different sources of natural materials leading to the production of zeolites with equivalent or better properties to their commercial analogues. In this way, cost effective and sustainable catalysts can be obtained for the heterogeneous catalysis of biodiesel in a more sustainable and environmentally friendly manner.

1.6   Significance of the study

This study has led to the beneficiation and use of kaolin and volcanic ash natural materials in the synthesis of sustainable zeolite catalysts. Sustainable optimized production of green biodiesel fuel from non-edible sources has also been achieved. This process could therefore significantly lower the cost of producing both zeolites and biodiesel products. The study has also identified the best pre-treatment method for clay material with NaOH prior to hydrothermal crystallization step. This has eliminated the current problem of variations and inconsistencies in the types of zeolites produced and leading to the production of zeolites with properties comparable to commercial zeolites. In overall, cost effective and sustainable catalysts were obtained for the heterogeneous catalysis of biodiesel in a more sustainable and environmentally friendly manner and which could minimize the current over reliance on non-renewable petro-diesel fuels as a source of energy.

CHAPTER 2

LITERATURE REVIEW

This chapter provide detailed explanation and summaries of previous and relevant researches that have been conducted on zeolites and their synthesis from kaolin and volcanic ash as well as their applications in transesterification of non-edible oils of JCO and WCO.

2.1   Zeolites

Zeolites are crystalline porous aluminosilicate materials built from the tetrahedra network of silica $[SiO_4]^{4-}$ and alumina $[AlO_4]^{5-}$ ions linked to each other by the sharing of oxygen atoms (Baerlocher et al., 2007). The structural formula of zeolite is based on the crystallographic formula unit expressed as (Johnson & Arshad, 2014);

$$M_{x/n}[x(AlO_2).y(SiO_2)].wH_2O,$$
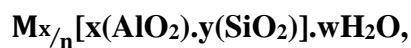
      where   M = an extra framework cation (usually group IA or IIA cation),

                              n = the valence of the cation,

                              w = the number of water molecules per unit cell,

                              x and y = the total number of tetrahedra per unit cell

Depending on the zeolite type, the ratio y/x can be as low as 1 to as high as over 100. Figure 2.1 shows the silica and alumina linkages in the zeolite formation. The Si and Al atoms forming the network structure are generally referred to as T-atoms, thus the zeolite structure can be considered as an inorganic polymer built from tetrahedra TO_4 units. The arrangement of the TO_4 tetrahedra during zeolite formation results into frameworks with pores and channels of varying dimensions depending on the zeolite type. The pores and channels are occupied by the charge balancing cations (to balance the negative charges of the Al atoms in the framework) as shown in Figure 2.1a, and molecules of water of hydration (Johnson & Arshad, 2014).

Dehydration of zeolites is largely reversible and occurs at temperatures mostly below 400 °C (Colella & Wise, 2014).

(a)

(b) Lewis acid site   Bronsted acid site
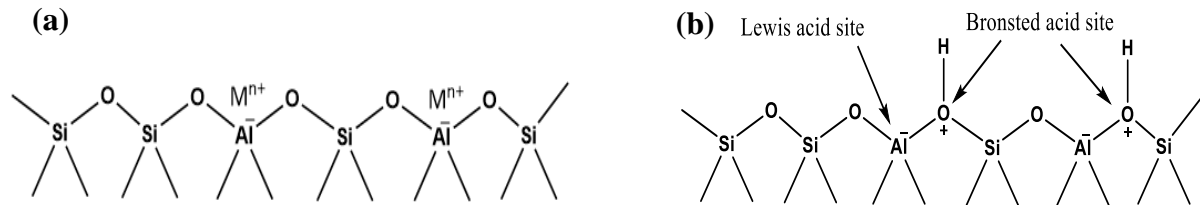
Figure 2.1; Silica and alumina linkages forming zeolite polymer structure.

Exchanging the charge balancing cations with a proton result into zeolite with both Lewis and Bronsted acid cites as shown in Figure 2.1b. In addition, the zeolite framework may be interrupted by the hydroxyl (-OH) or fluoride groups, which occupy a tetrahedron apex that is not shared with adjacent tetrahedra (Colella & Wise, 2014). Zeolites exist as natural as well as synthetic.

2.1.1   History of zeolites

The first natural zeolite mineral (stilbite) was discovered by Cronstedt, who was a Swedish mineralogist, in 1756 (Colella & Gualtieri, 2007). The name zeolite was derived from Greek words 'zeo' and 'lithos' meaning 'boiling stone' because they showed visible loss of water when they were heated. All other minerals which showed such property were subsequently called zeolites. Zeolites, especially chabazite was being used in sorption and molecular sieve applications because of its stability to dehydration, large pore volume and its pore size (Milton, 1989).

Discovery of natural zeolites was followed by the artificial mimicking of the geological conditions in which natural zeolites are formed (i.e., high temperature hydrothermal reactions). The first attempt in the zeolite synthesis was made in 1862 by St. Claire-Deville (Millini & Bellussi, 2017). However, it was not until 1940s when research on massive synthesis of zeolites was intensified. Despite the numerous synthesis attempts, the first synthetic zeolitic material with chabazite-like sorptive properties was synthesized in 1948 by Barrer (Barrer, 1948). The breakthrough in zeolite synthesis led to the subsequently new discoveries and the beginning of synthetic zeolite market. Zeolites A, B (now P), C (now HS) and X were all discovered by the end of 1949 by Milton and co-workers at the Union Carbide Corporation (Milton, 1989; Rabo & Schoonover, 2001). These zeolites were commercialized for gas and liquid separation and purification of materials. By mid-1950, a reproducible method for the synthesis of pure zeolite X had been achieved by Milton. This was followed almost immediately by the synthesis of chabazite, by Milton, in 1950-1951 (Milton, 1989) and zeolite Y, by Breck, in 1954 (Colella & Wise, 2014). The period between 1954-1980 saw a massive development and exploration of zeolites with varying SiO_2/Al_2O_3 ratios such as ZSM-5. The discovery of high silica ZSM-5 by Mobil in 1972 (Nastro & Aiello, 1989) led to a number of catalytic uses. It is estimated that at least 150 synthetic zeolites have been synthesized to date. However, the current interest and research have shifted to the synthesis of zeolites using sustainable and low-cost materials such as clay minerals and other natural and waste materials rich in aluminosilicates.

2.1.2 Zeolite frameworks

During zeolite framework formation, the TO_4 tetrahedra are arranged and oriented in such a manner that pores and channels are created in the framework. Each existing zeolite framework is assigned a letter code by the International Zeolite Association (IZA) Structure Commission irrespective of their composition (Baerlocher & McCusker, 2017). For example, SOD represent

all materials with sodalite topology. LTA represents all Linde Type A zeolite series with LTA topology, FAU represents all faujasite zeolite series with a FAU topology while GIS represents all gismondine zeolite series with a GIS topology. Heulandite are zeolite series with the HEU framework topology in which the Si/Al molar ratio is < 4, besides, clinoptilolite minerals also represents zeolites with the HEU framework topology but having a Si/Al molar ratio of ≥ 4 (Colella & Wise, 2014). Figure 2.2 show the framework structures of hydroxysodalite zeolite (HS) and zeolite P (GIS).
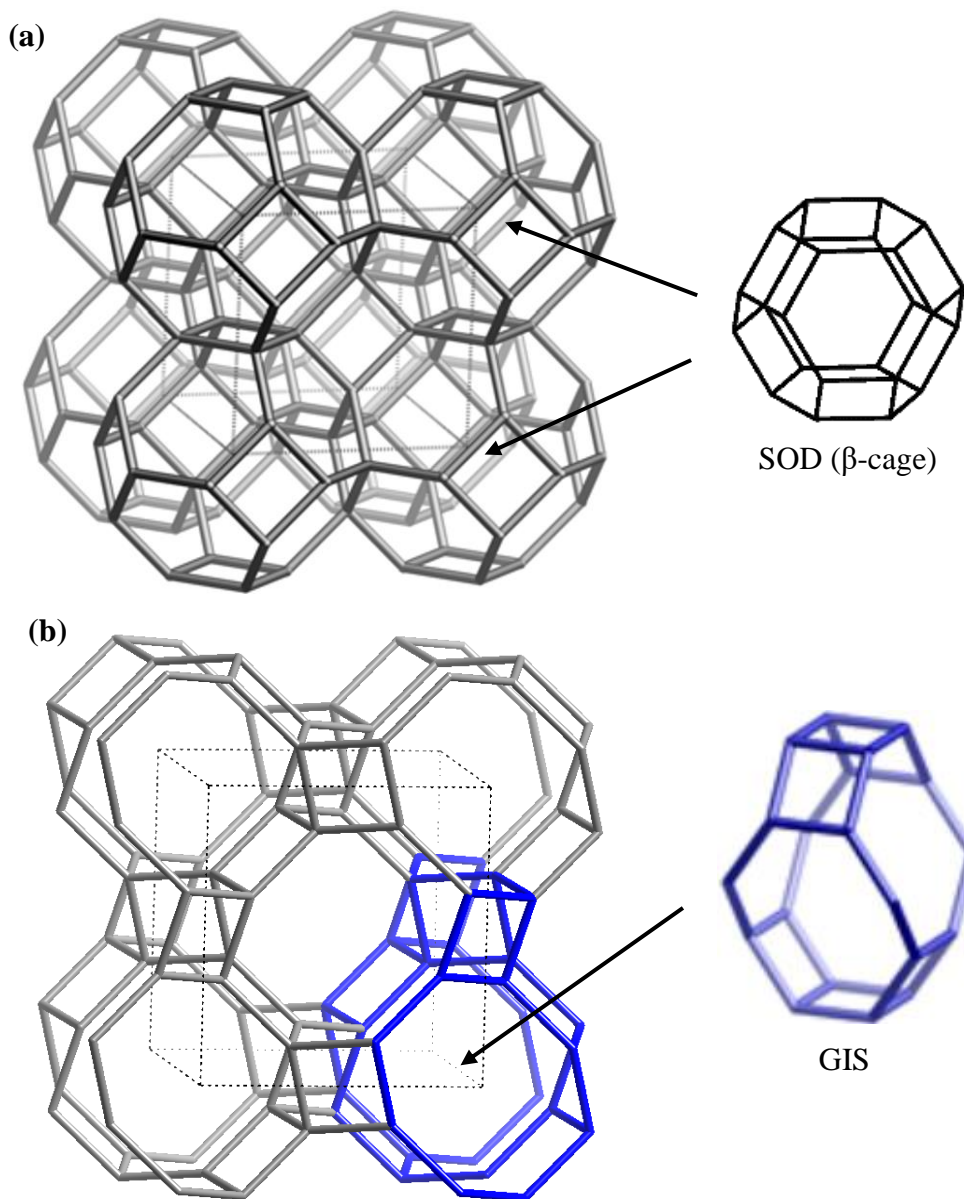
Figure 2.2; Framework structures of; (a). Hydroxyodalite (SOD), and (b). Gismondin (GIS) (Images generated using CrystalMaker®).

The hydroxysodalite framework consists of four SOD cages derived from single 6-rings (Baerlocher et al., 2007). The SOD cages are arranged such that a 6-ring aperture is formed on the framework. On the other hand, GIS framework is built from 4-rings and 8-rings secondary building units, and making double crankshaft chain (DCC) or GIS cage composite building units (Baerlocher et al., 2007). The GIS/ DCC units arranges in such a way that 8-ring pore channels in the [100] and [010] planes are created and having pore dimensions of 3.1 x 4.5 Å and 2.8 x 4.8 Å, respectively.

2.1.3 Zeolite synthesis

The primary building units (PBUs) of zeolites are the silicate $[SiO_4]^{4-}$ and aluminate $[AlO_4]^{5-}$ ions forming the non-chiral chain like secondary building units (SBUs) (Yahaya et al., 2014) containing up to 16 T-atoms (Mozgawa et al., 2011) linked through oxygen bridges. Some of the selected secondary building units for zeolites syntheses are shown in Figure 2.3.
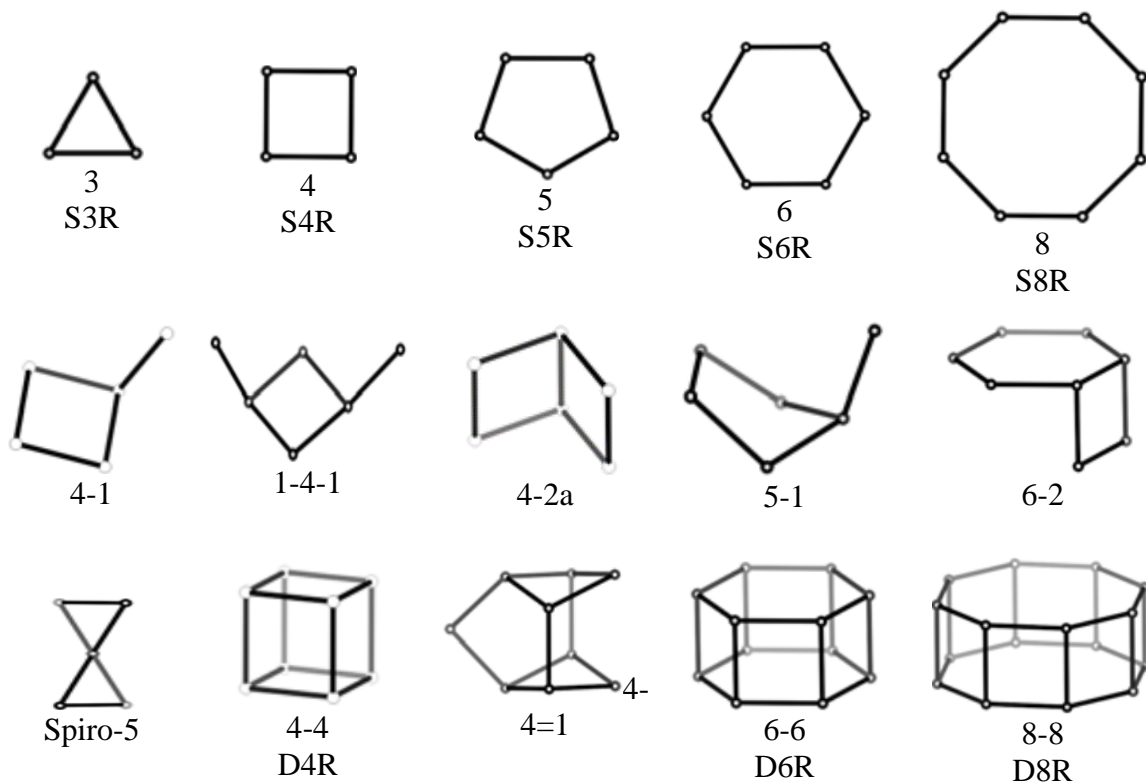
Figure 2.3; Some selected secondary building units (SBUs) (Baerlocher et al., 2007).

The wide variety of possible synthetic zeolite framework structures are therefore due to a large number of ways in which the PBUs and SBUs can be linked to form various polyhedral during zeolite formation. A wide variety of zeolite materials with desired properties and varying framework structure, chemical composition, pore dimensions and channel distributions are therefore obtained depending on the conditions of zeolite formation. The mechanism of structure building for zeolites is shown in Figure 2.4.
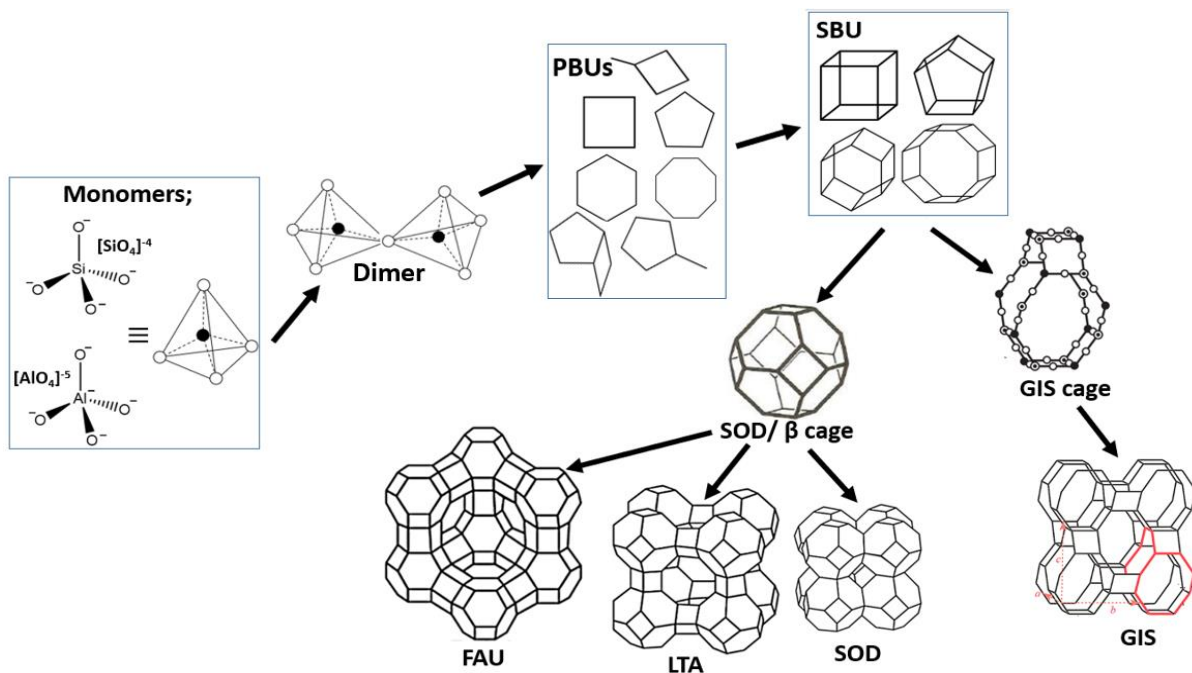
Figure 2.4; Mechanism of zeolite synthesis via PBUs, SBUs and composite building units, modified from (Lima et al., 2019).

The major requirements for zeolite synthesis are the silica and alumina sources because they are the structural building units in zeolite formation. Other requirements are mineralizing agent (alkali) and structure-directing agent (SDA) (Moneim & Ahmed, 2015; Taborda et al., 2011; Zhu et al., 2014). Structure-directing agents are used as pore size and pore volume determinants during synthesis. However, many syntheses have been achieved without SDAs and still produced zeolites with desired properties (Sang et al., 2004; Yilmaz et al., 2013).

Different methods have been reported for the synthesis of zeolites, these include; hydrothermal synthesis, molten salt, microwave assisted, as well as alkali activation methods (Makgabutlane et al., 2020; Park et al., 2000; Ríos et al., 2012; Ríos et al., 2009; Rios et al., 2007). Hydrothermal synthesis method is the most common method as it reflects the natural conditions in which natural zeolite minerals are formed. Hydrothermal process involves the treatment of silica and alumina with an alkaline solution to dissolve and gelatinize the components before crystalizing at low temperatures, usually below 350 °C, and elevated pressure, usually in an autoclave (Król, 2020).

2.1.4 Natural zeolites

Natural zeolites are mainly of volcanic origin where they are formed hydrothermally. Natural zeolites occur both in crystalline forms, in igneous and metamorphic rocks, as well as in grains of smaller diameters accumulated in sedimentary rocks (Król, 2020). They are formed as a result of the reaction of volcanic ash components with the basic waters. In addition, the formation of natural zeolites is not restricted to aluminosilicate minerals, because the tetrahedral 'T' position in the framework may be occupied by cations other than Si and Al, such as Be, P, Zn or others (Colella & Wise, 2014).

Natural zeolites are a plentiful resource and are inexpensive to mine since majority of deposits are found close to the earth's surface. According to the 2013 Handbook of Natural Zeolites, a special publication by International Zeolite Association, there are 93 zeolite mineral species belonging to 44 different frameworks and 3 unassigned frameworks (Colella & Wise, 2014). Some of the minerals with their chemical formula and framework codes are listed in Table 2.1. Some zeolites, such as chabazite, clinoptilolite, ferrierite, heulandite and phillipsite among others consists of two or more species that are distinguished on the basis of the most abundant of the channel cations.

Table 2.1; Names, general formulae, and framework types of some accepted zeolites (Colella & Wise, 2014).

Name	General formula	Framework-type code
Amicite	$\lvert K_4Na_4(H_2O)_{10}\rvert$ $[Al_8Si_8O_{32}]$	GIS
Ammonioleucite	$\lvert (NH_4)\rvert[AlSi_2O_6]$	ANA
Analcime	$\lvert Na(H_2O)\rvert$ $[AlSi_2O_6]$	ANA
Barrerite	$\lvert Na_8(H_2O)_{26}\rvert$ $[Al_8Si_{28}O_{72}]$	STI
Boggsite	$\lvert (Ca_{0.5},Na,K)_{18}(H_2O)_{70}\rvert$ $[Al_{18}Si_{78}O_{192}]$	BOG
Chabazite series	$\lvert (Ca_{0.5},Na,K)_x(H_2O)_{12}\rvert$ $[Al_xSi_{12-x}O_{24}]$ x = 2.4–5.0	CHA
Chabazite-Ca	$\lvert (Ca_{0.5},K,Na)_x(H_2O)_{12}\rvert$ $[Al_xSi_{12-x}O_{24}]$ x = 2.4–5.0	CHA
Chabazite-K	$\lvert (K,Na,Ca_{0.5})_x(H_2O)_{12}\rvert$ $[Al_xSi_{12-x}O_{24}]$ x = 3.0–4.5	CHA
Chabazite-Na	$\lvert (Na,K,Ca_{0.5})_x(H_2O)_{12}\rvert$ $[Al_xSi_{12-x}O_{24}]$ x = 2.5–4.8	CHA
Clinoptilolite series	$\lvert (Na,K,Ca_{0.5},Mg_{0.5})_6(H_2O)_{20}\rvert$ $[Al_6Si_{30}O_{72}]$	HEU
Clinoptilolite-Ca	$\lvert (Ca_{0.5},Na,K,Sr_{0.5},Ba_{0.5},Mg_{0.5})_6(H_2O)_{20}\rvert$ $[Al_6Si_{30}O_{72}]$	HEU
Clinoptilolite-K	$\lvert (K,Na,Ca_{0.5},Sr_{0.5},Ba_{0.5},Mg_{0.5})_6(H_2O)_{20}\rvert$ $[Al_6Si_{30}O_{72}]$	HEU
Clinoptilolite-Na	$\lvert (Na,K,Ca_{0.5},Sr_{0.5},Ba_{0.5},Mg_{0.5})_6(H_2O)_{20}\rvert$ $[Al_6Si_{30}O_{72}]$	HEU
Epistilbite	$\lvert (Ca,Na_2)_3(H_2O)_{16}\rvert$ $[Al_6Si_{18}O_{48}]$	EPI
Ferrierite series	$\lvert (K,Na,Mg_{0.5},Ca_{0.5})_6(H_2O)_{20}\rvert$ $[Al_6Si_{30}O_{72}]$	FER
Ferrierite-K	$\lvert (K,Na,Mg_{0.5},Ca_{0.5})_6(H_2O)_{20}\rvert$ $[Al6Si_{30}O_{72}]$	FER
Ferrierite-Mg	$\lvert (Mg_{0.5},K,Na,Ca_{0.5})_6(H_2O)_{20}\rvert$ $[Al_6Si_{30}O_{72}]$	FER
Ferrierite-Na	$\lvert (Na,K,Mg_{0.5},Ca_{0.5})_6(H_2O)_{20}\rvert$ $[Al_6Si_{30}O_{72}]$	FER
Garronite	$\lvert (Ca_{0.5},Na)_6(H_2O)_{14}\rvert$ $[Al_6Si_{10}O_{32}]$	GIS
Gismondine	$\lvert Ca_4(H_2O)_{18}\rvert$ $[Al_8Si_8O_{32}]$	GIS
Gobbinsite	$\lvert Na_5(H_2O)_{12}\rvert$ $[Al_5Si_{11}O_{32}]$	GIS
Gonnardite	$\lvert (Na,Ca_{0.5})_{8+x}(H_2O)_{12}\rvert$ $[Al_{8+x}Si_{12-x}O_{40}]$ x = 0.0–2.0	NAT
Harmotome	$\lvert (Ba_{0.5},Ca_{0.5},K,Na)_5(H_2O)_{12}\rvert$ $[Al_5Si_{11}O_{32}]$	PHI
Heulandite series	$\lvert (Ca_{0.5},Sr_{0.5},Ba_{0.5},Mg_{0.5},Na,K)_9(H_2O)_{24}\rvert$ $[Al_9Si_{27}O_{72}]$	HEU
Heulandite-Ca	$\lvert (Ca_{0.5},Sr_{0.5},Ba_{0.5},Mg_{0.5},Na,K)_9(H_2O)_{24}\rvert$ $[Al_9Si_{27}O_{72}]$	HEU
Heulandite-Na	$\lvert (Na,Ca_{0.5},Sr_{0.5},Ba_{0.5},Mg_{0.5},K)_9(H_2O)_{24}\rvert$ $[Al_9Si_{27}O_{72}]$	HEU
Heulandite-K	$\lvert (K,Ca_{0.5},Sr_{0.5},Ba_{0.5},Mg_{0.5},Na)_9(H_2O)_{24}\rvert$ $[Al_9Si_{27}O_{72}]$	HEU
Kirchhoffite	$\lvert Cs\rvert$ $[BSi_2O_6]$	ANA
Laumontite	$\lvert Ca_4(H_2O)_{18}\rvert$ $[Al_8Si_{16}O_{48}]$	LAU
Leucite	$\lvert K\rvert$ $[AlSi_2O_6]$	ANA
Stilbite series	$\lvert (Ca_{0.5},Na,K)_9(H_2O)_{30}\rvert$ $[Al_9Si_{27}O_{72}]$	STI
Stilbite-Ca	$\lvert (Ca_{0.5},Na,K)_9(H_2O)_{30}\rvert$ $[Al_9Si_{27}O_{72}]$	STI
Stilbite-Na	$\lvert (Na,K,Ca_{0.5})_9(H_2O)_{30}\rvert$ $[Al_9Si_{27}O_{72}]$	STI
Phillipsite series	$\lvert (K,Na,Ca_{0.5})_x(H_2O)_{12}\rvert$ $[Al_xSi_{16-x}O_{32}]$ x = 3.8–6.4	PHI
Phillipsite-Na	$\lvert (Na,K,Ca_{0.5})_x(H_2O)_{12}\rvert$ $[Al_xSi16\ xO_{32}]$ x = 3.7–6.7	PHI
Phillipsite-K	$\lvert (K,Na,Ca0.5)_x(H_2O)_{12}\rvert$ $[AlxSi_{16-x}O_{32}]$ x = 3.8–6.4	PHI
Phillipsite-Ca	$\lvert (Ca0.5,K,Na)_x(H_2O)_{12}\rvert$ $[AlxSi_{16-x}O_{32}]$ x = 4.1–6.8	PHI
Pollucite	$\lvert (Cs,Na)(H_2O)_n\rvert$ $[AlSi_2O_6]$ (Cs + n = 1)	ANA
Mordenite	$\lvert (Na_2,Ca,K_2)_4(H_2O)_{28}\rvert$ $[Al_8Si_{40}O_{96}]$	MOR

Mineable zeolite deposits are widespread in many countries across the world. The most common natural zeolites are clinoptilolite-heulandite, mordenite, chabazite, analcime and phillipsite (Marantos et al., 2012). Because of the natural environment where they are obtained, natural zeolites may contain impurities such as metal oxides, quartz, mica as well as other types of zeolite minerals (Kraljević Pavelić et al., 2018). These impurities in natural zeolites may enhance or reduce the catalytic capability of natural zeolites (Y. Li et al., 2017; Patil & Deng, 2009).

Despite the advantages such as easy availability and low cost, natural zeolites have not been fully utilized in various industrial applications because of the impurities, non-uniform pore openings and channels as well as their low ion exchange capacities (De Souza et al., 2018). However, with efficient pre-treatment and structure tuning, natural zeolites can be useful catalysts for various chemical reactions.

2.1.4.1 Zeolite clinoptilolite (HEU)

Clinoptilolite zeolite has heulandite framework topology and a Si/Al molar ratio of ≥ 4. Clinoptilolite zeolites are classified by the dominant exchangeable cation such as Ca, K and Na among other cations as shown in Table 2.1. Figure 2.5 shows the framework structure of clinoptilolite (HEU) zeolite.

The framework structure is formed by linking 4-4=1 secondary building units. The arrangement of the primary and secondary building units in clinoptilolite results into crystals structures exhibiting numerous pores and channels with varying sizes. The dimensions of the three channels found in clinoptilolite framework structure, labelled A, B and C in Figure 2.5, are 3.1 x 7.5 Å (10-ring), 3.6 x 4.6 Å (8-ring) and 2.8x 4.7 Å (8-ring), respectively (Baerlocher et al., 2007). The dimensions are however, variable because of considerable flexibility of framework. Channels A and B are parallel to each other and are intersected by channel C.

18
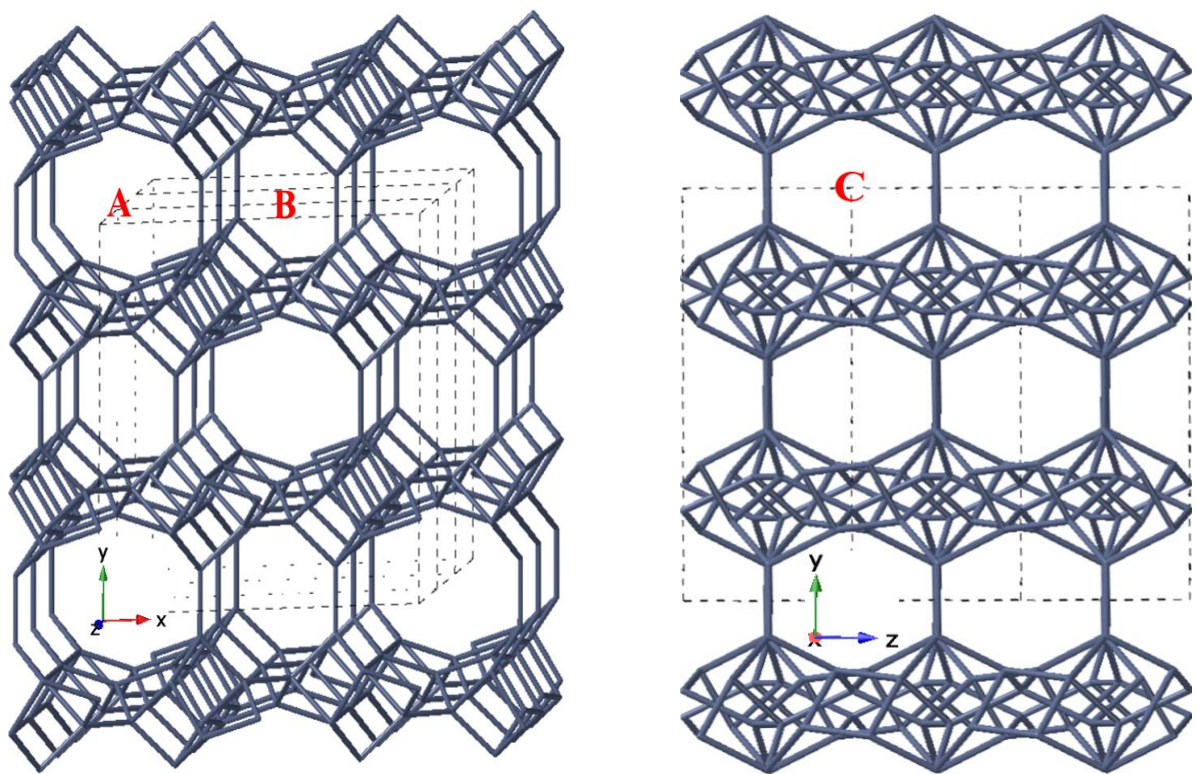
Figure 2.5; Framework structure of clinoptilolite (HEU) zeolite (Image generated using CrystalMaker®).

2.1.5 Synthetic zeolites

Although natural zeolite mineral species were the first to be discovered, to date there are more than one hundred different types of zeolite structures which have been obtained synthetically (Król, 2020). Synthetic zeolites are the commonly used group of zeolites because of their purity and uniformity of the particle sizes.

Despite their wide use, in comparison to the natural zeolites, the current use of costly commercially available sources of aluminosilicates raw materials may drive the cost of synthetic zeolite materials, and therefore the processes utilizing these zeolites, high. Alternative natural resources and recycled wastes, such as natural clays (Musyoka et al., 2014; Ríos et al., 2012), fly ash (Volli & Purkait, 2015), volcanic ash, rice husks (Cheng et al., 2012) and sewage sludge (Zhang et al., 2018) among others, which are rich in silica and alumina have

been tested. Natural clays and volcanic ash that are abundant in the earth's crust stand to be the best substitute for the long-term sustainability. Among clays, kaolin is more preferred because of its high aluminosilicate content and relative purity compared to other clay minerals (Huggett, 2005). Of interest to this study are therefore kaolin and volcanic ash materials.

2.1.5.1 Zeolite A (LTA)

Zeolite A belong to the Linde type A (LTA) family. It is a low silica zeolite with a SiO_2/Al_2O_3 molar ratio of 1.8-2.0, and having cubical crystal particles represented by the unit cell chemical formula: $|Na_{12} (H_2O)_{27}|_8[Al_{12}Si_{12} O_{48}]_8$ (Baerlocher et al., 2007). Zeolites A are classified into, 3A, 4A and 5A, representing K-A, Na-A and Ca-A zeolites, respectively. The LTA framework structure, shown in Figure 2.6, is formed by linking 4-ring, 6-ring, 8-ring, 4-4 or 1-4-1 secondary building units.
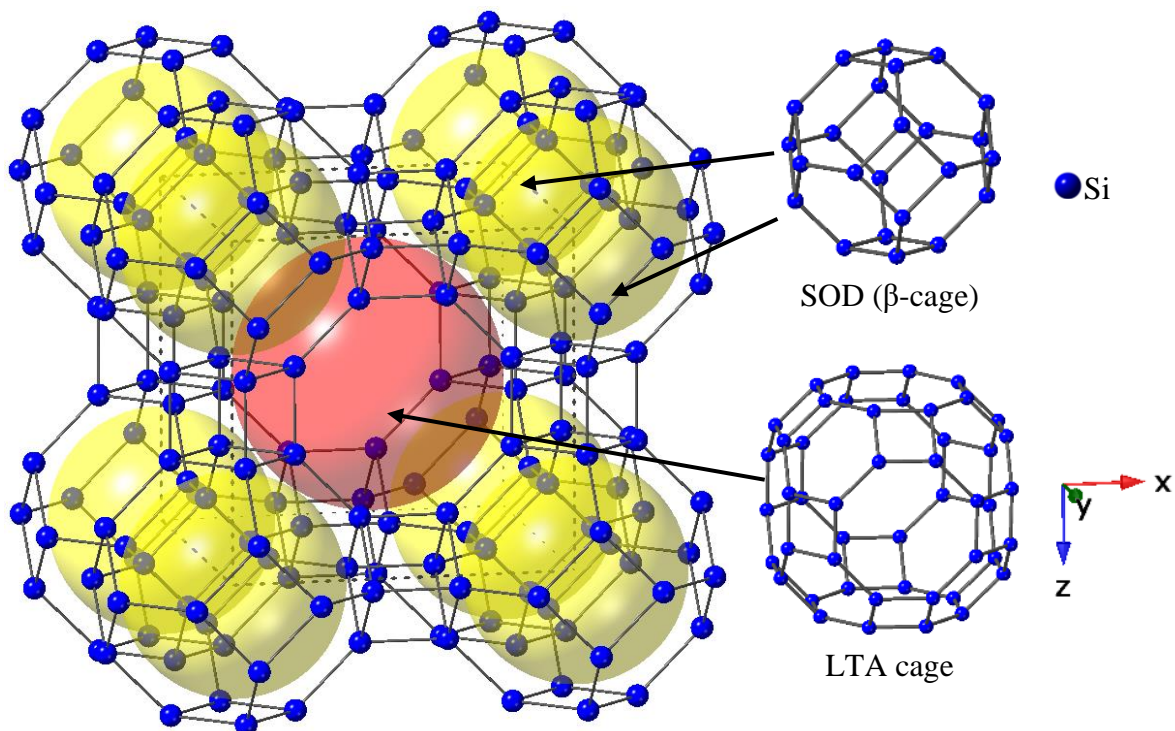
Figure 2.6; Framework structure of zeolite A (LTA), (Images generated using CrystalMaker®).

Linde Type A (LTA) zeolite frameworks are characterized by the presence of double 4-membered rings (D4R) and LTA cages. The arrangement of the D4R and SOD cages in the LTA framework structure results in LTA cages with 8-ring pore openings of 4.1 x 4.1 Å dimensions (Baerlocher et al., 2007).

2.1.5.2 Zeolite X and Y (FAU)

Faujasite (FAU) zeolites comprises zeolite X and zeolite Y which have the same frameworks. Faujasites are high silica zeolites, compared to zeolite A, with a SiO_2/Al_2O_3 molar ratio of 2.2-3.0 and 5-10 for zeolite X and Y, respectively (Ruren et al., 2008). Their cubic particles are represented by the unit cell chemical formula: $|(Ca,MgNa_2)_{29}(H_2O)_{240}|[Al_{58}Si_{134}O_{384}]$ (Baerlocher et al., 2007). FAU framework structure, shown in Figure 2.7, is formed by linking 4-ring, 6-ring, 4-2, 6-2, 6-6 or 1-4-1 secondary building units.

SOD (β-cage)

● Si
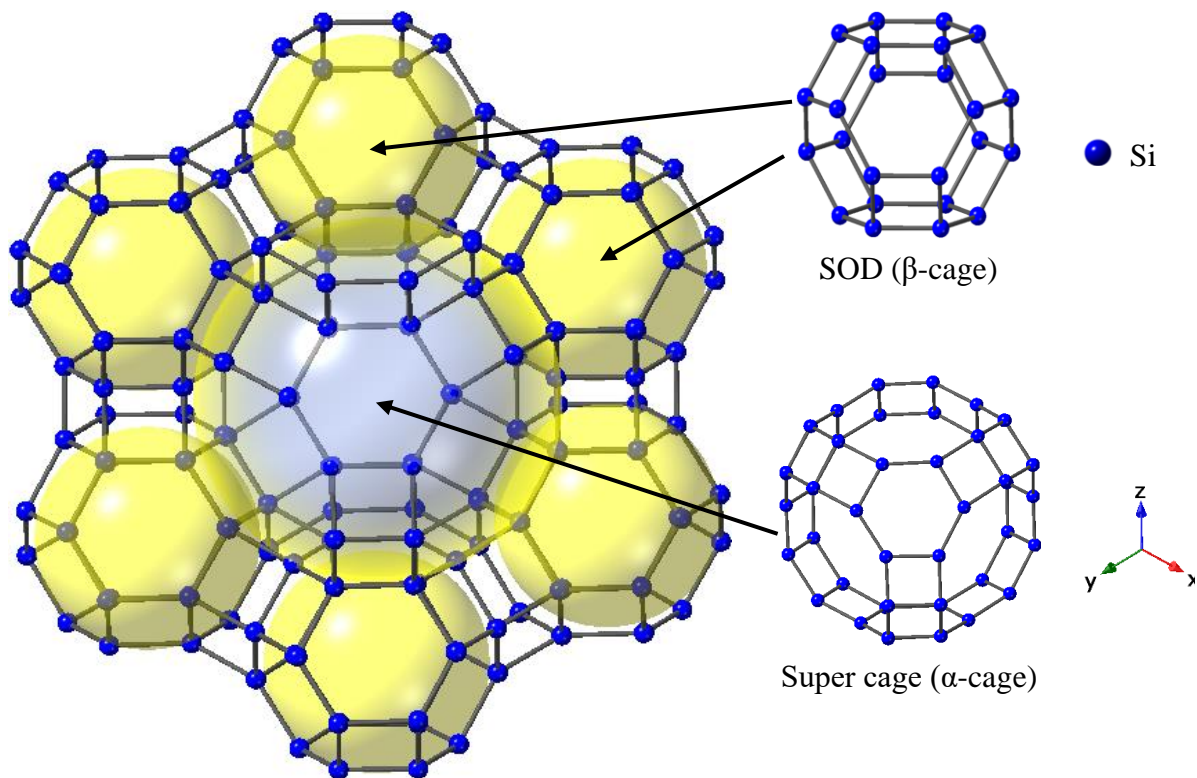
Super cage (α-cage)

Figure 2.7; Framework structure of faujasite (FAU), (Images generated using CrystalMaker®).

Faujasite zeolites frameworks are characterized by the presence of double 6-membered rings (D6R), sodalite cavity and a super cage (Sen et al., 2014). The arrangement of D6R and SOD cages in the faujasite framework structure results in super cages with 12-ring pore openings of 7.4 x 7.4 Å dimensions (Baerlocher et al., 2007). Besides, each unit cell has 8 super cages, 8 SOD cavities, 16 D6Rs, 16 12-rings, and 32 single 6-rings (S6Rs) (Sen et al., 2014).

2.1.6   Modification of zeolites

In order to obtain zeolitic materials with desired properties, modifications are usually carried out during synthesis process by varying the SiO_2/Al_2O_3 molar ratio of the zeolite (Kosanović et al., 2011). In addition, zeolites exhibit a high concentration of active sites because of their high porosity. The pores and channels are utilized in the post synthesis modification processes in the occlusion of guest atoms and compounds within the zeolite structure framework to improve zeolite properties to suit the intended applications (Baroi et al., 2014; Bi-Zeng et al., 2003; Li et al., 2014).

The charge balancing cations can also be reversibly exchanged with other cations by passing aqueous solutions of desired cation through the channels and voids (Georgiev et al., 2009). If H^+ ions are the charge balancing cations, then Bronsted acid sites are generated, see Figure 2.1b. Besides, the Al^{3+} ions have the tendency of acquiring pairs of electrons to fill their vacant p orbitals resulting in the formation of Lewis acid sites. In order to activate and increase their catalytic activity as well as to remove organic elements within the zeolite framework, modified zeolite catalysts are calcined at moderate temperatures prior to use (Helwani et al., 2016).

2.1.7   Applications of zeolites

Both natural and synthetic zeolites are widely used materials in various sectors such as industrial, agricultural as well as health, among others. The wide area of application is due to

their unique structure as well as chemical and physical properties. They are low density materials possessing defined channels and chambers and exhibiting high crystallinity, ion exchange capacity, sorption capacity of other molecules and high surface area and pore volume (Król, 2020).

Zeolites are used in adsorption of gasses (Wang et al., 2019; Warzybok & Warchoł, 2018), adsorption of ions from solutions (Cao et al., 2020; Pereira et al., 2018), catalysis (Dziedzicka et al., 2016), medical applications (Kraljević Pavelić et al., 2018), ion exchange (Covarrubias et al., 2006), water softening (Aragaw & Ayalew, 2018; Bessa et al., 2017) and as soil conditioners to improve soil chemical and physical properties (Cataldo et al., 2021). Some of the zeolite applications are summarized in Figure 2.8.
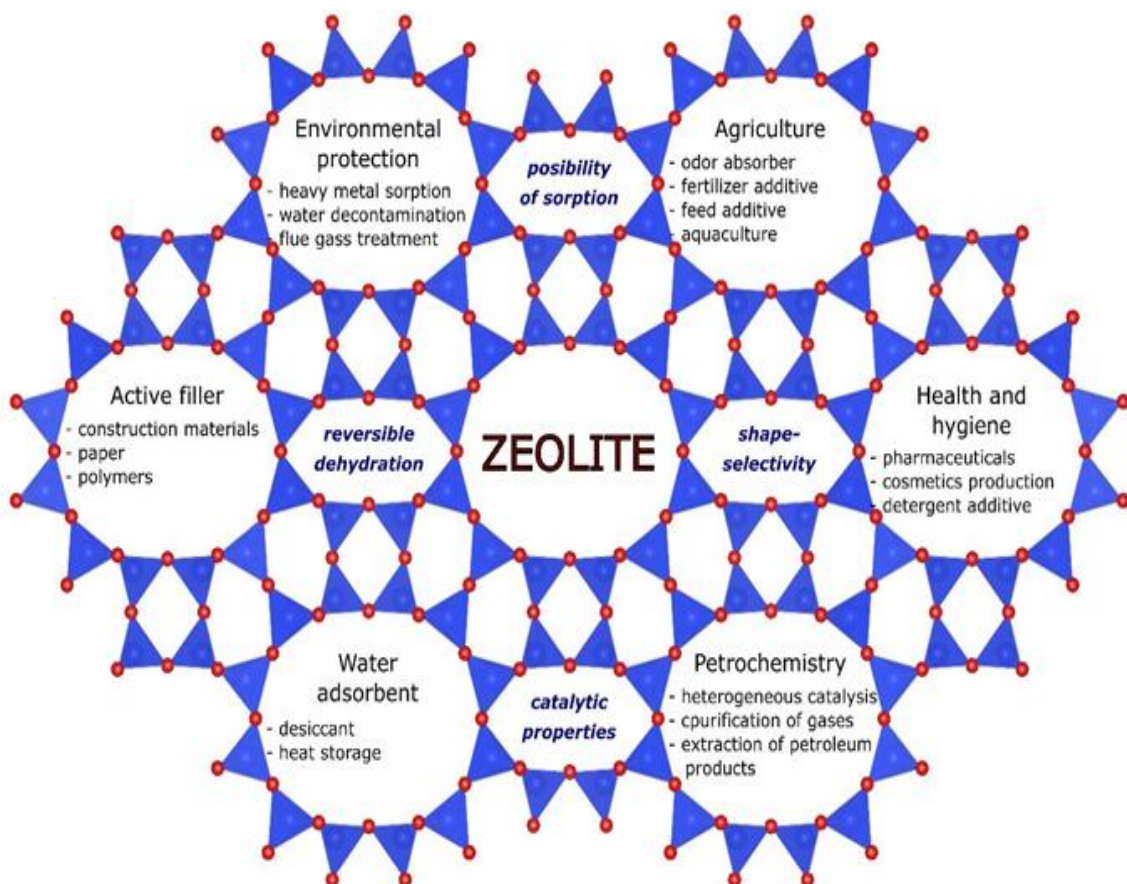
Figure 2.8; Zeolites applications, adopted from (Król, 2020).

2.2   Clay minerals

Clay minerals are also crystalline aluminosilicates. However, unlike zeolites, clays have a layered structure and is subject to swelling and shrinking as water is absorbed and removed between its layers. The framework structures of selected clay minerals are shown in Figure 2.9.
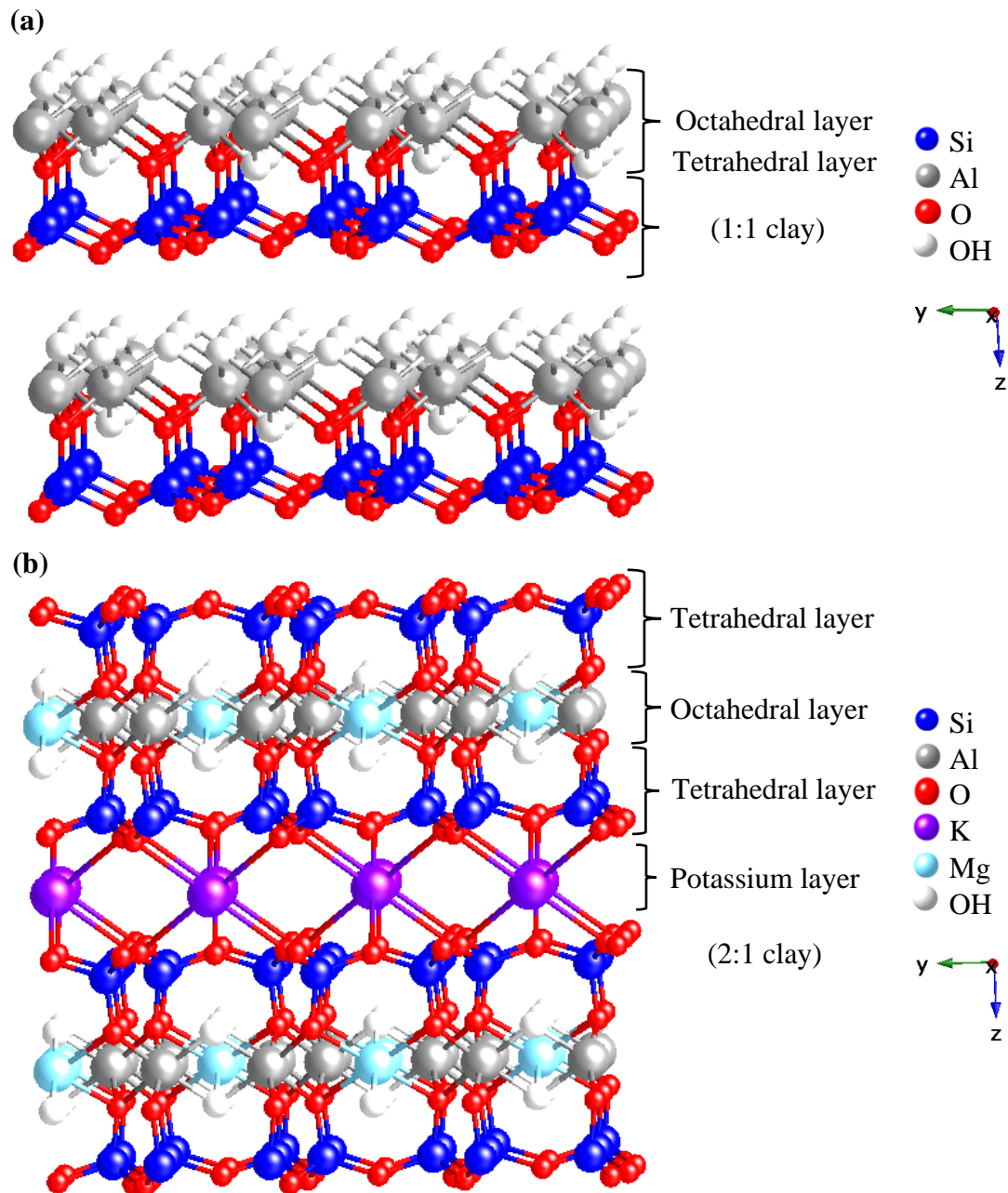
Figure 2.9; Framework structures of selected clay minerals; (a). Kaolin (1:1), and (b). Montmorillonite (2:1) (Images generated using CrystalMaker®).

The two-dimensional tetrahedral sheets are formed by TO_4 tetrahedra with each tetrahedron sharing three of its vertex oxygen atoms with other tetrahedra leading to a hexagonal array in two-dimensions (Vaculikova et al., 2011). The unshared fourth vertex of all the tetrahedra point in the same direction and are separated from other sheets by octahedral sheets formed from small cations, such as Al^{3+} and Mg^{2+}, coordinated by six oxygen atoms.

Clays consisting of Si octahedral sheet sandwiched between two Al tetrahedral sheets, Figure 2.9a, are commonly referred to as 1:1 clays while those consisting of two Si tetrahedral sheets with the unshared vertex of each sheet pointing towards each other and forming each side of the Al or Mg octahedral sheet, Figure 2.9b, are referred to as 2:1 clays (Vaculikova et al., 2011). Kaolin is an example of a 1:1 clay while illite and montmorillonite are 2:1 clay. The 2:1 clay has a net negative charge compensated by the K^+ ions sandwiching two layers.

2.2.1 Kaolin

Kaolin consists of the mineral kaolinite which has a chemical formula; $Al_2O_3.2SiO_2.2H_2O$, and SiO_2/Al_2O_3 molar ratio of 2 in addition to trace oxides of Fe, Ti, K, Mg and mica (Nyakairu et al., 2001). Kaolin is formed from the decomposition or weathering of feldspars and aluminium silicates. It exists in white, greyish-white, or slightly coloured forms. Kaolin structure (Figure 2.9a) is electrically neutral and the tetrahedra-octahedra layers are held together by van der Waals' bonds forming a single layer. In addition, kaolin is chemically stable with a low expansion coefficient. Water molecules, if present, sandwiches the neutral layers.

2.2.2 Synthesis of zeolites using kaolin

Kaolin materials are suitable for use as silica and alumina source in zeolite synthesis because of their high silica and alumina contents purity. The hydrothermal reaction of raw kaolin with NaOH solution was done by Rios and co-workers (Ríos et al., 2009; Rios et al., 2007) and

Kallai and Lapides (Heller-Kallai & Lapides, 2007; Lapides & Heller-Kallai, 2007). However, due to its crystallinity, kaolin was not fully dissolved to free ions during the alkaline dissolution step. A mixture of hydroxysodalite and cancrinite, products of high SiO_2/Al_2O_3 ratio and low NaOH concentrations, were therefore obtained alongside mixtures of other zeolite phases. The composition of the products also differed from one type of clay to the other (Heller-Kallai & Lapides, 2007). In order to overcome the problems of dissolution, the less reactive crystalline kaolinite is converted to a more reactive amorphous phase by metakaolinization through calcination at temperatures above its dehydroxylation temperature to metakaolinite (Kazemimoghadam, 2016) in the reaction given by equation (1):

$$Si_2Al_2O_5(OH)_4 \xrightarrow[Heat]{} Al_2O_3.2SiO_2 \quad + \quad 2H_2O \quad\quad (1)$$

Kaolin   Metakaolinite
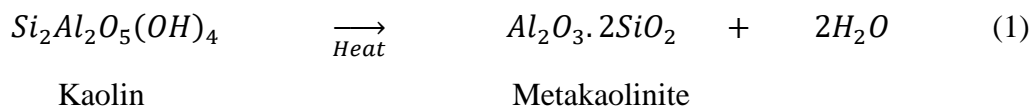
The reaction leads to the transformation of hydroxyls into two water molecules leaving two oxygen atoms in the final amorphous aluminosilicate products represented by equation (2).

$$4\,(OH)^- \rightarrow 2\,H_2O + 2\,O^{2-} \quad\quad\quad\quad\quad\quad\quad\quad\quad\quad\quad\quad (2)$$

The challenge with MK method is that different sources of clays have different grades of kaolinite with varying impurities such as muscovite mica and quartz among others. Quartz impurity, for example, is thermally stable and is not easily broken down within the MK conditions (Zhou et al., 2013). Thus, conversion of these impure materials, yet rich in silica, through MK to pure aluminosilicate ions for the production of quality and pure zeolites is

inefficient hence necessitating the need for pre-purification of kaolinite minerals to remove the thermally stable impurities. This process is cumbersome and costly.

Heating kaolin at high temperature in an alkaline media in the fusion method completely breaks down the kaolinite structure in clays to fused-metakaolinite (F-MK) (N. Li et al., 2017). It also promotes the dry reactions between the mineral phases present in the kaolinite including quartz and the alkaline activator leading to high dissolution of aluminates and silicates (Ayele et al., 2016; Ríos et al., 2012) in addition to producing more crystalline zeolite products (Zayed et al., 2017). A review of studies was done where kaolin is used as a starting material for the synthesis of zeolites via MK and F-MK methods, kaolin pre-treatment conditions as well as the resulting products and the review is presented in Table 2.2.

The review in Table 2.2 shows that different zeolite structures are formed from the two methods of kaolin treatment. Bahgaat et al., 2020 recently reported synthesis of zeolite Y from impure Egyptian kaolin prepared via MK without modification of the synthesis hydrogel. However, previous studies have shown that such MK hydrogels prepared without prior modification of their chemical compositions in most cases favour the formation of zeolite LTA (Ayele et al., 2016; Foroughi et al., 2021; Maia et al., 2019; Pereira et al., 2018; Ríos et al., 2012). In contrast, the fusion of kaolin to F-MK without further modification of the synthesis hydrogel composition, and therefore having the same hydrogel composition as in the MK hydrogels, was found in most cases to favour the formation of low silica FAU structures (Anderson et al., 2017; Belviso et al., 2013; Mezni et al., 2011). In addition, synthesis of hydroxysodalite (HS) and zeolite A alongside quartz and HS impurities have been reported in some studies using F-MKs derived hydrogels used without further modification of the hydrogel composition (Ayele et al., 2016; Belviso et al., 2013; Huggett, 2005; Musyoka et al., 2014; Ríos et al., 2012; Zayed et al., 2017).

27

Table 2.2; A review of studies where kaolin was used as a starting material for the synthesis of zeolites via MK and F-MK methods.

Kaolin source	Kaolin treatment	Hydrogel modification	Hydrogel composition	Zeolite product	% Cryst	A$_{(BET)}$	V$_{(Micro)}$	Reference
Brazil	MK at 850 °C/ 2 h	Na$_2$SiO$_3$	10 g MK & 15 g NaOH in 100 g of H$_2$O	Y, P*	78 %	555	n.d	(Bortolatto et al., 2017)
Sigma	MK at 900 °C/ 0.5 h	Na$_2$SiO$_3$.5H$_2$O	Na$_2$O:Al$_2$O$_3$:SiO$_2$:H$_2$O = 3.75:1.0:2.5:243.7	X, A, P, S	n.d	436	n.d	(Covarrubias et al., 2006)
Iraq	F-MK at 850 °C/ 3 h	Na$_2$SiO$_3$	50 g F-MK & 63 g Na$_2$SiO$_3$ in 500 ml H$_2$O	Y, I[a]	n.d	390	0.11	(Doyle et al., 2016)
Egypt	Patented	Na$_2$SiO$_3$	Patented	Y, Q, MK	n.d	n.d	n.d	(El-Mekkawi & Selim, 2012)
Nigeria	MK at 600 °C/ 50 min	Na$_2$SiO$_3$	Na$_2$O: Al$_2$O$_3$:SiO$_2$: H$_2$O = 15: 1:15: 450	Y, I[a],	n.d	n.d	n.d	(Kovo et al., 2009)
South Africa	F-MK at 550 °C/ 1.5 h	-	Al$_2$O$_3$:Na$_2$O:SiO$_2$:H$_2$O = 1: 9.70: 7.79: 403.20	S	n.d	n.d	n.d	(Musyoka et al., 2014)
		Al(OH)$_3$	Al$_2$O$_3$:Na$_2$O:SiO$_2$:H$_2$O = 1:7.11:4.71:292.35	X	n.d	n.d	n.d	
Poland	MK at 800 °C/ 6 h	Silica gel	Na$_2$O:SiO$_2$:Al$_2$O$_3$:H$_2$O = 10:10:1:200	Y, Q, M, P*	n.d	n.d	n.d	(Warzybok et al., 2015)
Poland	MK at 800 °C/ 6 h	-	Na$_2$O:SiO$_2$:Al$_2$O$_3$:H$_2$O = 10:10:1:200	Y, Q	n.d	686	0.26	(Warzybok & Warchoł, 2018)
Ethiopia	MK at 600 °C/ 3 h	-	SiO$_2$:Al$_2$O$_3$:Na$_2$O:H$_2$O = 2:1:1:37	A, Q	75 %	n.d	n.d	(Ayele et al., 2016)
	F-MK at 600 °C/ 1 h	-	SiO$_2$:Al$_2$O$_3$:Na$_2$O:H$_2$O = 2:1:1:37	A, S	84 %	n.d	n.d	
Tunisia	-	Al(OH)$_3$	SiO$_2$:Al$_2$O$_3$:Na$_2$O:H$_2$O = 3.4:1:10.4:319.8	S, Q, K, I	n.d	62	-	(Mezni et al., 2011)
	Fusion at 550 °C/ 2 h	Al(OH)$_3$	SiO$_2$:Al$_2$O$_3$:Na$_2$O:H$_2$O = 3.4:1:10.4:319.8	X, A*, S*	n.d	293	0.12	
Brazil	MK at 700 °C/ 2 h	-	Na/Al & Si/Al of 1.64 & 1, H$_2$O = 15 mL	A	n.d	n.d	n.d	(Maia et al., 2019)
Algeria	F-MK at 800 °C/ 2 h	Ludox (40 wt. % SiO$_2$)	Na$_2$O:Al$_2$O$_3$:SiO$_2$:H$_2$O = 4.01:1:9.37:156	Y	n.d	626	0.26	(Djeffal et al., 2017)
India	MK at 900 °C/ 1 h	Na$_2$SiO$_3$	SiO$_2$/Al$_2$O$_3$ = 7.5-15; Na$_2$O/SiO$_2$ = 0.5-1 and H$_2$O/Na$_2$O = 20-30	Y, P, P*	n.d	490	n.d	(Chandrasekhar & Pramada, 2004)
Jordan	MK at 650 °C/ 2 h	-	MK/NaOH solution of 1.0 g/25 mL	A, Q, S	n.d	n.d	n.d	(Gougazeh & Buhl, 2014)
England	F-MK at 600 °C/ 1 h	-	4.40 g F-MK in 21.5 mL water	A	n.d	n.d	n.d	(Ríos et al., 2012)
Egypt	MK at 800 °C/ 6 h	-	10 g MK in 100 mL of 1 M NaOH	Y, P	n.d	n.d	n.d	(Bahgaat et al., 2020)
Ghana	F-MK at 600 °C/ 2 h	-	F-MK/water in 1:5 w/w	X, Q, A*	n.d	389	0.84	(Anderson et al., 2017)
Brazil	F-MK at 700 °C/ 2 h	Na$_2$SiO$_3$	8.72 g MK, 16.63 g Na$_2$SiO$_3$, 6.28 g NaOH	Y	n.d	n.d	n.d	(Castro et al., 2019)

FAU = faujasite zeolite, ANA = analcime, SDA = structure directing agent, A = zeolite A, X = zeolite X, Y = zeolite Y, Q = quartz, S = hydroxysodalite, P = philipsite, M = muscovite, I = illite, K = kaolin, n.d = not done, A$_{(BET)}$ = BET surface area, V$_{\mu \text{ pore}}$ = t-plot micropore volume

* identified impurity, [a] unidentified impurity

On the other hand, modification of the synthesis hydrogels by addition of an extra source of silica, resulted in high silica products in both MK and F-MK methods. Like in the unmodified hydrogels, the reported structures and their properties, from the two treatment methods when extra silica was used are inconsistent. The structure types varied from one study to another. High silica faujasite X or faujasite Y structures were reported to have been formed when MK (Bortolatto et al., 2017; Chandrasekhar & Pramada, 2004; Covarrubias et al., 2006; El-Mekkawi et al., 2016; El-Mekkawi & Selim, 2012; Kovo et al., 2009), or F-MK (Anderson et al., 2017; Ayele et al., 2016; Belviso et al., 2013; Castro et al., 2019; Djeffal et al., 2017; Doyle et al., 2016; Ma et al., 2014; Mezni et al., 2011) methods were used.

Although fusion method leads to high dissolution of aluminosilicates, the inconsistencies therein of the synthesised zeolite products suggests that current practice involving pre-treatment of clays via F-MK may be ineffective. The properties of the raw materials used in the reaction mixture is important because they influence the properties of the resulting products. Besides, the homogeneity of the starting synthesis hydrogels is important for their effective transformation into crystalline zeolite material (Logar et al., 2009). This is the reason why pure chemical grade reagents are used to produce homogeneous and pure zeolite materials for industrial applications. These specifications need to be matched when using alternative sources of aluminosilicates such as kaolin and volcanic ash. It is therefore important to fully explore the efficient conversion of aluminosilicates in kaolin into a form that ensures complete dissolution to a homogeneous synthesis hydrogel and subsequent conversions to zeolite products.

In this work, various zeolites have been synthesized via metakaolinization and fused-metakaolinization methods using kaolin clay and volcanic ash materials. Fumed silica and sodium metasilicate pentahydrate were used where additional silica was required while sodium

aluminate was used where additional alumina was required. The effects of NaOH concentration, in the alkaline fusion step, on the zeolite products was also investigated by comparing partial fusion with full fusion of kaolin before hydrothermal crystallization. In addition, the effects of pre-treatment of kaolin with alkaline activator prior to fusion step have been explored by subjecting the raw clay to two regimes, namely, dry mixing with NaOH followed by dry fusion, or wet mixing with NaOH followed by wet/dry fusion. The fusion and synthesis conditions, i.e., alkaline fusion, hydrogel composition, ageing and hydrothermal synthesis were identical for all protocols. The findings of this study will inform on the choice of pre-treatment processes that may be applied to clay materials before fusion and hydrothermal synthesis of zeolites.

2.3 Factors affecting zeolite synthesis

Synthesis of zeolites is affected by a large number of modifiable factors making the process complex. These may include the SiO_2/Al_2O_3 molar ratio, hydrogel composition, its water content and pH, structure-directing agent, ageing period and conditions, reaction temperature and time of both calcination and crystallization stages as well as impurities originating from the starting materials (Abdullahi et al., 2017; Johnson & Arshad, 2014). These factors will affect the elemental composition, pore size, and channel distribution as well as crystal structures and sizes.

2.3.1.1 Silica to alumina (SiO_2/Al_2O_3) molar ratio of the hydrogel

The SiO_2/Al_2O_3 molar ratio of the synthesis hydrogel does not necessarily dictate the type of zeolite formed. In addition, the high SiO_2/Al_2O_3 molar ratio of precursor hydrogel does not significantly change the SiO_2/Al_2O_3 molar ratio of the product (Berger et al., 2005). However, a reaction hydrogel with the correct SiO_2/Al_2O_3 molar ratio carried out under optimized

conditions will play a significant role in giving the right type of zeolite with specific catalytic properties. The SiO_2/Al_2O_3 molar ratio of the synthesis hydrogel mixture for zeolites Na-A, Na-X and Na-Y, for example, should be in the range of 1.5-2, 3-5 and 5-10, respectively (Christidis & Papantoni, 2008; García et al., 2016; Hu et al., 2017; Lutz, 2014). In their study, Zhang et al., 2013 obtained pure zeolite Na-X using a synthesis hydrogel of SiO_2/Al_2O_3 molar ratio of 1.5-4.0, a mixture of Na-A and Na-X using synthesis hydrogel of SiO_2/Al_2O_3 ratio of 1.0 and pure Na-A from SiO_2/Al_2O_3 of 0.5.

The physical and chemical properties of the resulting zeolite products are also influenced by their SiO_2/Al_2O_3 ratios. A high SiO_2/Al_2O_3 ratio enhances zeolite hydrophobicity, crystallinity as well as thermal stability (Bacariza et al., 2018; Sun et al., 2015). In addition, the number of acid sites (Aboul-Fotouh et al., 2017) as well as the BET surface area and micropore volume (Zhang et al., 2013) of zeolites decreases as the SiO_2/Al_2O_3 molar ratio increases.

2.3.1.2 Concentration of alkali

A high concentration of NaOH in the hydrogel produces a faster dissolution of kaolinite (Rios et al., 2007). However, a very high concentration of NaOH and temperature leads to a mixture of zeolites (Yang et al., 2017). In addition, when the molar ratio of Si and Al in the reaction mixture are equal, the final product depends on the concentration of hydroxyl ions in the synthesis hydrogel (Breck, 1974).

2.3.1.3 Reaction time and temperature

At constant SiO_2/Al_2O_3 molar ratio of the synthesis hydrogel, crystallization time and temperature will determine the type of zeolite formed (Zhang et al., 2013). In addition, reaction time influences the degree of crystallinity of the synthesis products. At high SiO_2/Al_2O_3 molar ratio, LTA only forms at low reaction times and is dissolved into an amorphous aluminosilicate

material with extended reaction time to produce FAU (Rios et al., 2007) via Ostwald's ripening process. Performing synthesis of zeolites at high temperature of more than 100 °C produces small size zeolite crystals because of the increased rate of nucleation (Khan et al., 2010).

2.4   Biofuels

Biofuels are derived from several plant and animal materials such as biomass, bio-oils, and sugars. Cellulose and starch are the two major carbohydrate supplies for sugar-based fuels. Simple sugars such as sucrose are fermented to produce ethanol fuel, while complex carbohydrates are hydrolysed and broken down using enzymes or conventional catalysts. On the other hand, lignin of biomass is converted into fuels by gasification, catalytic dehydroxygenation or pyrolysis (Maryam et al., 2014). However, of interest to the current study is the biodiesel which has prospects of being a potential substitute for the conventional petroleum diesel (petro-diesel) (Okoronkwo et al., 2012).

2.4.1   Biodiesel

Biodiesel differs from petro-diesel in that petro-diesel is a mixture of hydrocarbon molecules of between 8 to 21 carbon atoms in the chain and is a product of the fractional distillation of non-renewable fossil fuels. Biodiesel, on the other hand, is a mixture of fatty acid alcohol esters of various carbon chains in the same range as of petro-diesel and is a product of transesterification and/ or esterification of renewable lipid sources, containing glycerides and free fatty acids, with low molecular weight alcohols in the presence of an enzyme, acid or alkaline catalysts (Lotero et al., 2005; Perego & Bosetti, 2010).

Triglycerides (TGs), esters of three fatty acid chains bonded to a glycerine backbone, are not suitable for use directly as fuels due to their high molecular weight and viscosity (Maryam et al., 2014; Perego & Bosetti, 2010). The tangling of the fatty acid (FA) tails of glycerides

increases the oil viscosity leading to solidification of oils, encrustations in the internal combustion chambers and blockage of the fuel injectors at low temperatures. The longer the FA chains the higher is the interactions. The TGs must therefore be converted to biodiesel before use. Although the current biodiesel production is still too low, the production has been on steady growth as shown in Figure 2.10 and is expected to continue growing in the future.
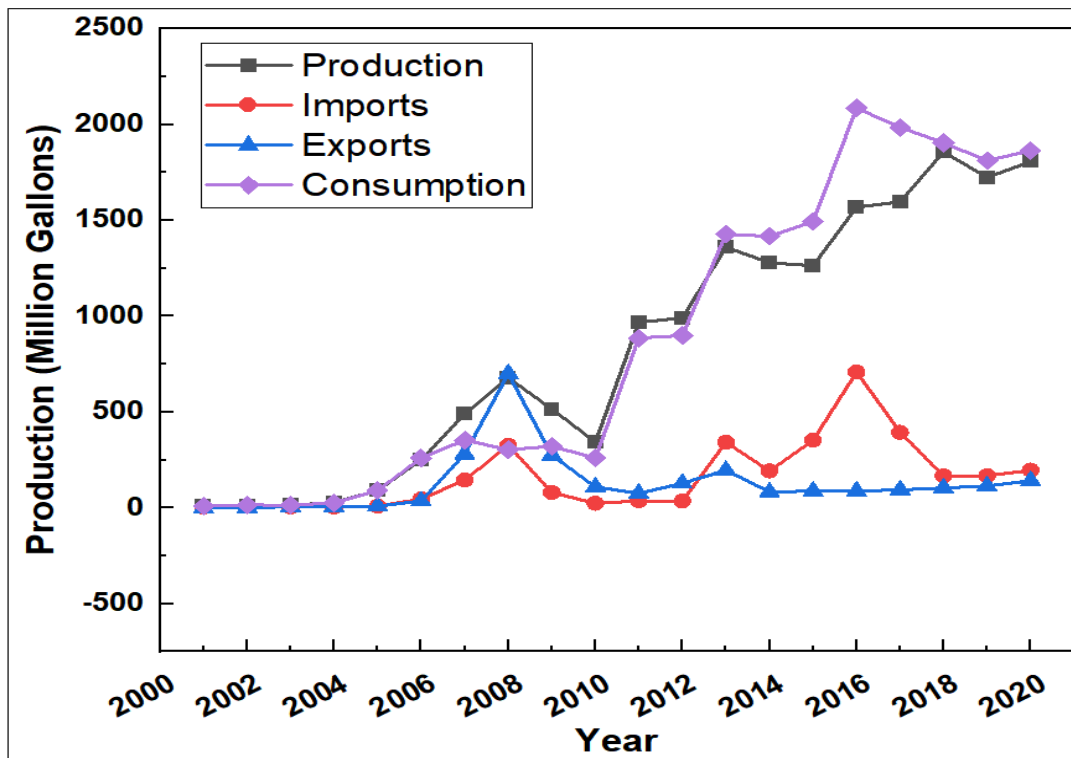
Figure 2.10; U.S. Biodiesel production, exports, and consumption, data obtained from (NREL, 2019).

Biodiesel is used either as a blend, where it is blended with petro-diesel and in this case, no engine modification is required (Chhabra et al., 2017; Mohsin et al., 2014), or as pure biodiesel (B100) in which engine modification must be done (Kakati & Gogoi, 2016). Mostly employed blends are B10 and B20, where 10 and 20 refer to the weight per cent of biodiesel blended with petro-diesel. For example, B10 stand for a biodiesel blend consisting of 10 % by weight of biodiesel and 90 % by weight of petro-diesel. Research has also shown that biodiesel blends give almost similar fuel consumption rate with petro-diesel (Kakati & Gogoi, 2016) in addition

to improved fuel properties (Negm et al., 2017). However, with these added advantages of using biodiesel, latest statistics have shown that only a few regions in the world, as shown in Figure 2.11, currently led by the European Union have adopted its technology and use (Kamzolova et al., 2011; Mizik & Gyarmati, 2021; OECD/FAO, 2020). The low consumption of biodiesel is due to the current production technologies using edible vegetable oils and therefore making it expensive and uneconomical for struggling or growing economies.
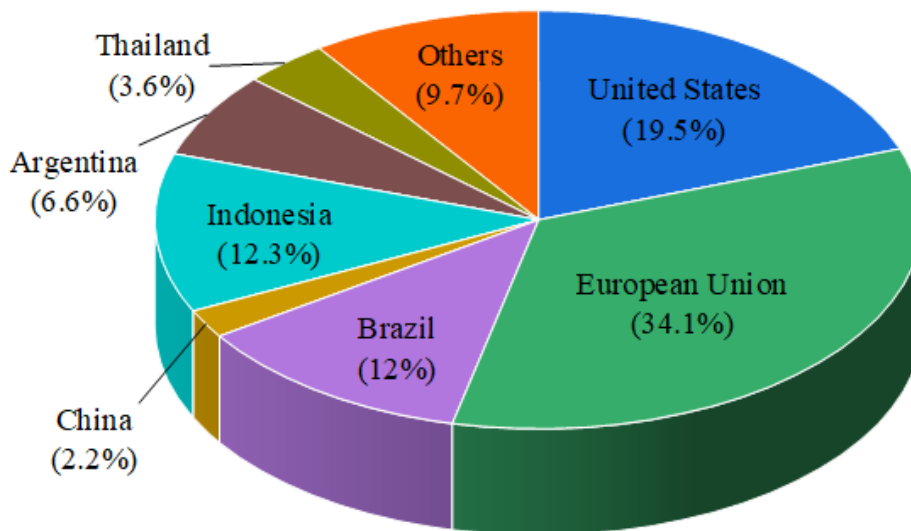
Figure 2.11; Regional ranking of biodiesel production; data obtained from (OECD/FAO, 2020).

Actively used oils are obtained from palm (Roschat et al., 2016), soybean (Meloni et al., 2016), sunflower (Santana et al., 2016), canola (Antonova et al., 2015), coconut (Qiu et al., 2016) and pongamia (Jaya et al., 2015) among others. These oils are also competitively used for human and animals food production. There is therefore, a need for alternative non-edible oils with low value to humans such as *Jatropha curcas* and waste cooking oils. *Jatropha curcas* oil (JCO) and waste cooking oil (WCO) are non-edible oils with low value to humans thus can be good alternative sources of feedstock for biodiesel production. Developed zeolites will be used for the synthesis of biodiesel using JCO and WCO.

2.5 Jatropha curcas

Jatropha curcas is a hardy shrub belonging to the family Euphorbiaceae (Meloni et al., 2016) commonly found in most of the tropical and sub-tropical regions of the world (Singh & Padhi, 2009) with cultivation limits at 30ºN and 35ºS and can grow on poor soils with low rainfall (Anil et al., 2011; Shambhu et al., 2013). It has a productive life span of 40-50 years but short gestation period. Its seeds contain as high as over 50 % of oil content (Kumar & Das, 2018), but with high FFAs content of >1 % (Silitonga et al., 2013). The presence of phorbol esters which are toxic to animals (Nakao et al., 2015) renders the JCO non-edible. They are therefore expected not to attract competition as a food oil. The oils also contain more than 75 % unsaturated fatty acids with high palmitic, oleic and linoleic acids as shown in Table 2.3. The composition of fatty acids generally depends on the maturity stage of the plant, the interaction with environment and genetics (Achten et al., 2008; Sinha et al., 2015). The high content of FFA makes JCO unsuitable for the alkaline catalysed transesterification process.

Table 2.3; Physical and chemical properties of *Jatropha curcas* oil (Silitonga et al., 2013).

Fatty Acid Composition			Physical Properties	Value
Fatty Acid	**Saturation**	**Composition (%)**	Kinematic viscosity (mm^2/s)	28.35
Lauric	12:0	0.1	Density (kg/m^3)	915.0
Myristic	14:0	0.1	Flashpoint (°C)	190.5
Palmitic	16:0	13.0	Calorific value (MJ/kg)	38.96
Palmitoleic	16:1	0.7	Acid value (mg KOH/g)	12.70
Stearic	18:0	5.8	Iodine value (g I_2/100 g)	80.8
Oleic	18:1	44.5		
Linoleic	18:2	35.4		
Linolenic	18:3	0.3		
Arachidic	20:0	0.2		

2.6   Waste cooking oils

Frying conditions involve high temperatures and the presence of moisture and air. Continuous subjection of the cooking oils to these conditions results in degradation reactions due to hydrolysis, oxidation, and polymerization of oils (Choe & Min, 2007). This results in waste cooking oils (WCOs) with heterogeneous physicochemical properties with the properties depending largely on the source of waste oil (Şanli et al., 2011), for example, the fatty acids composition of canola WCO is shown in Table 2.4. WCOs cause severe environmental degradation, clogging of sewer lines and creating odour if not well monitored. In addition, oils reaching the water sources increase the organic pollution load and prevent oxygen exchange in covered surfaces.

Table 2.4; Fatty acids composition of canola waste cooking oil (Chhetri et al., 2008).

Fatty Acid Composition		
Fatty Acid	**Saturation**	**Composition (%)**
Myristic	14:0	0.9
Palmitic	16:0	20.4
Palmitoleic	16:1	4.6
Stearic	18:0	4.8
Oleic	18:1	52.9
Linoleic	18:2	13.5
Linolenic	18:3	0.8
Arachidic	20:0	0.12
Eicosenic	20:1	0.84

Using WCOs will not only lower the cost of biodiesel production but also provide a better method of converting these wastes into a sustainable green energy source and therefore reduce pollution loads in the environment. However, as in JCOs, the major drawback in their use as

feedstock for biodiesel production is in their high FFA and traces of water contents which are not suitable for most catalytic esterification and transesterification reactions (Maryam et al., 2014; Patil et al., 2012).

2.7   Biodiesel synthesis

Esterification and transesterification reactions of oils are catalysed by enzymes (Brask et al., 2015) as well as homogeneous and heterogeneous catalysts. Homogeneous basic catalysts such as alkalis (Rodríguez-Guerrero et al., 2013) and alkoxides (Eevera & Pazhanichamy, 2013) and acid catalysts such as HCl (Su, 2013), H_2SO_4 (Patil et al., 2012), H_3PO_4 and organic sulfuric acid RSO_3H (Alegría & Cuellar, 2015) are the mainly used catalysts for the esterification and transesterification reactions of oils. The general transesterification reaction of triglyceride with methanol is shown in equation (3).

$$\text{Triglyceride (TG)} \quad \text{Methanol} \quad \longrightarrow \quad \text{Glycerol} \quad \text{Fatty acid methy esters (FAMEs/ Biodiesel)} \quad (3)$$
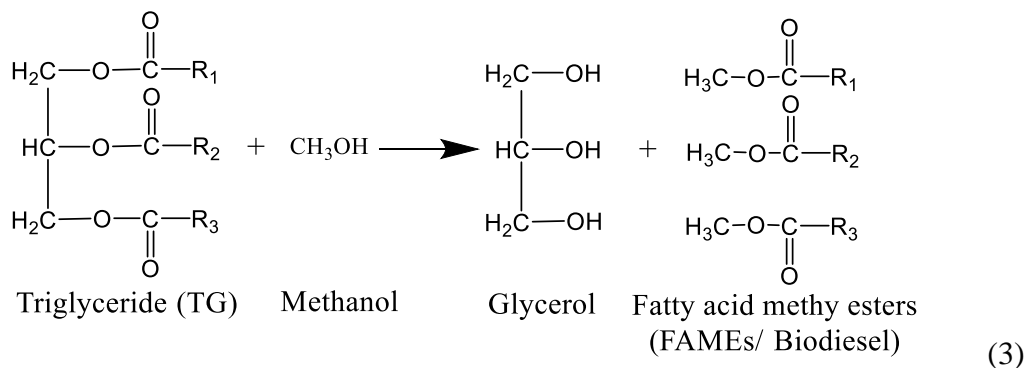
where R_1, R_2, and R_3, are fatty acid chains.

Basic homogeneous catalysts require anhydrous conditions and feedstocks with low levels of FFAs. The presence of FFAs and water in the feedstock during transesterification leads to loss of catalyst, formation of soap as well as hydrolysis of the esters (Eevera & Pazhanichamy, 2013; Patil et al., 2012). In addition, homogeneous catalysts cannot be reused and the process of purification of the resulting products is cumbersome leading to the generation of large volumes of wastes.

A suitable catalyst, which must be able to withstand the oils' conditions and be able to effectively and efficiently catalyse the reaction is therefore required. Replacing homogeneous catalysts with heterogeneous catalysts will have the advantages of reduced corrosion and environmental problems associated with liquid catalysts as well as reducing the processes involved in product purification. This will significantly simplify the processes involved in biodiesel production in addition to lowering the production costs.

2.7.1 Synthesis of biodiesel using heterogeneous catalysts

A variety of heterogeneous catalysts have been used in biodiesel synthesis. Organic polymer functionalized with sulfonic acid groups (Gomes et al., 2016), activated carbon from the waste of polyethylene terephthalate (PET) (Fadhil et al., 2016), zirconium containing metal-organic frameworks (Zr-MOFs) (Cirujano et al., 2015) and sulphated zirconia are among the acid catalysts which have been used. The proposed mechanism for heterogeneous acid catalysis in both esterification and transesterification is given in Figure 2.12.
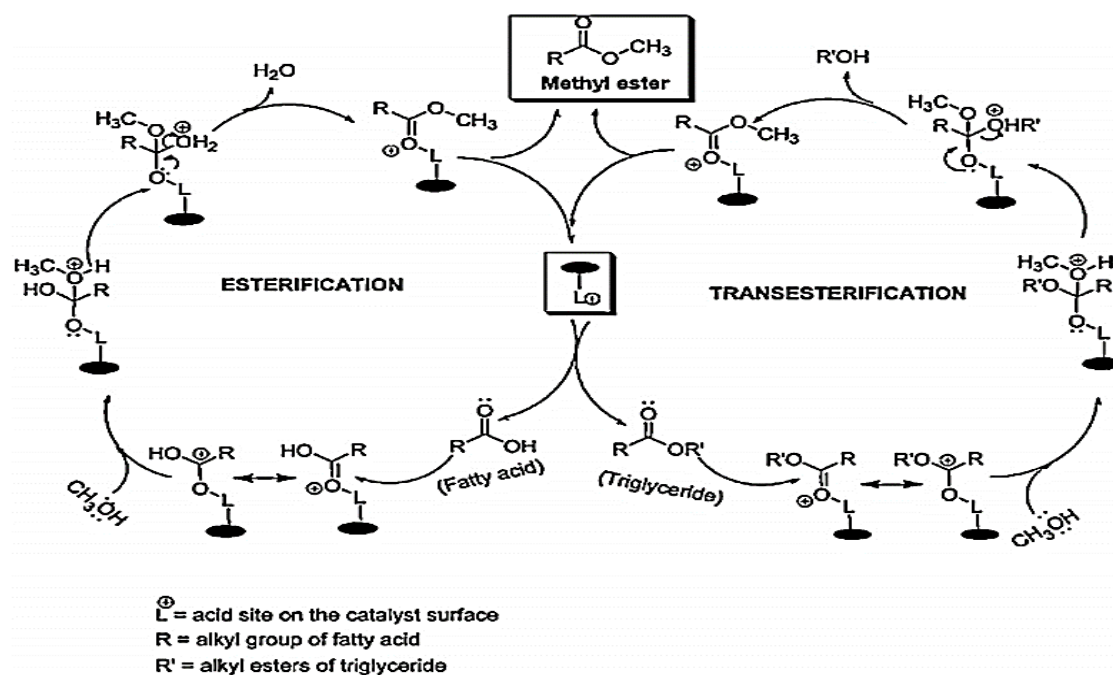
Figure 2.12; Solid acid-catalyzed simultaneous esterification and transesterification of oil, as adopted from (Yahaya et al., 2014).

38

On the other hand, La_2O_3 and nano La_2O_3 catalysts (Zhou et al., 2015), CaO and supported CaO catalysts with zeolites (Roschat et al., 2016; Wu et al., 2013) and $CaO-SiO_2$ catalysts (Chen et al., 2015) have been used as heterogeneous basic catalysts. However, in addition to catalyst costs, catalyst surface area, stability and therefore multiple reuses and regeneration, as well as mass transfer limitations are still some of the factors hindering applications of heterogeneous catalysts. Furthermore, catalysts which can carry out transesterification at conditions of high FFA is still a challenge.

2.7.2 Zeolites as heterogeneous catalysts for biodiesel synthesis

A lot of work has been done on zeolites as a heterogeneous catalyst for the transesterification of oils to overcome the disadvantages of homogeneous catalysts currently used in the industrial production of biodiesel. Zeolite catalysts perform better than metal catalysts (Suppes et al., 2004). However, zeolites in their pure form show very little or no activity towards oil conversion reactions (Kay & Yasir, 2012). For effective catalytic activity, they are modified with specific cations to improve on their catalytic activity. Zeolites are used either as acid catalysts or base catalysts depending on identity of species used in their modifications. The pore size and zeolite pore distribution are also important as they play a significant role in the mass transfer process. Đặng et al., 2017 obtained a high yield of biodiesel at 92.8 % using zeolite LTA synthesized from kaolin. Although catalysts could be used for at least three consecutive reaction cycles, the catalyst load of 72 wt. % of triolein weight is very high and therefore not sustainable in the long term. LTA has small pore sizes and therefore the mass transfer of lipids is a limiting factor.

In acid catalysis, zeolites are modified using mineral acids and acidic cations including Ag, Ni, Fe, Zn, Sn, and Ti among others, which supply either Bronsted or Lewis acid sites to the zeolite structure, see Figure 2.1. Chung and Park used H^+ ion exchanged MFI type ZSM-5 and

mordenite zeolite catalysts for esterification of oleic acid of soybean oil (Chung & Park, 2009). H-ZSM-5 zeolites showed high catalytic activity owing to both Bronsted and Lewis acid sites. But the smaller pores and pore distribution were limiting factors affecting ZSM-5 as catalysts for conversion of lipids in transesterification reactions where diffusion restrictions to the mass transfer of triglycerides in and out of zeolite porosity need to be minimized (Carrero et al., 2011). In order to overcome the mass transfer limitations in zeolite framework structure, dealumination was done to enhance the pore sizes and porosity (Vieira et al., 2017). However, this practice might result in interference with the framework structure and even structure collapse. In solving the problem of low catalytic surface area, Baroi et al. used tungsten oxide (WO$_3$) and 12-tungstophosphoric acid (TPA) supported on H-Y, H-β and H-ZSM-5 zeolites as catalysts for esterification of FFAs and transesterification of TGs of green seed canola oil (Baroi et al., 2014). The TPA impregnated H-Y zeolite showed higher catalytic activity for esterification, while TPA impregnated H-β zeolite showed higher catalytic activity for the transesterification reaction. Recently, commercial H-Y and ZSM-5 zeolites were compared as acid catalysts for the esterification of palmitic acid (Prinsen et al., 2018). H-Y catalyst was highly effective yielding 100 % conversion after 3 h at 70 °C and a 2:1 of methanol/palmitic acid molar ratio. The reaction depended more on the porosity and the hydrophobic/hydrophilic balance of the microporous materials and the reactants. Despite these efforts, catalysts that can perform both esterification and transesterification reactions efficiently are still a challenge (SathyaSelvabala et al., 2011), especially for high FFA feedstocks.

Zeolites modified with alkali cations are used as catalysts in reactions requiring basic sites. The occlusion of the alkali metal oxide clusters in the zeolite pores through the decomposition of their salts in thermal activation step results in a further increase in the basicity (Suppes et al., 2004). The basic strength of the resulting catalyst increases with the increasing electropositivity of the cation used. Alkali hydroxides have been used in loading the metal ions into the zeolite

pores, however, this led to structure collapse and subsequent loss of active sites (Zhu et al., 2021). Milder conditions using alkali salts are therefore employed in achieving the same effect. Alkali acetates, chlorides, and nitrates are therefore employed in achieving the same effect (Manadee et al., 2017; Martínez et al., 2014; Peña et al., 2013) resulting in high ester yields.

Suppes et al., 2004 carried out transesterification of soybean oil using Na-X modified with sodium acetate and sodium azide. It was found that the fatty acid methyl esters (FAME) yield increased with the number of sodium ions occluded in the super cages. Ramos et al., 2008 in their study of transesterification of sunflower oil looked at mordenite, beta and X zeolites loaded with different metal ions through either incipient wet impregnation or ion exchange. Zeolite X occluded with three excess sodium ions per super cage was found to be the best active catalyst. The same results were also obtained by Manadee et al., 2017 while working on potassium ion occlusion on Na-X zeolite catalyst for JCO. Zeolite Na-X has a high concentration of super basic sites compared to other zeolites and the basicity increases with increasing alkali metal concentration. Agus et al., 2014 used platinum and palladium ions. They found that Pt and Pd impregnated into HZSM-5 zeolites not only leads to an increase in surface area, pore diameter, and volume but also leads to improved yield and selectivity of biodiesel. However, the costs of these two cation compounds are very high.

2.7.2.1 Optimization of biodiesel synthesis using zeolite catalysts

During synthesis, reaction conditions; temperature, catalyst concentration as well as molar ratios of reactants, must be optimized as they have been shown to affect the catalytic process, (Chung & Park, 2009; Fan et al., 2011; Joshi et al., 2008; Karuppasamya et al., 2013; Neha et al., 2013; Okoronkwo et al., 2012; Shu et al., 2009; Zhang et al., 2001). Optimum esterification and transesterification reactions have been studied by several researchers and vary depending on the type of zeolite catalyst as well as the catalyst modification method. However, the

optimum conditions have been found to be methanol to oil molar ratio of 10-30, catalyst loading of 2-20 wt. % and reaction temperature and time of 60-80 °C and 6-12 h respectively, (Kay & Yasir, 2012; Martínez et al., 2014; Peña et al., 2013; Sun et al., 2015; Supamathanon et al., 2011; Suppes et al., 2004; Volli & Purkait, 2015).

2.7.3   Benefits of biodiesel

Biodiesel offers a number of benefits. It is sources are renewable, environmentally benign fuel with almost zero SO_x and CO_2 emissions. According to Peng, 2015, biodiesel fuel has approximately 10 wt.% oxygen content which may lower the emissions by promoting a more complete combustion. Besides, using biodiesel fuel contributes to the reduction on CO, hydrocarbons (HC) and carbon granules (smoke) emissions by up to 25.2, 18.57 and 19.6 %, respectively (Peng, 2015). Biodiesel also exhibits low viscosity and possesses good engine combustion efficiency and high lubricity and can therefore enhance engine longevity (Tan et al., 2015). It is also effective in reducing particulate emissions from the engine when used in blend form with petro-diesel (Maryam et al., 2014; Okoronkwo et al., 2012).

2.7.4   Disadvantages of biodiesel

Although biodiesel has shown several benefits to the environment and combustion engine, it also has some drawbacks. The cost of biodiesel is higher than that of petro-diesel because of the high cost of raw materials currently being used (Singh et al., 2020). Biodiesel is likely to produce less power with high fuel consumption (7.38 % higher) than petro-diesel (Peng, 2015) because of its low gross calorific value (energy content) in comparison to petro-diesel (McCarthy et al., 2011). In addition, variations in quality of biodiesel obtained from various sources have been previously observed, e.g., palm oil biodiesel is more efficient than biodiesel produced from tallow and canola oil (Singh et al., 2020). Other disadvantages associated with the use of biodiesel include deforestation and risk of limitation in food supply due to

competition in land use with biodiesel plant oils (Aransiola et al., 2014), increased NO_x emissions by 10.34 % (Peng, 2015; Thangarasu et al., 2021), limited use in very cold areas due to clogging in engine (Yeong et al., 2022) and damage the rubber houses of some engines (Reddy et al., 2016).

CHAPTER 3

MATERIALS AND METHODS

This chapter outlines the materials used, the research methods and the methods of data collection. All figures and tables used in this chapter were generated in this study, unless otherwise stated.

3.1 Materials

All chemicals and reagents used in this study were of analytical grade unless otherwise specified. The clay material was an off-white mineral powder supplied by the Department of Inorganic Chemistry, University of Yaoundé 1 - Cameroon. Raw natural zeolite was supplied by the Centre for Scientific and Industrial Research (CSIR) - South Africa. Volcanic ash was obtained from the slopes of Mt. Eburu Volcano (0°34'27.2"S 36°15'43.9"E) in Nakuru county-Kenya. The volcanic ash used is referred to here as the Kenyan volcanic ash (KVA). Molecular sieve 4A powder and molecular sieve 13X powder (4-8 mesh) were obtained from Alfa Aesar Chemicals - UK. Sodium hydroxide (NaOH) pellets 99 %, potassium hydroxide (KOH) pellets 99 %, hydrochloric acid (HCl) 37 %, n-hexane ≥95 %, n-heptane ≥99.9 %, methanol ≥99.9 % and chloroform ≥99 % were obtained from Fisher Scientific - UK. Sodium metasilicate pentahydrate ($Na_2SiO_3 \cdot 5H_2O$) ≥95 % and fumed silica powder (SiO_2) of 0.007 μm particle size were obtained from Sigma Aldrich Chemicals - UK while sodium aluminate ($NaAlO_2$) was obtained from MP Biomedicals, LLC - USA. Magnesium sulphate (general grade) and sodium acetate anhydrous ≥99 % salts were obtained from Alfa Aesar Chemicals - UK. Lithium tetraborate (≥ 99.9 % trace metal basis) was from Honeywell – UK.

Fatty acid methyl esters (FAMEs) references and internal standards including Supelco FAME mix GLC-10, Supelco methyl oleate ≥99 % and methyl nonadecanoate ≥98 % were obtained from Sigma Aldrich - UK. The 28 components standard solution containing 100 ml/L of each

metal ion component in 5 % HNO_3 and the silicon standard solution (100 ml/L) in 5 % HNO_3 were obtained from Fisher Scientific - UK. Whatman filter papers grade 1 and 1.3 mm Whatman 4.5 µm polytetrafluoroethylene (PTFE) filters were obtained from Fisher Scientific - UK. Deionized water was prepared using an Elga PURELAB Option 4463 water deionizer.

3.2 Methodologies

In this study, the words protocol and method have been used interchangeably to mean the same thing.

3.2.1 Extraction of volcanic ash

The extraction procedure for the volcanic ash is summarized in Figure 3.1.

Volcanic tuff   Volcanic ash in 10 % HCl   Acid washed Volcanic ash (KVA-10%A
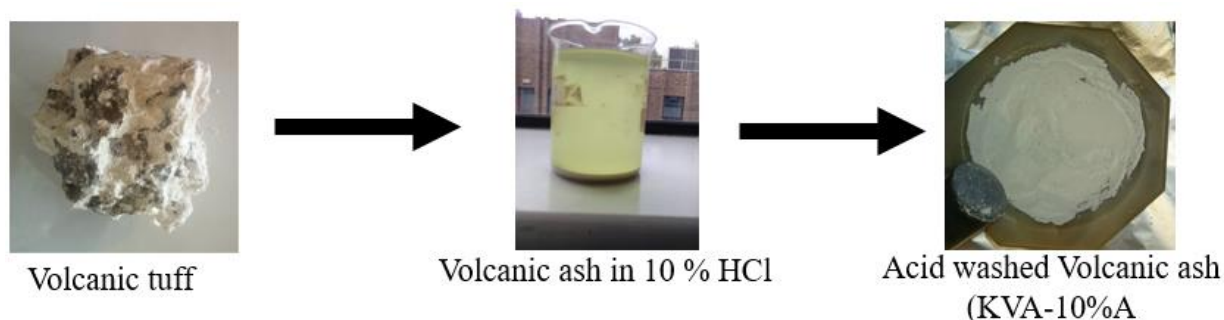
Figure 3.1; Extraction of Kenyan volcanic ash material from volcanic tuff.

The raw Kenyan volcanic ash (KVA-Raw) was extracted from the volcanic tuffs by carefully extracting the white soft solids from the rock samples. The extracted material was then ground to powder and the powder passed through a magnetic surface to remove the magnetic components from the ash. The resulting powder (KVA-Raw) was washed six times at room temperature with deionized water before drying in an oven at 100 °C for 24 h. The dried powder was further washed to remove inorganic impurities by taking 100 g of the dried powder and magnetically stirring it at 600 rpm at room temperature in 600 ml of 10 % HCl (wt. %) for 24

h. The resulting material was washed six times with deionized water to pH ca. 7 before drying in the oven at 100 °C for 24 h to obtain acid-washed volcanic ash (KVA-10%A).

3.2.2   Zeolite synthesis

Synthesized zeolites were prepared from clay and volcanic ash materials as sources of aluminosilicates through hydrothermal crystallization process at 100 °C. The clay material was used as received. The clay was either heated at high temperature or fused with NaOH at similar temperatures prior to hydrothermal synthesis. Modification was done through addition of fumed silica, sodium metasilicate pentahydrate or sodium aluminate. Different protocols were followed in carrying out the syntheses tasks as described in the following sections.

3.2.2.1   Hydrothermal crystallization of zeolites - Protocol 1

In this first protocol, zeolites were synthesized through the pre-treatment of kaolin material by either metakaolinization in protocol 1a or fused-matakaolinization in protocol 1b prior to hydrothermal crystallization step. Synthesis was based on modifications of previous reports by Ríos et al., 2012 and Ríos et al., 2009. Figure 3.2 show the schematic flow of protocol 1. Initially, zeolites were synthesized from clay material without modification of the synthesis hydrogels. In the MK protocol 1a, the clay was calcined by heating at 10 °C/min to 750 °C and then holding at this temperature for 8 h. The mixing of heat-treated clay (MK) and NaOH was then done in such a way that a 1/1.2 weight ratio of MK to NaOH was achieved. Specifically, 3.1 g of MK was mixed with 34.5 ml of 2.7 M NaOH solution in a 50 ml PTFE lined autoclave.

In the F-MK protocol 1b, the clay material was dry mixed with NaOH pellets in a 1/1.2 weight ratio by grinding in an agate motor before heating the resulting mixture as described above at 750 °C for 8 h. The resulting F-MK1 was then ground to powder. A mass of 4.4 g of the powder was then dissolved in 21.5 ml of deionized water in a 50 ml PTFE lined autoclave. Both MK

46

and F-MK syntheses batches were stirred at 25 °C for 4 h at 600 rpm to dissolve the components and achieve a homogeneous hydrogel mixture (with $Na_2O:SiO_2:Al_2O_3:H_2O$ of 5.6:4.2:1:182.9) before allowing the hydrogel to age for 24 h at 25 °C. After aging, the hydrogels were placed in a box furnace or in an oven to crystallize at 100 °C under static conditions for different periods of time from 8 h to 240 h. Synthesized crystals were washed with deionized water to pH < 8 followed by drying at 100 °C for 24 h in the oven. The dried zeolites were kept in caped vials awaiting characterization and catalytic modifications.
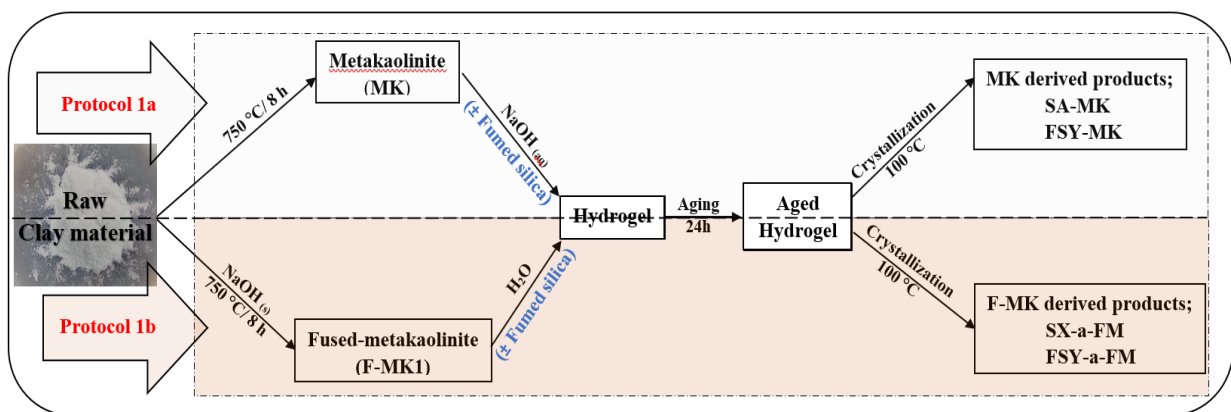
Figure 3.2; Schematic flow for protocol 1.

The SiO_2/Al_2O_3 molar ratio of the synthesis hydrogels were also modified in both protocols 1a and 1b by the addition of fumed silica to achieve a hydrogel $Na_2O:SiO_2:Al_2O_3:H_2O$ molar ratio of 10:1:7.98:120 based on modification of previous reports (Christidis & Papantoni, 2008; Lutz, 2014). In the MK protocol 1a, 5.5 g of MK, 11.1 g fumed silica, 8.4 g NaOH and 44.5 ml H_2O while 10.0 g of F-MK, 8.0 g fumed silica and 35.1 ml H_2O water was used in F-MK protocol 1b. The resulting syntheses hydrogels were subjected to similar conditions as described above before hydrothermal crystallization step.

3.2.2.2 Hydrothermal crystallization of zeolites - Protocol 2

In protocol 2, F-MK method was implemented by varying the amount of NaOH used in the fusion step and modification of the hydrogel using sodium metasilicate pentahydrate

(Na$_2$SiO$_3$.5H$_2$O). The variation of the amount of NaOH in the fusion step was achieved through the partial fusion (protocol 2a) based on the previously reported method (Doyle et al., 2016) and a full fusion (protocol 2b) which was designed to match protocol 1b above. However, the Na$_2$O concentration was later made up in the hydrogel in protocol 2a before hydrothermal crystallization step by the addition of compensating amount of NaOH. The syntheses hydrogels were prepared such that a chemical composition of SiO$_2$:Al$_2$O$_3$:Na$_2$O:H$_2$O of 7:1:10:282 was achieved in all cases. The details on the experimental design are shown in the schematic flow in Figure 3.3.
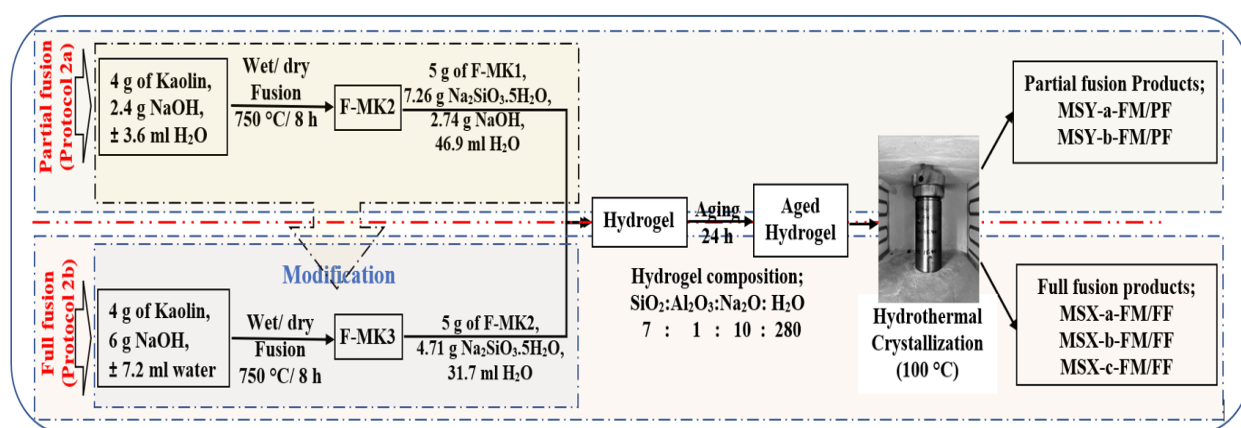
Figure 3.3; Schematic flow for protocol 2.

In the partial fusion protocol 2a, F-MK2 was prepared by grinding in agate mortar 4 g of kaolin with 2.4 g of NaOH pellets followed by fusion at 750 °C for 8 h. The resulting F-MK2 was then ground to powder. Synthesis hydrogel was prepared by dissolving 5 g of powdered F-MK2, 7.26 g of sodium metasilicate pentahydrate and 2.74 g of NaOH pellets in 46.9 ml of deionized water. On the other hand, in the full fusion protocol 2b, the partial fusion protocol was modified by carefully calculating and grinding the total amount of NaOH activator with kaolin before fusion. Specifically, 4.0 g of clay mineral was mixed with 6.0 g NaOH by grinding in agate mortar followed by fusion as described above. The resulting F-MK3 was ground to powder. The hydrogel was then prepared by adding 6.4 g of sodium metasilicate

pentahydrate to 6.8 g of F-MK3 before dissolving the mixture in 41.4 ml of deionized water. The resulting hydrogels were stirred, aged and hydrothermally crystalized at 100 °C for various duration of time between 48-168 h.

3.2.2.3 Effects of the pre-treatment methods of clay with NaOH before fusion

The effects of kaolin pre-treatment methods before fusion step were investigated by performing three different methods of kaolin treatment methods in both wet and dry mixing of raw kaolin with NaOH before either wet or dry fusing the resulting mixture. The first pre-treatment, also referred to as dry mixing before dry fusion, was achieved by dry grinding raw kaolin with NaOH pellets in agate motor before dry fusing the mixture as described above. In the second pre-treatment method, also referred to as wet mixing before wet fusion, the mixing was achieved by grinding kaolin in agate motor with 3.6 ml of 16.7 M NaOH for partial fusion in protocol 2a and 7.2 ml of 20.8 M NaOH solution for the full fusion in protocol 2b, before fusing the wet mixture. In the third pre-treatment, also referred to as wet mixing before dry fusion, the mixing was achieved by wet mixing of kaolin with NaOH solution as described in the second pre-treatment method above. The water content of the mixture was then removed by drying the mixture at 100 °C for 48 h in an oven before dry fusing the resulting dry mixture. Subsequent hydrogel preparation and hydrothermal crystallization of all fused pre-treated mixtures were performed as described in section 3.2.1.2.

In further investigations, the three pre-treatment procedures were performed following protocol 1b above where F-MK method with additional fumed silica was used in the synthesis hydrogel. For the first pre-treatment method (dry mixing followed by dry fusion), F-MK was prepared by fusing a ground mixture of 6 g of kaolin with 7.2 g of NaOH pellets at 750 °C for 8 h. The second and third pre-treatment methods were achieved by adding 7.2 ml of water in the grinding step before wet or dry fusing the mixture at the same conditions as described above.

Subsequent synthesis hydrogels were prepared by dissolving 10.0 g of F-MKs and 8 g of fumed silica in 35.1 ml of H_2O to give the same synthesis hydrogel composition of $SiO_2:Al_2O_3:Na_2O:H_2O$ molar ratio of 14.08:1:7.13:150.18.

3.2.2.4 Hydrothermal crystallization of zeolites - Protocol 3

In protocol 3, zeolites were synthesized using the Kenyan volcanic ash (KVA), kaolin and sodium aluminate as sources of aluminosilicates. In the synthesis of zeolites, protocol similar to the wet mixing method followed by dry fusion described above was used. In brief, 3.07 g of sodium hydroxide was added to a mixture of 3.13 g of sodium aluminate and 4.69 g of KVA-10%A. 3.5 ml of water was then added to dissolve NaOH and aid in achieving a homogenous mixture of the materials as a paste. The paste was then dried in an oven at 100 °C for 48 h before fusing at similar conditions as described above at 750 °C for 8 h. 6.83 g of the resulting fused KVA-10%A material (F-KVA) was then dissolved in 50.6 ml of water followed by starring at 600 rpm for 4 h to achieve a homogeneous hydrogel. The hydrogel was aged and crystalized at similar conditions as described above. The washing and drying of the resulting zeolite products were also done as described above. The effects of SiO_2, Al_2O_3, Na_2O and H_2O contents of the synthesis hydrogels were also investigated by varying the $SiO_2:Al_2O_3:Na_2O:H_2O$ of the hydrogels as shown in Table 3.1.

Natural zeolites were crushed to fine powder in agate motor. The zeolite powder was washed six times at room temperature with deionized water. The washed zeolite cake was then dried in an oven at 100 °C for 24 h. 10 g of the dried powder was further washed by magnetically stirring at 600 rpm at room temperature in 250 ml 10 % HCl (wt. %) for 24 h to remove inorganic impurities and free the voids (Imandiani et al., 2018). The resulting zeolites were then washed six times with deionized water to pH ca. 7 before drying in the oven at 100 °C for

24 hours. The prepared zeolites were kept in a 5 mL vial awaiting characterization and catalytic modifications.

Table 3.1; Variations in the synthesis hydrogels in protocol 3 and the resulting products.

Aluminosilicate source	Hydrogel composition $SiO_2:Al_2O_3:Na_2O:H_2O$	Product code
KVA-10%A-750C + Sodium aluminate	2.4:1.0:3.0:120.6	SZ1-c-FVA
KVA-10%A-750C + Sodium aluminate	4.1:1.0:3.0:221.1	SZ2-c-FVA
KVA-10%A-750C + Sodium aluminate	2.0:1.0:1.9:107.0	SZ3-c-FVA
KVA-10%A-750C + Kaolin	7.2:1.0:10.0:282.1	KaVo-c-FM

3.2.3   Preparation of natural zeolite

3.2.4   Modification of zeolites

Modification of both washed natural and synthesized zeolites was done through wet impregnation with sodium acetate salt. A mass of 1 g of zeolite was mixed with 2 ml of 1.46 M CH_3COONa salt solution and the mixture stirred at 600 rpm at 65 °C for 4 h. Calculation of the cation concentration was based on the fact that 1 g of zeolite Na-X contain 3.38×10^{19} unit cells and therefore a total of 2.7×10^{20} super cages (Mentus et al., 2009; Sen et al., 2014; Ursini et al., 2006). The resulting zeolite was dried at room temperature for 24 h in a vacuum before further drying in the oven at 100 °C for 24 h. The sodium salt in the modified zeolite was decomposed by heating the dried modified zeolites in air at 5 °C/min to 500 °C and then holding at this temperature for 4 h to give Na_2O occluded zeolite. Prior to use, the calcined zeolite catalysts were outgassed by heating at 250 °C for 20 min in a box furnace followed by cooling in a desiccator under vacuum.

3.3   Preparation of Lipids

3.3.1   Collection and preparation of *Jatropha curcas* oil

Jatropha curcas seeds were obtained from Dala Rieko in Asembo Bay, Kisumu County - Kenya (0°11'14.2"S 34°23'12.1"E). The procedure for the *Jatropha curcas* oil extraction from the seeds is summarized in Figure 3.4.
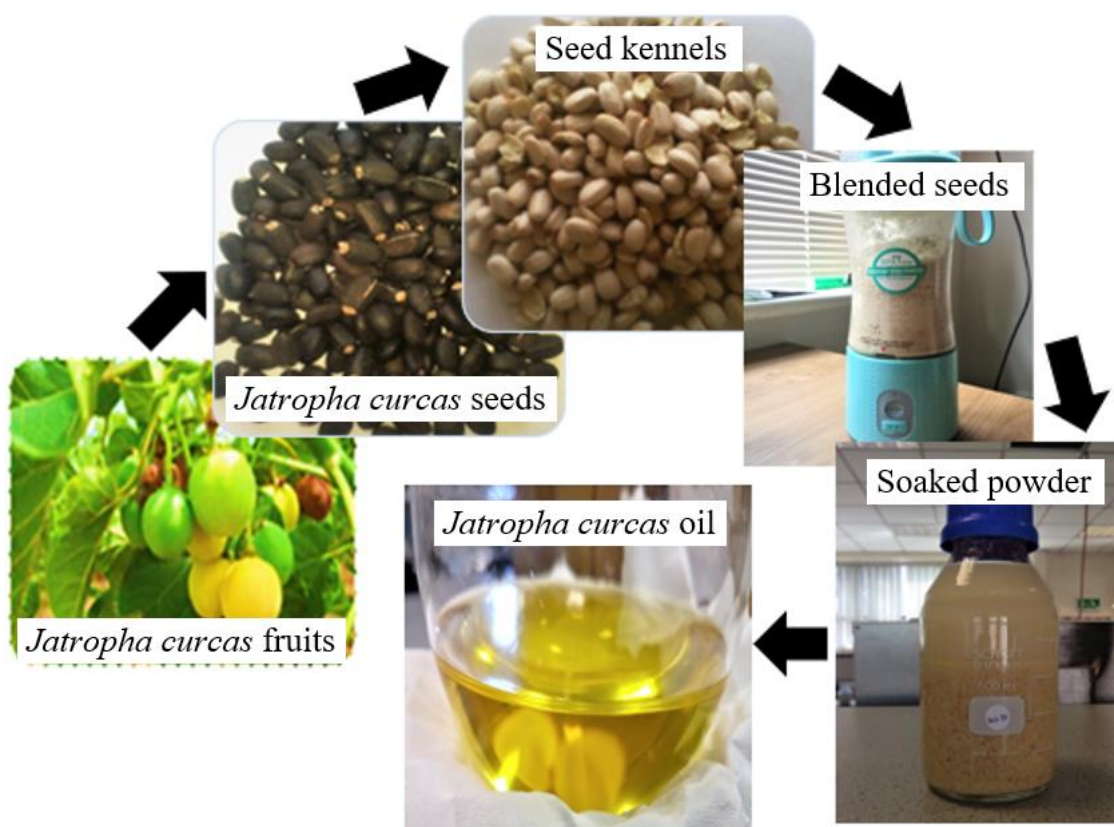
Figure 3.4; Extraction of *Jatropha curcas* oil from the seeds.

The seeds were manually sorted by hand by removing low quality seeds and impurities by hand-picking. The seed kennels were obtained by manually removing the seed husks from the seeds. The seed kennels were washed in deionized water, dried in air for 24 h and then crushed in a blender to fine powder before further drying in the oven at 100 °C for 4 hours. The dry seeds powder was soaked in n-hexane (1 g of powder in 2 ml of hexane) in a sealed 2.5 L Winchester glass bottle for 24 hours. Seeds fibre was filtered off, using grade 1 Whatman filter

paper, and rinsed with extra hexane. The hexane solvent was then separated through rotor vaporization in vacuum at 35 °C to recover the extracted oil. The prepared oil was placed in a tightly sealed glass container and then refrigerated below 4 °C to avoid rancidity as noted by Silitonga et al., 2013 awaiting analysis and transesterification reactions.

3.3.2   Collection and preparation of waste cooking oil

Waste cooking oil was obtained from Maseno University Kisumu Hotel, Kisumu county - Kenya (0°06'23.6"S 34°45'09.0"E). The oil was dark brown in colour and containing suspended solid particles. The oil was filtered to remove large suspended solids particles using 200 µm cheesecloth before washing with hot deionized water six times to remove the fine dirt and water-soluble components. Further purification was done by dissolving the oil in n-hexane, (1:2 oil/hexane, v/v), vigorously shaking the contents and leaving it to stand for 24 hours in a closed glass vessel. Immiscible layers and fine solid particles were decanted off and filtered through a grade 1 filter paper respectively. The cleaned oil was then recovered from hexane through rotor vaporization in vacuum. The clean oil was further dried in an oven at 100 °C for 12 h before placing in a sealed container and then refrigerating below 4 °C as noted by Silitonga et al., 2013 awaiting analysis and biodiesel synthesis.

3.3.3   Biodiesel synthesis

Transesterification reactions were performed in triplicates in a batch process by reacting JCO and WCO with methanol in the presence of prepared zeolite catalysts as shown in Figure 3.5. Biodiesel synthesis and preparation procedure reported by the Laboratory Analytical Procedure developed by the National Renewable Energy Laboratory (NREL) (Van Wychen et al., 2016) was used with some modifications in this study. In brief, the required amount of catalyst was weighed in a 10 ml round bottomed flask. The catalyst was evacuated by heating in a box furnace at 250 °C for 20 min before cooling in a vacuum as previously described. Required

amount of methanol and oil was then added to the flask containing evacuated catalyst followed by 5 ml of 10 mg/ml methyl nonadecanoate (C19:0Me) internal standard in heptane.

Transesterification reaction was done by refluxing the flask content in an oil bath while magnetically stirring at 600 rpm. At the end of the reaction, the products were cooled to room temperature. Volume of 1 ml chloroform, 3 ml heptane and 3 ml deionized water were added to the flask contents after cooling to room temperature. The flask was stoppered, vortexed for 15 s and then allowed to separate for 1 h. To the organic layer, 2 g of freshly dried $MgSO_4$ was added and the content vortexed before allowing to stand in a sealed vial for 3 h. The dry organic layer was withdrawn using a 2 ml plastic syringe and filtered through a 0.45 µm PTFE membrane filter into a 2 ml GC vial for GC analysis. The vials were stored at 4 °C or -20 °C in cases of delayed GC analysis as noted by Van Wychen et al., 2016.

Figure 3.5; Batch transesterification reaction of *Jatropha curcas* and waste cooking oils.

3.3.4 Optimization of the biodiesel synthesis

The optimal transesterification parameters were achieved using a design of experiments where a scheme of experiments in different conditions was developed using Taguchi experimental design (Garshasbi et al., 2017).

3.3.4.1 Experimental design array

The Taguchi method is a statistical experimental design approach for multifactor process optimization (Garshasbi et al., 2017). It is a fractional factorial design of experiments based on orthogonal arrays to evaluate the maximum number of effects from a minimum number of runs in an experiment while allowing for differences in the number of factor levels. Taguchi approach is favoured over single process at a time optimization because it gives an extensive information about the interaction between the process parameters, in addition to the optimized condition being achieved with a limited number of experiments (Kumar et al., 2017). Taguchi orthogonal array is represented as $L_a(Q^b)$, where a denotes the number of experimental runs, Q is the number of levels, and b is the number of factors being optimized.

A four level (L_{16} (4^4)) Taguchi orthogonal array design of experiments with a total of 16 experimental runs was developed in Minitab 18.1.0.0 software. Table 3.2 show the levels for chosen independent factors. The experiments were done in triplicates.

Table 3.2; Levels of chosen independent factors in the L_{16} (4^4) Taguchi design of experiments.

Factors	Level			
	low		high	
Temperature (°C)	50	60	70	80
Oil/Methanol ratio (mol/mol)	1:5	1:10	1:15	1:20
Time (h)	0.5	2	5	8
Catalyst load (w. %)	0.5	2	5	8

The L$_{16}$(4^4) experimental design matrix used in the optimization study is show in Table 3.3.

Table 3.3; The L$_{16}$(4^4) experimental design matrix developed in Minitab 18.1.0.0 software.

Experiment trial	Reaction Temp (°C)	Reaction Time (h)	Cat load (wt. %)	MeOH/Oil molar ratio
1	50	0.5	0.5	5
2	50	2	2	10
3	50	5	4	15
4	50	8	8	20
5	60	0.5	2	15
6	60	2	0.5	20
7	60	5	8	5
8	60	8	4	10
9	70	0.5	4	20
10	70	2	8	15
11	70	5	0.5	10
12	70	8	2	5
13	80	0.5	8	10
14	80	2	4	5
15	80	5	2	20
16	80	8	0.5	15

3.3.4.2 Analysis of variance (ANOVA)

Taguchi method leads to the determination of the factors affecting the process. The signal to noise ratio (S/N) is used to measure the quality characteristics deviating from the desired value. Based on the S/N ratio, it is possible to get the optimum level of the individual process parameters providing the highest yield of biodiesel. In this study, ''larger is better'' S/N ratio, formular shown in equation (4), was selected to attain maximum yield of biodiesel.

$$\frac{S}{N} = -10 \times log_{10} \left(\sum_{j=1}^{N} \frac{\left(\frac{1}{y_j^2} \right)}{n} \right) \tag{4}$$

where y_j is the mean value of response (FAME yield), j is the trial number and n is the number

of repetitions of each experiment. The term $\left(\sum_{j=1}^{N} \dfrac{\left(\frac{1}{y_j^2} \right)}{n} \right)$ is the mean square deviation.

To identify the factor with the most significant effect on the FAME yield and the response

magnitude, statistical analysis of variance (ANOVA) of the response data was used. The basic

property in ANOVA is that the total variation is equal to the sum of the squares of the deviations

(ss) of all the condition parameters and the error components (Kumar et al., 2015). The

percentage of contribution of the factors was evaluated using equation (5).

$$Contribution\ factor\ (\%) = \frac{sum\ of\ squares\ of\ f^{th}\ factor}{total\ sum\ of\ squares} \times 100\ \% \qquad (5)$$

3.4   Characterization

3.4.1   Characterization of clay and zeolites

Powder XRD patterns were obtained in a continuous mode with 2 θ scan step size of 0.026°

using a PANalytical X-Pert Pro X-ray powder diffractometer (Almelo, Netherlands)

employing Cu-Kα radiation (λ = 0.15406 nm). X-rays were generated from the Cu anode at 40

kV and a current of 40 mA. The samples were ground into powder before loading on the 20

mm XRD quartz sample holder. The diffraction of the sample was recorded over the 2 θ range

from 5° to 50° in the steps of 0.026° at room temperature. Zeolite phases were identified by

comparison with the reference XRD patterns in the zeolite database from the International

Zeolite Association (Baerlocher & McCusker, 2017) and that of commercial molecular sieve

13X. The percentage crystallinity was estimated by comparing the peak areas of ten selected strong peaks (at 2θ of 6.15°, 10.06°, 15.51°, 20.11°, 23.34°, 26.67°, 30.35°, 30.98°, 32.06° and 33.61° for Na-X, and at 7.27°, 10.24°, 16.17°, 21.71°, 24.05°, 27.17°, 30.88°, 32.59°, 33.43° and 34.21° for Na-A), with those of commercially available zeolite 13X and zeolite 4A, respectively (García-Soto et al., 2013). The peak areas were determined with the aid of OriginLab 9.80.200 software.

The presence of functional groups was monitored by Infrared spectroscopy between 400-4000 cm-1 using a Bruker Alpha Attenuated Total Reflectance - Fourier Transform Infrared (ATR-FTIR) spectrometer (Germany). About 1 mg of the solid or 0.1 µL liquid sample was placed on the diamond crystal and the anvil lowered to enforce contact of the solid sample with the crystal. Thermogravimetric analysis (TGA) was performed using a TA Instrument SDT Q600 thermal analyser (Canada). A mass of 10 mg of the sample was loaded to the TGA pan before heating the sample between 25 °C and 1000 °C at 10 °C/min under flowing air (100 mL/min). The surface morphology of the samples was explored via scanning electron microscopy (SEM) using a Field Electron and Ion (FEI) Quanta 200 3D Dual Beam focused ion beam (FIB) microscope (USA). The powdered samples were placed on the double-sided adhesive carbon tab mounted on the SEM pin stub. The samples were carbon or palladium coated before EDX or SEM analysis, respectively.

Chemical composition was obtained using an energy dispersive spectrometer (EDX) during SEM analysis (USA) and Perkin Elmer Inductively Coupled Plasma Optical Emission Spectroscopy (ICP-OES) Optima 2000 DV (Shelton, USA) fitted with an auto sampler. For the ICP-OES, the samples were prepared using the reported procedure by Zamechek, 2001. In brief, 0.1 g of the sample was thoroughly mixed with 1.5 g lithium tetraborate in a 15 ml platinum crucible. The mixture was covered and fused in a box furnace by heating at 20 °C/min

to 1000 °C then holding at this temperature for 2 h. After cooling to room temperature, the fused material was dissolved by placing the crucible and its content in a 100 ml beaker containing a hot 10 % HNO_3 solution. The dissolution was enhanced by magnetically stirring the hot content in the fume hood for 30 min. The beaker content was then transferred to a 250 ml volumetric flask before making to the mark using milliQ water. The Prepared solutions were refrigerated, at similar temperatures previously stated, awaiting ICP-OES analysis. During analysis, argon gas was used to generate the plasma for the ICP-OES. All concertation measurements were performed in triplicate and the average value used in the subsequent calculations. The concentrations of reference standards (multicomponent and silicon standard) used in preparing the calibration curves are shown in Table 3.4.

Table 3.4; Concentrations for calibration curves.

	Multicomponent Std Concentration (mg/L)	Silicon Std Concentration (mg/L)
1	0.05	50
2	0.1	100
3	0.5	200
4	1	300
5	2	400
6	5	500
7	10	
8	20	
9	50	
10	100	
11	200	
12	300	

The concentration range for the multicomponent reference standard was extended to very low concentrations in order to accommodate the analysis of trace elements in the samples. The wavelengths in nm used for the analysis of Si, Al, Ti, Fe, Cu, K and Na using ICP-OES were 251.611, 396.153, 334.84, 234.349, 222.778, 766.49 and 589.592, respectively.

Textural properties of the materials and synthesized zeolites were analysed using a Micromeritics 3FLEX sorptometer (USA) employing N_2 gas as a sorbate at liquid nitrogen temperature (-196 °C). Approximately 100 mg of the sample was loaded into the BET ports. The samples were outgassed under vacuum at 300 °C for 16 h prior to analysis. The surface area was calculated using the Brunauer-Emmett-Teller (BET) method. The total pore volume was calculated from the nitrogen uptake at close to saturation pressure (i.e., at P/Po ~ 0.99) while micropore surface area, external surface area and micropore volume were determined from t-plot analysis. Horvath-Kawazoe model, assuming spherical pore geometry due to the three-dimensional pore structure of zeolites (Cheng & Yang, 1994), was used in modelling the pore distribution of the synthesized zeolites.

3.4.2 Characterization of oils and biodiesel

Characterization of oils and biodiesel samples was done by testing the physical and chemical properties of the oils and their corresponding FAMEs. The thermal and functional groups analysis of the oils and biodiesel were performed using TGA and FT-IR spectroscopy as described above. The fatty acid composition of the oils as well as the FAME content of transesterification products were determined by gas chromatography Trace 1310, (Thermo Scientific - USA). The GC was fitted with the flame ionization detector and SGE BP1 column (30 m × 0.25 mm × 0.25 μm) and helium used as a carrier gas. All analyses were performed in triplicate and the average value used in subsequent calculations.

A supelco multicomponent GLC-10 reference standard was used for the optimization of GC-FID instrument parameters and for the calibration and determination of response factor (RF). GLC-10 consists of 20 % (wt. %) each of methyl palmitate (C16:0Me), methyl stearate (C18:0Me), methyl oleate (C18:1Me), methyl linoleate (C18:2Me) and methyl linolenate (C18:3Me). Other properties of oils and biodiesel products including density, acid value,

viscosity and saponification value were analysed according to the European Norm (EN-14214:2008, 2009) developed by the European Committee for Standardization.

3.4.2.1 Optimization of GC-FID instrument parameters

Optimization of GC-FID instrument parameters was performed before oils and biodiesel analysis. Table 3.5 shows the optimum conditions for the GC-FID analysis obtained using GLC-10 reference standard. The conditions were based on the better separation of the methyl stearate (C18:0Me), methyl oleate (C18:1Me) and methyl linoleate (C18:2Me) peaks of the GLC-10 reference standard.

Table 3.5; Optimum GC-FID conditions obtained using GLC-10 reference standard.

Parameter	Conditions
GC column	SGE BP1 30m × 0.25 mm × 0.25 μm
Carrier gas	Helium, at 1 ml per min flow
Inlet;	
Injector temperature	250 °C
Injection	1μL (auto injection)
Split ratio	10:1
Oven programme	Rump; 120 °C for 1 min, then 6 °C/ min up to 250 °C and then hold for 5 min
Detector;	
Type	Flame ionization
Detector temperature	280 °C
Gas	H_2
Flow	450 ml/min air
	40 ml/min H_2
	30 ml/min Helium
Total run time	28 min

The optimized GC-FID conditions were used for the subsequent characterization of oils and transesterification products using GC-FID.

3.4.2.2 Determination of the response factor (RF)

The response factors (RFs) for individual FAMEs in the GLC-10 reference standard were also determined before characterization of oils and transesterification products. The RF is a measure of the relative mass spectral response of an analyte compared to its internal standard. The determination of RF was achieved by generating the calibration curves for each FAME component of GLC-10 reference standard and following the method developed by Van Wychen et al., 2016. Individual FAME peaks of the GLC-10 reference standard were identified by their retention times from the GC spectrum generated using optimized conditions above. Table 3.6 show the five levels of reference standards (r.s) alongside internal standards (i.s), and their corresponding concentrations, prepared for the generation of calibration curves for the determination of RF.

Table 3.6; Five levels of reference standards for the determination of RF.

Ref. std (r.s) level	[r.s] (mg/mL)	[i.s] (mg/mL)
1	0.0099	0.025
2	0.0298	0.025
3	0.0994	0.025
4	0.2485	0.025
5	0.497	0.025

[r.s] is the concentration of the reference standard, [i.s] is the concentration of the internal standard

The RF for each FAME component was calculated using the gradients of linear plots obtained from the calibration curves by following Laboratory Analytical Procedure (Van Wychen et al., 2016).

3.4.2.3 Determination of the fatty acid composition of the oils

The fatty acid composition of the oils was determined using GC-FID by following the Laboratory Analytical Procedure (Van Wychen et al., 2016). In brief, 30 mg of oil was weighed in a 5 ml round bottomed flask. 1.2 ml of 0.6 M HCl, 0.8 ml of 2/1 chloroform/methanol and 0.1 ml 10 mg/ml of C19:0Me internal standard was added to the flask. The content was vortexed for 15 s followed by transesterification reaction at 85 °C for 1 h. The reaction content was then stopped and allowed to cool for 1 h to room temperature. A volume of 1 ml of chloroform and 1 ml of deionized water was then added to the flask and the content vortexed for 15 s before allowing to separate for 1 h. a mass of 2 g of dried $MgSO_4$ was added to the organic layer and the content vortexed for 15 s. The vial was then allowed to stand for 3 h to separate the solids from liquid. The liquid layer was carefully withdrawn using a 2 ml syringe and filtered through a 4.5 µm PTFE membrane filter into GC vials for analysis. The vials were tightly caped before storage at -20 °C where analysis was delayed.

The individual FAME peaks of the JCO and WCO derived FAMEs were identified by comparing their retention times with those of the GLC-10 reference standards in their respective GC spectra.

3.4.2.4 Determination of FAME content of transesterification products

The FAME contents of various biodiesel samples were determined using GC-FID. The FAME yield (%) of the transesterification product was calculated using the formula in equation (6);

$$FAME\ Yield\ (\%) = \frac{\sum FAME}{w_{oil}} \times 100\ \% \tag{6}$$

where ∑FAME is weight summation of fatty acid methyl ester content of individual fatty acids in the biodiesel, while w_{oil} is the dry weight of the oil sample used in the transesterification.

CHAPTER 4

RESULTS AND DISCUSSION

This chapter details the results and discusses them. All figures and tables in this chapter were generated from this study.

4.1 Characterization of raw materials

The raw materials considered here are the clay mineral and volcanic ash which were utilized in the subsequent sections in the synthesis of zeolites.

4.1.1 Characterization of clay material

In order to investigate the vibrational characteristics of the bonds and to identify the phases present in the clay materials, Fourier transform infrared (FTIR) and X-ray diffraction (XRD) spectroscopies were performed on raw and treated clay material. Figure 4.1 show the resulting FTIR spectra of the raw and treated clay materials in metakaolinite and fused-metakaolinite methods. The FTIR bands between 400-1100 cm^{-1} describes the modes of vibrations of silica and alumina groups in the clay. The bands at ca. 525 and 1025 cm^{-1} are due to Si-O-Si bending and stretching vibrations respectively, and similar results had also been observed by Bukalo et al., 2017. The bands at 997 and 1114 cm^{-1} are due to Si-O in plane and out of plane stretching vibrations respectively, while those at 540 and 911 cm^{-1} are due to the Al-O stretching of the AlO_6 octahedron and the Al-OH inner surface bending vibration respectively. The doublet bands at ca. 792 and 751 cm^{-1} due to Si-O from quartz phase have also been previously observed in other studies by Saikia & Parthasarathy, 2010. The four bands between 3600-3900 cm^{-1} are characteristic to the triclinic layer structure of kaolin (Djomgoue & Njopwouo, 2013). In specific, the band at ca. 3620 cm^{-1} is due to stretching vibrations of inner -OH groups (Al-OH),

while others at ca. 3654, 3667 and 3687 cm^{-1} are due to stretching vibrations of surface -OH groups.
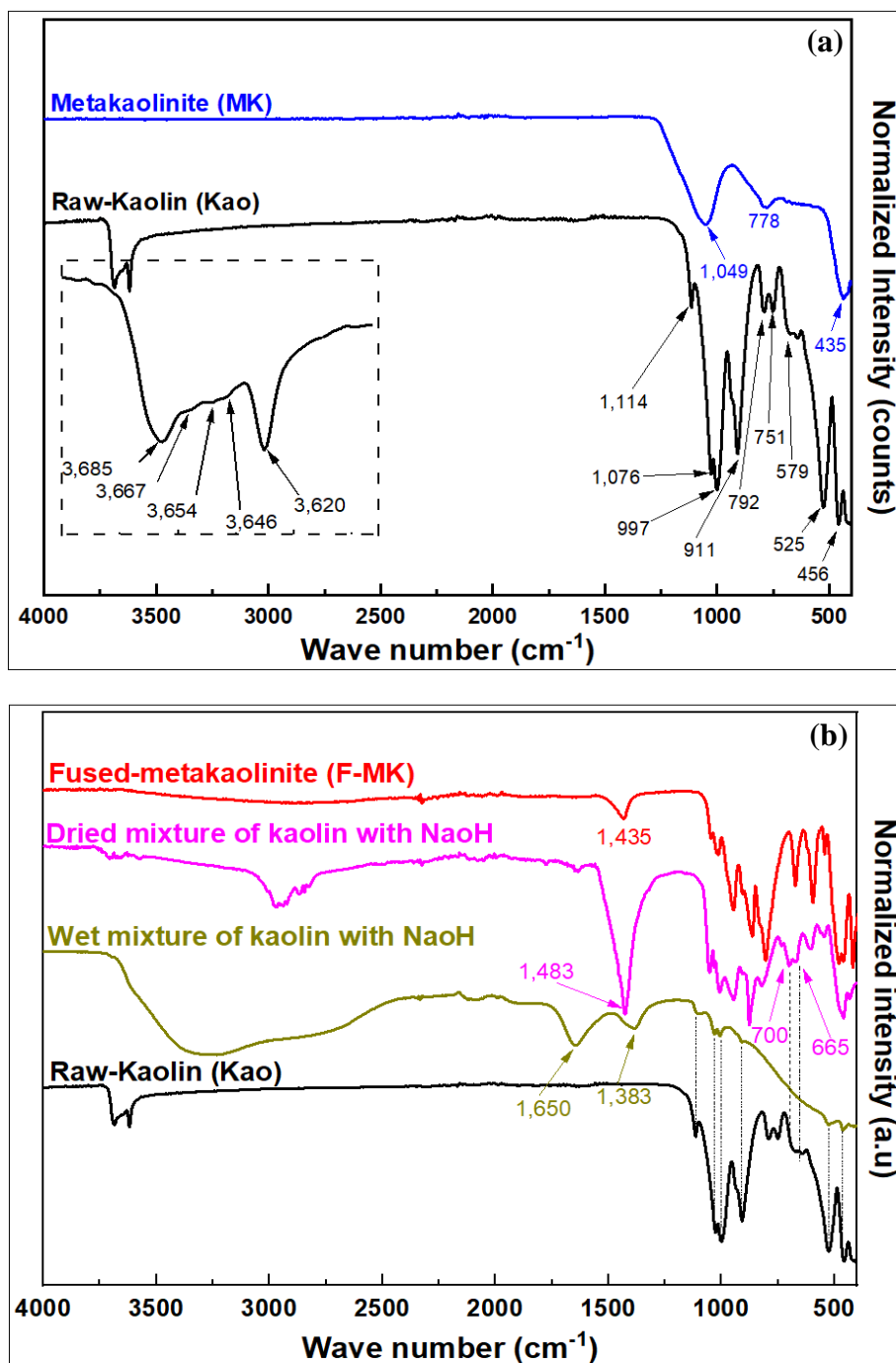
Figure 4.1; The FTIR spectra of; (a). raw clay and metakaolinite, and (b). raw clay, treated clay and fused-metakaolinite.

In Figure 4.2a, apart from the quartz bands in the matakaolinite (MK), which were still visible within the broad band of MK at 778 cm^{-1}, all other -OH and characteristic bands in the raw

clay were not observed after metakaolinization. All the Si-O and Al-O-Si bands of kaolinite shifted to higher wave numbers in MK with the new broad bands centred at 1049 and 435 cm^{-1} representing amorphous aluminosilicate vibrations. The FTIR spectrum for the wet mixture of raw clay with NaOH solution in Figure 4.2b reveals masked bands of quartz and kaolinite mineral. The kaolinite bands were however suppressed after drying out the water solvent leading to formation of new bands. Further treatment of the dried mixture by fusion at 750 °C eliminated the kaolinite and the quartz bands, and led to the formation of additional new bands in the low wave number region.

Figure 4.2(a & b) show the resulting XRD patterns of raw and treated clay materials in metakaolinite and fused-metakaolinite methods, respectively. The XRD pattern of raw clay mineral in both Figure 4.2(a & b) reveals peaks at 2 θ of 12.4° and 24.9° corresponding to characteristic 7.1Ǻ and 3.7Ǻ d-spacings for the kaolinite phase, which have also been reported in other studies by Senoussi et al., 2016. Other kaolinite peaks appear at 19.9°, 20.5°, 35.0°, 36.0° and 38.5°. The other peaks at 2θ of 20.9°, 26. 7°, 36.6°, 39.5°, 42.5° and 45.8° in the pattern correspond to quartz phases. In Figure 4.2a, the expected broad peak between 2 θ of 13°-30° corresponding to newly formed amorphous aluminosilicates in metakaolinite (MK) was masked by the intense quartz peaks. Pre-treatment of raw clay by wet mixing with NaOH and then drying out of water solvent in Figure 4.2b led to the suppression of kaolinite peaks and emergence of new peaks alongside quartz peaks. Kaolinite and quartz peaks were not observed in the fused-metakaolinite (F-MK), however, there was formation of additional new XRD peaks in the higher 2θ values. The observations made in the XRD patterns are therefore in agreement with those made in the FTIR spectra. The occurrence of new FTIR bands and the presence of new XRD peaks in the fused-metakaolinite might imply the formation of new phases.
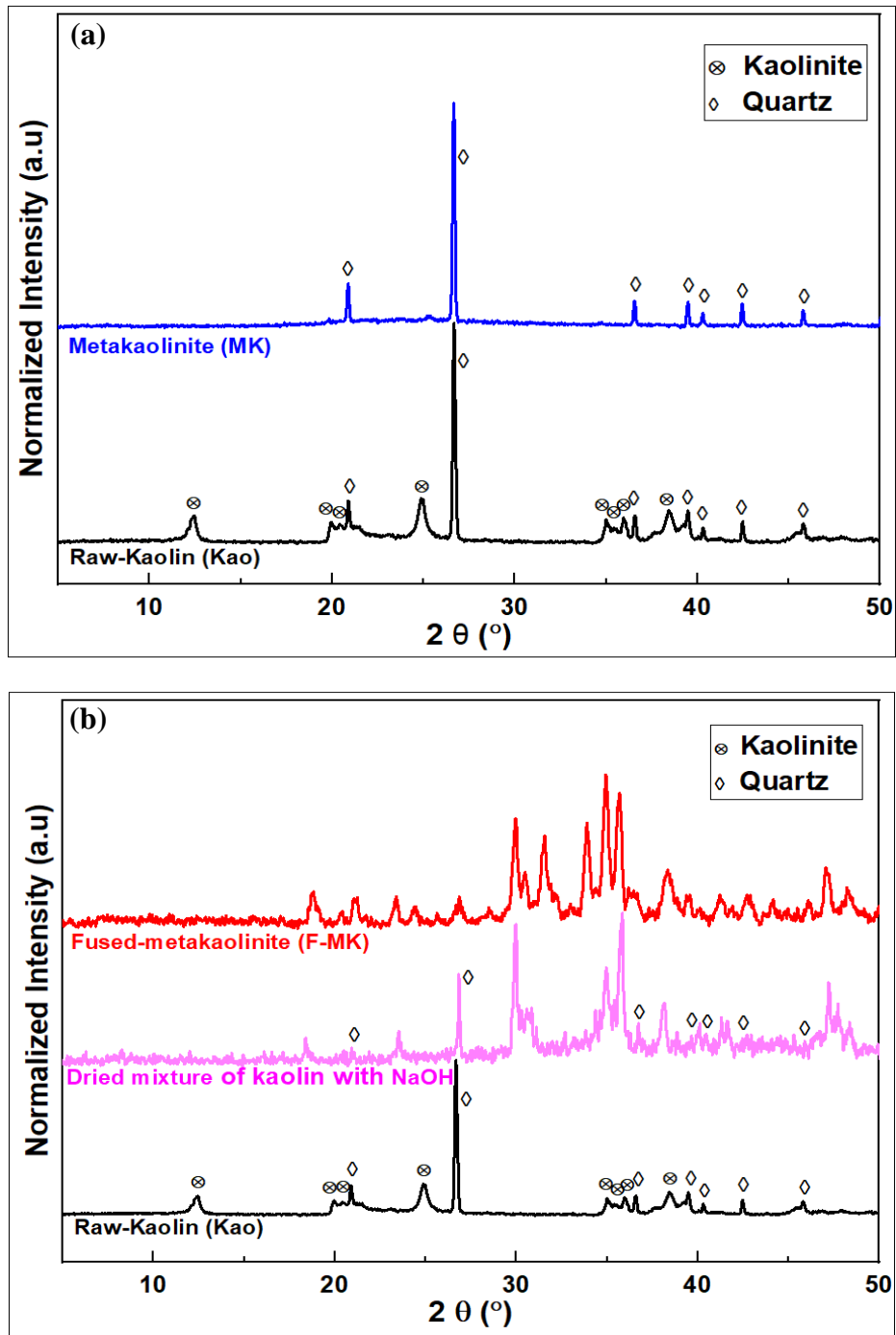
Figure 4.2; The XRD pattern of; (a). raw clay and metakaolinite, and (b). raw clay, treated clay and fused-metakaolinite.

To explore the surface morphology of the raw clay and metakaolin materials, SEM imaging was performed. The SEM image of raw clay and MK are shown in Figure 4.3. The SEM image of the raw clay in Figure 4.3(a & b) depicts a pseudohexagonal platy morphology typical of kaolinites (Hanlie et al., 2012). The kaolinite flakes are also visible in both Figure 4.3(a & b).

The flakes and platy morphology were, however, not observed in Figure 4.3c for the MK. The SEM image of MK also reveal some layered morphology besides the observed amorphous phases. The layered morphology in MK might imply the presence of unconverted phases, even after heat treatment, alongside amorphous MK phase.
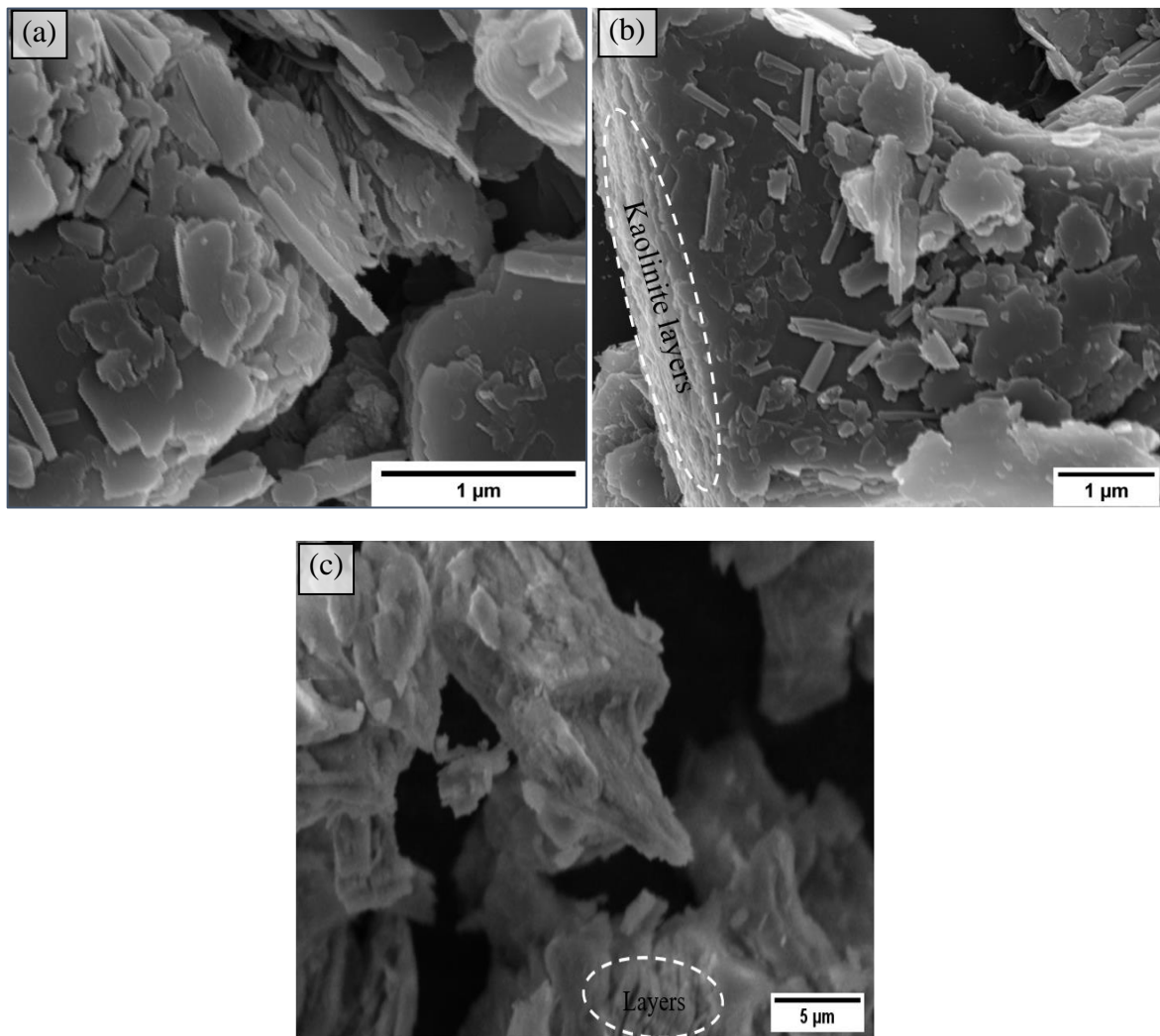
Figure 4.3; SEM image of raw clay (a & b), and metakaolinite (c).

In order to determine the chemical composition of the raw and treated clay materials, ICP-OES analysis was performed on the raw and treated materials. The chemical analysis of the raw clay and F-MK is shown in Table 4.1. The calibration curves used in the determination of elemental composition for Al, Si, Na, Fe, K and Cu are shown in Appendices 1-7.

Table 4.1; Chemical composition of raw and treated clay.

Sample	Percent oxide (wt. %)							LOI*	SiO$_2$/Al$_2$O$_3$	Calculated Chemical formula
	Al$_2$O$_3$	SiO$_2$	Na$_2$O	TiO$_2$	Fe$_2$O$_3$	K$_2$O	CuO			
Raw clay	30.34	56.74	0.54	1.07	0.45	0.18	0.18	10.49	3.17	Fe$_{0.93}$Cu$_{0.39}$Ti$_{4.89}$Na$_{2.69}$K$_{0.69}$Al$_{100}$Si$_{158.70}$O$_{475.76}$
Washed Fused-metakaolinite (F-MK)	27.38	35.08	36.23	0.72	0.32	0.15	0.12	-	2.17	Fe$_{0.75}$Cu$_{0.28}$Ti$_{1.74}$Na$_{217.69}$K$_{0.58}$Al$_{100}$Si$_{108.71}$O$_{481.43}$

Total SiO$_2$ content of raw clay = 56.74 %;

	SiO$_2$ in the kaolin structure	SiO$_2$ in quartz
wt. %	35.71	21.03

* Loss on ignition

The weight loss on ignition (LOI) for the clay material, due to dehydroxylation to MK, was 10.49 %. Apart from Ti, Fe, Na, K and Cu elements which were detected in trace amounts, the main oxides in the clay mineral were Al_2O_3 (30.34 wt. %) and SiO_2 (56.74 wt. %). The SiO_2/Al_2O_3 molar ratio of the clay material was found to be 3.17, which was higher than the expected value of 2 for the 1:1 kaolinite clay material (Schulze, 2005). The extra SiO_2 is therefore present in the form of quartz also observed in the FTIR spectra and XRD patterns in Figure 4.1 and 4.2, respectively. Based on the chemical formula of kaolin, calculations in the present study showed that, of the 56.74 % of SiO_2 in raw clay, 21.03 % is quartz phase while 35.71 % is the silica forming the kaolinite structure. For the washed fused-metakaolinite, obtained by washing out excess alkali and free ions from the F-MK, the Na_2O composition significantly increased to 36.23 % while the SiO_2/Al_2O_3 molar ration reduced to 2.17 (i.e., in comparison with the kaolin starting material). The increase in Na_2O is due to the successful reaction of NaOH with kaolin components at high fusion temperature, while the reduction in SiO_2/Al_2O_3 might imply leaching out of SiO_2 in the clay material and subsequent loss of unreacted silica ions in the aqueous solution.

Understanding the thermal properties of a material is important because it illustrates the response of the material when heat is supplied thus giving information on changes accompanying physical or chemical quantities, phase transitions and initiated chemical reactions. Thermogravimetric analysis of the raw and modified kaolin was performed in the temperature range of 25-1000 °C to understand their thermal behaviours. Figure 4.4 shows the thermogravimetric analysis (TA), differential thermogravimetric analysis (DTA) and differential scanning calorimetry (DSC) curves for raw clay, F-MK and wet mixed clay with NaOH then dried. Positive derivative of weight (DTA) curve indicates mass loss while positive derivative of heat flow (DSC) curve indicates heat released/exothermic process.
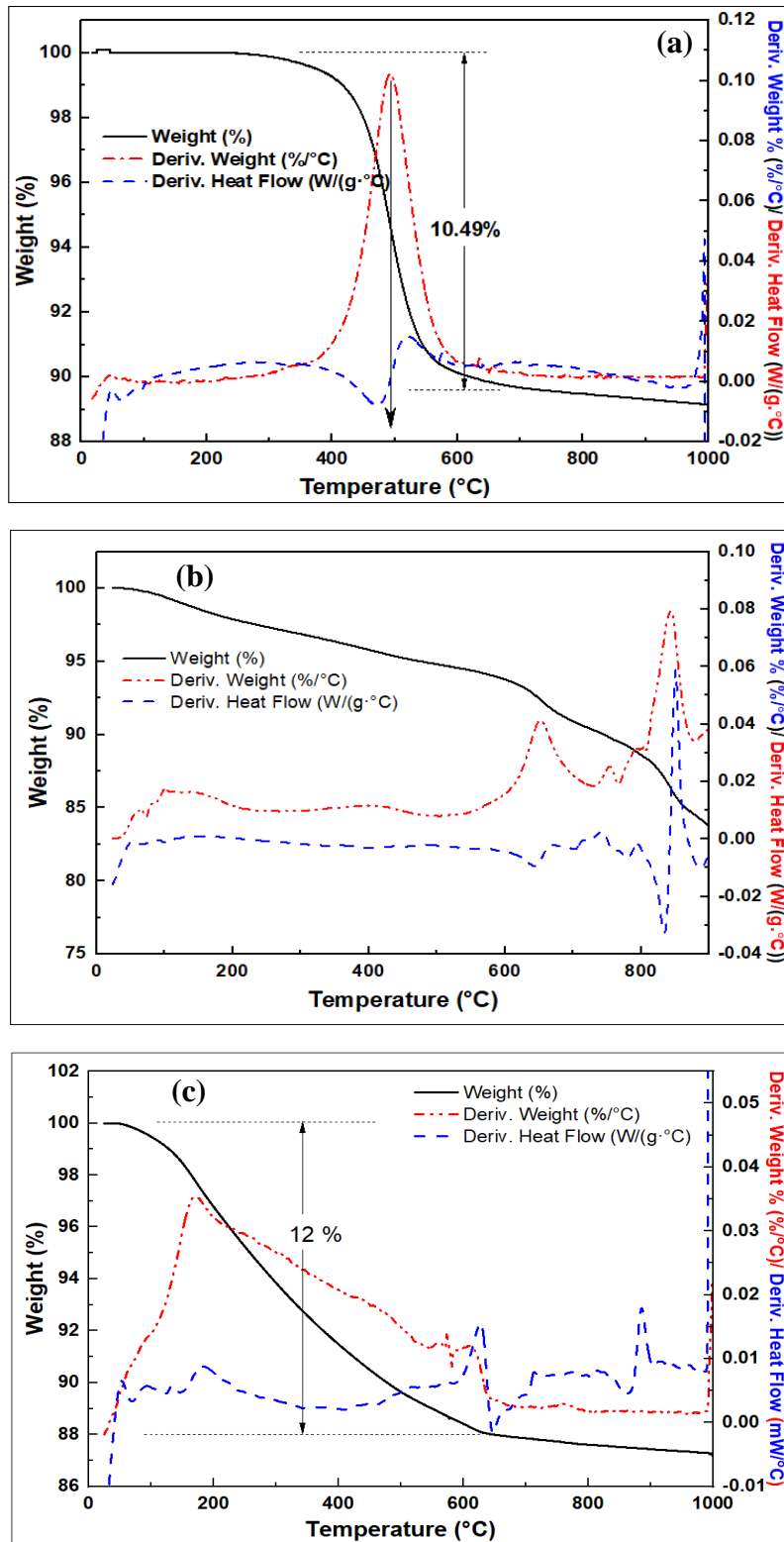
Figure 4.4; TGA analysis of clay; (a). raw clay, (b). wet mixed raw clay with NaOH then dried, and (c). washed F-MK.

Raw kaolin in Figure 4.4a is stable up to 400 °C with subsequent exothermic weight loss (LOI) of 10.49 % at 500 °C. The weight loss is due to the dehydroxylation reaction of kaolin to

metakaolin (Michot et al., 2011). The treated clay (wet mixed with NaOH then dried) in Figure 4.4b shows a multiple step weight loss. The first step, ca. 5 % weight loss occurring between 30-500 °C, is attributed to the loss of absorbed water. The second step occurs between 500-720 °C and is due to the decomposition of NaOH and subsequent loss of associated water. The subsequent two steps between 720-810 °C could be due to the rearrangement of atoms during the structure building and the associated weight loss. The other steps are in the range of 810-1000 °C might be due to change in sodium aluminosilicate phases to metastable phases. On the other hand, ca. 12 % gradual weight loss between 50 °C and 600 °C due to the absorbed water molecules was recorded for the F-MK. In addition, the positive derivative of heat flow for the F-MK at ca. 900 °C, not accompanied by weight loss, is likely due the structural collapse of the F-MK to form high temperature phases.

To explore the porosity and textural properties of raw kaolin, BET analysis by N_2 sorption at liquid nitrogen temperature (-196 °C) was performed. The textural properties of the raw kaolin material are shown in Figure 4.5 and Table 4.2.
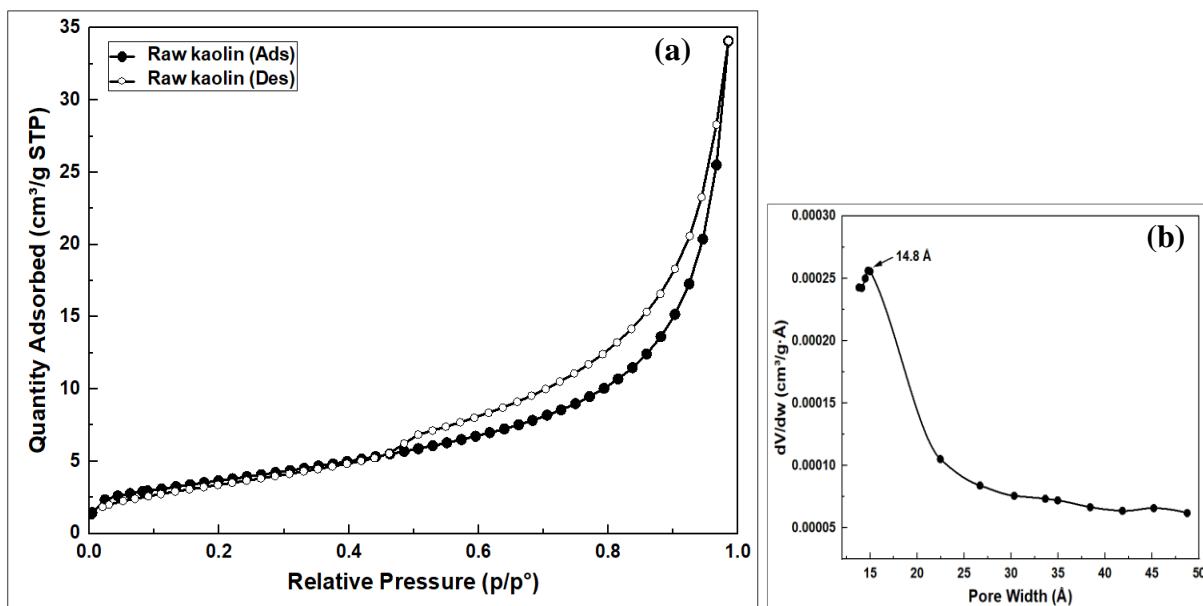
Figure 4.5; Porosity analysis of raw kaolin material; (a). N_2 sorption isotherm, and (b). Horvath-Kawazoe pore size distribution.

Table 4.2; Textural properties of raw kaolin material.

Sample	Specific Surface area (m²/g)	Micropore surface area (m²/g)	External surface area (m²/g)	Micropore volume (cm³/g)	Total pore volume (cm³/g)	Pore size (Å)
Raw-Kaolin	13	-	15	-	0.05	-

The BET isotherm of kaolin material in Figure 4.5a exhibited a reversible type II isotherm, showing unrestricted monolayer-multilayer adsorption up to high P/P_0, with a type H3 hysteresis loop for the non-rigid aggregates of plate-like particles of clay material (Thommes et al., 2015). The low BET surface area in Table 4.2, also observed in the BET isotherm in Figure 4.5a, is due to the layered characteristics of kaolin clay. The pore width distribution in Figure 4.5b reveals microporous porosity at 14.8 Å for the kaolin.

4.1.2 Characterization of the volcanic ash material

The ICP-OES and X-ray fluorescence spectroscopy were performed on the raw and purified volcanic ash to determine their chemical composition. The chemical composition of the raw (KVA-Raw), acid-washed (KVA-10%A) and calcined (KVA-10%A-750C) volcanic ash is shown in Table 4.3. A total of 33 % weight loss was observed as loss on ignition (LOI). The chemical analysis of raw volcanic ash shows that its major constituents by weight percent are CaO and SiO_2 at 47.09 % and 18.38 % respectively. Other oxides of Na, Ti, Fe, K and Cu were present in trace amounts. The CaO was eliminated by washing raw volcanic ash (KVA-Raw) by stirring in aqueous solution of 10 % HCl (wt. %) at room temperature for 24 h to give acid-washed volcanic ash (KVA-10%A). The composition of the resulting KVA-10%A was 99 % SiO_2 and 1% trace oxides. The composition stayed at 99 % of SiO_2 even after heating at 750 °C.

Table 4.3; Chemical composition of the raw, acid-washed and calcined volcanic ash.

Sample	Percent oxide (wt. %)							CuO	SiO$_2$/Al$_2$O$_3$	LOI	Method	Chemical formula
	Al$_2$O$_3$	SiO$_2$	Na$_2$O	TiO$_2$	Fe$_2$O$_3$	K$_2$O	CaO					
KVA-Raw	0.36	18.38	-	0.15	0.03	0.03	47.09	-	88.23	33	XRF	Ca$_{242.26}$Fe$_{0.05}$Ti$_{0.28}$K$_{0.17}$Al$_{10}$Si$_{44.11}$O$_{211.67}$
KVA-10%A	0.24	98.92	0.57	0.02	0.06	0.04	-	0.16	707.67	-	ICP-OES	Fe$_{0.15}$Cu$_{0.42}$Ti$_{0.05}$Na$_{3.96}$K$_{0.19}$Al$_1$Si$_{353.81}$O$_{711.95}$
KVA-10%A-750C	-	99.39	0.20	-	-	0.10	-	-	-	-	SEM-EDX	Ca$_{0.10}$Na$_{0.38}$K$_{0.22}$Mg$_{0.39}$Si$_{100}$O$_{200.85}$

The surface morphology analysis by SEM of the raw and acid-washed volcanic ash are shown in Figure 4.6. The SEM image of the raw volcanic ash in Figure 4.6a show a porous material with a very rough topology. A non-porous amorphous material in Figure 4.6b was, however, obtained after washing the KVA-Raw and eliminating the CaO with 10 % HCl.
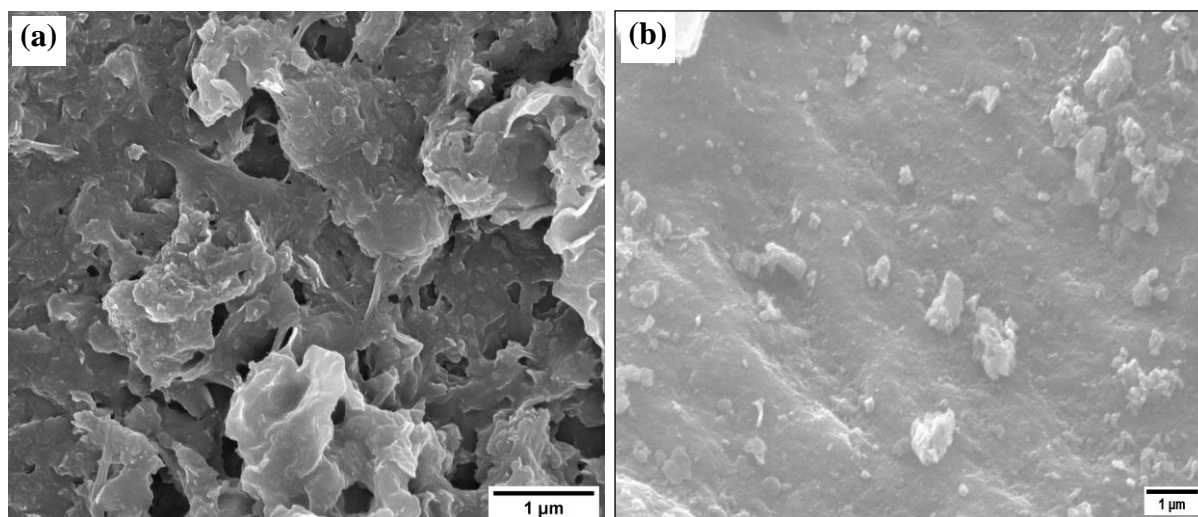
Figure 4.6; The SEM images of volcanic ash; (a). KVA-Raw, and (b). KVA-10%A-750C.

The X-ray and Fourier transform infrared spectroscopies were performed on raw and purified volcanic ash materials in order to identify the phases present and to investigate the vibrational characteristics of the bonds involved, respectively. Figure 4.7 show the resulting FTIR spectra and XRD patterns of the raw (KVA-Raw), acid-washed (KVA-10%A) and calcined acid-washed volcanic ash (KVA-10%A-750C). The bands in Figure 4.7a appearing at 449, 794 and 1062 cm^{-1} are due to Si-O symmetric bending, in plane and out of plane stretching vibrations of the amorphous SiO_2, respectively. The band at ca. 779 cm^{-1} is due to Si-O of quartz phase (Saikia & Parthasarathy, 2010). The FTIR bands at ca. 712, 872, and 1412 cm^{-1} in the KVA-Raw are characteristics of calcite polymorph of calcium carbonate mineral and corresponds to the in-plane bending (v_4), out of plane bending (v_2) and symmetric stretching (v_3) modes of vibration for the calcite's -CO_3 group. Similar bands have also been reported for calcite by other researchers, (Legodi et al., 2001; Singh et al., 2016).
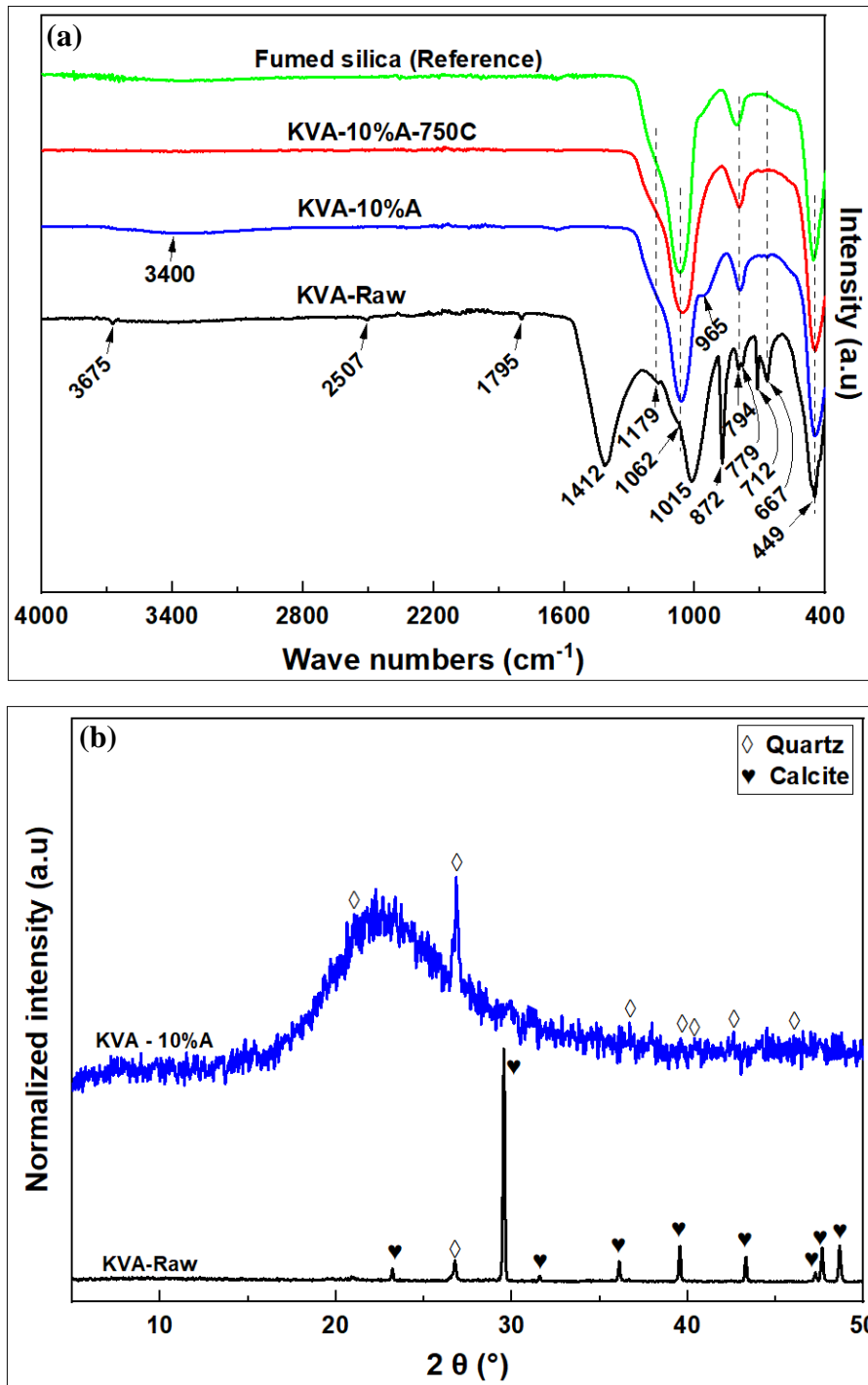
Figure 4.7; (a). FTIR spectra of raw volcanic ash (KVA-Raw), acid-washed (KVA-10%A) and calcined acid-washed volcanic ash (KVA-10%A-750C), and (b). XRD patterns of raw volcanic ash and acid-washed volcanic ash.

Other calcium carbonate bands appear at ca. 1796, 2507 and 3695 cm^{-1} (Kamba et al., 2013; Singh et al., 2016). The other bands at 667 and 1015 cm^{-1} observed here were reported for the poorly ordered amorphous $CaCO_3$ phase (Rodriguez-Blanco et al., 2011).The calcium in the

raw volcanic ash is therefore present inform of calcite polymorph. All the calcite bands were eliminated by washing the raw volcanic ash with aqueous solution of 10 % HCl. The bands due to amorphous SiO_2 were masked in the KVA-Raw spectrum by the calcite bands. The resulting FTIR spectra of the calcined volcanic ash (KVA-10%A-750C) is in good agreement with that of fumed silica reference.

The XRD patterns of the raw and acid-washed volcanic ash is shown in Figure 4.7b. The peaks at 2 θ of 23.2°, 29.5°, 31.6°, 17.4°, 39.5°, 43.3°, 47.3°, 47.7° and 48.7° in the raw volcanic ash pattern are characteristic of calcite polymorph of $CaCO_3$. Similar peaks were observed by Fatimatul et al., 2019. All the calcite peaks were eliminated after washing the volcanic ash with 10 % HCl leaving behind amorphous silica phase with a broad peak between 17-34°. The other sharp peaks in the KVA-10%A pattern at 2θ of 21.1°, 26.8°, 36.7°, 39.6°, 40.3°, 42.6° and 46.0° belong to the quartz phase. The amorphous silica and the quartz peaks were however suppressed in the XRD pattern of the KVA-Raw by the intense calcite peaks. The observations made in the XRD patterns are therefore in good agreement with the observations made in the FTIR spectra, SEM images and the chemical analysis for volcanic ash material.

In order to understand the thermal behaviour of the raw and the purified volcanic ash, thermogravimetric analysis of KVA-Raw and KVA-10%A were performed. Figure 4.8 shows the TA, DTA and DSC thermal analysis curves for the raw and acid-washed volcanic ash materials. The raw volcanic ash in Figure 4.8a was stable up to 620 °C with only 1 % weight loss being recorded between 20-620 °C due to the loss of small quantity of absorbed water. A total of 33 % weight loss (LOI), due to the decomposition of calcium carbonates to calcium oxide and subsequent loss of CO_2 (Kamba et al., 2013), was observed between 620-815 °C with the integral peak appearing at 790 °C. On the other hand, only 3 % weight loss, due to small quantity of absorbed water, was recorded for the acid-washed volcanic ash in Figure 4.8b.
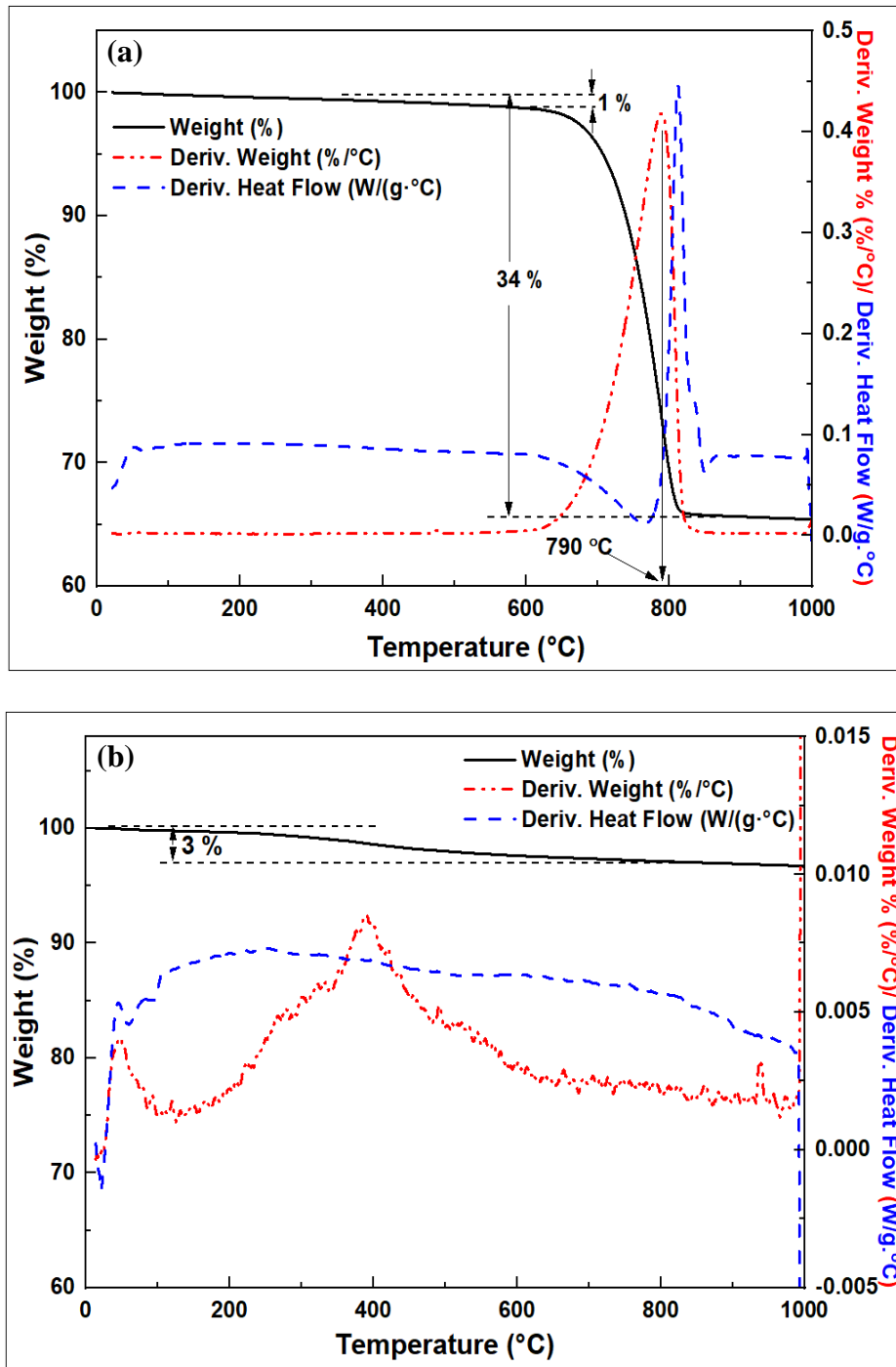
Figure 4.8; Thermograms of; (a). Raw volcanic ash (KVA-Raw), and (b). Acid-washed
volcanic ash (KVA-10%A).

The textural properties of the raw volcanic ash material by BET N_2 sorption are shown in Figure
4.9 and Table 4.4.
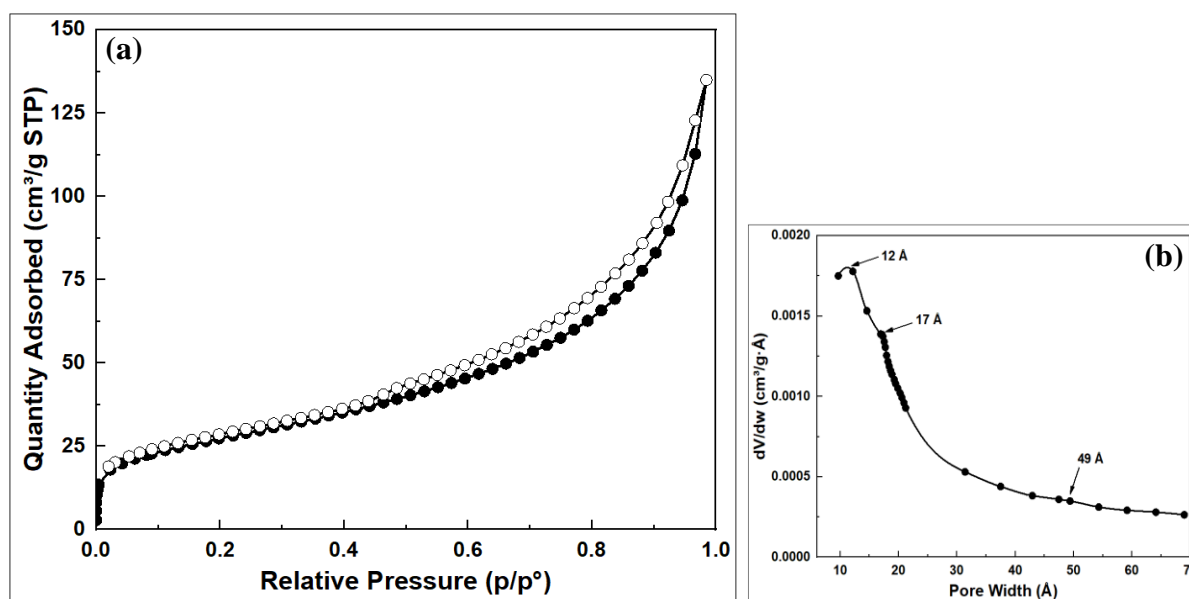
Figure 4.9; Porosity analysis of KVA-Raw material; (a). N_2 sorption isotherm, and (b). Horvath-Kawazoe pore size distribution.

Table 4.4; Textural properties of KVA-Raw material.

Sample	Specific Surface area (m²/g)	Micropore surface area (m²/g)	External surface area (m²/g)	Micropore volume (cm³/g)	Total pore volume (cm³/g)	Pore size (Å)
KVA-Raw	97.42	5.17	92.32	0.002	0.21	12, 17 & 49

A type II adsorption isotherm was observed for KVA-Raw material showing unrestricted monolayer-multilayer adsorption with a hysteresis loop (Thommes et al., 2015). The raw clay material also exhibited a multi size range pore, i.e., two micropores of 12 and 17 Å and a mesopore of 49 Å.

4.2 Hydrothermal crystallization products - Protocol 1

In protocol 1, the effect of metakaolinization and fused-metakaolinization on the resulting zeolite products was investigated. The kaolin material was used for the synthesis of both MK (in protocol 1a) and F-MK (in protocol 1b) products with and without modification of the synthesis hydrogel composition by using additional fumed silica in the hydrogel.

4.2.1 Metakaolinite derived product (protocol 1a)

The effect of metakaolinization on the resulting zeolites was investigated by calcining kaolin at 750 °C before dissolving the calcined metakaolinite in concentrated NaOH solution. The chemical rection of kaolin at 750 °C and resulting into amorphous aluminosilicates (metakaolin) is represented in equation 1 in section 2.2.2. Based on the chemical composition of the clay material in Table 4.1, the MK hydrogel's $Na_2O:SiO_2:Al_2O_3:H_2O$ molar composition used in protocol 1a, when clay was used without modification of the hydrogel, was calculated to be at 5.6:4.2:1:182.9.

To investigate the vibrational characteristics of the bonds involved in the making of the product, FTIR spectroscopy was performed on the MK hydrogel and its resulting product. The transformation of kaolin through MK to the MK derived product (SA-MK-48h) in protocol 1a is shown in Figure 4.10. The FTIR bands below 1100 cm^{-1} describes the modes of vibrations of silica and alumina groups in the resultant product. As silica and alumina bonds of crystalline polymer are formed, the FTIR bands of the MK at 1049 and 435 cm^{-1} (due to O-T bonds of amorphous aluminosilicates) in Figure 4.2a shifted to lower wave numbers at 967 and 435 cm^{-1} in Figure 4.10a, respectively. The FTIR bands at 3300 and 1641 cm^{-1} are due to hydroxyl stretching and bending vibrations respectively, associated with the aqua-complex and water of hydration in the zeolite pore channels (Król et al., 2012; Tounsi et al., 2009). The band at 543 cm^{-1} corresponds to the ring opening vibrations of the double four membered ring (D4R) for the zeolite Na-A (Mozgawa et al., 2011).

Other bands at ca. 967 cm^{-1}, 667 cm^{-1} and 457 cm^{-1} are due to the asymmetric stretching, symmetric stretching and bending vibration, respectively, of Si-O-Si(Al) bridges in the TO$_4$ tetrahedral (Belaabed et al., 2016). In order to process and resolve the FTIR spectrum of the MK synthesis hydrogel and to compare its characteristics with that of the product,

deconvolution of the hydrogel spectrum was performed. The deconvoluted FTIR bands of the aged MK hydrogel in Figure 4.10b reveals bands of preformed zeolite seeds which are subsequently transformed into zeolite products during the hydrothermal crystallization.
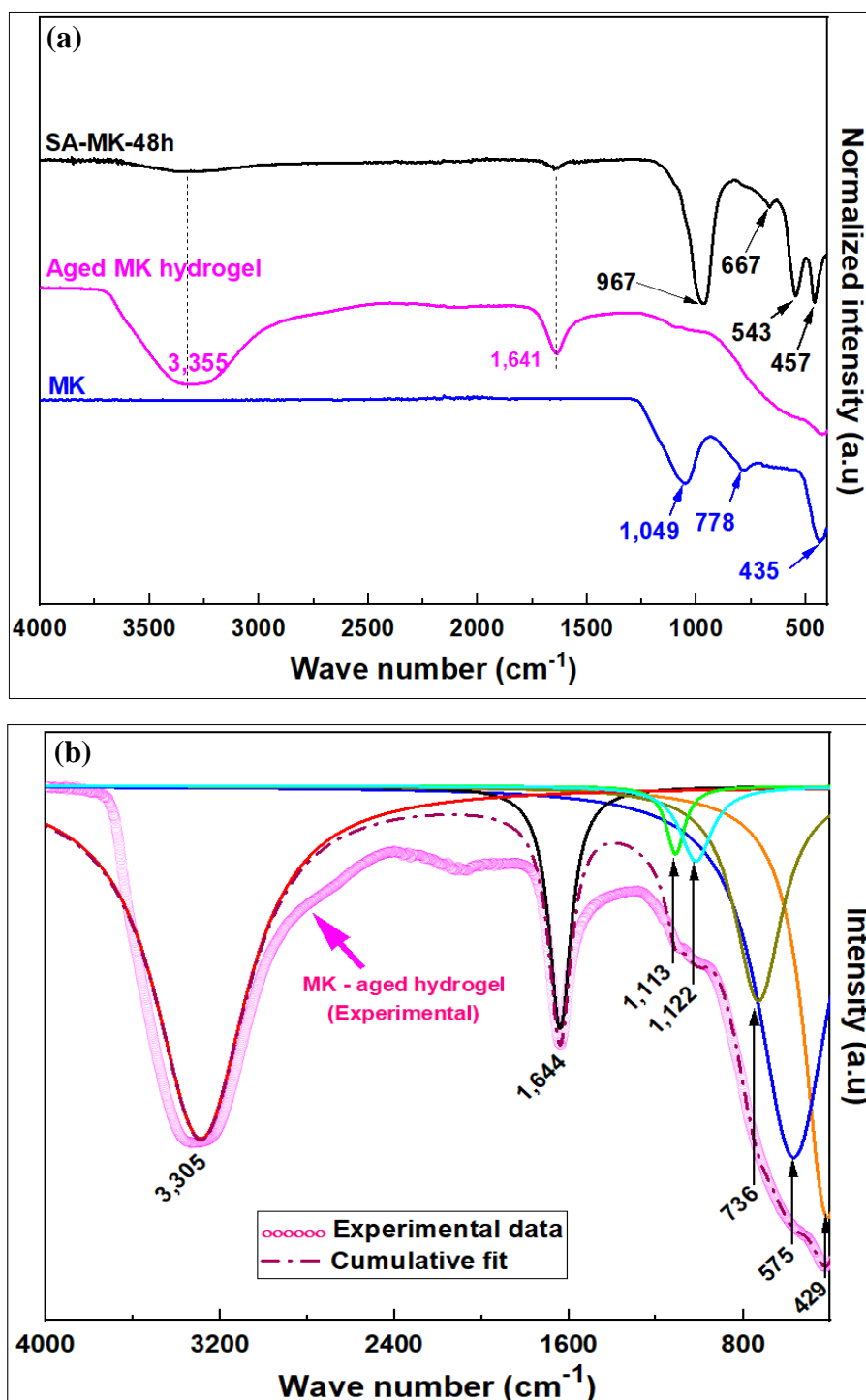
Figure 4.10; Characterization of MK product; (a). FTIR spectra of MK transformation, and (b). Deconvoluted FTIR peaks of aged MK hydrogel.

In order to identify the various phases present in the synthesized product, and to explore its surface morphology, the XRD and SEM analysis were performed on the SA-MK-48h product, respectively. The XRD patterns and SEM image of the resulting products are shown in Figure 4.11.
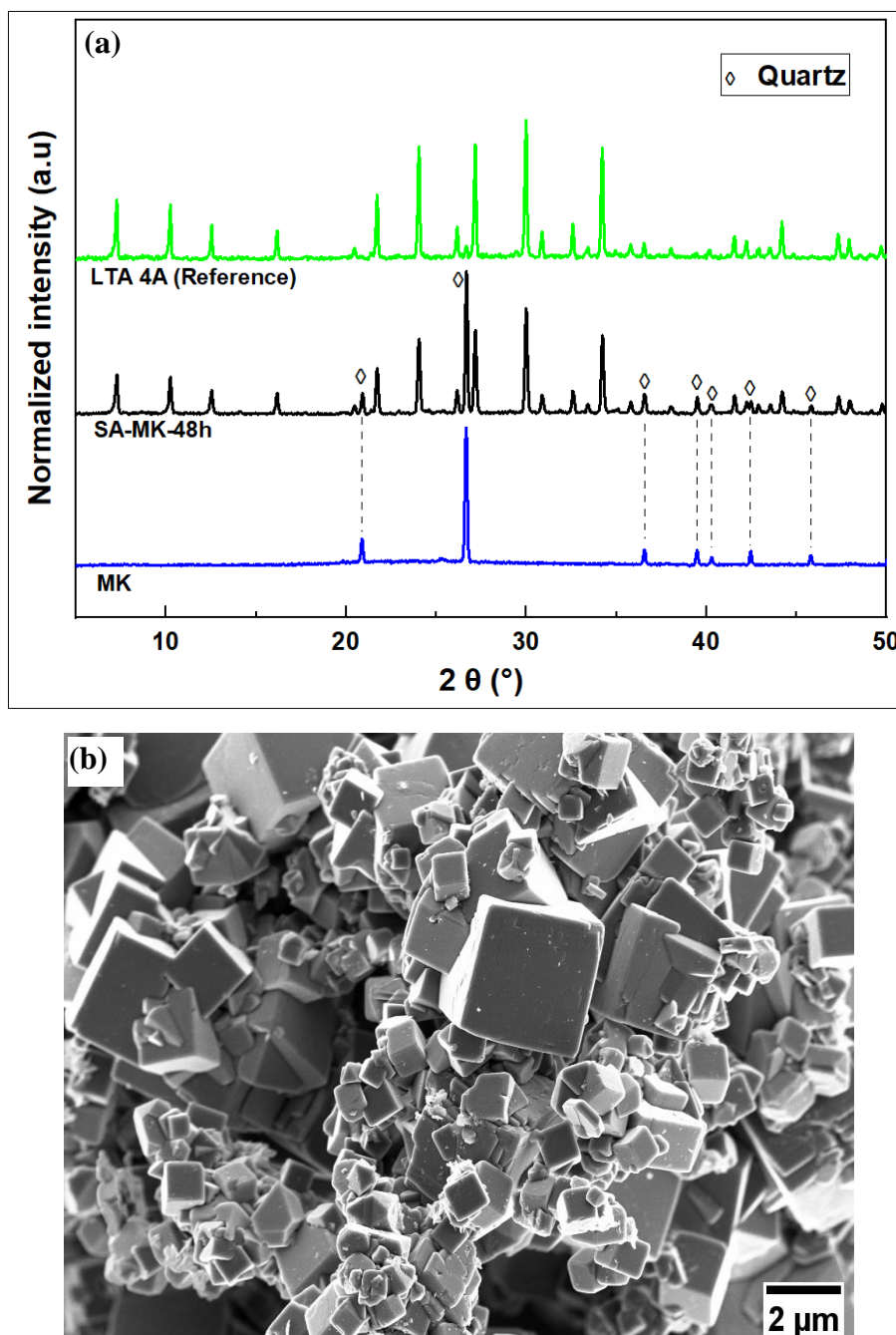
Figure 4.11; Characterization of MK product; (a). XRD patterns of MK transformation, and (b). SEM image of MK derived product.

For the XRD pattern in Figure 4.11a, the peaks at 2 θ of 20.9°, 26. 7°, 36.6°, 39.5°, 42.5° and 45.8° belong to quartz phase and are derived from the parent kaolin (see Figure 4.2a). All the remaining peaks at 2 θ of ca. 7.3°, 10.2°, 16.2°, 21.7°, 24.1°, 27.2°, 30.9°, 32.6°, 33.4° and 34.2° are characteristic of Linde type zeolite Na-A (LTA) (Baerlocher & McCusker, 2017). The calculated percentage crystallinity of the synthesized Na-A was 88.1 %. In addition, the SEM image in Figure 4.11b revealed cubic crystallite particles ranging between 0.2- 3.5 µm in size. The cubic crystals further confirm the presence of zeolite Na-A products. The particles exhibit overgrowths and inter-growths of crystals.

4.2.2 Fused-metakaolinite derived product (protocol 1b)

The effect of fused-metakaolinization on the resulting zeolites was investigated by heating a mixture of kaolin with NaOH at 750 °C before dissolving the F-MK in deionized water. The proposed chemical rection of kaolin with NaOH taking place at 750 °C and resulting into sodium aluminosilicates (fused-metakaolin) is represented in equation (7).

$$Si_2Al_2O_5(OH)_4 \; + \; 6NaOH \; \rightarrow \; 2Na_2SiO_3 \; + \; 2NaAlO_2 \; + \; 5H_2O \qquad (7)$$
$$\text{Kaolin} \qquad\qquad\qquad \text{Sodium aluminosilicates}$$
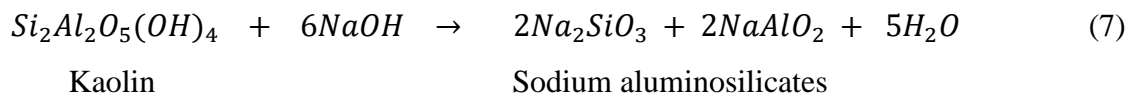
Based on the chemical composition of kaolin in Table 4.1, and assuming that there was no loss of inorganic components during fusion, the MK hydrogel's $Na_2O:SiO_2:Al_2O_3:H_2O$ molar composition used in protocol 1b was the same as in protocol 1a at 5.6:4.2:1:182.9.

To investigate the vibrational characteristics of the bonds involved in the formation of F-MK product, FTIR spectroscopy was performed on the F-MK hydrogel and its resulting product (SX-FM-48h). The transformation of kaolin through F-MK to the SX-a-FM-48h product in protocol 1b is shown in the FTIR spectra in Figure 4.12. The FTIR spectra of the fusion product

and its F-MK precursor are relatively identical. The bands positions of F-MK in Figure 4.12 shifts to higher wavenumbers as crystalline zeolite product are formed. The FTIR bands of SX-a-FM-48h at 957, 749 and 442 cm^{-1} arise from the asymmetric stretching, symmetric stretching and symmetric bending vibrations of T-O bonds in the tetrahedra, respectively (Mozgawa et al., 2011). The band at 558 cm^{-1} is due to symmetric stretching vibrations associated with the double six membered rings (D6R) of zeolites Na-X (Mozgawa et al., 2005). Other bands observed at 1,644 and 3,491 cm^{-1} are for water of hydration and are discussed in section 4.2.1.
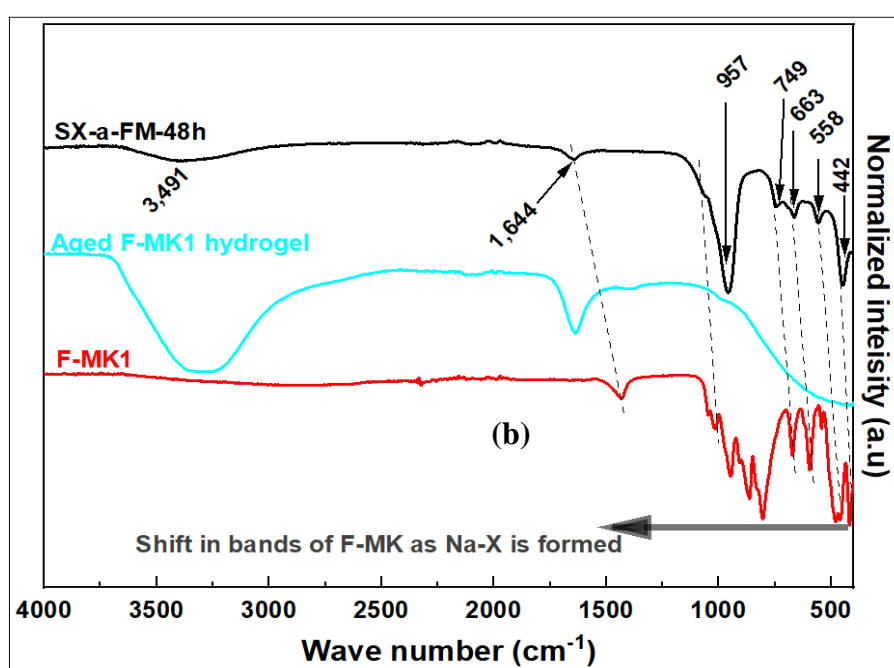
Figure 4.12; FTIR spectra of F-MK, aged F-MK hydrogel and the resulting SX-a-FM-48h resulting product.

In order to identify the phases present in the synthesized product, and to explore its surface morphology, the XRD and SEM analysis were performed on the SA-MK-48h product. The XRD patterns and SEM image of the SX-a-FM-48h product is shown in Figure 4.13. The XRD peaks of F-MK1 tends to shift to low 2 θ values as it is transformed to zeolite products. The peaks at 2θ of 6.15°, 10.06°, 15.51°, 20.11°, 23.34°, 26.67°, 30.35°, 30.98°, 32.06° and 33.61° for the SX-FM-48h are characteristic of zeolite Na-X of the faujasite (FAU) family (Baerlocher

& McCusker, 2017). The calculated percentage crystallinity of the synthesized Na-X was at 95.9 %. The SEM image of SX-a-FM-48h in Figure 4.13b reveals octahedral shaped crystals with varying crystallite sizes ranging from 50 nm to 800 nm. The octahedral crystals are characteristic of zeolite X in the FAU family. The crystals were smaller in size compared to those obtained in Figure 4.11b for zeolite Na-A synthesized in protocol 1a.
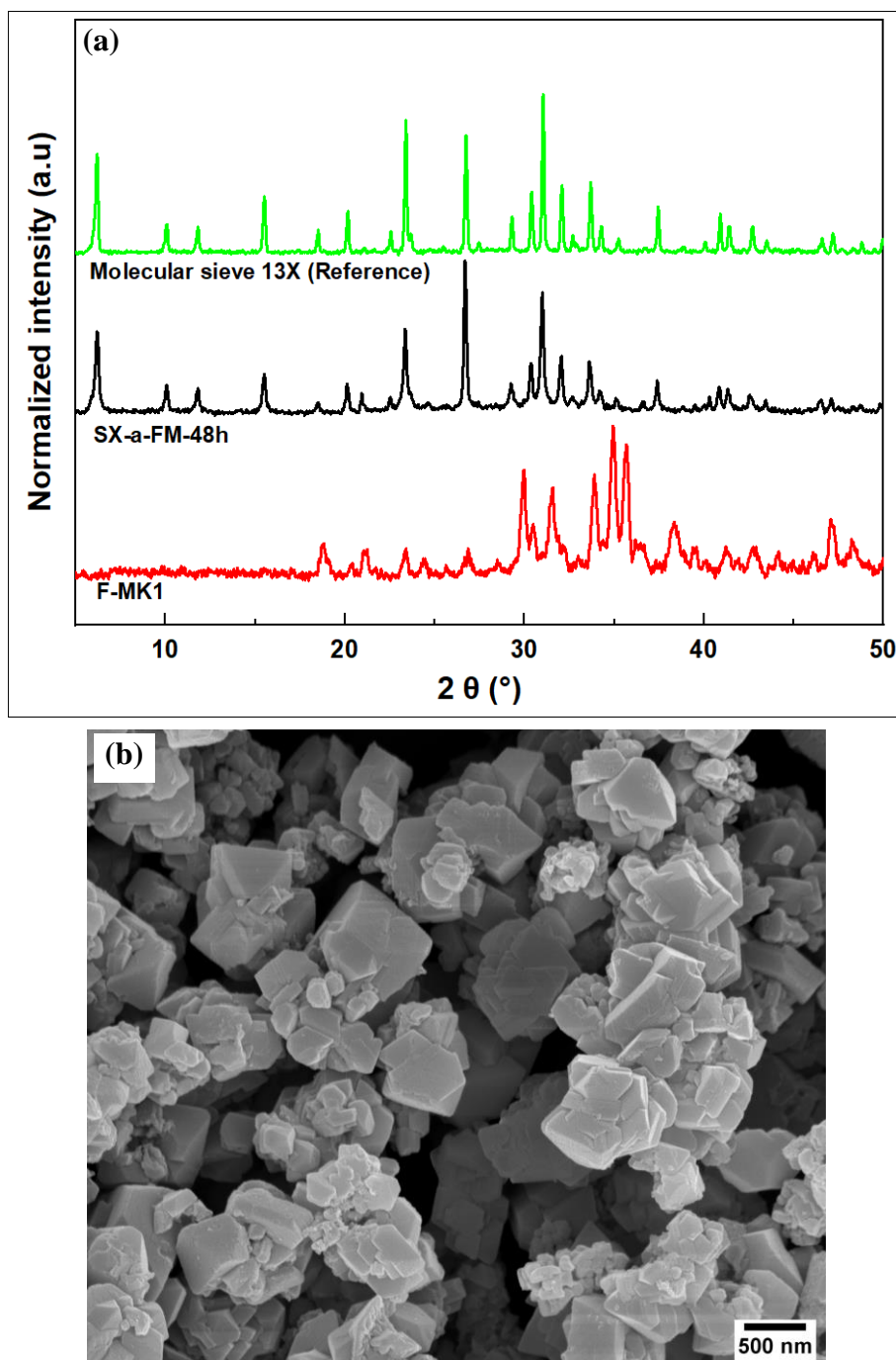
Figure 4.13; Characterization of F-MK product; (a). XRD pattern of F-MK transformation, and (b). SEM image of F-MK derived product.

4.2.3 Chemical analysis of protocol 1 products

To determine the chemical composition of the products obtained in protocol 1, chemical analysis by ICP-OES spectroscopy was performed on the products and compared to their parent starting materials. The chemical analysis results are shown in Table 4.5. The observed silica content of MK product (i.e., SA-MK-48h) was high as shown in the SiO_2/Al_2O_3 molar ratio of 3.25. This is higher than the expected composition for the Na-A zeolite (Hu et al., 2017). This additional silica, also observed for the kaolin in Table 4.1 is due to the presence of undecomposed quartz phase originating from the parent clay mineral. The chemical composition for the zeolite Na-X product (SX-a-FM-48h) was the same as that of washed F-MK precursor in Table 4.1 and having a SiO_2/Al_2O_3 molar ratio of 2.22. Based on the chemical analysis data, the chemical formula of the SX-a-FM-48h product was calculated to be $Fe_{0.91}Cu_{0.43}Ti_{2.42}Na_{126.67}K_{0.44}Al_{100}Si_{110.89}O_{441.97}$, which is consistent with other reports for the zeolite Na-X product (Guesmi & Massiani, 2011; Olson, 1995).

Table 4.5; Chemical composition of products obtained in protocol 1.

Sample	Percent oxide (wt. %)							SiO_2/Al_2O_3	Calculated Chemical formula
	Al_2O_3	TiO_2	Fe_2O_3	K_2O	CuO	Na_2O	SiO_2		
SA-MK-48h	26.77	0.97	0.42	0.20	0.20	20.18	51.25	3.25	$Fe_{1.00}Cu_{0.48}Ti_{2.41}Na_{124.00}K_{0.80}Al_{100}Si_{162.43}O_{544.06}$
SX-a-FM-48h	31.86	1.16	0.45	0.13	0.21	24.53	41.64	2.22	$Fe_{0.91}Cu_{0.43}Ti_{2.42}Na_{126.67}K_{0.44}Al_{100}Si_{110.89}O_{441.97}$
FSY-a-FM-48h	25.92	0.55	0.16	0.22	0.21	20.62	52.31	3.42	$Fe_{0.40}Cu_{0.51}Ti_{1.41}Na_{130.89}K_{0.92}Al_{100}Si_{171.22}O_{562.28}$
FSY-a-FM-120h	25.21	0.63	0.16	0.19	0.21	20.72	52.89	3.56	$Fe_{0.40}Cu_{0.52}Ti_{1.65}Na_{135.25}K_{0.83}Al_{100}Si_{178.04}O_{578.53}$

4.2.4   Formation of LTA versus FAU zeolite in protocol 1

It should be noted that in the first protocol (both 1a and 1b), the difference in the synthesis procedure was in the pre-treatment method of raw kaolin by either metakaolinization or fused-metakaolinization, the other factors including synthesis hydrogel composition remained the same. As observed from the analysis of MK and its products in Figure 4.2, 4.3, 4.10 and 4.11, the quartz phase in the starting kaolinite material is stable even after high temperature and pressure treatment in the metakaolinization and hydrothermal crystallization processes. In hydrothermal synthesis using MK route, although the nominal SiO_2/Al_2O_3 molar ratio in the starting clay material is 3.17 (Table 4.1), the actual amount of silica ions $((SiO_4)^{4-})$ available in the sodium aluminosilicate gel as primary building units is lower than the calculated nominal concentration as some of the silica is present in the form of crystalline quartz and other phases. Such a low concentration of silica ions in the hydrogel would be conducive for the transformation of the aluminosilicate gel to zeolite Na-A products. On the other hand, in protocol 1b using F-MK method, the high alkaline conditions in the fusion step at high temperatures leads to the complete dissolution of kaolin and the decomposition of the crystalline quartz (N. Li et al., 2017) and therefore increasing the concentration of silica ions in the hydrogel solution. The synthesis hydrogel in this case is consequently richer in silicate ions, which is conducive building blocks for the transformation of the aluminosilicate gel to zeolite Na-X (FAU Na-X) products.

Alternatively, in the F-MK method, it is possible that the formation of Na-X seeds occurs early during the fusion step, which encourages the formation of this type of zeolite. Unlike the amorphous phase of the MK in Figure 4.2a, the XRD pattern of the F-MK material in Figure 4.13a reveals the presence of new peaks of crystals formed during the fusion step. The peaks at 2θ between 23° and 32° tends to shift to higher 2θ values as products are formed in the

hydrothermal crystallization step. In addition, the FTIR spectra of the fusion product and its F-MK1 precursor in Figure 4.12 are relatively identical with the spectral bands of the later shifting to higher wave numbers as the zeolite products are formed. The deconvoluted FTIR peaks of the aged F-MK1 hydrogel in Figure 4.14 also reveals spectral bands at 3310, 1641, 991, 712, 566 and 423 cm^{-1} wave numbers which appear relatively at the same positions as those observed in the zeolite SZ-a-FM-48h (Na-X) product in Figure 4.12. These observations might imply that the high temperature dry reaction between kaolin with NaOH result in the formation of secondary and/ or tertiary building blocks with D6R structure that acts as seeds and are favoured in the hydrothermal synthesis of zeolite Na-X under conditions that are similar to those that lead to LTA zeolites via the MK route.
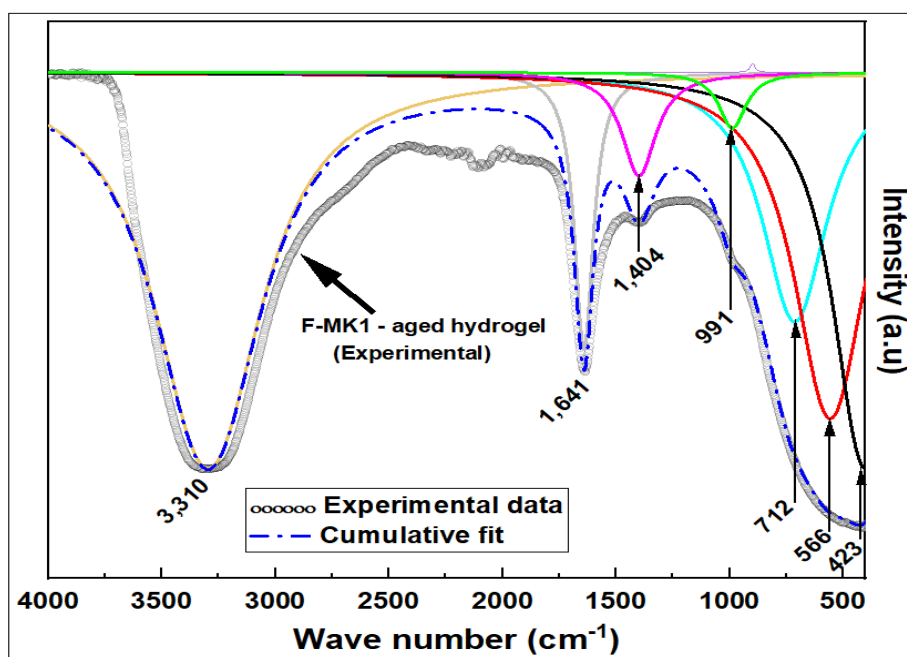
Figure 4.14; Deconvoluted FTIR peaks of aged F-MK1 hydrogel.

4.2.5   Effect of crystallization time on MK derived product (protocol 1a)

The effects of hydrothermal crystallization time for the MK derived products obtained without synthesis hydrogel modification in protocol 1a was achieved by varying the syntheses time

between 8 and 168 h. Figure 4.15 show the FTIR spectra and the XRD patterns of the resulting products prepared at varying hydrothermal crystallization periods.
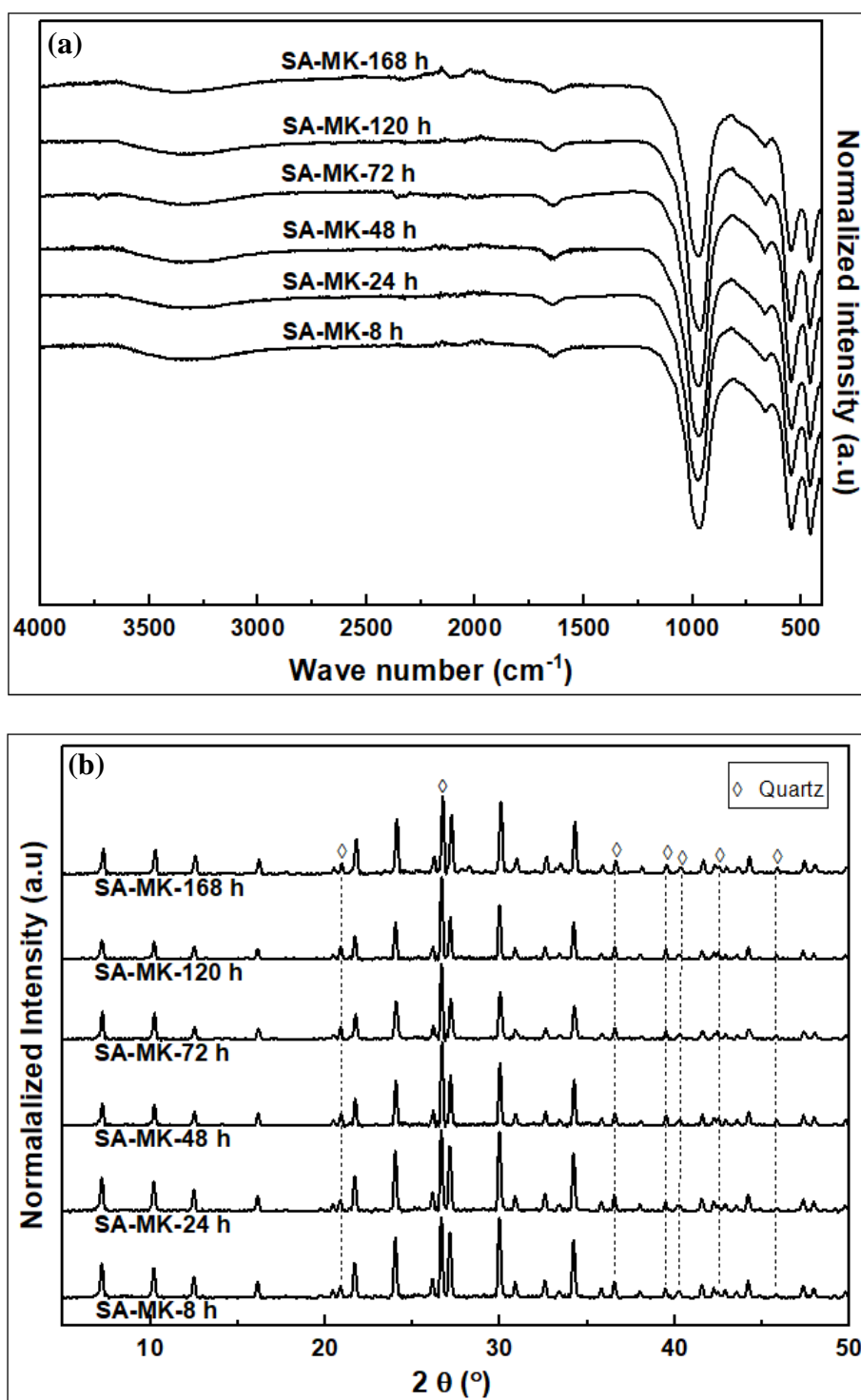
Figure 4.15; Analysis of MK derived products at different crystallization time; (a). FTIR spectra of SA-MK, and (b). XRD patterns of SA-MK.

There was no observed change in the FTIR spectra of the products obtained in Figure 4.15a. In the XRD patterns in Figure 4.15b, apart from quartz, zeolite Na-A of more than 90 % crystallinity was generated within 8 h of hydrothermal crystallization. However, the crystallinity dropped to less than 70 % after 120 h, which is also reflected by the slight reduction in XRD peak intensities with time. It is also worth noting that no phase transition was observed for the duration of study (up to 168 h). This is in contrast to other reports where a more stable hydroxysodalite (HS) phase was formed just after 48 h (Maia et al., 2011; Tounsi et al., 2009).

4.2.6 Effects of SiO_2/Al_2O_3 molar ratio on protocol 1 product

The effects of SiO_2/Al_2O_3 molar ratio on protocol 1 was studied by modifying the chemical composition of the synthesis hydrogels in both MK and F-MK methods using fumed silica. The $Na_2O:SiO_2:Al_2O_3:H_2O$ molar composition of both MK and F-MK synthesis hydrogels was modified to 7.1:14.1:1:150.2. Chemical analysis of the products in Table 4.5 show a significant increase in SiO_2/Al_2O_3 molar ratio from 2.22 of SX-a-FM-48h product (obtained from the unmodified F-MK synthesis hydrogel) to 3.42 of FSY-a-FM-48h product (obtained from the modified F-MK synthesis hydrogel). In addition, marginal increase in the SiO_2/Al_2O_3 molar ratio from 3.42 to 3.56 was observed for the F-MK product (i.e., FSY-a-FM-120h) after increasing its synthesis time from 48 h to 120 h.

The vibrational characteristics of the bonds involved in the making of the products obtained from modified MK and F-MK synthesis hydrogels were explored via FTIR spectroscopy. The FTIR spectra in Figure 4.16 shows the formation of MK and F-MK products obtained via modified synthesis hydrogels with fumed silica. The FTIR spectra of the FSY zeolite products in Figure 4.16a shows T-O spectral bands appearing at ca. 451, 567, 690, 769 and 972 cm^{-1}. These bands are at slightly higher wave numbers compared to T-O bands of Na-X zeolites in

Figure 4.12. The other bands at 1640 and 3350 cm^{-1} are due to water of hydration and are discussed in section 4.2.1.
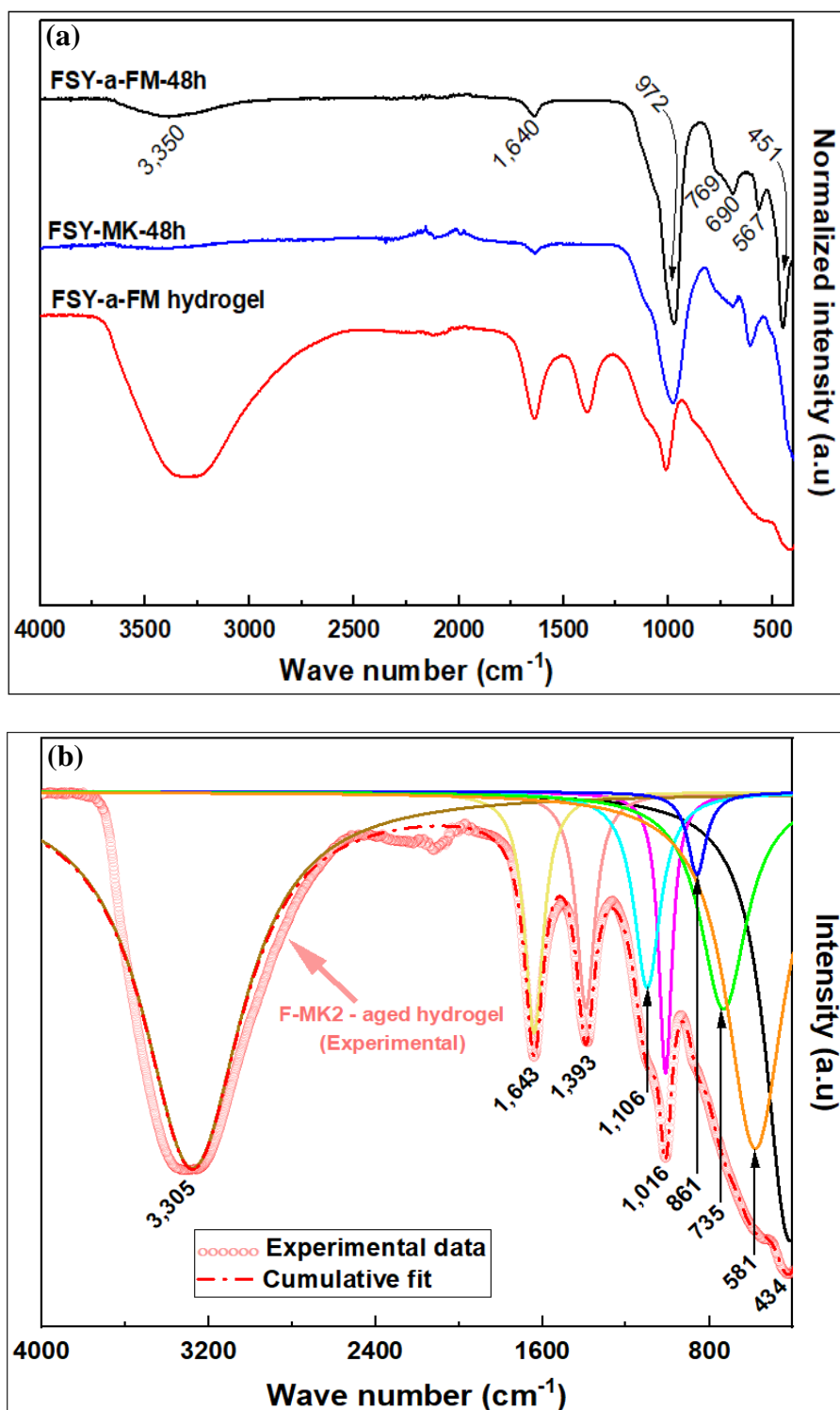
Figure 4.16; FTIR spectra of the MK and F-MK products derived from modified hydrogel; (a). Aged F-MK2 hydrogel, and MK & F-MK derived products, and (b). Deconvoluted bands of FSY-a-FM hydrogel.

The deconvoluted FTIR bands of the aged F-MK hydrogel modified with fumed silica in Figure 4.16b also shows the presence of bands of preformed zeolite seeds at relative positions to those of the FSY zeolites products. The intense bands appearing at ca. 1,016 and 1,393 cm^{-1} (which were missing in the deconvoluted FTIR bands of unmodified F-MK1 hydrogel in Figure 4.14) can be attributed to the Si-OH bending and Si-O stretching vibrations of the fumed silica, respectively. In addition, the surface morphology of the resulting zeolites was explored via SEM imaging of the FSY-MK-48h and FSY-a-FM-48h products and are shown in Figure 4.17.
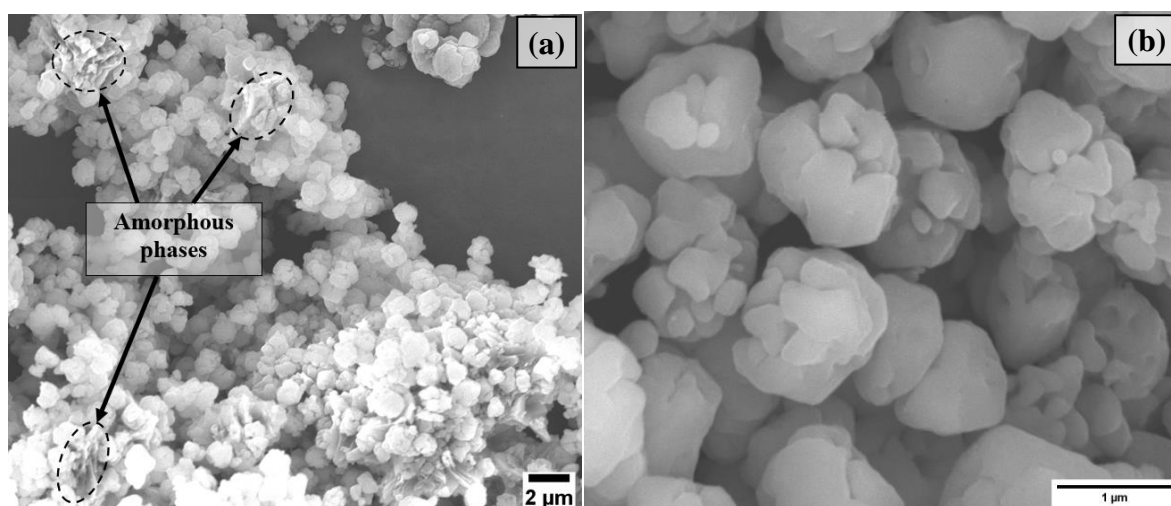
Figure 4.17; SEM images of; (a). FSY-MK-48h, and (b). FSY-a-FM-48h.

The SEM image of FSY-MK-48h in Figure 4.17a show the presence of some amorphous phases alongside the zeolite crystals. On the other hand, octahedral crystals, which are characteristic of faujasite structures, as large as 1 µm and exhibiting fractured segments ranging from 100-500 nm were observed in the SEM image of FSY-a-FM-48h product Figure 4.17b.

Crystal patterns and phase identification of the synthesized zeolites were explored using XRD crystallography. The XRD patterns of the FSY products derived from the MK and F-MK hydrogels modified with fumed silica are shown in Figure 4.18.
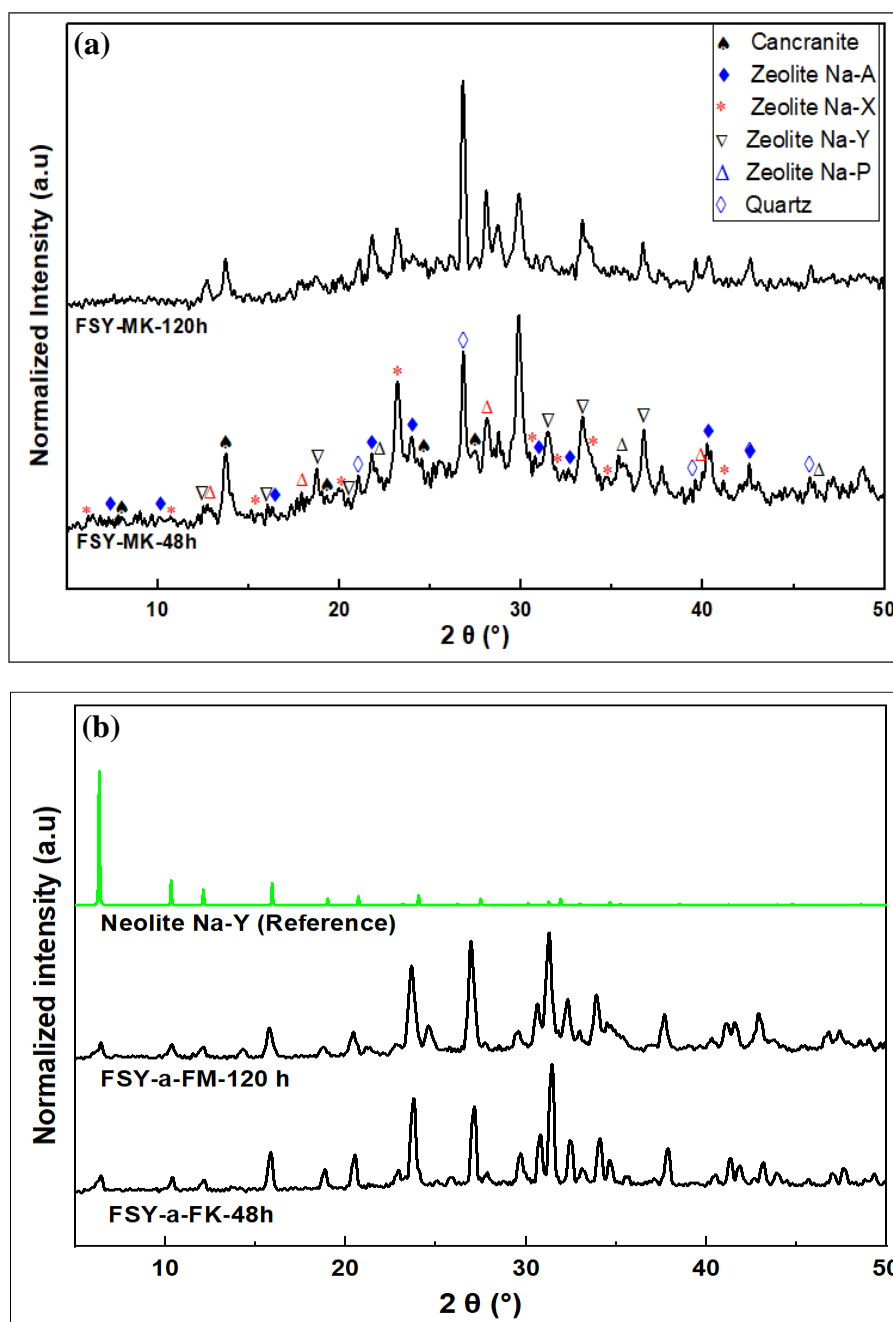
Figure 4.18; The XRD patterns of MK and F-MK products derived from modified hydrogels; (a). MK derived products after 48 and 120h, and (b). F-MK derived products after 48 & 120h.

There was no observed significant change in crystallinity in both MK and F-MK products with increased crystallization time from 48 h to 120 h. In the XRD patterns of MK derived product in Figure 4.18a, apart from quartz, a mixture of zeolites was obtained in the MK method. The XRD peaks at 2θ of 6.4°, 10.2°, 12.1°, 15.8°, 18.8°, 20. 5°, 23.7°, 27.2°, 29.7°, 31.3° and 34.7° are characteristic of zeolite Na-Y. Other peaks associated with cancrinite (7.9°, 13.9°, 19.1°,

24.5° and 27.5°), Na-P (12.5°, 17.8°, 28.2°and 40.2°), Na-A and Na-X, (Baerlocher & McCusker, 2017) were also observed. In addition, the large hump at 2θ of 18-45°, attributed to the unreacted amorphous phases in the starting MK precursor, suggested that more time was required for the complete transformation of the sodium aluminosilicate gel to occur. This observation is in agreement with the observed SEM image of FSY-MK-48h in Figure 4.17. On the other hand, pure phase zeolite Na-Y was obtained in the F-MK method. It is likely that faujasite seeds (having D6R building blocks) that formed during the fusion step for the F-MK route in protocol 1b accelerated the reaction rate so as to result in a complete gel reaction, and therefore elimination of the hump observed in MK based products in protocol 1a, and leading to relatively pure Na-Y phase from the rich silica hydrogel.

4.2.7 BET surface area and porosity analysis of protocol 1 products

To investigate the textural properties of the products obtained in protocol 1, BET analysis by N_2 sorption was performed. The porosity analysis of the products obtained in protocol 1 are shown in Figure 4.19 and Table 4.6. Various types of adsorption isotherms were obtained in protocol 1 depending on whether MK or F-MK method was followed in addition to the resultant zeolite type. Both SA-MK-48h (i.e., zeolite Na-A alongside quartz) and FSY-MK-48h (i.e., a mixture of zeolites) products, which were obtained from unmodified and modified MK synthesis hydrogels in protocol 1a, respectively, exhibited a reversible type III isotherms having relatively weak adsorbent-adsorbate interactions with clustered adsorbed molecules (Thommes et al., 2015). On the other hand, the SX-a-FM-48h (zeolite Na-X) and FSY-a-FMs (zeolites Na-Y), which were obtained from unmodified and modified F-MK synthesis hydrogels in protocol 1b, respectively, showed a reversible Type I(a) adsorption isotherms exhibiting steep slopes at very low partial pressure (P/P_0), a characteristic of microporous materials (Thommes et al., 2015).

96
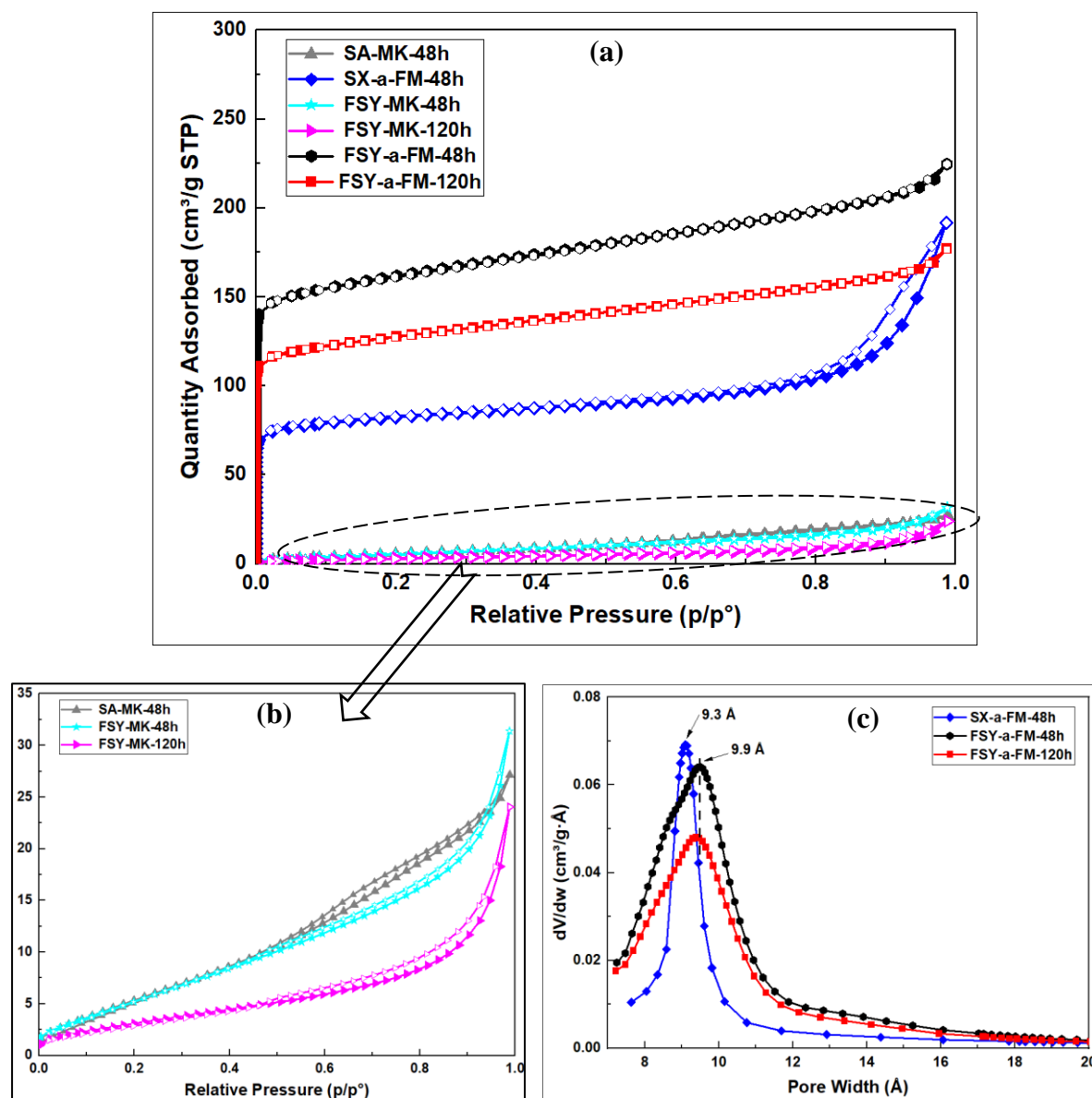
Figure 4.19; Porosity analysis of the products obtained in protocol 1; (a & b). N$_2$ sorption

isotherms, and (c). Horvath-Kawazoe pore size distribution curves.

Table 4.6; Textural properties of synthesized zeolites in protocol 1.

Sample	Specific Surface area (m²/g)	Micropore surface area (m²/g)	External surface area (m²/g)	Micropore volume (cm³/g)	Total pore volume (cm³/g)	Pore size (Å)
SA-MK-48h	18	-	38	-	-	-
SX-a-FM-48h	307	236	71	0.1	0.3	9.3
FSY-MK-48h	17	-	36	-	0.05	-
FSY-MK-120h	10	-	17	-	0.04	-
FSY-a-FM-48h	599	445	154	0.18	0.35	9.9
FSY-a-FM-120h	473	355	118	0.15	0.27	9.9

Zeolites obtained through F-MK hydrogels showed high surface area, micropore surface area, micropore volume and pore size. The Na-Y (FSY-a-FM-48h) zeolite obtained from modified F-MK hydrogels had the highest BET surface area, micropore surface area and micropore volume at 599 m^2/g, 445 m^2/g and 0.18 cm^3/g, respectively. On the other hand, the zeolites obtained through MK hydrogels (i.e., SA-MK-48h, FSY-MK-48h and FSY-MK-120h) had very low adsorption surface area. The low adsorption of N_2 on the synthesized zeolite Na-A (SA-MK-48h) was due to its small pores of size 0.42 nm (Bronić et al., 2012) which hindered the sorption of N_2 molecules. Besides, the low adsorption of N_2 FSY-MK-48h and FSY-MK-120h zeolites might be due to the blockage of pores with impurities and unreacted materials. It can also imply that the zeolite Y and X constituents of the MK products were much less than those of small pore zeolites Na-A, Na-P, cancrinite and quartz phases, and also having hindered sorption of N_2 molecules. The fact that the N_2 molecules cannot readily enter the Na-A, Na-P and cancrinite pores means that the small pore channels were not detectable in the pore size distribution plot in Figure 4.19b. Increasing the crystallization time from 48 h to 120 h for the Na-Y zeolite in the modified hydrogel of protocol 1b led to a decrease in the surface area and the pore volume from 599 to 473 m^2/g and 0.18 to 0.15 cm^3/g respectively. This decrease might be because of the narowing of the pores and channels as zeolite structure continues to develop with time. However, the zeolite median pore width remained the same at 0.99 nm.

4.2.8 Thermogravimetric analysis (TGA) of protocol 1 products

Thermogravimetric analysis of the zeolite products obtained in protocol 1 was performed in the temperature range of 25-1000 °C to understand their thermal behaviours. Figure 4.20 shows the TA, DTA and DSC curves for synthesized products. All synthesized zeolites were thermally stable up to 800 °C. For the products obtained using unmodified MK and F-MK synthesis

hydrogels a total of 17 % and 15 % of zeolite mass was lost in the SA-MK-48h and SX-a-FK-48h products in Figure 4.20(a & b), respectively. As revealed by the derivative of heat flow curves, the mass loss occurred in two exothermic steps. The first step at 50-180 °C resulted into 13 % and 8 % mass loss for SA-MK-48h and SX-a-FK-48h products, respectively. This first step is due to the loss of water of hydration and water within the crystal lattice. This was followed by a slower second step between ca. 200-400 °C (4 %) and 200-320 °C (7 %) for SA-MK-48h and SX-a-FK-48h products, respectively. This second mass loss is due to loss of adsorbed water from within the zeolite micropores (Duvarcı et al., 2007). The second step was slower in zeolite Na-A than zeolite Na-X due to there being a greater diffusion barrier during desorption of water through the narrower channels of small pore Na-A. A large mass loss of 17 % for the SA-MK-48h (i.e., Na-A) in contrast to the low BET surface area observed in Figure 4.19 and Table 4.6 further corroborates the fact that Na-A pores hinders the N_2 sorption.

The TGA analysis of the products obtained from modified hydrogels are shown in Figure 4.20(c-f). The TGA curves in Figure 4.20(c & d) for FSY-MK-48h and FSY-MK-120h products synthesized from modified MK hydrogels at varying synthesis time exhibited multiple weight loss steps characterized by water loss from multiple zeolites, with varying porosities, present in the product. On the other hand, FSY-a-FM-48h and FSY-a-FM-120h products from modified F-MK synthesis hydrogels at different synthesis time in Figure 4.20(e & f) both had a single step weight loss of 19 % and 18 %, respectively, occurring in the 50-300 °C temperature range. This implies that the large pores and channels of zeolite Na-Y results in the uniform and unhindered desorption of sorbed water molecules in FSY-a-FM-48h and FSY-a-FM-120h products. The changes in derivative of heat flow curves between 750-1000 °C (not accompanied by weight loss) correspond to structural changes in the products formed in all cases.
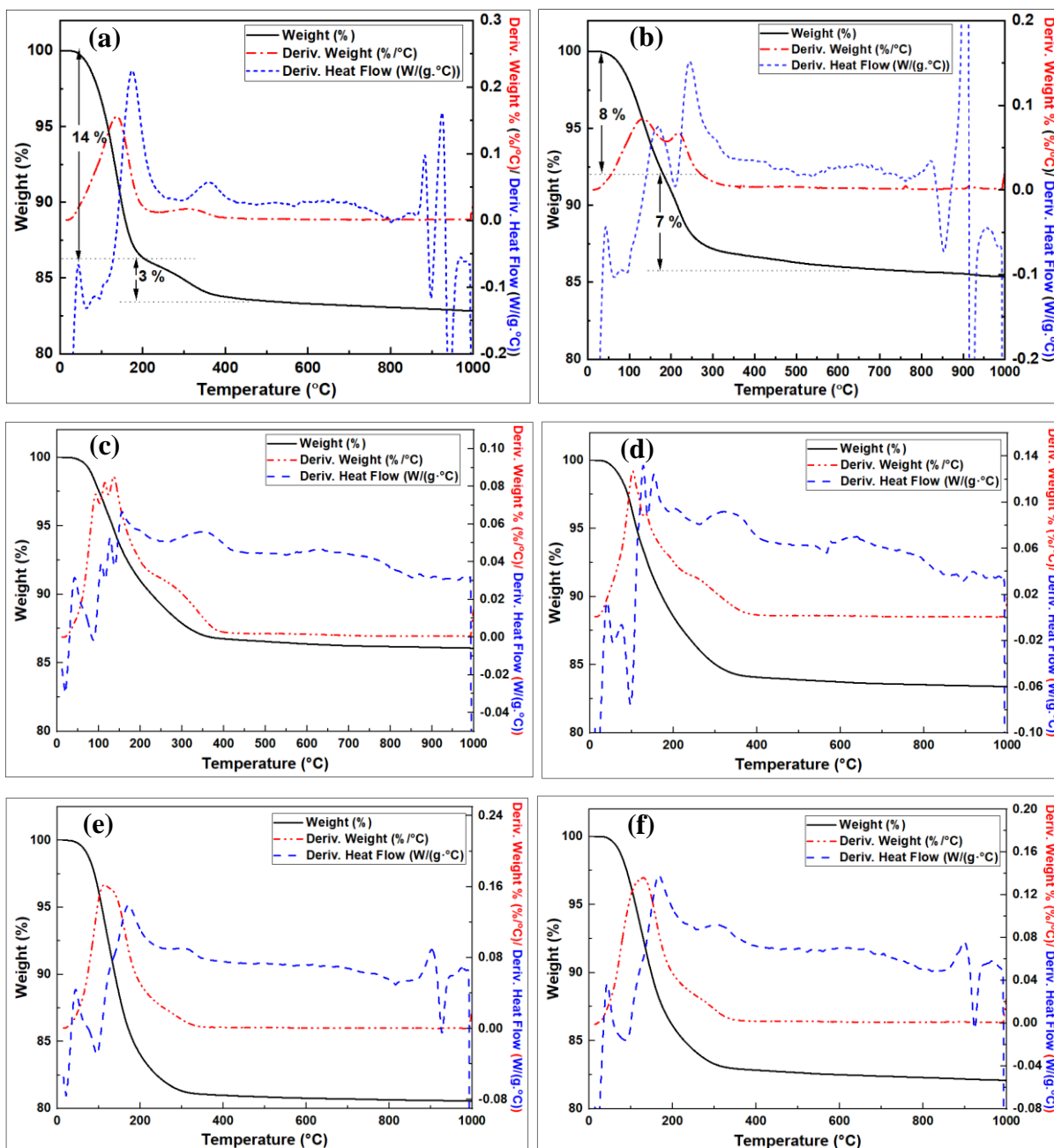
Figure 4.20; TGA and DSC analysis of synthesized products in protocol 1; (a). SA-MK-48h, (b). SX-a-FK-48h, (c). FSY-MK-48h, (d). FSY-MK-120h, (e). FSY-a-FM-48h, and (f). FSY-a-FM-120h.

4.3 Hydrothermal crystallization products - Protocol 2

In protocol 2, the F-MK method was further implemented by modification of the hydrogel using sodium metasilicate pentahydrate in both full fusion in protocol 2a and partial fusion in protocol 2b methods. The pre-treatment methods of clay before fusion were also implemented

by either dry mixing or wet mixing with NaOH pellets before dry fusion or wet fusion. The products obtained from the partial fusion and the full fusion are denoted as MSY-(a/b)-FM/PF and MSX-(a/b/c)-FM/FF, respectively. Where MSY and MSX denote zeolites related to the zeolite Y and the zeolite X families, respectively, FM denotes fused-metakaolinite while PF and FF represent partial fusion and full fusion, respectively. The letter a, b or c denotes products obtained via the pre-treatment of kaolin by dry mixing with NaOH before dry fusion, wet mixing with NaOH before wet fusion or wet mixing with NaOH followed by evaporation of the water solvent before dry fusion, respectively.

4.3.1 Characterization of the products obtained in protocol 2

Based on the chemical composition of the clay material in Table 4.1, the $SiO_2:Al_2O_3:Na_2O:H_2O$ composition of the hydrogel was calculated to be 7.2:1:10:282.1. The synthesis hydrogel composition in both partial fusion (protocol 2a) and full fusion (protocol 2b) was kept the same by adjustments where relevant. All other subsequent synthesis conditions were identical. Any variations in the resulting zeolite structure would therefore be due to the role played by the Na_2O content at the fusion step or in the hydrothermal crystallization step.

4.3.2 Effect of NaOH concentration in the fusion step on the resultant products

The effect of NaOH concentration in the F-MK on the resultant zeolite product was investigated by performing partial fusion vs full fusion before the hydrothermal crystallization step. In the partial fusion method in protocol 2a, 40 % of NaOH solution (i.e., NaOH/clay weight ratio of 6/10) was used in the pre-treatment of kaolin material before the fusion step, the residual NaOH was then added in the resulting hydrogel to meet the hydrogel molar composition in section 4.3.1. On the other hand, in the full fusion method in protocol 2b, all the required NaOH for the synthesis, with the same composition as in partial fusion, was mixed

101

with kaolin (i.e., NaOH/clay weight ratio of 1.5/1) in the pre-treatment stage before the fusion step.

The chemical composition and the calculated chemical formula of the products obtained in protocol 2 at different synthesis time are shown in Table 4.7. It is worth noting that both EDX-SEM and ICP-OES methods of the chemical analysis showed relatively similar chemical composition as observed in the analysis of MSX-c-FM/FF-48h using both EDX-SEM and ICP-OES techniques. The SiO_2/Al_2O_3 molar ratios of the resulting products were not affected by the concentration of NaOH in the fusion step, i.e., by performing either partial or full fusion, as observed in the MSY-b-FM/PF and MSX-b-FM/FF products obtained in the partial and full fusion, respectively. Besides, the molar composition of the products was not affected by the crystallization time as observed in MSX-c-FM/FF-10h, MSX-c-FM/FF-24h, MSX-c-FM/FF-48h and MSX-c-FM/FF-72h products. The SiO_2/Al_2O_3 molar ratio of the products was however affected by the pre-treatment method of the kaolin. The wet fusion products (MSX-b-FM/FF-48h and MSY-b-FM/PF-48h) had the least SiO_2/Al_2O_3 molar ratio of ca. 2.3, while the dry fusion products, both in dry mixing and wet mixing, (MSX-a-FM/FF and MSX-c-FM/FF) had slightly higher SiO_2/Al_2O_3 molar ratio of ca. 2.5.

Table 4.7; Chemical composition of the products obtained in Protocol 2.

Sample	Percent oxide (wt. %)								Method	Chemical formula
	Al_2O_3	SiO_2	Na_2O	TiO_2	Fe_2O_3	K_2O	CuO	SiO_2/Al_2O_3		
MSX-a-FM/FF-48h	30.83	49.40	16.70	1.48	0.34	0.10	0.95	2.72	EDX-SEM	$Fe_{0.7}Ti_{3.1}Na_{89.1}K_{0.6}Al_{100}Si_{136}O_{477}$
MSX-a-FM/FF-96h	31.20	48.91	17.52	1.36	0.44		0.54	2.66	EDX-SEM	$Fe_{0.9}Ti_{2.8}Na_{92.4}K_{0.2}Al_{100}Si_{133}O_{472.1}$
MSX-b-FM/FF-48h	33.01	45.75	20.08	0.78	0.14	0.26		2.35	EDX-SEM	$Fe_{0.3}Ti_{1.5}Na_{100.1}K_{1.4}Al_{100}Si_{117.6}O_{440.9}$
MSX-c-FM/FF-10h	29.94	45.31	23.15	0.95	0.30	0.18	0.17	2.57	ICP-OES	$Fe_{0.63}Cu_{0.37}Ti_{2.10}Na_{127.2}K_{0.66}Al_{100}Si_{128.42}O_{476.29}$
MSX-c-FM/FF-24h	30.33	44.71	23.23	1.01	0.30	0.18	0.23	2.50	ICP-OES	$Fe_{0.63}Cu_{0.48}Ti_{2.22}Na_{125.99}K_{0.65}Al_{100}Si_{125.08}O_{469.32}$
MSX-c-FM/FF-48h	29.89	44.96	23.30	1.01	0.42	0.17	0.22	2.55	ICP-OES	$Fe_{0.90}Cu_{0.47}Ti_{2.24}Na_{128.27}K_{0.62}Al_{100}Si_{127.63}O_{476.00}$
MSX-c-FM/FF-48h	31.60	48.50	18.74	0.90	0.21			2.60	EDX-SEM	$Fe_{0.4}Ti_{1.8}Na_{97.6}K_{0.3}Al_{100}Si_{130.2}O_{465.4}$
MSX-c-FM/FF-72h	30.02	43.79	24.58	1.00	0.30	0.13	0.17	2.48	ICP-OES	$Fe_{0.63}Cu_{0.36}Ti_{2.20}Na_{134.70}K_{0.48}Al_{100}Si_{123.75}O_{470.81}$
MSY-b-FM/PF-48h	31.87	42.83	18.91	1.38	0.35			2.33	EDX-SEM	$Fe_{0.7}Ti_{2.8}Na_{97.6}Al_{100}Si_{114}O_{436.2}$

To determine the functional groups of the resulting products, FTIR spectroscopy was performed on the F-MKs and their resulting products in both protocol 2a and 2b. The transformation of kaolin, through fused-metakaolinite (F-MK) and its hydrogel modified with sodium metasilicate pentahydrate to synthesized products in protocol 2 is shown in the FTIR spectra in Figure 4.21. The FTIR analysis shows that two sets of products were obtained depending on the protocol used in the pre-treatment of the kaolin material, i.e., partial fusion products (Figure 4.21a) or full fusion (Figure 4.21b). The FTIR bands at 450, 675 and 970 cm^{-1} are due to the symmetric bending, symmetric stretching and asymmetric stretching vibration, respectively, of aluminosilicate T-O tetrahedral bonds of zeolite (Belaabed et al., 2016). The band at 556 cm^{-1} is due to symmetric stretching vibrations associated with the six-member rings (D6R) of the faujasite structure (Mozgawa et al., 2005).

Analysis of the deconvoluted bands of the aged full fusion hydrogel modified with sodium metasilicate pentahydrate in Figure 4.21c also shows the presences of spectral bands at 1639, 991, 758 and 422 cm^{-1}, which are consistent with the bands of the formed MSX zeolites. These deconvoluted bands are similar to those obtained from the F-MK hydrogel modified with fumed silica in Figure 4.14. However, the Si-OH bending and Si-O stretching vibrations bands appearing at 991 and 1,396 cm^{-1} are less intense in Figure 4.21c, which might be an indication of more or complete tetrahedral bonding for silica atoms in MSX hydrogels. The FTIR bands at 3400 and 1647 cm^{-1} are associated with the hydroxyl stretching and bending vibrations of water of hydration present within the zeolite structure (Tounsi et al., 2009). The hydroxyl bands are more prominent in the full fusion products obtained in protocol 2b (MSX zeolites) than in the partial fusion products obtained in protocol 2a (MSY zeolites) because the former is more hydrophilic, or have large pores for holding more water.
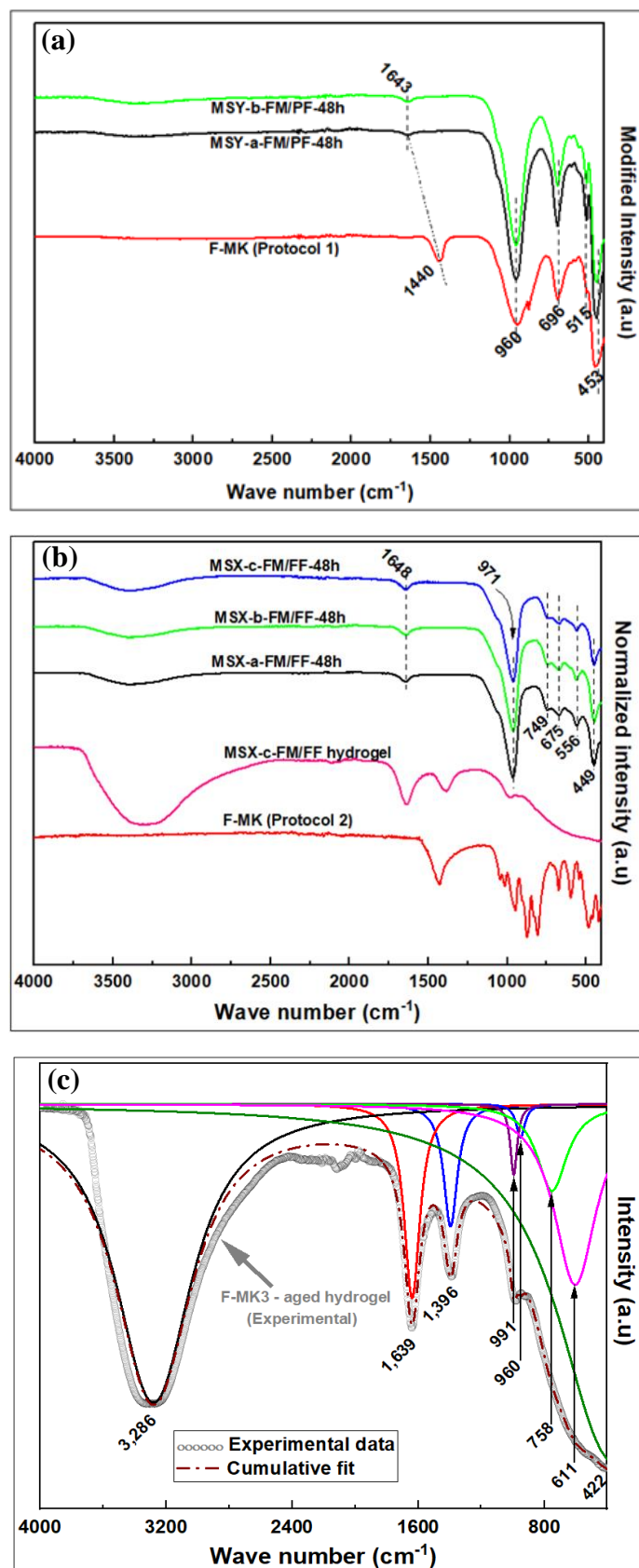
Figure 4.21; The FTIR spectra of the products obtained in protocol 2; (a). Partial fusion (PF) products, (b). Full fusion (FF) products, and (c). Deconvoluted FTIR peaks of the aged FF hydrogel modified with sodium metasilicate pentahydrate.

The SEM images of the synthesized products in Figure 4.22 show octahedral-like crystals with smooth surfaces concealing spongy porous interior, in Figure 4.22a. According to (Ma et al., 2014), such octahedral-like crystals are characteristic of Faujasite zeolites. Zeolite crystals, with varying particle sizes of up to 0.5 µm and 2 µm for MSX-a-FM/FF-48h and MSY-b-FM/FF-48h products, respectively, were produced. Such size ranges are not unique as (Ye et al., 2017) also obtained crystals in the range of 0.1 to 1.5 µm.
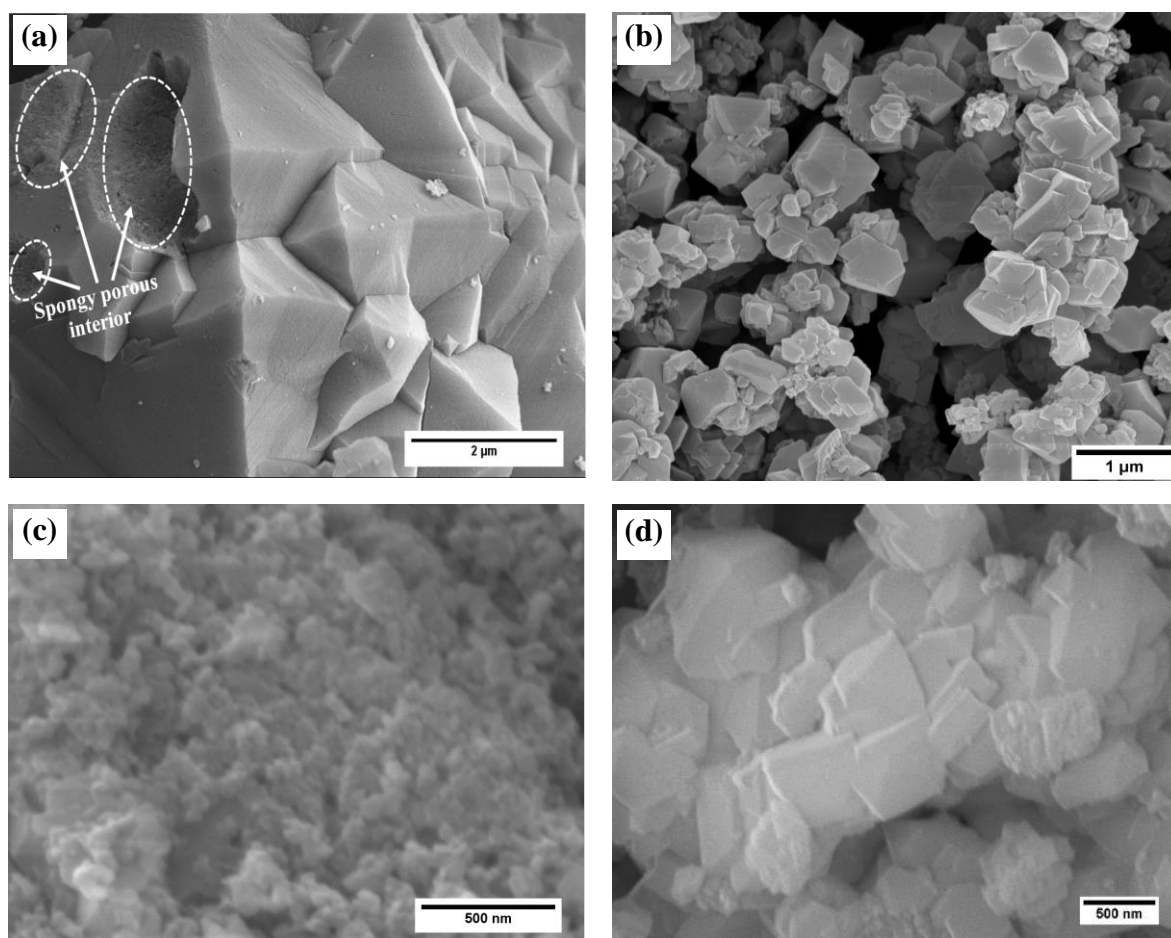
Figure 4.22; The SEM images of the products obtained in protocol 2; (a). MSY-b-FM/PF-48h, (b). MSX-a-FM/PF-48h, (c). MSX-b-FM/PF-48h, and (d). MSX-c-FM/PF-48h.

To distinguish the types of zeolites formed and their crystallinities, X-ray diffraction was performed on the synthesized zeolites. Figure 4.23 shows the XRD patterns of zeolites obtained in protocol 2.
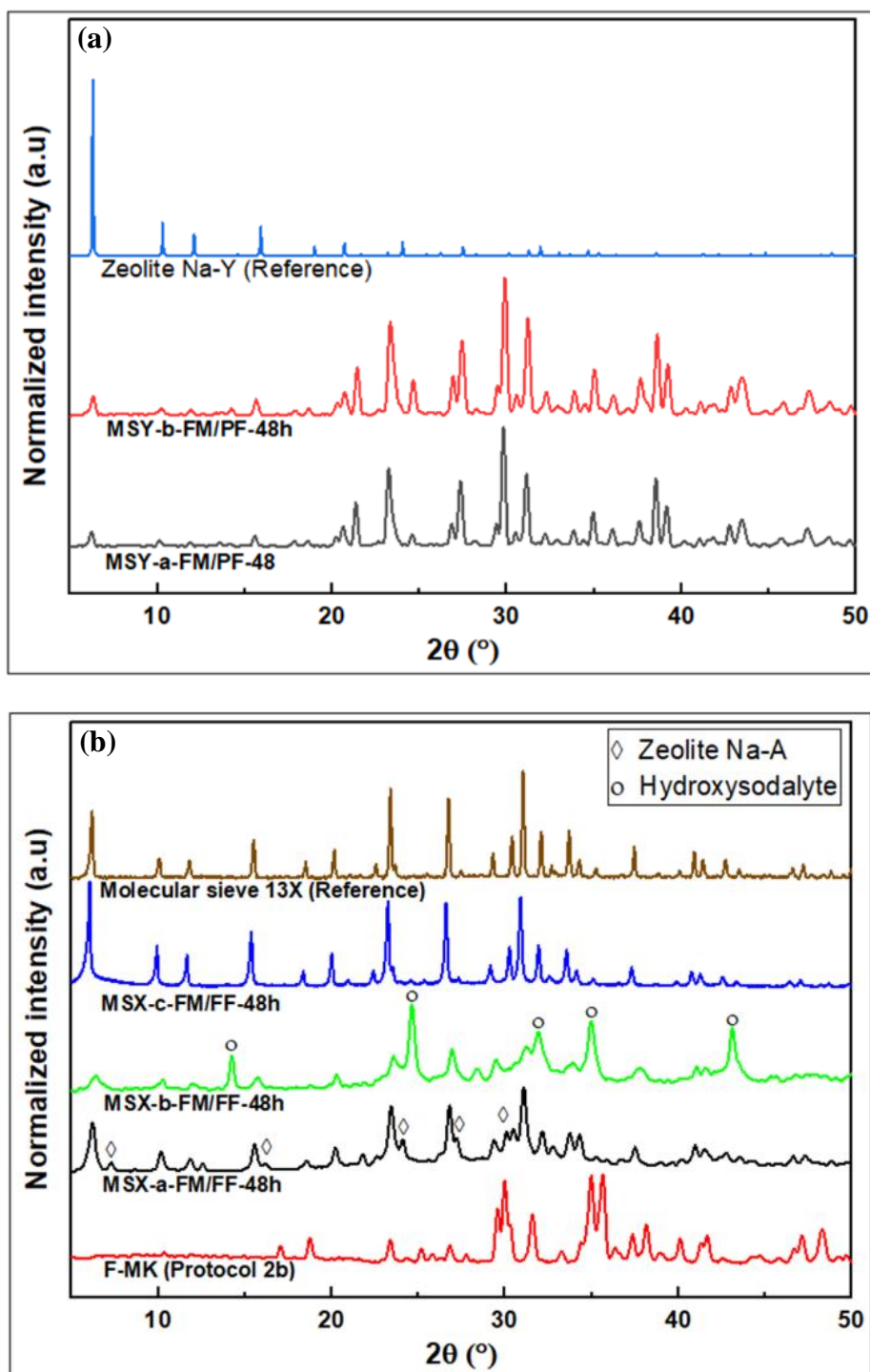
Figure 4.23; The XRD patterns of the products obtained in protocol 2; (a). Partial fusion products, and (b). Full fusion products.

Two sets of zeolite structures were obtained depending on whether partial or full fusion was used in the pre-treatment of the kaolin material, corresponding to the observations made in the

FTIR spectra in Figure 4.21. The partial fusion products recorded lower intensities peaks in the low 2θ region than those of the full fusion method.

The XRD peaks of MSY-a-FM/PF-48h and MSY-b-FM/PF-48h, obtained from the partial fusion methods, at 2θ values of 6.4°, 10.3°, 11.9°, 15.6°, 17.9°, 21.4°, 23.3°, 24.6° and 27.4° in Figure 4.23a are characteristic of zeolite Na-Y (Baerlocher & McCusker, 2017), and are consistent with the zeolite Y product obtained by Doyle et al., 2016. On the other hand, the XRD peaks of MSX-a-FM/FF-48h, MSX-b-FM/FF-48h and MSX-c-FM/FF-48h in Figure 4.23b, obtained from the full fusion method, exhibited slightly lower 2θ values at 6.3°, 10.2°, 11.8°, 15.5°, 20.3°, 24.1°, 27.3°, 29.4°, and 30.1° which are consistent with zeolite Na-X (Baerlocher & McCusker, 2017). In addition to the observed Na-X peaks in the XRD patterns for the full fusion products, other peaks whose intensities depended on the method of pre-treatment performed on the clay material were also observed.

4.3.3 Formation of zeolite Na-X versus zeolite Na-Y

Because of the high alkaline environment, faujasite dimers, oligomers or polymers building units might be forming during the high-temperature reaction of NaOH with kaolin, also discussed in section 4.2.4. The low amount of NaOH in the partial fusion method of protocol 2a may also be resulting in the incomplete conversion of kaolin components to less reactive aluminosilicate components (Tchadjie & Ekolu, 2018), reaction represented in equation (1), alongside the more reactive sodium silicate and sodium aluminate (i.e., sodium aluminosilicates) components, see reaction in equation (7). The presence of aluminosilicates in the hydrogel might therefore be responsible for the transformation of the faujasite building units, during nucleation and/or crystallization, to zeolite Y. This is in agreement with the trends in literature (Table 2.2) where zeolite Y was the main product when MK (aluminosilicate) hydrogels were used rather than F-MK (sodium aluminosilicates) hydrogels.

In contrast, the high alkaline environment created in the full fusion method of protocol 2b is facilitating a complete conversion of the kaolin components to sodium aluminosilicates (Ayele et al., 2016; N. Li et al., 2017). The resulting synthesis hydrogel, in this case, is therefore rich in highly reactive sodium aluminosilicates rather than the less reactive aluminosilicates, the faujasite building units formed are, in this case, transformed to zeolite Na-X. The structure of the final product is therefore significantly influenced by the nature of the starting materials that are present in the synthesis hydrogel. The hydrogels that are rich in aluminosilicates favour the formation of faujasite Y, while those rich in sodium aluminosilicates favour the formation of faujasite X structures.

4.3.4   Thermogravimetric analysis of the protocol 2 derived products

The TGA analysis of the resulting products derived from protocol 2 was performed to understand their thermal behaviour in the temperature range of 25-1000 °C. Figure 4.24 shows the TA, DTA and DSC curves for the zeolite products obtained in both partial and full fusion methods of protocol 2. All zeolite products were thermally stable up to 800 °C. Up to 11 % and 23 % weight loss, for partial fusion and full fusion products, respectively, occurring between 60-400 °C as a result of desorption of water molecules from within the zeolite framework was observed. This is an indication that zeolites generated through full fusion are more hydrophilic and therefore retain or absorb more water in their pore channels compared to partial fusion products. The MSY-b-FM/PF-48h and MSX-b-FM/FF-48h products, obtained through wet fusion in the partial and full fusion categories, respectively, had the least weight loss occurring in two exothermic steps. The MSX-c-FM/FF-48h product obtained through wet mixing followed by the dry fusion in the full fusion recorded the highest weight loss of 23 % occurring in a single exothermic step representing the desorption of water molecules from uniform pore channels.
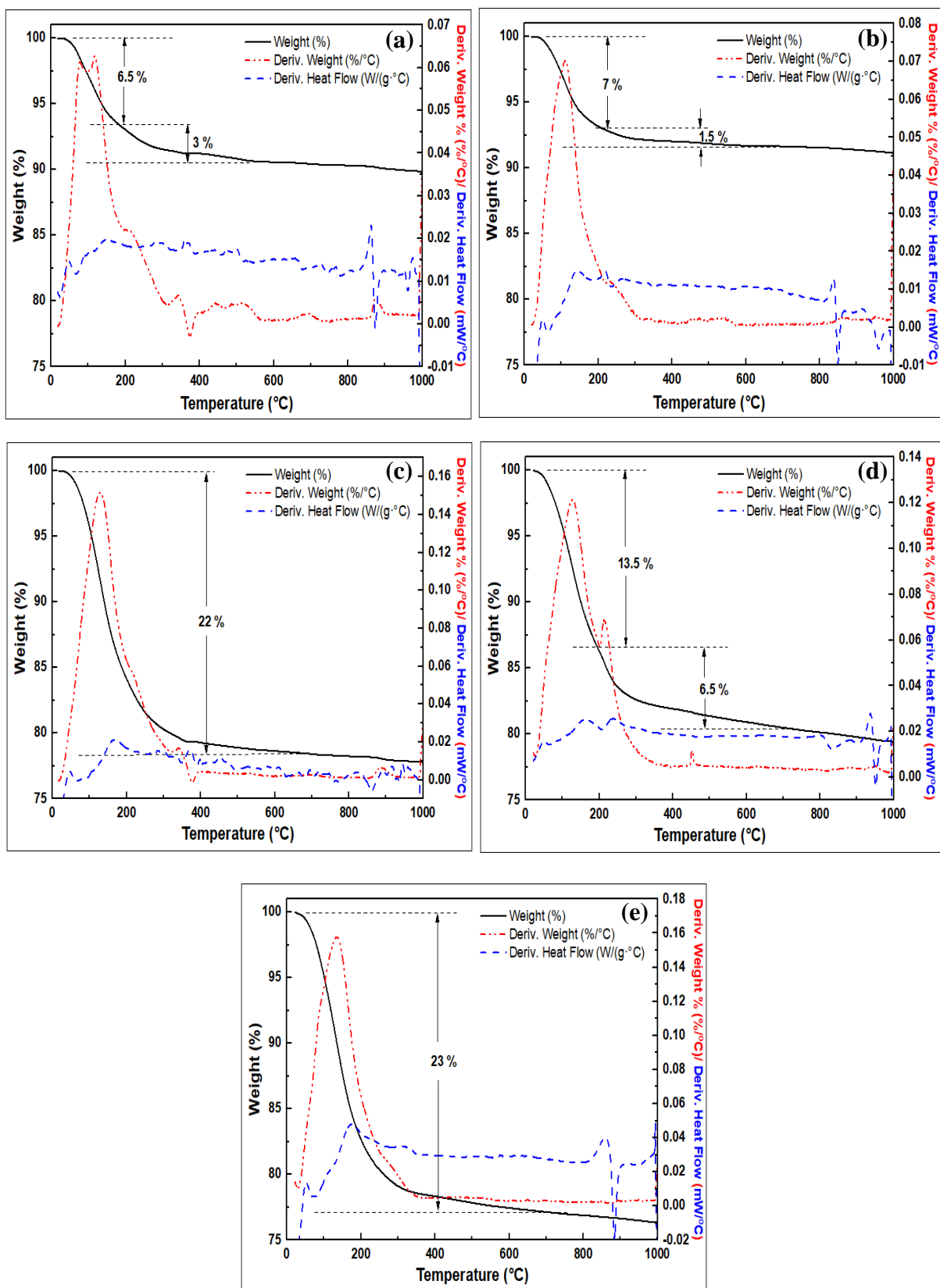
Figure 4.24; TGA curves of the products obtained in protocol 2; (a). MSY-a-FM/PF-48h, (b). MSY-b-FM/PF-48h, (c). MSX-a-FM/FF-48h, (d). MSX-b-FM/FF-48h, and (e). MSX-c-FM/FF-48h.

4.3.5   BET surface area and porosity analysis of protocol 2 products

To investigate the textural properties of the protocol 2 products, a BET analysis of the products was performed by N_2 sorption. Porosity analysis for the protocol 2 derived products is shown in Figure 4.25 and Table 4.8.
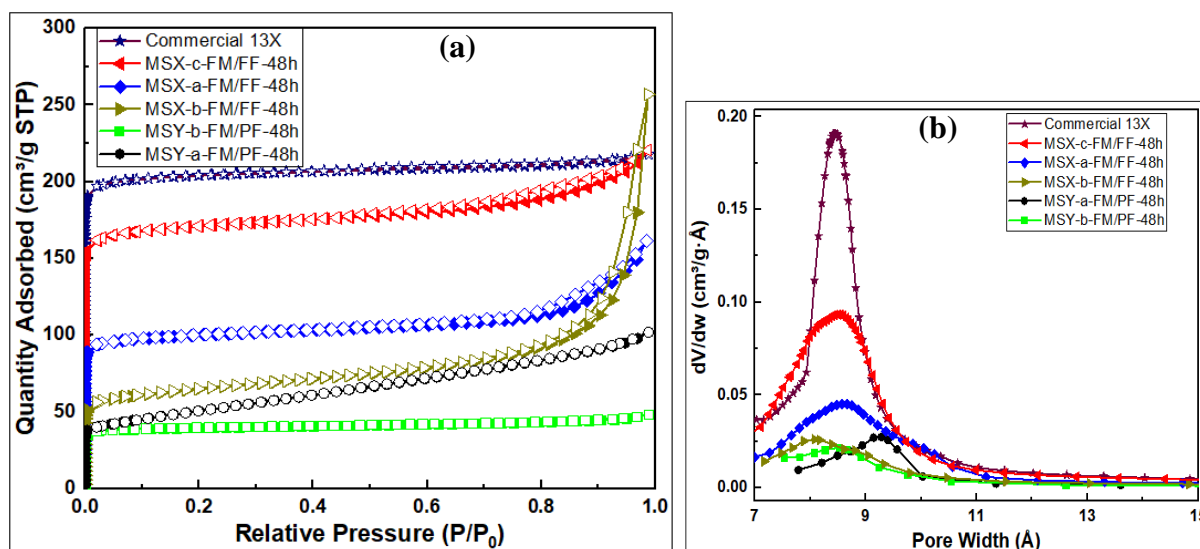
Figure 4.25; Porosity analysis of the products obtained in protocol 2; (a). N_2 sorption isotherms, and (b). Horvath-Kawazoe pore size distribution curves.

Table 4.8; Textural properties of synthesized zeolites in protocol 2.

Sample	Specific Surface area (m²/g)	Micropore surface area (m²/g)	External surface area (m²/g)	Micropore volume (cm³/g)	Total pore volume (cm³/g)	Pore size (Å)
MSY-a-FM/PF-48h	180	58	122	0.03	0.14	9.3
MSY-b-FM/PF-48h	151	134	17	0.05	0.06	8.5
MSX-a-FM/FF-48h	376	327	49	0.13	0.22	8.7
MSX-b-FM/FF-48h	239	152	86	0.06	0.32	8.0
MSX-c-FM/FF-48h	645	579	67	0.24	0.28	8.7
Commercial 13X	772	726	46	0.30	0.27	8.7

Table 4.8 shows that the partial fusion product obtained via protocol 2a had the least specific surface area, micropore surface area and pore volume of 180 m²/g, 58 m²/g, and 0.03 cm³/g, respectively. On the other hand, MSX-c-FM/FF-48h product obtained via full fusion in

protocol 2b-iii had the highest specific surface area, micropore surface area and pore volume of 645 m^2/g, 579 m^2/g and 0.24 cm^3/g, respectively. Pore channels of size 8.7 Å were also observed for MSX-a-FM/FF-48h and MSX-c-FM/FF-48h products. Product MSY-a-FM/PF-48h had slightly larger pores of size 9.3 Å, while MSX-b-FM/FF-48h had slightly smaller pores of 8.0 Å.

The textural properties of the MSX-c-FM/FF-48h, i.e., faujasite X product (645 m^2/g and 0.24 cm^3/g) are higher than the reported values to date for similar zeolites type obtained in kaolin and are comparable to those of commercially available zeolite 13X (772 m^2/g and 0.30 cm^3/g). The micropore volume was in the ascending order of; MSY-a-FM/PF-48h < MSY-b-FM/PF-48h < MSX-b-FM/FF-48h < MSX-a-FM/FF-48h < MSX-c-FM/FF-48h. Comparing the products obtained in protocol 2 with those obtained in protocol 1 (Table 4.6), the products in protocol 2 exhibited improved properties and larger pore size than the Na-X and Na-Y zeolites obtained in protocol 1. This might be due to the high SiO_2/Al_2O_3 molar ratio of the products in protocol 2. Although the MSX-b-FM/FF-48h product was of comparable composition with other protocol 2 products, the presence of water in the wet fusion encouraged reactions or growths of zeolite polymers that led to the narrowing of the zeolite channels and cavities, from 8.7 Å for other Na-X zeolites to 8.0 Å for MSX-b-FM/FF-48h product, and formation of hydroxysodalite and other mesoporous or amorphous products.

4.3.6   The effect of pre-treatment method for kaolin

The pre-treatment of raw kaolin before the fusion step was done by either dry mixing or wet mixing with NaOH pellets before either dry fusing or wet fusing the mixture. In the partial fusion method, MSY-a-FM/PF-48h product was obtained through dry mixing of kaolin before dry fusion (protocol 2a-i), while MSY-b-FM/PF-48h was obtained from wet mixing of kaolin before wet fusion (protocol 2a-ii). On the other hand, MSX-a-FM/FF-48h, MSX-b-FM/FF-48h

and MSX-c-FM/FF-48h were the products obtained in the full fusion method. The MSX-a-FM/FF-48h was obtained via pre-treatment of kaolin by dry mixing before dry fusion (protocol 2b-i), MSX-b-FM/FF-48h via wet mixing before wet fusion (protocol 2b-ii) while MSX-c-FM/FF-48h was via wet mixing followed by evaporation of the water solvent before dry fusion (protocol 2b-iii).

The functional groups observed in the FTIR spectra in Figure 4.21a and 4.20b for the products obtained in both partial and full fusion methods, respectively, corresponds to those of zeolite materials (Belaabed et al., 2016; Mozgawa et al., 2005). As discussed in section 4.3.1, the XRD patterns in Figure 4.23 for both methods further showed that zeolites Na-Y and Na-X were the products in the partial fusion and full fusion protocols, respectively. In the partial fusion in protocol 2a, the method of kaolin pre-treatment did not influence the resulting zeolites types and their crystallinity as observed in the XRD patterns of MSY-a-FM/PF-48h and MSY-b-FM/PF-48h in Figure 4.23a which were zeolite Na-Y obtained through dry mixing of kaolin with NaOH before dry fusion and wet mixing of kaolin with NaOH before wet fusion of kaolin, respectively. However, for the full fusion products obtained in protocol 2b, the intensity and purity of the resulting zeolite Na-X depended on the method of pre-treatment performed on kaolin before the hydrothermal crystallization step, Figure 4.23b. Apart from the zeolite Na-X, low-intensity peaks at 2θ of 7.3°, 16.2°, 24.1°, 27.2° and 29.9°, which are consistent with zeolite Na-A (Belaabed et al., 2016), were also observed for the MSX-a-FM/FF-48h product where dry mixing of kaolin with NaOH followed by dry fusion was performed in protocol 2b-i. The MSX-b-FM/FF-48h product derived from the wet mixing of kaolin with NaOH followed by the wet fusion in protocol 2b-ii showed zeolite-Na-X with poor crystallinity and having HS impurity characterized by the XRD peaks at 2θ values of 14.3°, 24.7°, 31.9°, 35.0° and 43.1°, (Baerlocher & McCusker, 2017), while the MSX-c-FM/FF-48h product derived from wet

mixing of kaolin with NaOH followed by evaporation of the water solvent before dry fusion showed highly crystalline zeolite Na-X with no impurities.

The presence of zeolite Na-A impurity alongside zeolite Na-X in the MSX-a-FM/FF-48h product obtained from protocol 2a-i is, therefore, an indication of an inhomogeneous dry reaction of NaOH with kaolin during the fusion step resulting in F-MK (basically sodium aluminosilicates) besides some heat-treated pure kaolin or MK (basically aluminosilicates) in the fusion product. This inhomogeneous dry reaction is a result of inefficient dry mixing of the NaOH with kaolin during the pre-treatment step. The F-MK, which forms the bulk of the material, is thus converted to zeolite Na-X during the hydrothermal crystallization process, while the trace MK is transformed to zeolite Na-A in the process discussed in sections 4.2.2 and 4.2.1, respectively. The product obtained via dry mixing of NaOH with kaolin followed by dry fusion before hydrothermal crystallization step, therefore, depends on the degree of mixing achieved. Less efficient mixing may therefore explain the presence of Na-A impurities in previous reports involving this method (Bortolatto et al., 2017; Chandrasekhar & Pramada, 2004; Covarrubias et al., 2006; Doyle et al., 2016; El-Mekkawi et al., 2016; El-Mekkawi & Selim, 2012; Kovo et al., 2009; Logar et al., 2009; Ma et al., 2014).

In both MSX-b-FM/FF-48h and MSX-c-FM/FF-48h products, a high degree of mixing was achieved and therefore a uniform mixture of kaolin with NaOH was obtained in the wet mixing method in the pre-treatment step, implying that the starting kaolin material was fully converted to F-MK in the fusion step leading to the absence of zeolite Na-A in the final products. However, the presence of water molecules in the fusion step in the wet fusion method in protocol 2b-ii for the MSX-b-FM/FF-48h product may engender the formation of non-uniform structural building units consisting of narrow pore zeolite seeds alongside faujasite seeds during the wet fusion. The narrow pore building blocks are therefore responsible for the

formation of HS alongside the poor crystallinity zeolite Na-X product arising from the faujasite building blocks, consistent with the observed SEM image in Figure 4.22c showing very small particles tending towards being amorphous. Although the fusion process was performed at a very high temperature of 750 °C, the narrow pore structures which formed hydroxysodalite might have been formed during the temperature ramping stage of the furnace when the temperature was high enough to lead to chemical reactions of clay with NaOH and water molecules was still present within the material to influence the reaction to small pore structures. On the other hand, the absence of water molecules in the dry fusion of kaolin in protocol 2b-iii for the MSX-c-FM/FF-48h may be forming uniform secondary and tertiary faujasite building units suitable for the subsequent conversion to zeolite Na-X and leading to the observed pure Na-X product in Figure 4.23b.

The formation of zeolite Na-X with varying impurities and crystallinities in protocol 2b, arising because of the differences in the pre-treatment methods of kaolin before the fusion step is further proof that the resulting zeolite structures and their purity are strongly determined in the high-temperature reaction at the fusion step, see equation (7) in section 4.2.2.

4.3.7 Effect of crystallization time on full fusion derived products

Because of their improved quality and properties, the full fusion products were further investigated by studying the effects of crystallization time on the resulting products. The hydrothermal crystallization period was varied between 48 and 168 h. Figure 4.26 shows the FTIR spectra and the XRD patterns of the resulting synthesis products from the dry mixing followed by dry fusion and wet mixing followed by the dry fusion before hydrothermal crystallization, in protocol 2b-i and 2b-iii, respectively, at different periods.
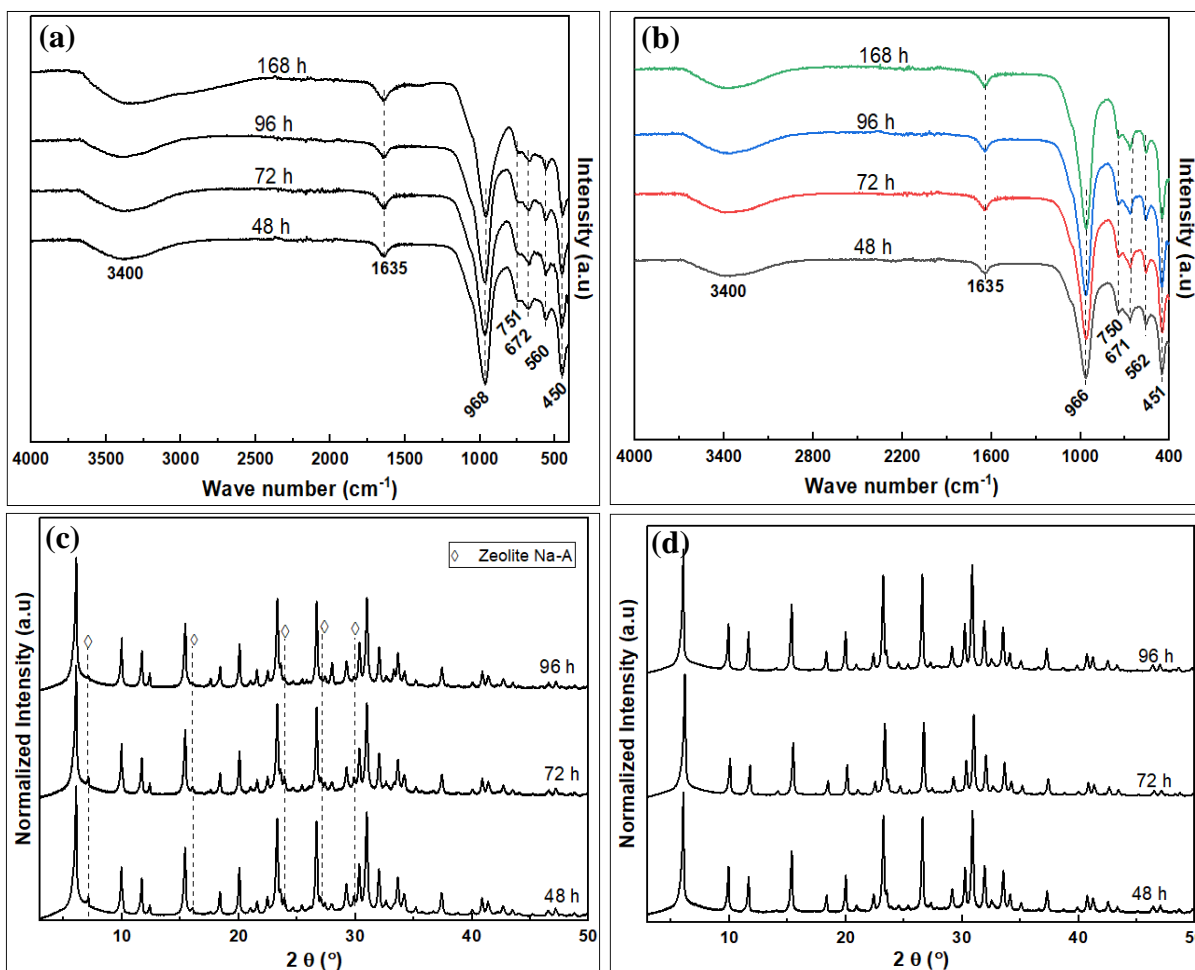
Figure 4.26; The FTIR spectra and the XRD patterns of the products obtained in protocol 2b at different crystallization time; (a). FTIR spectra of protocol 2b-i products, (b). FTIR spectra of protocol 2b-iii products, (c). XRD patterns of protocol 2b-i products, and (d). XRD patterns of protocol 2b-iii products.

The FTIR spectra in both protocol 2b-i and 2b-iii had the same functional groups belonging to zeolite Na-X (Mozgawa et al., 2005). As in the case with the SX-a-FM/FF products in section 4.2.4, the XRD pattern of protocol 2b-i where dry mixing of kaolin with NaOH followed by dry fusion method showed that zeolite Na-X was formed alongside zeolite Na-A at low crystallization time. As crystallization time increased, Na-A was transformed via dissolution to form greater amounts of Na-X via the process of Ostwald's ripening (Greer et al., 2009), with Na-X being the abundant phase after 96 h. In contrast, pure zeolite Na-X phases were

obtained even at low reaction time when the wet mixing of kaolin with NaOH followed by the dry fusion was applied, and no phase change was observed even at prolonged reaction time. The method leading to the formation of MSX-c-FM/FF is therefore the most efficient for the conversion of kaolin components and the production of pure and quality zeolite products within a short time.

4.3.8   The effect of pre-treatment method for kaolin on protocol 1b products

The effects of pre-treatment methods for kaolin on the resulting synthesized products were also investigated on protocol 1b synthesis method which had resulted in zeolite Na-X and zeolite Na-Y products in sections 4.2.2 and 4.2.6 using unmodified hydrogel and hydrogel modified with fumed silica, respectively. The three pre-treatment methods, i.e., the dry mixing followed by dry fusion, wet mixing followed by the wet fusion and the dry mixing followed by the dry fusion was done following protocols 2b-i, 2b-ii and 2b-iii, respectively, but this time, using the previously discussed chemical composition of the hydrogel in sections 4.2.2 and 4.2.6. The chemical composition of the products obtained under different pre-treatment methods in protocol 1b is shown in Table 4.9.

Table 4.9; Chemical composition of the products obtained in protocol 1b under different pre-treatment methods.

Sample	Percent oxide (wt. %)						Chemical formula
	Al_2O_3	SiO_2	Na_2O	TiO_2	Fe_2O_3	SiO_2/Al_2O_3	
SX-c-FM-48h	33.1	43.0	22.8	0.8	0.3	2.20	$Fe_{0.6}Ti_{1.5}Na_{113.3}K_{0.1}Al_{100}Si_{110.1}O_{432.3}$
SX-a-FM-48h	34.0	45.8	18.1	1.1	1.8	2.28	$Fe_{3.4}Ti_{2.1}Na_{87.5}K_{0.9}Al_{100}Si_{114.4}O_{434.4}$
FSY-a-FM-48h	25.2	53.8	15.5	0.6	0.2	3.63	$Fe_{0.2}Ti_{1.5}Na_{101.4}K_{1.2}Al_{100}Si_{181.5}O_{596.7}$
FSY-b-FM-48h	25.3	57.8	15.2	0.9	0.1	3.88	$Fe_{0.3}Ti_{2.2}Na_{98.8}K_{5.4}Al_{100}Si_{193.9}O_{596.9}$
FSY-c-FM-48h	25.7	57.6	15.4	0.7	0.0	3.81	$Fe_{0.1}Ti_{1.8}Na_{98.5}K_{3.9}Al_{100}Si_{190.2}O_{587}$

The products derived from unmodified hydrogel, i.e., SX-a-FM-48h and SX-c-FM-48h, had a relatively similar SiO_2/Al_2O_3 molar ratio of ca. 2.2. On the other hand, the products derived from the hydrogels modified with fumed silica, i.e., FSY-a-FM-48h, FSY-b-FM-48h and FSY-c-FM-48h showed high SiO_2/Al_2O_3 molar ratios of 3.68, 3.88 and 3.81, respectively. These observations are consistent with the observations made for the products obtained in protocol 1 as seen in Table 4.5.

The SEM images of the products obtained in protocol 1b under different pre-treatment methods are shown in Figure 4.27 and 4.28.
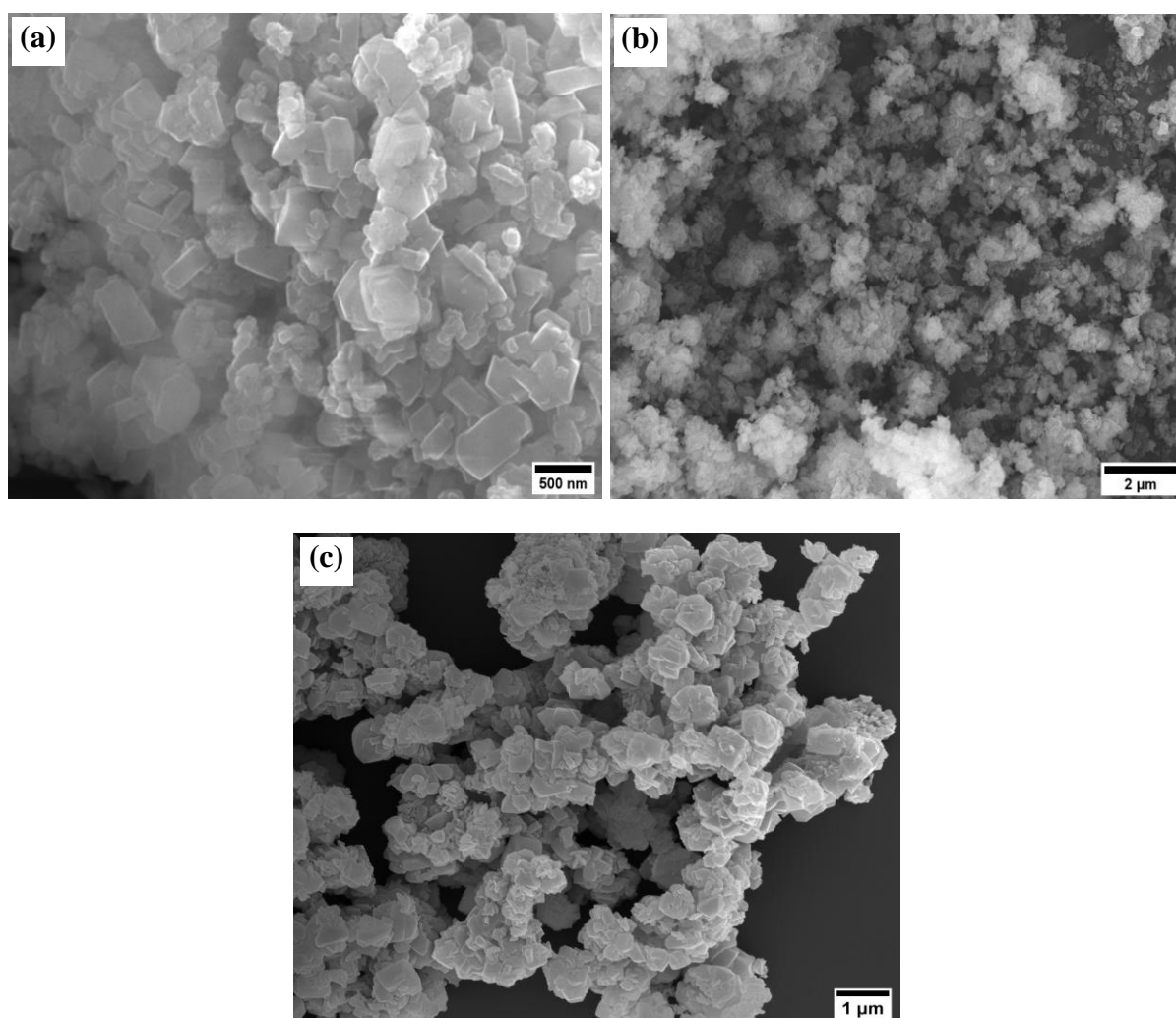
Figure 4.27; The SEM images of the products obtained in protocol 1b under different pre-treatment methods using unmodified hydrogel; (a). SX-a-FM-48h, (b). SX-b-FM-48h, and (c). SX-c-FM-48h.

The SEM images of the SX-a-FM-48h and SX-c-FM-48h products in Figure 4.27 exhibited octahedral-like crystals, belonging to faujasite zeolites, with varying particle sizes. The SX-b-FM-48h showed small crystals tending towards the amorphous phase, in agreement with the observed SEM image of SMX-b-FM/FM-48h in Figure 4.22.
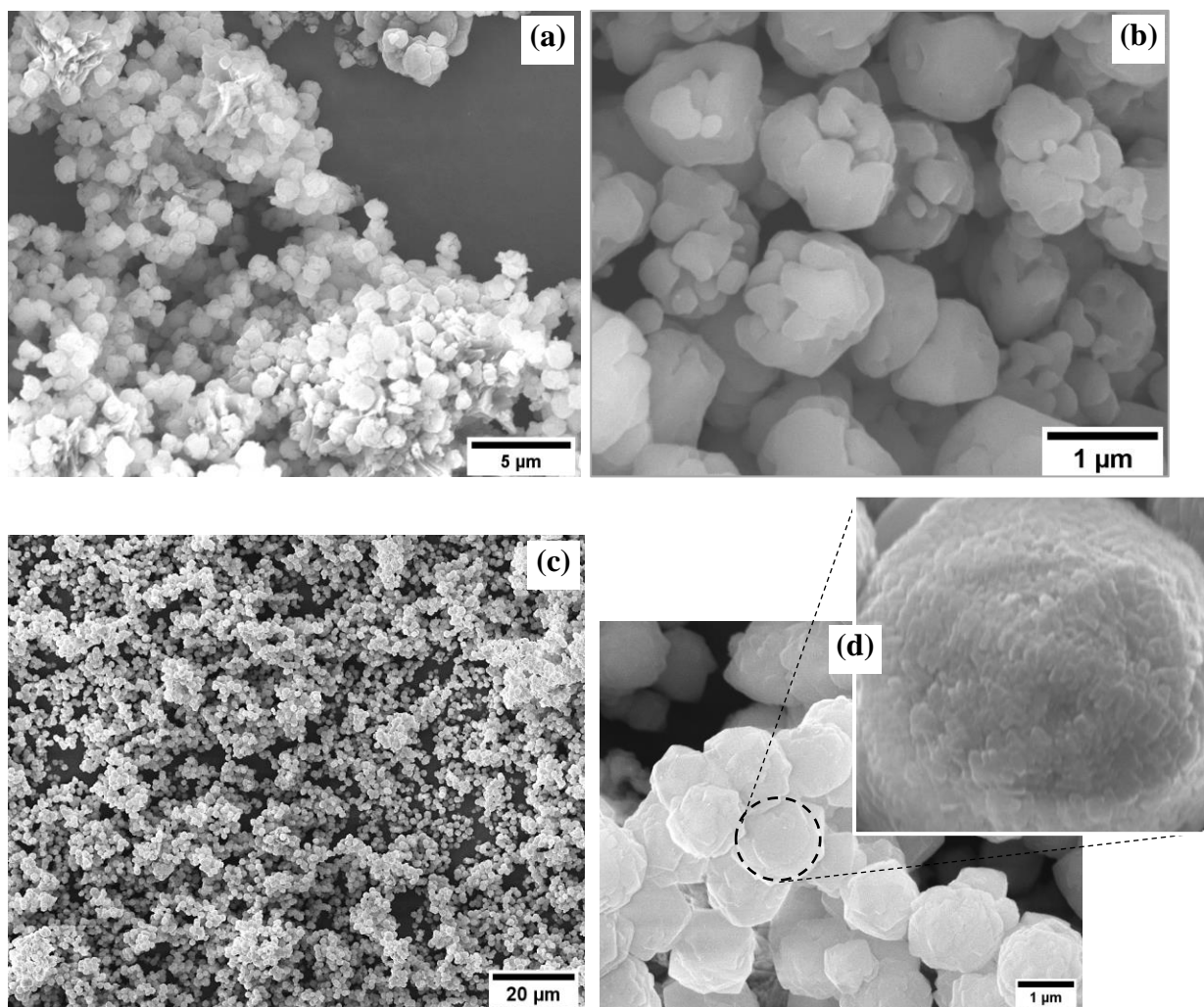
Figure 4.28; The SEM images of the products obtained in protocol 1b under different pre-treatment methods using fumed silica modified hydrogel; (a & b). FSY-a-FM-48h, (c). FSY-b-FM-48h, and (d). FSY-c-FM-48h.

Amorphous phases, due to unconverted raw materials, were observed for the SY-a-FM-48h product (in Figure 4.28a). Besides, non-uniform and fractured crystals were observed for the SY-a-FM-48h product in Figure 4.28b. On the other hand, FSY-c-FM-48h obtained from wet

mixing before dry fusion showed fully formed and uniform crystals exhibiting relatively smooth surfaces, Figure 4.28(c & d).

To investigate the vibrational characteristics of the bonds, identify the functional groups and the types of zeolites and their crystallinity, FTIR and X-Ray spectroscopies were performed on the resulting products in protocol 1b. Figure 4.29 shows the FTIR spectra and the XRD patterns of the synthesized zeolites in protocol 1b under different pre-treatment methods.
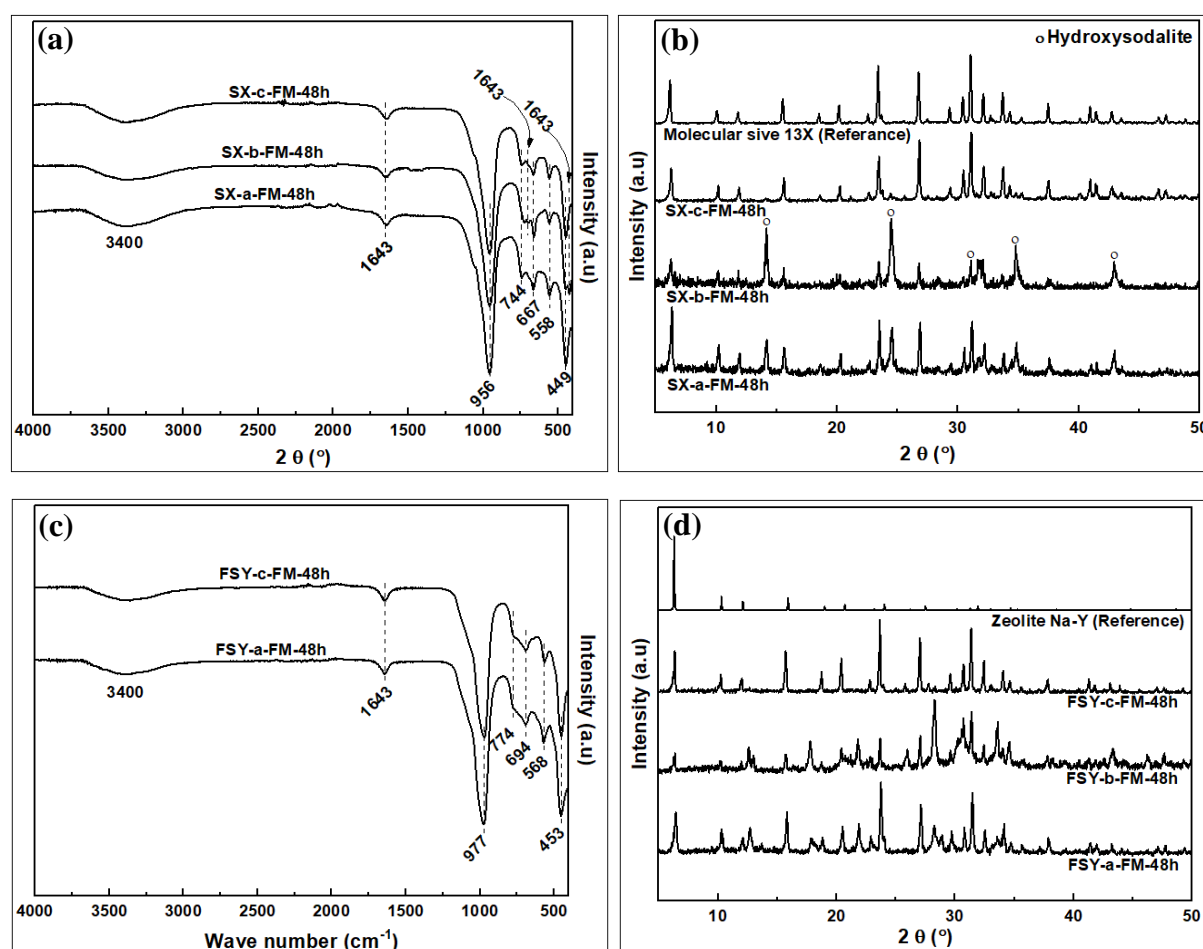
Figure 4.29; Analysis of the products obtained in protocol 1b under different pre-treatment methods; (a & b). FTIR spectra and XRD patterns of the products obtained using unmodified hydrogel, and (c & d). FTIR spectra and XRD patterns of the products obtained using fumed silica modified hydrogel.

The FTIR spectra and the XRD patterns of the SX products obtained from unmodified hydrogel are related to zeolite Na-X (Baerlocher & McCusker, 2017) and are the same as the product

obtained in protocol 1b (in Figure 4.12 of section 4.2.2) under similar condition of the unmodified hydrogel. On the other hand, the FTIR spectra and the XRD patterns of FSY products obtained from hydrogels modified with fumed silica are related to zeolite Na-Y (Baerlocher & McCusker, 2017) and are in agreement with the product obtained in protocol 1b (in Figure 4.18b of section 4.2.6) under the similar condition of fumed silica modified hydrogel.

The properties of the products under protocol 1b in both unmodified hydrogels and hydrogels modified with fumed silica were in agreement with those observed under similar pre-treatment conditions in section 4.3.6. The Na-X product in SX-a-FM-48h obtained through dry mixing of kaolin with NaOH followed by dry fusion before hydrothermal crystallization resulted in the zeolite with impurities, Figure 4.29b. The SX-b-FM-48h product obtained through the wet mixing of kaolin with NaOH followed by wet fusion before hydrothermal crystallization resulted in Na-X zeolite with poor crystallinity besides some observed impurities. However, the SX-c-FM-48h product obtained through wet mixing of kaolin with NaOH followed by dry fusion before hydrothermal crystallization resulted in the pure zeolites with better properties. Similar results were observed for zeolite Na-Y in FSY-a-FM-48h, FSY-b-FM-48h and FSY-c-FM-48h as shown in Figure 4.29d which were obtained under similar conditions.

The surface area and textural analysis of the resulting products under different pre-treatment conditions in protocol 1b are shown in Figure 4.30. The synthesized zeolites exhibited reversible type I BET isotherms, Figure 4.30(a & c). The SX-b-FM-48h and FSY-b-FM-48h products, obtained via wet fusion had the least specific surface area, micropore surface area and pore volume of 266 m²/g, 225 m²/g and 0.09 cm^3/g, respectively, for the SX-b-FM-48h and 167 m²/g, 143 m²/g, and 0.06 cm^3/g for the FSY-b-FM-48h product, see Table 4.10. On the other hand, the SX-c-FM-48h and the FSY-c-FM-48h product had the highest specific surface area, micropore surface area and pore volume of 617 m^2/g, 566 m^2/g and 0.23 cm^3/g,

respectively, for the SX-c-FM-48h product, and 845 m^2/g, 549 m^2/g and 0.23 cm^3/g for the FSY-b-FM-48h product.
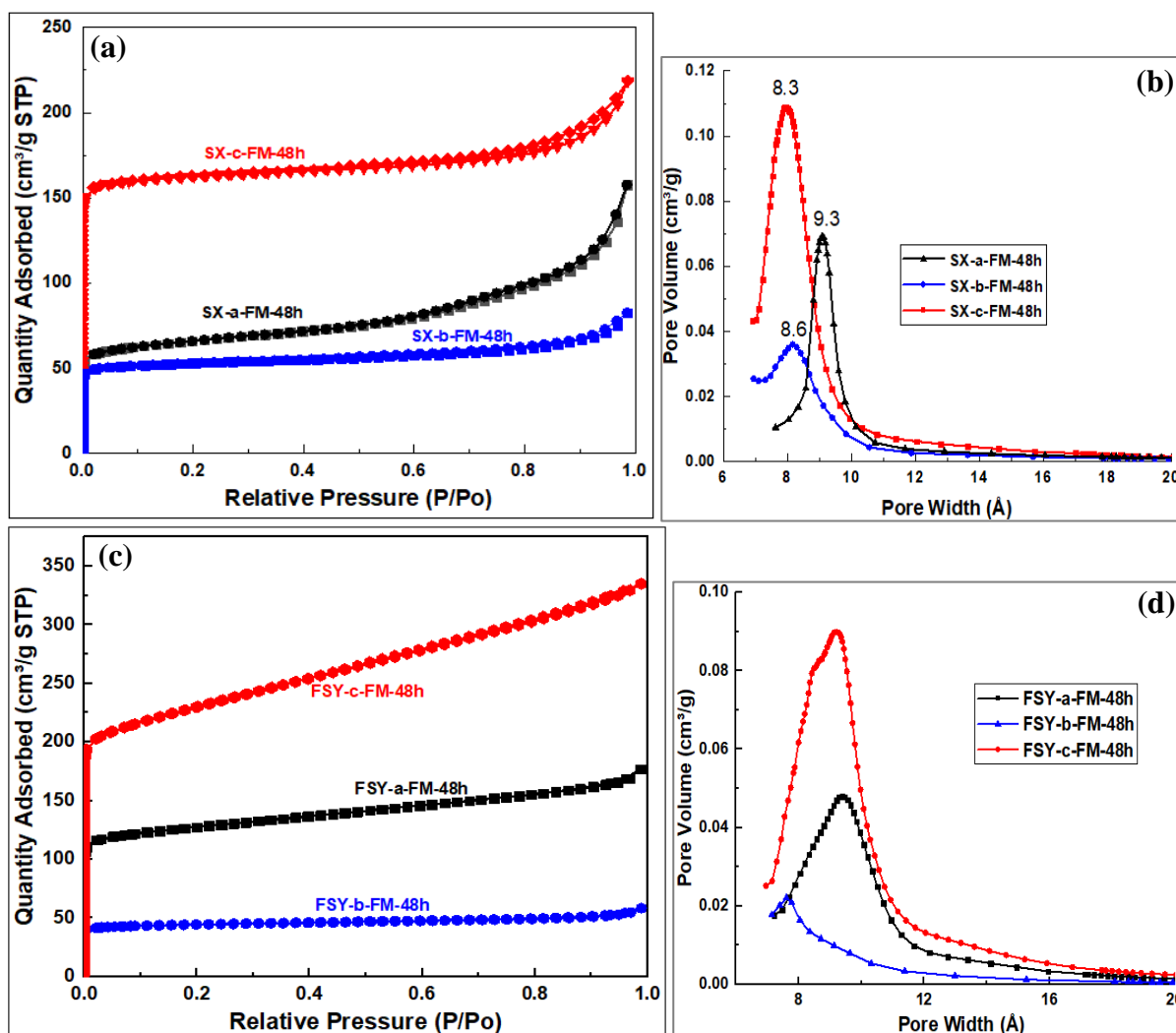
Figure 4.30; The surface area and textural analysis of the products obtained in protocol 1b; (a & b). N$_2$ sorption isotherms and Horvath-Kawazoe pore size distribution, respectively, of the products from unmodified hydrogel, (c & d). N$_2$ sorption isotherms and Horvath-Kawazoe pore size distribution, respectively, of the products from fumed silica modified hydrogel.

For the products of unmodified hydrogel, the SX-a-FM-48h and SX-c-FM-48h products recorded pore size of 9.3 and 8.6 Å, respectively. The SX-b-FM-48h product, on the other hand, had a slightly lower pore size of 8.3 Å. Similarly, for the products from hydrogels modified with fumed silica, the FSY-a-FM-48h and FSY-c-FM-48h products recorded pore size of 9.9 and 9.6 Å, respectively, while the FSY-b-FM-48h product recorded a slightly lower pore size

of 8.9 Å. The observed surface area and textural properties were therefore in agreement with the observed properties of the products in section 4.2.2 under similar treatment conditions.

Table 4.10; Textural properties of synthesized zeolites obtained using different pre-treatment methods of kaolin in protocol 1b.

Sample	Specific Surface area (m²/g)	Micropore surface area (m²/g)	External surface area (m²/g)	Micropore volume (cm³/g)	Total pore volume (cm³/g)	Pore size (Å)
SX-a-FM-48h	307	236	71	0.10	0.30	9.3
SX-b-FM-48h	266	225	41	0.09	0.17	8.6
SX-c-FM-48h	617	566	51	0.23	0.34	8.3
FSY-a-FM-48h	473	355	118	0.15	0.27	9.9
FSY-b-FM-48h	167	143	24	0.06	0.09	8.9
FSY-c-FM-48h	845	549	297	0.23	0.51	9.6

4.4 Hydrothermal crystallization products - Protocol 3

In protocol 3, natural volcanic ash, kaolin and sodium aluminate were used as raw materials in the synthesis of zeolites. Wet mixing of raw materials (KVA-10%A-750C, kaolin and $NaAlO_2$) with NaOH was used because it resulted in high quality zeolites with good properties in section 4.3. Based on the chemical composition in Table 4.3, KVA-10%A-750C material was taken and subsequently used as pure silica (volcanic silica).

The products obtained in protocol 3 are denoted as SZ1-c-FVA, SZ2-c-FVA, SZ3-c-FVA and KaVo-c-FM. The SZ1-c-FVA, SZ2-c-FVA and SZ3-c-FVA products were obtained using synthesis hydrogels prepared from a fused mixture of KVA-10%A-750C and $NaAlO_2$ with Na_2O (i.e., FVA). The KVA and FVA denotes Kenyan volcanic ash and fused volcanic ash, respectively. The SiO_2:Al_2O_3:Na_2O:H_2O oxide molar ratios of the synthesis hydrogels were calculated to be 2.38:1:3:120.65, 4.09:1:3.01:221.13 and 2:1:1.98:107 for SZ1-c-FVA, SZ2-c-FVA and SZ3-c-FVA respectively. The KaVo-c-FM product was synthesized using a synthesis hydrogel prepared from a fused-metakaolinite with KVA-10%A-750C added as a source of

extra silica. The KaVo denotes a product obtained using kaolin and acid-washed volcanic ash while FM denotes fused-metakaolin. Based on the chemical composition of the clay material in Table 4.1, the $SiO_2:Al_2O_3:Na_2O:H_2O$ molar composition of the KaVo-c-FM synthesis hydrogel was 7.2:1:10:282.1.

4.4.1 Characterization of protocol 3 derived products

The chemical composition of the products obtained in protocol 3 and the calculated chemical formula is shown in Table 4.11. The difference between SZ1-c-FVA-48h and SZ2-c-FVA-48h synthesis hydrogels was on the amount of SiO_2 used, with the SZ2-c-FVA-48h hydrogel having greater amounts SiO_2. On the other hand, the difference between SZ1-c-FVA-48h and SZ3-c-FVA-48h synthesis hydrogels was on the amount of Na_2O used, with the SZ1-c-FVA-48h hydrogel having greater amounts Na_2O.

The corresponding differences in the levels of SiO_2 and Na_2O of the synthesis hydrogels was not however reflected in the SiO_2 and Na_2O quantities of the corresponding products. The SiO_2 content of SZ1-c-FVA-48h and SZ2-c-FVA-48h products was relatively similar with both products having the same $SiO_2:Al_2O_3$ molar ratio of 2.6. On the other hand, the Na_2O composition of SZ1-c-FVA-48h and SZ3-c-FVA-48h were the same at ca. 24 %. The oxide composition of the resulting products is therefore not dictated by the synthesis hydrogel composition but rather by the resulting products types.

Table 4.11; Chemical composition of the products obtained in Protocol 3.

Sample	Percent oxide (wt. %)							SiO_2/Al_2O_3	Method	Chemical formula
	Al_2O_3	SiO_2	Na_2O	TiO_2	Fe_2O_3	K_2O	CuO			
SZ1-c-FVA-48h	30.27	46.71	22.63	0.01	0.07	0.13	0.17	2.62	ICP-OES	$Fe_{0.14}Cu_{0.35}Ti_{0.03}Na_{123.01}K_{0.48}Al_{100}Si_{130.93}O_{474.23}$
SZ2-c-FVA-48h	29.84	46.44	23.05	0.02	0.23	0.27	0.14	2.64	ICP-OES	$Fe_{0.50}Cu_{0.31}Ti_{0.04}Na_{127.09}K_{0.98}Al_{100}Si_{132.04}O_{479.25}$
SZ3-c-FVA-48h	34.11	40.65	24.48	0.52	0.24			2.02	SEM-EDX	$Fe_{0.44}Ti_{0.98}Na_{118.05}Al_{100}Si_{101.11}O_{413.85}$

The vibrational characteristics of the bonds found in the fused volcanic ashes (F-KVAs) and the resulting products in protocol 3 were investigated via Fourier transform infrared spectroscopy. The transformation of F-KVA to synthesized products are shown in the FTIR spectra in Figure 4.31.
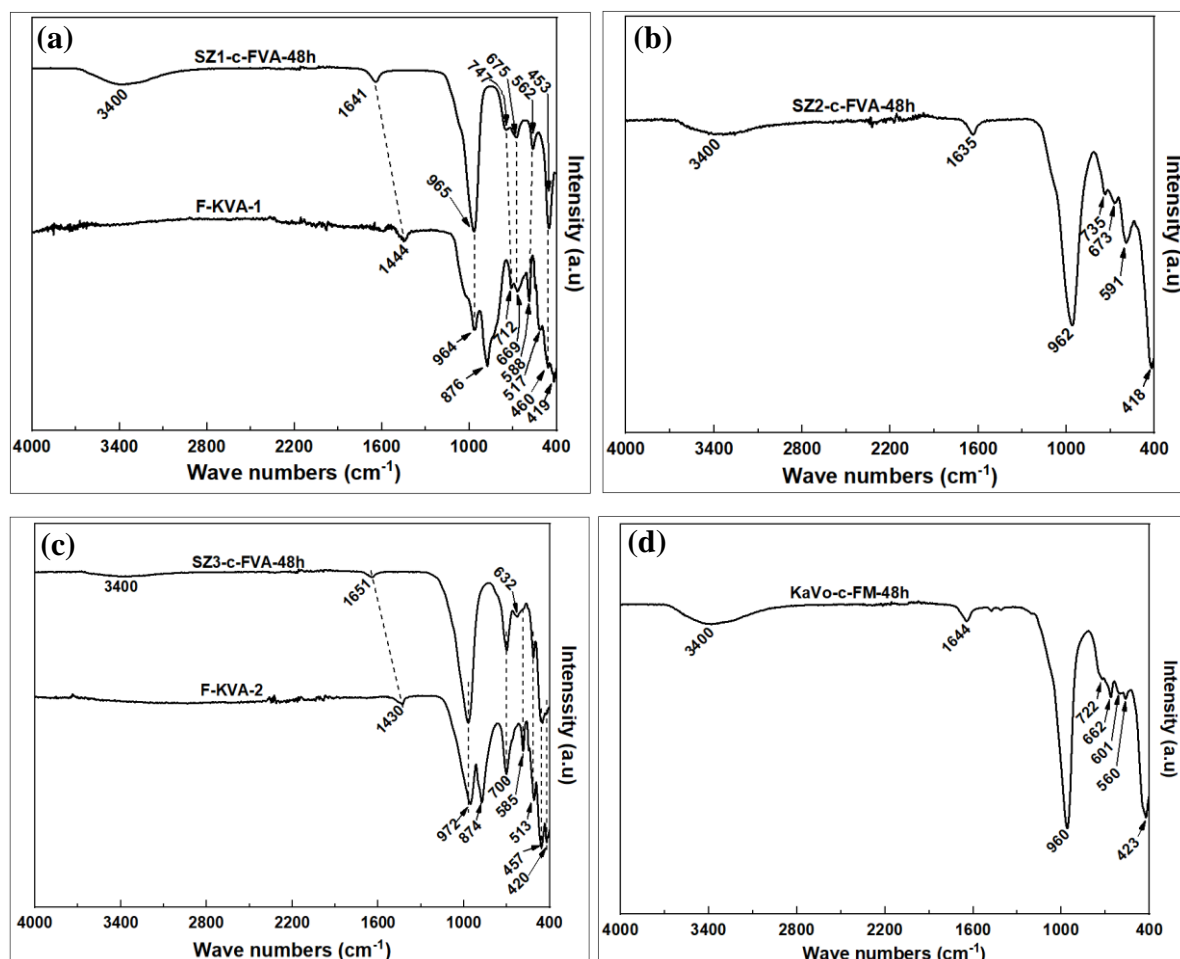
Figure 4.31; The FTIR spectra of the F-KVA and the derived products in protocol 3; (a). SZ1-c-FVA-48h, (b). SZ2-c-FVA-48h, (c). SZ3-c-FVA-48h, and (d). KoVo-c-FM-48h.

Different products were obtained in protocol 3. The differences in the products are evident in the FTIR spectral range of 400-1000 cm^{-1}. The spectral bands of various products obtained in protocol 3 and their assignments are shown in Table 4.12. All the absorption bands for F-KVA1 and SZ1-c-FVA-48h are similar to those observed for the F-MK1 and SX-a-FM-48h and MSX-c-FM/FF-48h products in Figure 4.13 of section 4.2.2 and Figure 4.29 of section 4.3.8 and are

characteristic of zeolite Na-X (Mozgawa et al., 2005). Same absorption bands were observed for both SZ2-c-FVA-48h and KaVo-c-FM-48h products.

Table 4.12; Spectral bands of the products obtained in protocol 3 and their assignments.

Spectral bands (cm^{-1})						Assignment	Reference
A	B	C	D	E	F		
	419	418		420	423	Single four-membered ring (S4R) of the sodalite – adsorption at 428 cm^{-1}	
443	460		457	457		Symmetric bending vibrations of T-O tetrahedral	(Belaabed et al., 2016)
	517		513	513		*	
562	588	591	585	585	560	Symmetric stretching vibrations associated with the six-member rings (D6R) of the faujasite structure	(Mozgawa et al., 2005)
					601	Double four-membered ring (D4R) *	
675	669	673	632		662	Internal symmetric stretching of zeolitic T-O tetrahedral	(Belaabed et al., 2016)
747	712	735	700	700	722	External symmetric stretching vibration of T-O-T	
	876			874		*	
965	964	962	972	972	960	Internal asymmetric stretching vibrations of zeolitic T-O-T tetrahedral	(Belaabed et al., 2016)
1641	1444	1635	1651	1430	1644	Bending vibration of adsorbed water	(Tounsi et al., 2009)
3400		3400	3400		3400	Stretching vibration of adsorbed water	(Tounsi et al., 2009)

A = SZ1-c-FVA-48h, B = F-KVA-1, C= SZ2-c-FVA-48h, D = SZ3-c-FVA-48h, E = F-KVA-2, F = KaVo-c-FM-48h,   * = unidentified bands

The fingerprints absorption bands at 420 cm^{-1}, 457 cm^{-1}, 700 cm^{-1}, 972 cm^{-1} for SZ3-c-FVA-48h product are characteristics of hydroxysodalite, which have also been observed by other researchers (Esaifan et al., 2019; Naskar et al., 2011).

Identification of the product phases and their crystallinities were achieved via X-ray diffraction spectroscopy was performed on the synthesized products. The XRD patterns of the products

obtained in protocol 3 are shown in Figure 4.32. The four products had different XRD patterns.

All the XRD peaks for the SZ1-c-FVA-48h in Figure 4.32a matched those of the zeolite Na-X

reference (Baerlocher & McCusker, 2017).
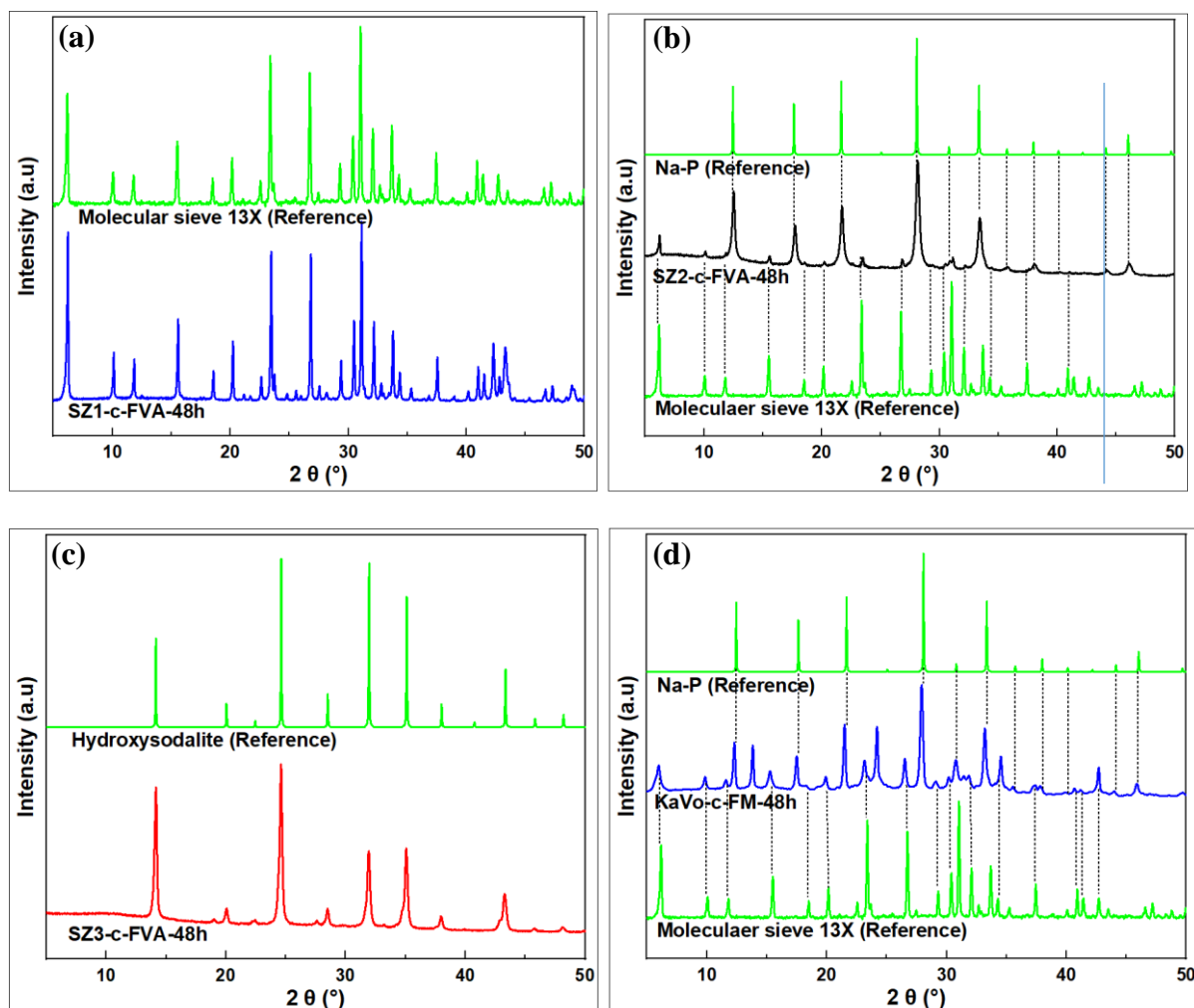
Figure 4.32; The XRD diffraction patterns of the products obtained in protocol 3; (a). SZ1-c-
FVA-48h, (b). SZ2-c-FVA-48h, (c). SZ3-c-FVA-48h, and (d). KoVo-c-FM-48h.

The XRD pattern of both SZ2-c-FVA-48h and KaVo-c-FM-48h products in Figure 4.32b and

4.32d respectively pointed to the production of a mixture of zeolites. The intense XRD peaks

at 2θ values of 12.5°, 17.6°, 21.7°, 28.1°, 33.4°, 38.0° and 46.0° are characteristic of zeolite

Na-P (Baerlocher & McCusker, 2017), while the low intensity peaks at 2θ values of 6.2°, 10.0°,

15.5°, 18.51°, 20.2°, 23.4°, 26.8°, 29.3°, 3.4° and 32.1° among others belong to the zeolite Na-

X (Baerlocher & McCusker, 2017). On the other hand, all the XRD peaks for the SZ3-c-FVA-48h product in Figure 4.32c at 2θ values of 14.2°, 20.0°, 22.5°, 24.6°, 28.5°, 32.0°, 35.1°, 38.0°, 40.8°, 43.4°, 45.8° and 48.2° belong to the HS (Baerlocher & McCusker, 2017). The XRD findings for the SZ3-c-FVA-48h as HS relates well with the chemical analysis results which showed that the $SiO_2:Al_2O_3$ molar ratio was 2.02, typical of hydroxysodalites.

To investigate the crystallite structures and morphologies of the synthesized products, scanning electron microscopy was performed on the protocol 3 products. The SEM images of the SZ2-c-FVA-48h and SZ3-c-FVA-48h products are shown in Figure 4.33.
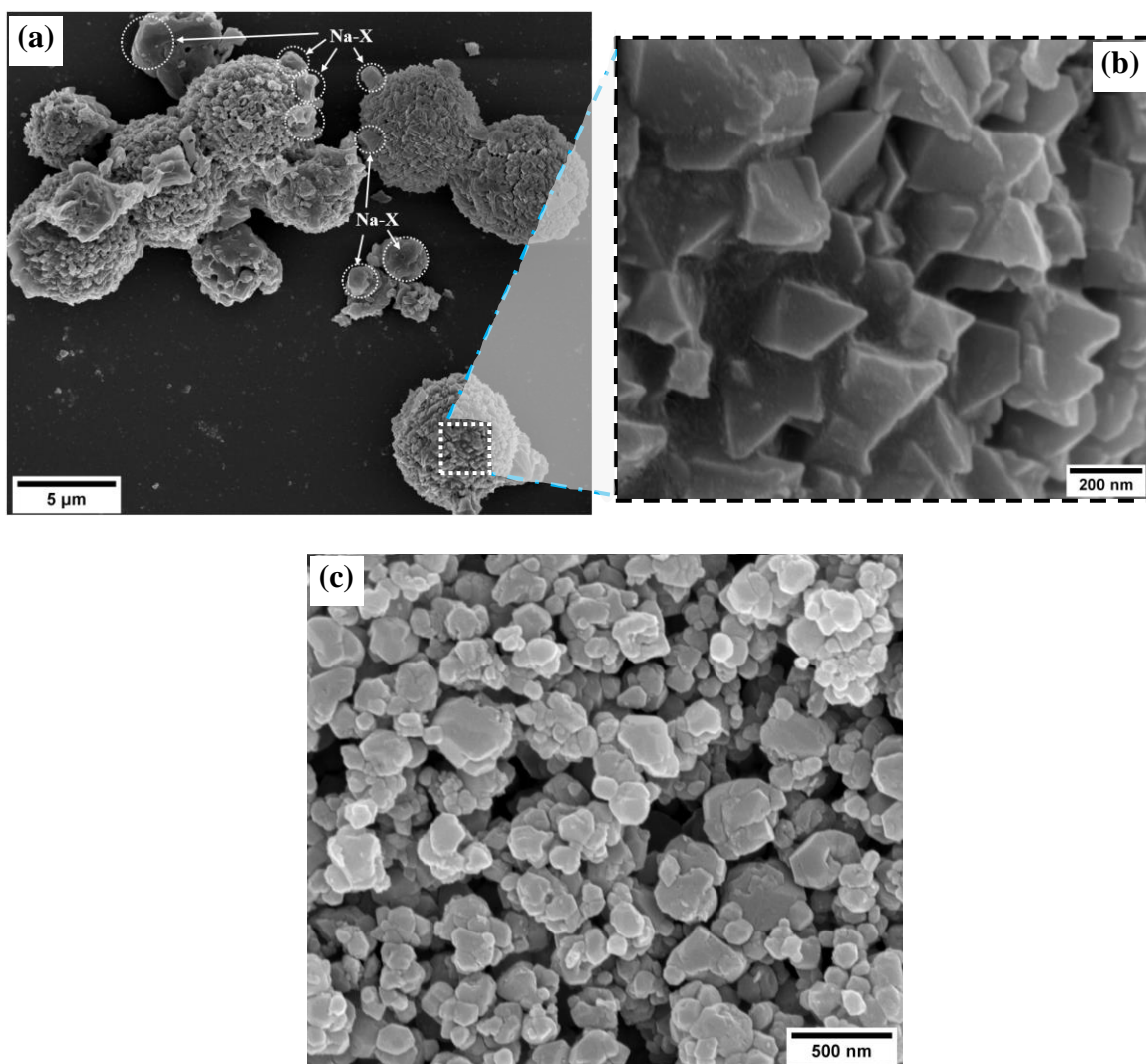
Figure 4.33; The SEM images of protocol 3 products; (a & b). SZ2-c-FVA-48h, and (c). SZ2-c-FVA-48h.

The SEM image of SZ2-c-FVA-48h in Figure 4.33a consist of aggregates in spherical shapes with sizes as large as 5 µm in diameter. The spheres exhibit rugged surface morphology consisting of prismatic particles with sharp edges and points, Figure 4.33b. Such aggregates and morphology are characteristics of zeolite Na-P, and are consistent with other reports (Sharma et al., 2016; Zou et al., 2016).

The few clusters of octahedral crystals among the Na-P spheres and on the surface of the spheres belongs to the Na-X. The small number of Na-X crystals in the SEM micrograph is in agreement with the observed low intensity for Na-X peaks in the XRD pattern in Figure 4.32b. On the other hand, the SZ3-c-FVA-48h in Figure 4.33c consists of irregular shaped cubic and spherical particles of sizes ranging between 50-300 nm. The irregular cubic and spherical structures for hydroxysodalite products have also been observed by Naskar et al., 2011. The self-assembly of hydroxysodalite particles with the progress of reaction time after 6 h to form spherical coral-like morphology which had previously been reported (Naskar et al., 2011) was however not observed in this case.

4.4.2 Thermogravimetric analysis of the protocol 3 derived products

To investigate the thermal stability of the zeolite products in protocol 3, TGA analysis was performed in the temperature range of 25-1000 °C. The TA, DTA and DSC curves for each product is shown in Figure 4.34. For SZ1-c-FVA-48h and SZ3-c-FVA-48h products in Figure 4.34(a & c), an exothermic desorption of water occurred in a single step between 25-400 °C accompanied with 23 % and 7.5 % weight loss respectively. The single step weight loss corresponds to the desorption of water from a uniformly distributed pores of Na-X and Na-HS pure zeolites. The desorption of water was a slow process in the SZ3-c-FVA-48h product because of the mass trasfer barier of the water molecuse from the small pore HS crystals compared to large pore Na-X crystals of the SZ1-c-FVA-48h product. On other hand, multiple

steps of weight loss were observed in both SZ2-c-FVA-48h and KaVo-c-FM-48h products. About 18 % of weight loss taking place in 4 steps between 25-800 °C was observed in both cases. The multiple steps correspond to desorption of water from different pores of the Na-X and Na-P zeolite mixture in the products. The steepest section between 25-150 °C in both SZ2-c-FVA-48h and KaVo-c-FM-48h represent the weight loss from the large pore Na-X while the less steep section between 150-400 °C represent desorption from small pore Na-P.
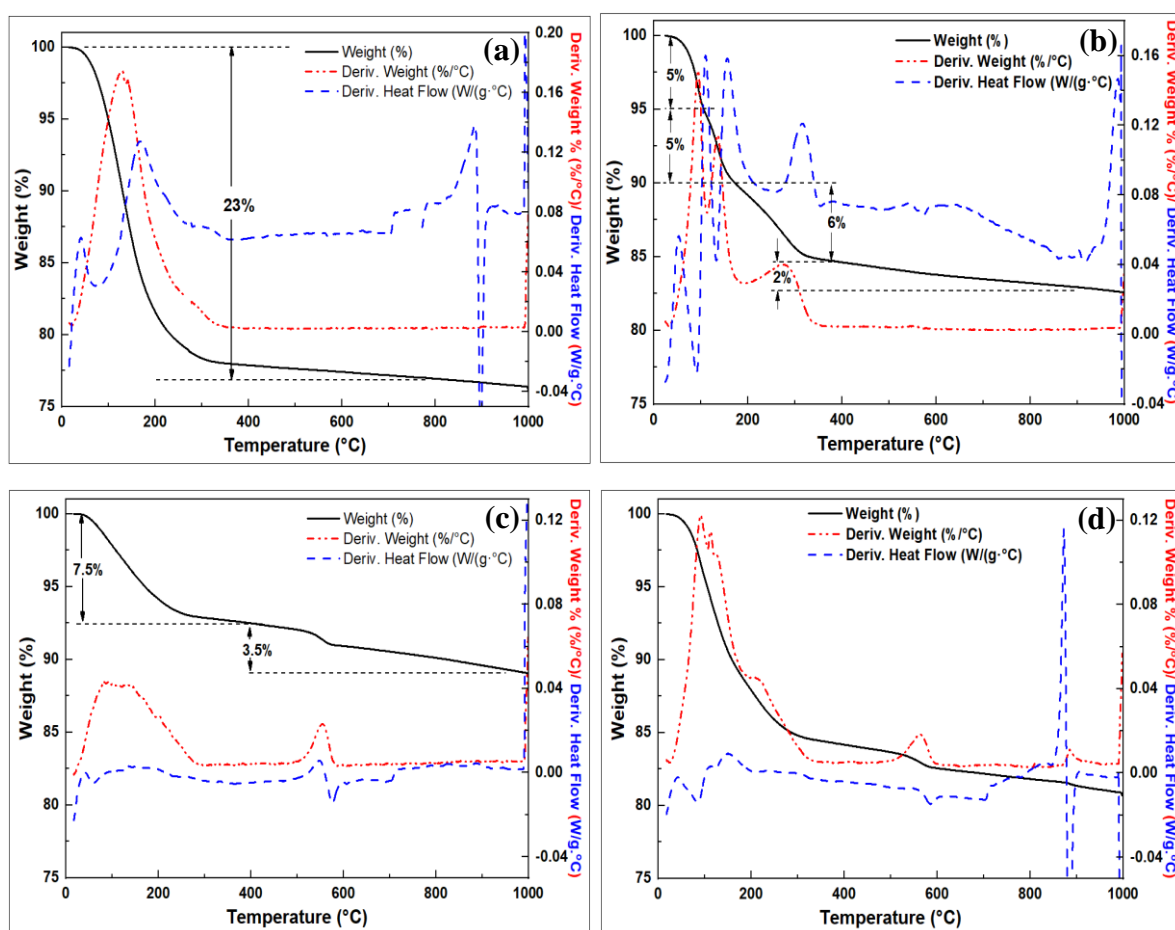
Figure 4.34; TGA analysis of protocol 3 products; (a). SZ1-c-FVA-48h, (b). SZ2-c-FVA-48h, (c). SZ3-c-FVA-48h, and (d). KaVo-c-FM-48h.

4.4.3 BET surface area and porosity analysis of protocol 3 products

To investigate the textural properties of the products in protocol 3, BET analysis was performed by N_2 sorption on the products. Porosity analysis for the products from protocol 3 is shown in

Figure 4.35 and Table 4.13. A type II isotherm was observed in KaVo-c-FM-48h product. All other zeolite products showed a type I isotherm (Thommes et al., 2015). The textural properties of the zeolite products are summarised in Table 4.13. The SZ2-c-FVA-48h product had the least surface area and total pore volume of 12.38 m²/g and 0.04 cm³/g, respectively. On the other hand, the SZ1-c-FVA-48h (pure Na-X) product recorded the highest surface area, micropore surface area and pore volume of 766.41 m²/g, 644.16 m²/g and 0.26 cm³/g, respectively.
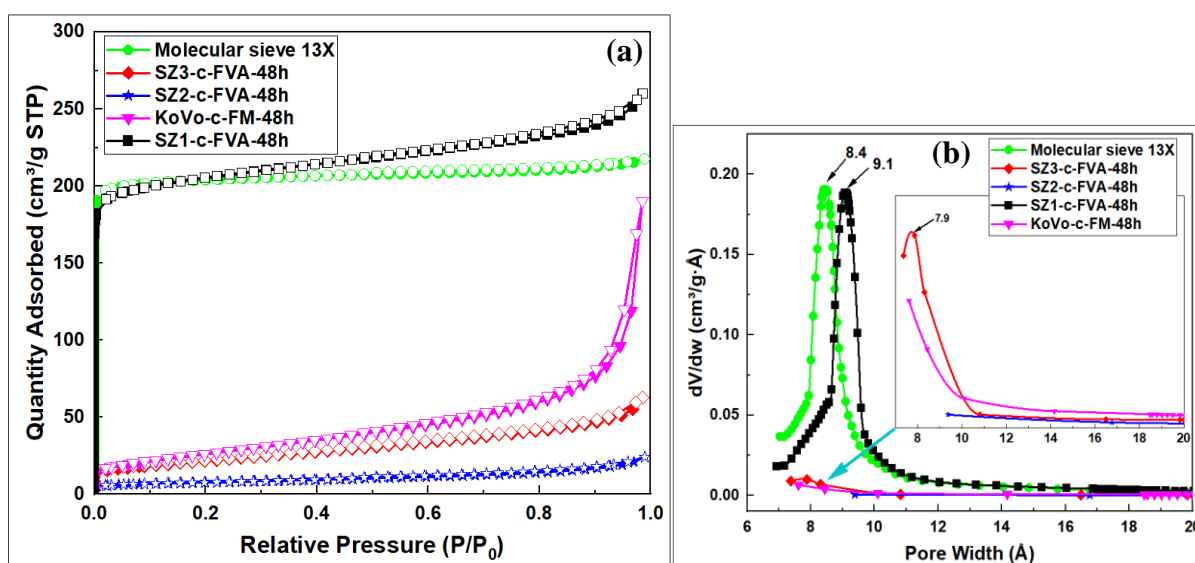
Figure 4.35; Porosity analysis of synthesized zeolites in protocol 3; (a). N_2 sorption isotherms, and (b). Horvath-Kawazoe pore size distribution curves.

Table 4.13; Textural properties of synthesized zeolites in protocol 3.

Sample	Specific Surface area (m²/g)	Micropore surface area (m²/g)	External surface area (m²/g)	Micropore volume (cm³/g)	Total pore volume (cm³/g)	Pore size (Å)
SZ1-c-FVA-48h	766.41	644.16	122.25	0.26	0.40	9.1
SZ2-c-FVA-48h	12.38	-	17.89	-	0.04	-
SZ3-c-FVA-48h	75.34	4.51	70.82	0.003	0.10	7.7
KaVo-c-FM-48h	78.17	14.9	63.27	0.16	0.26	-
Molecular sieve13X	772	726.60	46.32	0.30	0.34	8.7

The textural properties of SZ1-c-FVA-48h are comparable to those of commercially available molecular 13X (772 m²/g and 0.30 cm³/g). The SZ2-c-FVA-48h and KoVo-c-FM-48h products

recorded very low surface area and micropore volume because the Na-P zeolite, (which, considering their intense peaks in Figure 4.32 and the SEM images in Figure 4.33, might be in greater amounts in the mixture), have crystals with small pores of 2.9 Å (Sharma et al., 2016). In addition, low surface area and micropore volume recorded for the SZ3-c-FVA-48h product is due to the small pore opening of the hydroxysodalite 4.2 Å (Shirani Lapari et al., 2015). The small pores in Na-P and Na-HS creates a barrier to the N_2 sorption. Pore size of 9.1 Å and 7.7 Å were observed for Na-X in SZ1-c-FVA-48h and Na-HS in SZ3-c-FVA-48h products, respectively.

4.4.4   The effects of crystallization time on the SZ3-c-FVA product

The effects of crystallization time on the hydroxysodalite synthesis were studied by performing crystallization of SZ3-c-FVA between 10-96h. The FTIR spectra and the TGA curves of the products at 10 h, 48 h, 72 h and 96 h are shown in Figure 4.36. The positions of FTIR bands of the products in Figure 4.36a remained the same even with the increase in crystallization time. There was however a slight reduction in the intensity of the peaks with the reaction progress. The observed additional bands at 1147 and 1204 cm^{-1} for the SZ3-c-FVA-10h product below 10 h of crystallization time is an indication that the reactants did not fully convert to the products below 10 h of reaction time. In the TGA analysis in Figure 4.36b, all the products obtained under different crystallization periods showed three stages of weight loss. The amount of weight lost however, increased with the increase in crystallization time because the formation of zeolite crystals and pores improved with the increase in crystallization time. The steep weight loss in the second stage for the SZ3-c-FVA-10h also points to the possible presence of unconverted fused volcanic ash material after just 10 h of hydrothermal crystallization.
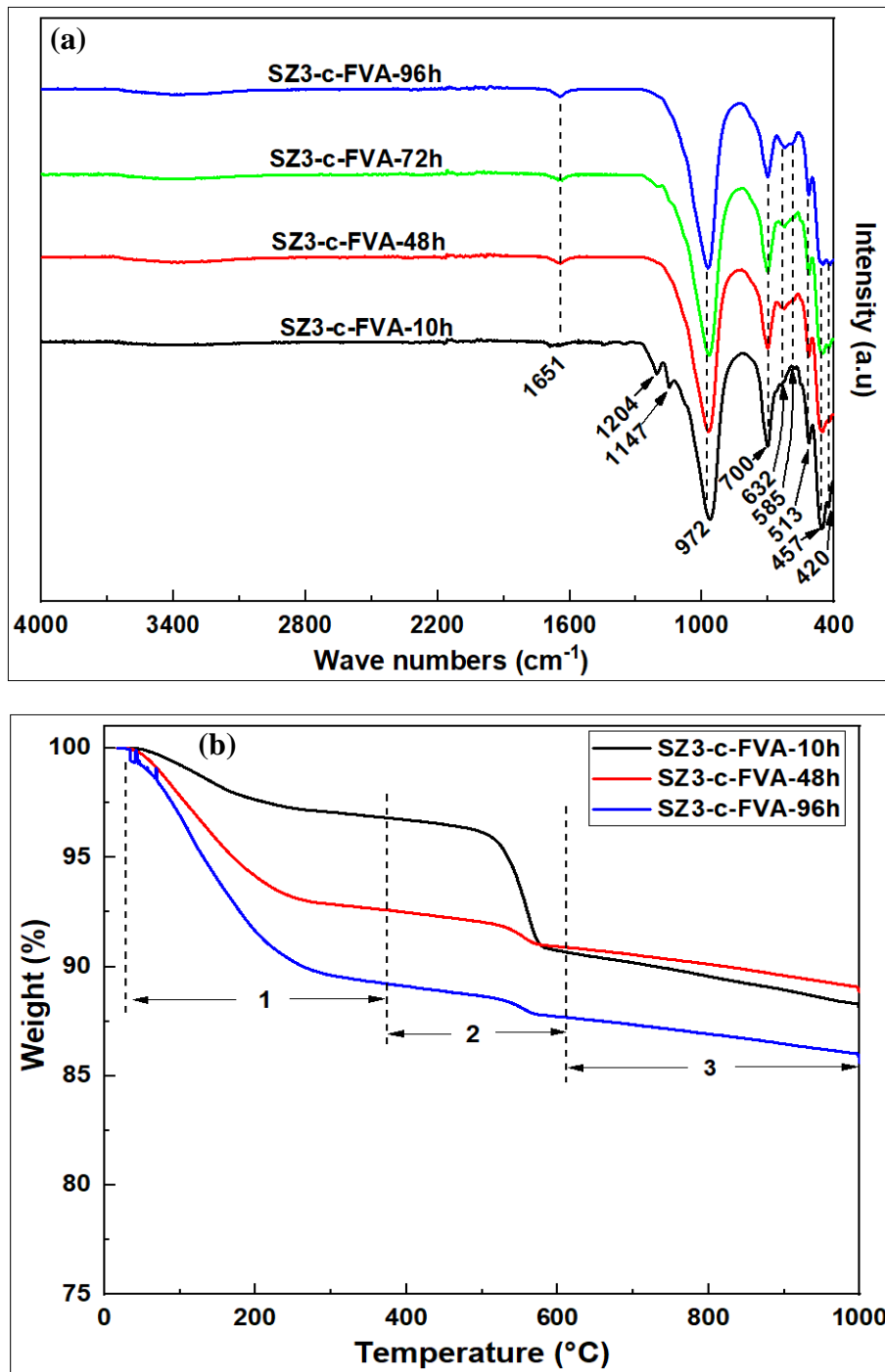
Figure 4.36; Analysis of the SZ3-c-FVA products at different crystallization periods; (a). FTIR spectra, and (b). TGA analysis curves.

The textural properties of the HS products at different crystallization periods are shown in the BET isotherms in Figure 4.37 and Table 4.14.
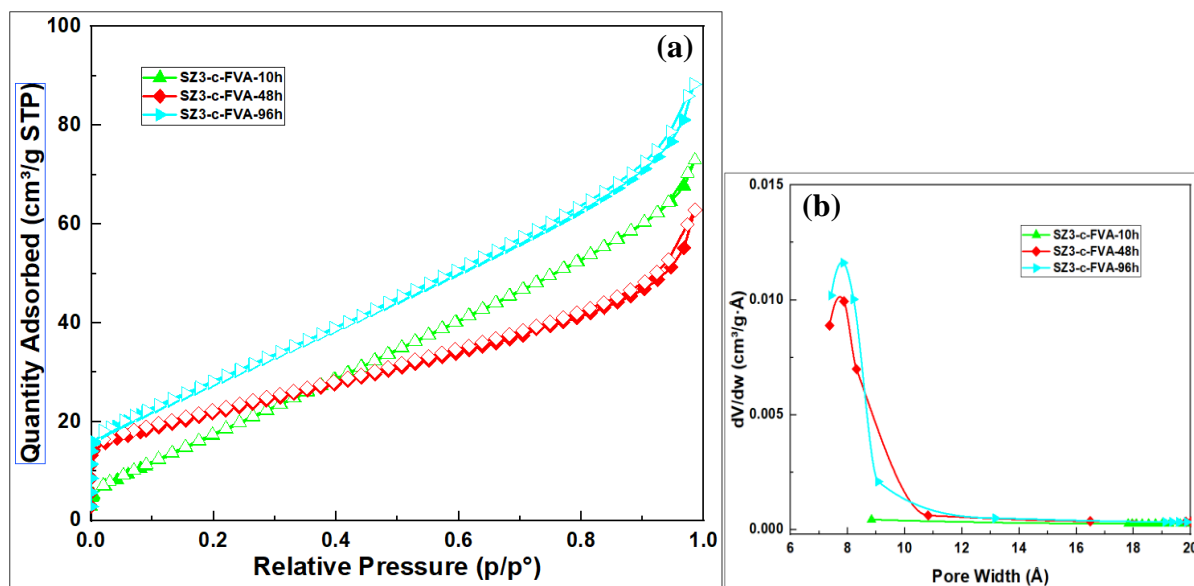
Figure 4.37; Porosity analysis of SZ3-c-FVA zeolites obtained at different crystallization time; (a). N_2 sorption isotherms, and (b). Horvath-Kawazoe pore size distribution curves.

Table 4.14; Textural properties of SZ3-c-FVA zeolites obtained at different crystallization time.

Sample	Specific Surface area (m²/g)	Micropore surface area (m²/g)	External surface area (m²/g)	Micropore volume (cm³/g)	Total pore volume (cm³/g)	Pore size (Å)
SZ3-c-FVA-10h	56.58	-	130.21	-	0.11	-
SZ3-c-FVA-48h	75.34	4.51	70.82	0.003	0.10	7.7
SZ3-c-FVA-96h	93.43	-	126.90	-	0.14	7.7

A type I adsorption isotherm was observed for all products. There was an observed increase in the BET surface area from 56.58 m²/g to 93.43 m²/g as the crystallization time was increased from 10 h to 96 h. This increase is consistent with the observed increase in weight loss with crystallization time in the TGA curves in Figure 4.36b. The observed pore size of the hydroxysodalite after 48 h was at 7.7 Å.

4.5 Characterization of natural zeolite

The chemical composition of the raw (Nat-SA-Pristine) and acid-washed (Nat-SA-10%A) natural zeolite, by ICP-OES spectrometry, is shown in Table 4.15. The natural zeolite had a

high SiO_2 content. Small quantities of Al, Na and K oxides were lost after washing the raw natural zeolite with 10 % HCl solution. The loss of these oxides led to a marginal increase in SiO_2/Al_2O_3 molar ratio from 10 to 12. Similar chemical composition and formula was also reported for clinoptilolite zeolite by Mozgawa, 2001.

Table 4.15; Chemical composition of the pristine and acid-washed natural zeolites.

| Sample | Percent oxide (wt. %) | | | | | | | SiO_2/Al_2O_3 | Method | Chemical formula |
	Al_2O_3	SiO_2	Na_2O	TiO_2	Fe_2O_3	K_2O	CuO			
Nat-SA-Pristine	13.11	77.94	2.74	0.14	1.20	4.65	0.21	10.09	ICP-OES	$Fe_{5.85}Cu_{1.03}Ti_{0.72}Na_{34.38}K_{38.40}Al_{100}Si_{504.41}O_{1206.45}$
Nat-SA-10%A	11.17	82.37	0.87	0.62	1.34	3.43	0.20	12.51	ICP-OES	$Fe_{7.64}Cu_{1.15}Ti_{3.66}Na_{12.79}K_{38.23}Al_{100}Si_{625.70}O_{1444.35}$

The X-ray and Fourier transform infrared spectroscopies showing the diffraction patterns and vibration characteristics, respectively, of raw (Nat-SA-Pristine) and acid-washed (Nat-SA-10%A) natural zeolite materials are shown in Figure 4.38.
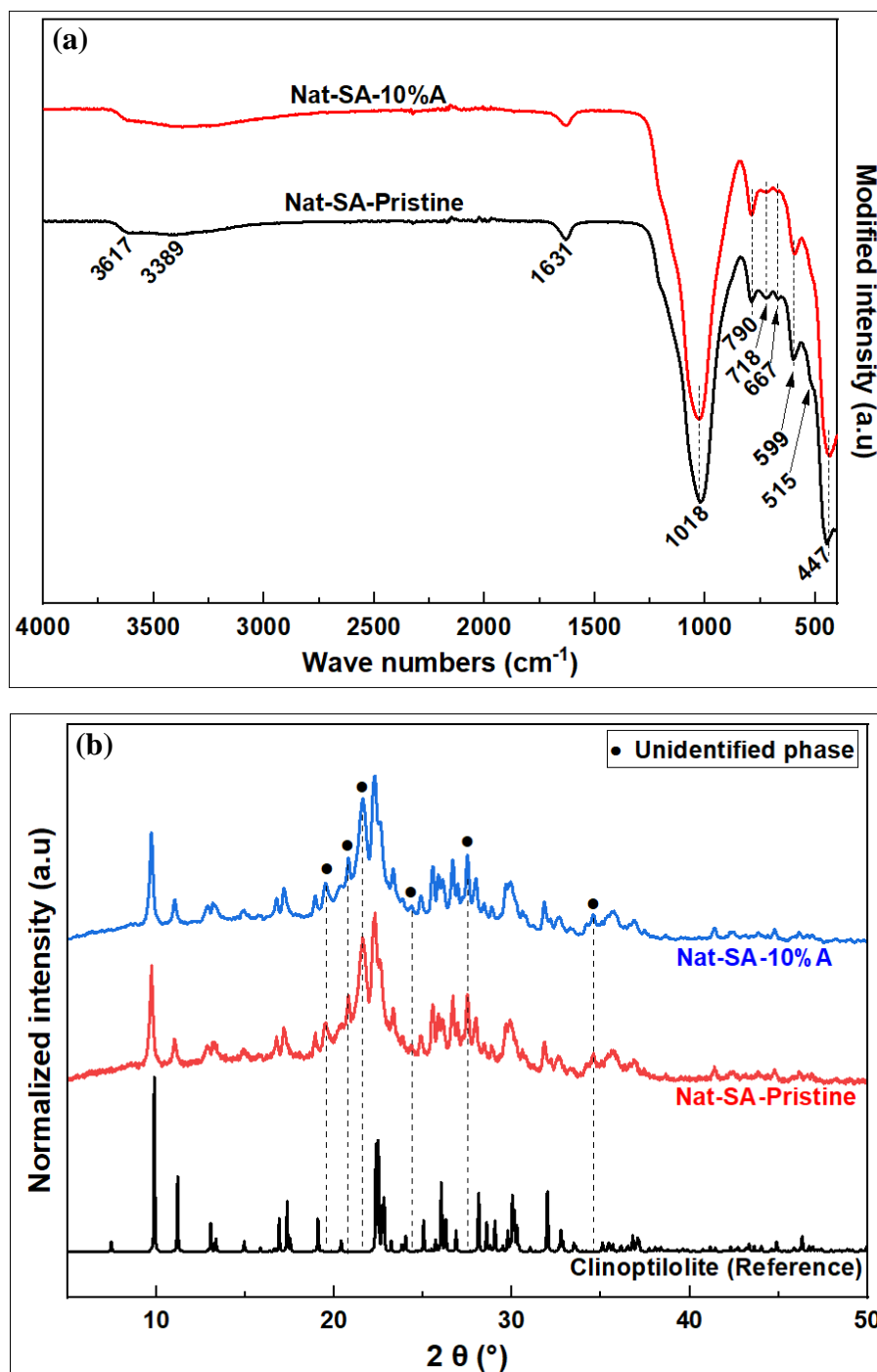
Figure 4.38; Analysis of the raw (Nat-SA-Pristine) and acid-washed (Nat-SA-10%A) natural zeolite materials; (a). FTIR spectra, and (b). XRD patterns.

Figure 4.38a shows the FTIR spectra of the Nat-SA-Pristine and Nat-SA-10%A. The broad double bands between 3300 and 3650 cm^{-1} together with that at 1631 cm^{-1} are characteristic vibrations of zeolitic water. In specific, the broad band at 3389 cm^{-1} is attributed to the stretching vibrations of the -OH of the bonded water, the sharp band at 3617 cm^{-1} is attributed to stretching modes of the -OH groups of free water of hydration, while the band at 1631 cm^{-1} is for the bending vibrations of water (Favvas et al., 2016; Perraki & Orfanoudaki, 2004). The spectral band at 1018 cm^{-1} is attributed to the internal asymmetric stretching vibrations of zeolitic T-O-T tetrahedron (Belaabed et al., 2016). The band at 447 cm^{-1} is assigned to a T-O-T bridges bending mode (Perraki & Orfanoudaki, 2004). The band at 790 cm^{-1} is attributed to the Si-O stretching vibration (Mozgawa et al., 2005). The band at 790 cm^{-1} also indicate that SBU structure is formed by the single 4-membered ring (S4R) or double 4-membered (D4R), and also 4-4-1 or 4-1 rings of clinoptilolite zeolites (Mozgawa et al., 1999). Washing the natural clinoptilolite with 10 % HCl led to a reduction in the intensity of the bands in the region of 500-750 cm^{-1}.

The XRD peaks at 2 θ values of 9.80°, 13.08°, 17.26°, 22.26°, 25.65°, 26.77°, 29.98° and 31.97° in Figure 4.38b corresponds to clinoptilolite phases (Baerlocher & McCusker, 2017). Other peaks appearing at 19.49°, 20.78°, 21.60°, 24.35°, 27.49° and 34.57° are impurities of the unidentified phases. The XRD patterns are in agreement with the observed FTIR spectra.

4.5.1   Thermogravimetric analysis of natural clinoptilolite zeolite

The thermal property of natural clinoptilolite zeolite was investigated using thermogravimetric analysis in the temperature range of 25-1000 °C. The TA, DTA and DSC curves for raw and acid-washed zeolite is shown in Figure 4.39. Four steps of weight loss were observed for the Nat-SA-Pristine zeolite. The first and second steps with a total of 6 % weight loss occurred between 25-250 °C and are attributed to loss of superficial water.
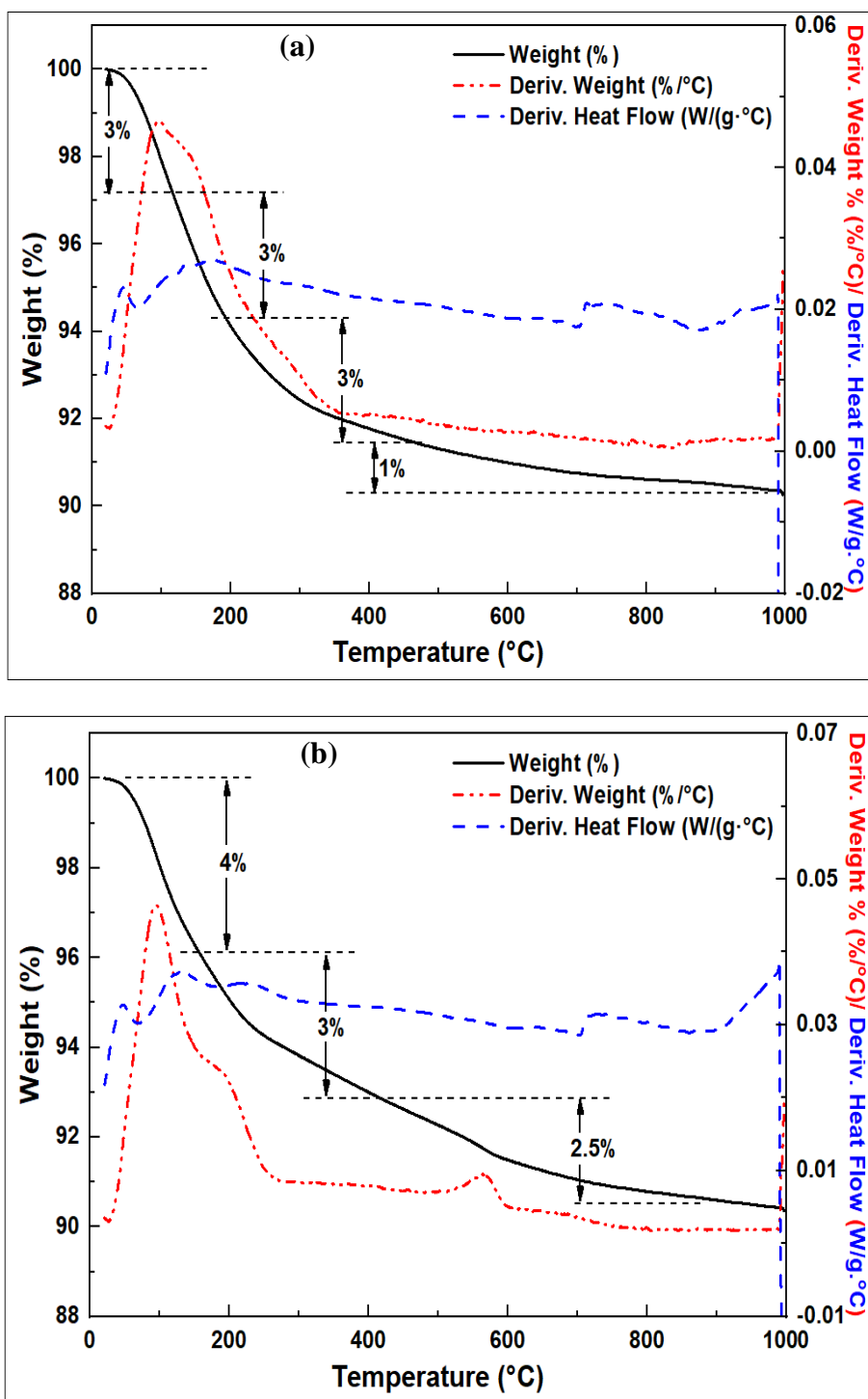
Figure 4.39; Thermal analysis of natural zeolites; (a). Raw (Nat-SA-Pristine), and (b). Acid-washed (Nat-SA-10%A).

The third step occurred between 250-450 °C due to loss of water from the crystallite pore channels and cavities. The fourth step involving 1 % of weight loss might be due to the loss of silanol groups bound water within the zeolite pore structure. On the other hand, three steps of

weight loss were observed for the Nat-SA-10%A zeolite. The multiple steps are due to the desorption from multiple porosity from the HEU framework structure shown in Figure 2.5. The first step of 4 % weight loss occurred between 25-200 °C and is due to loss of superficial water. The second step of 3 % weight loss between 200-450 °C is due to loss of water from the pore channels and cavities. The third step of 2.5 % weight loss is due to the loss of bound water. Heat absorption from 900-1000 °C, in the DSC curve without weight loss is an indication of zeolite decomposition and structural changes (Johnson et al., 2003).

4.6   Modification of zeolites

Prior to their use in the transesterification reaction of oils, zeolite catalysts were prepared by modifying both synthesized and natural zeolites through wet ion impregnation using 1.46 M sodium acetate (CH_3COONa) salt solution (Mentus et al., 2009; Sen et al., 2014; Ursini et al., 2006). The zeolites were stirred in the salt solution at 65 °C for 4 h before drying out the water solvent in a vacuum at room temperature.

4.6.1   Characterization of the modified zeolite catalysts

Figure 4.40 shows the FTIR and XRD patterns of raw kaolin, as-synthesized zeolite Na-X and its modified versions. The FTIR spectra in Figure 4.40a show an introduction of new hydroxyl bands at 1418 and 1578 cm^{-1} after modification of both Kaolin and synthesized zeolite Na-X (SX-a-FM-48h). The two bands shift to higher wave numbers at 1449 and 1656 cm^{-1} in addition to the decrease in their intensities after calcining the modified zeolite at 500 °C.

For the XRD patterns, the new XRD peaks at 2 θ of 9.14°, 19.46°, 27.54°, 31.22° and 32.51° for the unidentified phases in the modified Kaolin (Act/Kaolin) in Figure 4.40b is due to the Na-acetate. Modification of synthesized zeolite (SX-a-FM-48h) by impregnation with Na-Acetate in Figure 4.40c did not destroy the zeolite crystallinity, it however, resulted in the

reduction in intensity of the zeolite peaks. Zeolite crystallinity was retained even after using the zeolite in the transesterification reactions.
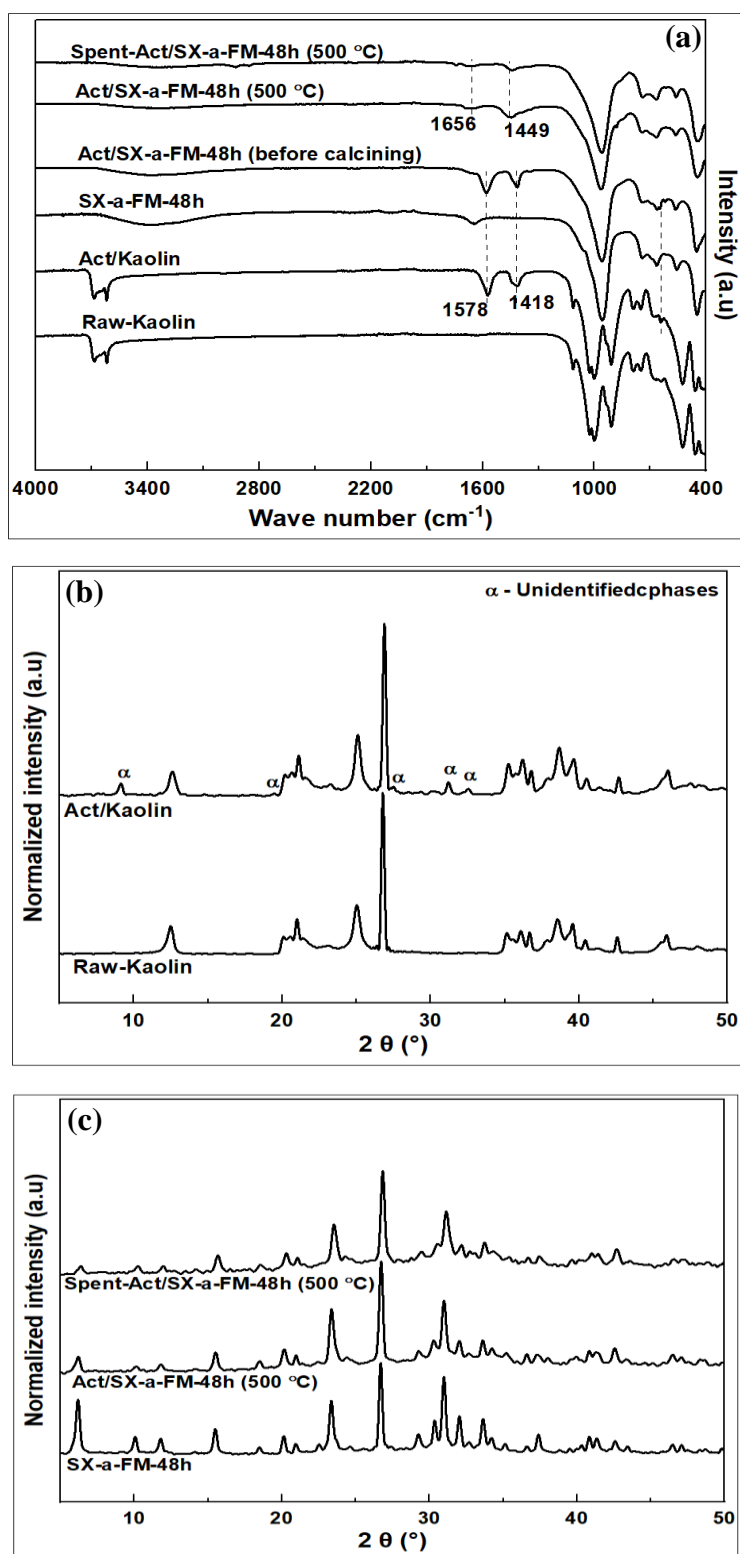
Figure 4.40; The XRD patterns of; (a). Raw kaolin and kaolin modified with Na-acetate, and (b). Synthesized zeolite Na-X and zeolites modified with Na-acetate.

The chemical composition of Act/SX-a-FM-48h zeolite in comparison to the chemical composition of as synthesized SX-a-FM-48h zeolite is shown in Table 4.16. With the exception of Na_2O, the oxide composition of both unmodified and modified zeolite Na-X is relatively the same. The Na_2O content of the modified zeolite is higher (25.7 %) than the unmodified (18.7 %) implying that Na^+ ions were successfully incorporated into the modified zeolite structure.

Table 4.16; The chemical composition of unmodified and modified synthesized zeolite Na-X.

	Percent oxide (wt. %)						
Sample	Al_2O_3	SiO_2	Na_2O	TiO_2	Fe_2O_3	SiO_2/Al_2O_3	Chemical formula
SX-a-FM-48h	31.6	48.5	18.7	0.9	0.2	2.60	$Fe_{0.4}Ti_{1.8}Na_{97.6}Al_{100}Si_{130.2}O_{465.4}$
Act/SX-a-FM-48h	29.1	44.1	25.7	0.8	0.3	2.58	$Fe_{0.6}Ti_{1.8}Na_{145.2}Al_{100}Si_{128.7}O_{486.4}$

The SEM images of both unmodified and modified zeolite in Figure 4.41 also show the presence of octahedral crystals with varying crystal sizes. The crystal structures of the zeolite were not destroyed after zeolite impregnation, which is in good agreement with the observations made in the XRD patterns.
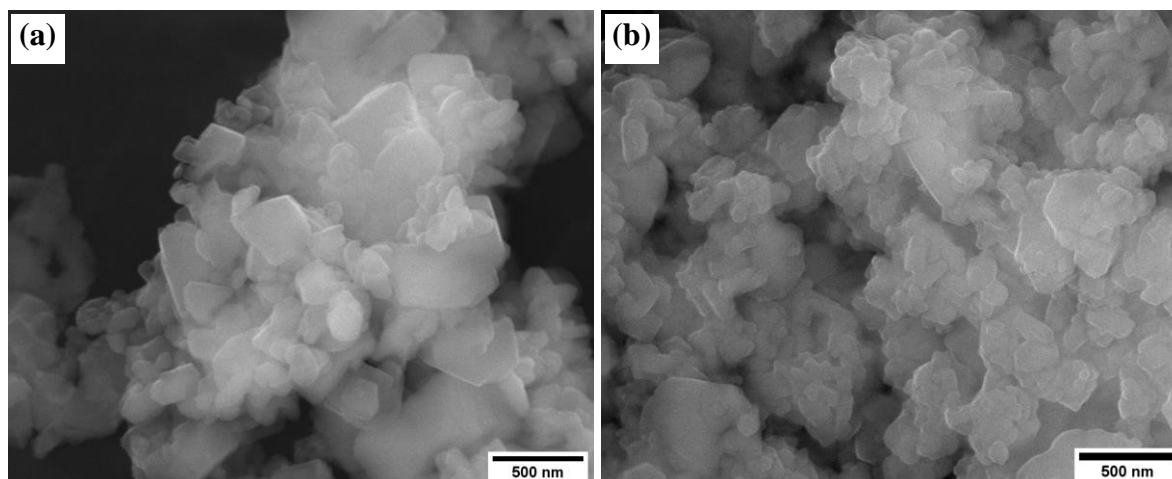
Figure 4.41; The SEM images of; (a). SX-a-FM-48h, and (b). Act/SX-a-FM-48h.

The textural properties and porosity analysis of the modified zeolite Na-X in comparison to those of unmodified zeolite is shown in Figure 4.42 and Table 4.17. Figure 4.42a shows a

significant reduction in BET and micropore surface area from 473.34 and 428.80 m^2/g to 38.92 and 0.58 m^2/g, respectively after modification of zeolite SX-c-FM-48h. The reduction in surface area is attributed to the occupation of Na_2O clusters and bridges within the pores leading to narrow pores which therefore hinders N_2 sorption in the modified zeolites.
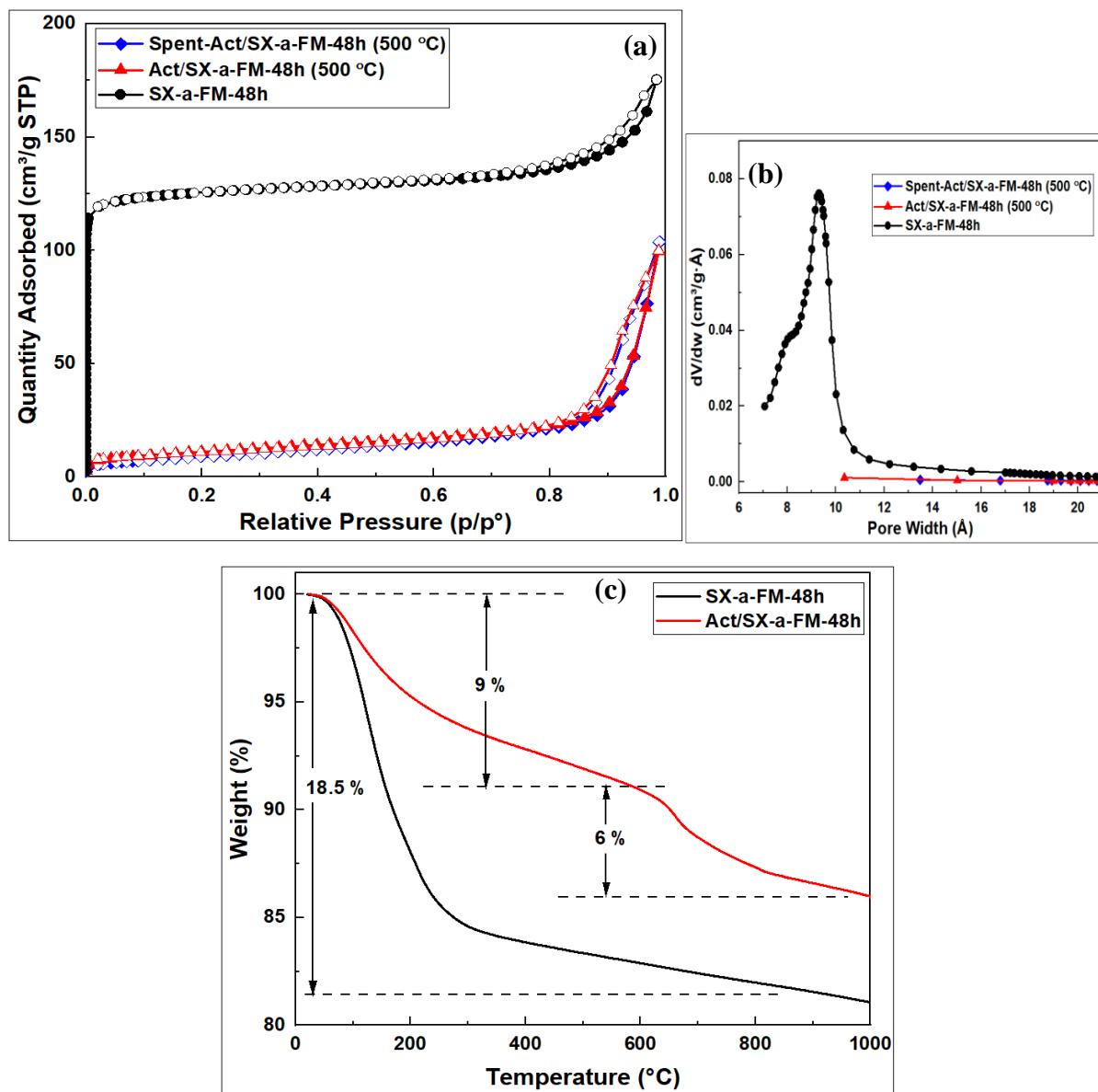
Figure 4.42; Porosity and thermal analysis of SX-a-FM-48h and Act/SX-a-FM-48h; (a). N_2 sorption isotherms, (b). Horvath-Kawazoe pore size distribution curves, and (c). Thermogravimetric analysis curves.

The narrowing of pores is also shown by the porosity distribution curve in Figure 4.42b where the pore width distribution of the Act/SX-a-FM-48h could not be determined.

Table 4.17; Textural properties of unmodified and modified synthesized zeolites.

Sample	Specific Surface area (m²/g)	Micropore surface area (m²/g)	External surface area (m²/g)	Micropore volume (cm³/g)	Total pore volume (cm³/g)	Pore size (Å)
SX-a-FM-48h	473.34	428.80	44.54	0.18	0.27	9.3
Act/SX-a-FM-48h (550 °C)	38.92	0.58	38.33	-	0.15	-
Spent-Act/SX-a-FM-48h (550 °C)	31.49	-	37.26	-	0.16	-

The thermal analysis curves for the modified and unmodified zeolite Na-X are shown in Figure 4.42c. A total of 18.5 % weight of zeolite, due to the absorbed water, was lost in a single step for the SX-a-FM-48h. On the other hand, a two-step weight loss was observed for the modified Act/SX-a-FM-48h. The first step (50-600 °C) involved 9 % weight loss due to the sorbed water, while the second step (600-1000 °C) involved 6 % of weight loss and might be due to the decomposition of the zeolite material. The significant reduction in weight loss due to the absorbed water, observed in the Act/SX-a-FM-48h in comparison to that of as synthesized SX-a-FM-48h, is therefore in good agreement with the observations made in the BET and porosity analysis.

4.7   Transesterification of *Jatropha curcas* and waste ccoking oils

Transesterification of JCO and WCO with methanol under various reaction conditions in the presence of prepared zeolite catalysts was performed in batch processes.

4.7.1   Identification of GC peaks and determination of response factor (RF)

Using response factors while performing quantitative analysis using GC are important because they eliminate variability in the instrument response. Individual FAME components of the JCO and WCO were identified by comparing their retention times with those of the GLC-10

reference standard. Figure 4.43 shows the gas chromatographs of the GLC-10 reference standard, JCO and WCO obtained from the GC-FID analysis.
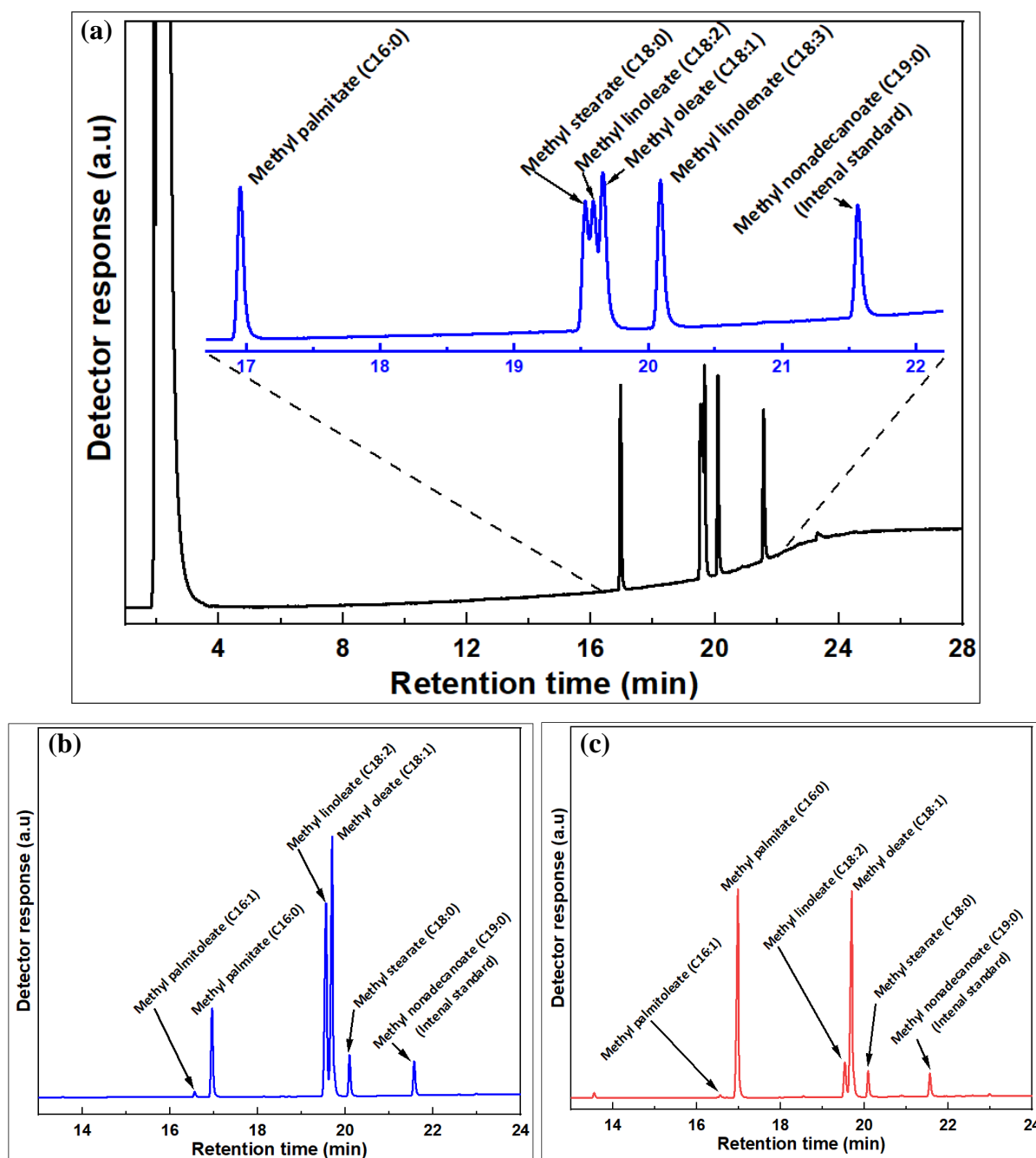
Figure 4.43; GC chromatographs of; (a). Supelco FAME mix GLC-10 reference standard, (b). *Jatropha curcas* oil, and (c). waste cooking oil.

The calibration curves used in the calculations of the GC-FID response factors are shown in Appendices 8-12. The RFs were calculated using the formula;

$$\text{Response factor (RF)} = \frac{\bar{A}_{p(i.s)} \times [r.s]}{\bar{A}_{p(r.s)} \times [i.s]} \tag{8}$$

where ($\bar{A}_{p(r.s)}$ is the average peak area of individual FAME in the reference standard, $\bar{A}_{p(i.s)}$ is the average peak area of the internal standard, [i.s] is the concentration of internal standard, while [r.s] is the concentration of reference standard (components of GLC-10).

On linearization of equation (8), the response factor is calculated using the formula;

$$RF = \frac{\bar{A}_{p(i.s)} \times [r.s]}{\bar{A}_{p(r.s)}} \times \frac{1}{[i.s]} \quad \equiv \quad y = mx + c \tag{9}$$

$$RF = (\text{slope} \times [i.s])^{-1} \tag{10}$$

Where slope $= \dfrac{\bar{A}_{p(r.s)}}{\bar{A}_{p(i.s)} \times [r.s]}$, i.e., slope of $\dfrac{\bar{A}_{p(r.s)}}{\bar{A}_{p(i.s)}}$ vs [r.s] curves in Appendices 8-12.

The calculated RFs for each FAME component of the GLC-10 reference standard are summarized in Table 4.18.

Table 4.18; GC-FID response factors for each FAME component of GLC-10 reference standard.

FAME	Retention time, R_t, (min)	Response Factor (RF)
Methyl palmitate (C16:0Me)	17.0	1.0122
Methyl stearate (C18:0Me)	19.5	1.2116
Methyl linoleate (C18:2Me)	19.6	1.2316
Methyl oleate (C18:1Me)	19.7	0.9053
Methyl linolenate (C18:3Me)	20.1	1.0202

4.7.2 Optimization of transesterification reaction

The $L_{16}(4^4)$ experimental design matrix used in the optimization study of transesterification of JCO and the response values (FAME yield (%)), S/N ratio and predicted FAME yield are shown in Table 4.19.

147

Table 4.19; The $L_{16}(4^4)$ experimental design matrix with FAME yield response values and S/N ratio.

Experiment trial	Reaction Temp (°C)	Reaction Time (h)	Cat. load (wt. %)	MeOH/Oil molar ratio	Avg FAME content (%)	Std Deviation	S/N ratio	Predicted FAME content (%)
1	50	0.5	0.5	5	3.95	0.04	11.92	2.51
2	50	2	2	10	8.80	0.08	18.89	10.45
3	50	5	4	15	46.76	0.17	33.40	47.79
4	50	8	8	20	65.09	0.29	36.27	68.87
5	60	0.5	2	15	10.24	0.26	20.20	14.01
6	60	2	0.5	20	3.31	0.19	10.35	4.33
7	60	5	8	5	55.03	0.57	34.81	56.68
8	60	8	4	10	61.25	0.59	35.74	54.80
9	70	0.5	4	20	56.59	0.32	35.05	58.25
10	70	2	8	15	64.40	0.03	36.20	58.10
11	70	5	0.5	10	5.77	0.18	15.21	9.54
12	70	8	2	5	10.17	0.06	20.14	11.20
13	80	0.5	8	10	67.55	0.71	36.59	68.59
14	80	2	4	5	35.70	0.53	31.05	39.48
15	80	5	2	20	27.97	0.27	28.93	21.51
16	80	8	0.5	15	4.86	0.26	13.71	6.52

The main effects plot for the means data and S/N ratios are shown in Figure 4.44. From both data mean and S/N ratio plots in Figure 4.44, it is evident that catalyst loading has the strongest influence on oil transesterification. A higher mean of the control factor is an indication of its stronger effect at that level on the FAME yield. The highest FAME yield was observed at catalyst loading of 8 %. It can also be seen that for the catalyst loading the increase in FAME yield was very steep as compared to other parameters where the extent of rise was very low. The ranking of parameters tested from the S/N ratio response in Table 4.20 also show that catalyst loading had the highest influence on the FAME yield followed by reaction time, methanol to oil molar ratio and finally the reaction temperature.
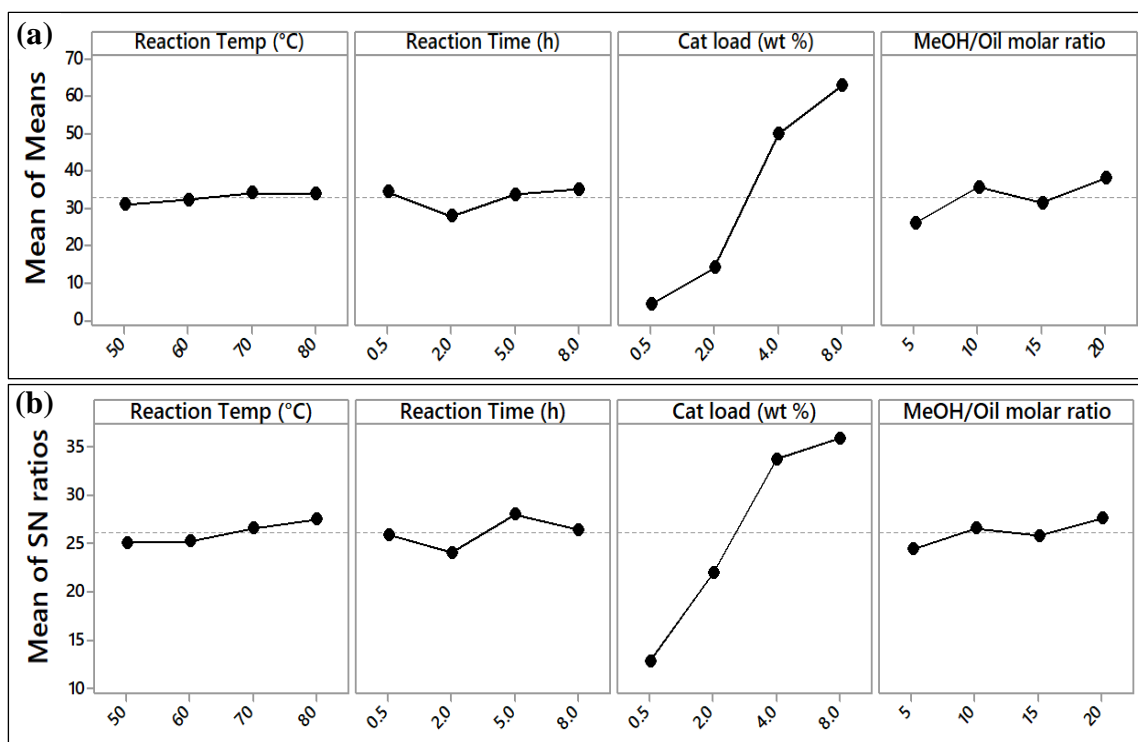
Figure 4.44; The main effects plot for (a). data mean, and (b). S/N ratios for the FAME yield.

Table 4.20; Response Table for Signal to Noise Ratios.

Level	Reaction Temp (°C)	Reaction Time (h)	Cat loading (wt. %)	Methanol/Oil molar ratio
1	25.12	25.94	12.80	24.48
2	25.28	24.12	22.04	26.61
3	26.65	28.09	33.81	25.88
4	27.57	26.47	35.97	27.65
Delta	2.45	3.96	23.17	3.17
Rank	4	2	1	3

Because 'larger is better' was selected in determination of optimum conditions, the highest points in the mean of S/N ratios plots, in Figure 4.44, were taken as the optimum conditions for the transesterification process. This would imply that 20:1, 8 % by mass, 80 °C and 5 hours are the optimum mole ratio of methanol:oil, catalyst loading, reaction temperature and reaction time, respectively. However, the slopes of temperature and methanol to oil molar ratio plots in Figure 4.44 are very low because of their low significance in the transesterification

149

process, see the rankings of the factors at the bottom of Table 4.20. In addition, the difference in the FAME yields when moving from 70 to 80 °C temperature and from 10:1 to 20:1 methanol:oil molar ratio is less than 1 % in both cases. Therefore, in this study, 70 °C and 10:1 was selected as the optimum temperature and methanol to oil molar ratio, respectively. Selection of lower temperature and molar ratio of materials could lower the cost of energy and materials in the production process without impacting on the transesterification efficiency. The optimum conditions for the transesterification reaction of oils were therefore found to be 10/1 as the mole ratio of methanol/oil, 8 % by mass as catalyst loading, 70 °C as the reaction temperature and 5 hours as the reaction time.

To test the accuracy of the chosen model, a plot of actual versus predicted yields was made. Figure 4.45 show a plot of experimental FAME yield vs predicted FAME yield.
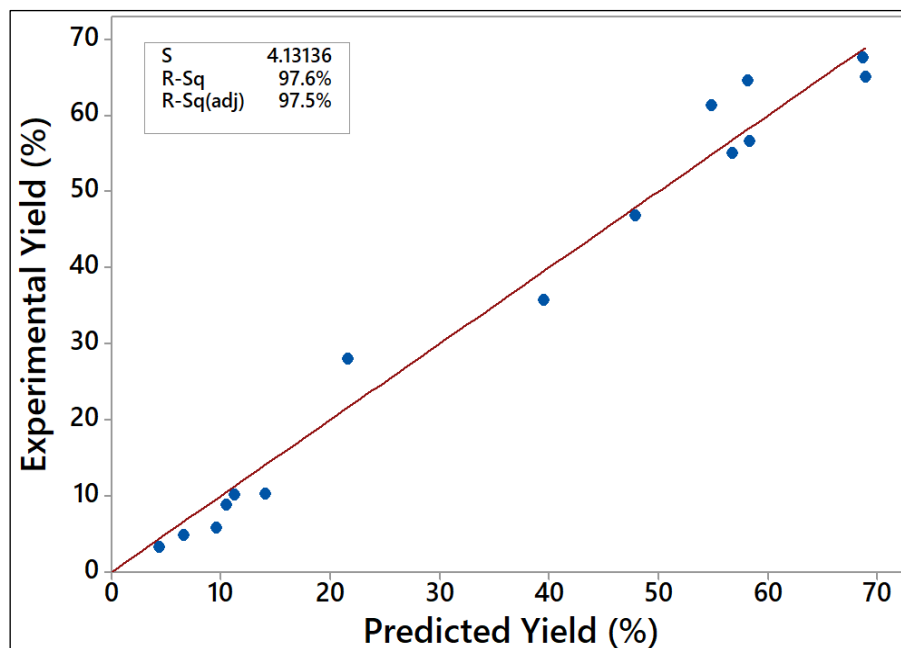
Figure 4.45; A plot of experimental FAME yield vs predicted FAME yield.

The closeness of points to the 45° regression line and high R^2 values show the model fits well the experimental data. The difference between the R^2 and adjusted R^2 values is also less than

the acceptable margin of 0.2 thereby indicating that the experimental data are therefore accurate (Olubunmi et al., 2020).

4.7.2.1 Analysis of variance (ANOVA)

The analysis of variance provides statistical parameters for analysis of the significance of every transesterification parameter and their impacts on the FAME yield. The Fischer's test (F-test) value denotes the significance of a particular experimental factor, a high F-test value is obtained when the experimental data fits well with the model chosen or when the noise is high (Dhawane et al., 2016). The high F-test value is verified by the probability value (P-value). P-value below 0.05 show that F-value is due to the well fit of the model and not due to noise.

ANOVA results are shown in Table 4.21. The contribution from the catalyst loading is more significant at 93.79 %, other factors; reaction time, methanol to oil molar ratio and reaction temperature have very low significance at 2.14 %, 1.43 % and 1.10 % respectively. The catalyst loading has the highest F-value (60.82) and the least P-value of 0.003), confirming its highest significance among the four actors considered. The model is therefore significant and can be used to optimize the transesterification of oils using Na-acetate modified zeolites as a catalyst.

Table 4.21; Analysis of Variance for SN ratios.

Source	DF	Seq SS	Adj SS	Adj MS	F	P	%SS
Reaction Temp (°C)	3	16.40	16.40	5.467	0.71	0.607	1.09807
Reaction Time (h)	3	32.02	32.02	10.674	1.39	0.397	2.143914
Cat load (wt. %)	3	1400.78	1400.78	466.927	60.82	0.003	93.78988
MeOH/Oil molar ratio	3	21.29	21.29	7.098	0.92	0.525	1.425482
Residual Error	3	23.03	23.03	7.678			1.541984
Total	**15**	**1493.53**					**100**

DF; Degrees of freedom, Seq SS: Sequential sum of squares , Adj SS: Adjusted sum of squares, Adj MS: Adjusted mean squares, F: Fischer's test value, P: Probability value, %SS: Percent sum of squares

4.7.3 Characterization of JCO, WCO and transesterification product

In order to investigate the vibrational characteristics and determine the functional groups of the oils and their derived biodiesel products, FTIR spectroscopy was performed on JCO, WCO and their respective biodiesel and glycerol products. The FTIR spectra of the oils and their derived products are shown in Figure 4.46. The spectra of JCO and WCO and their products are the same. Besides, in the formation of biodiesel, glycerol backbone of the triglyceride (of the oil) is removed and replaced by the light weight methanol in the hydrocarbon chain. As shown in Figure 4.46, the FTIR spectra of the oil is therefore expected to be largely similar to that of biodiesel (FAMEs). The small differences are however observed in region between 400-1500 cm^{-1}. According to (Rafati et al., 2019), the observed bands at 1198 and 1435 cm^{-1} in the biodiesel spectra (which are missing in the triglyceride spectra) are associated with the bending and stretching vibrations of $–OCH_3$ group. In addition, the band at 1160 cm^{-1} for the triglyceride, corresponding to the stretching vibration of the C-O group attached to $–CH_2$ of the glycerol backbone, slightly shifts to the peak at 1167 cm^{-1} for the FAMEs, corresponding to the stretching vibration of C-O group attached to $–CH_3$ of the introduced methanol.

The observed spectral bands were assigned as follows; the broad band at 3320 and 1568 cm^{-1} (-OH stretching vibration), 3009 cm^{-1} (unsaturated carbon chain =C-H stretching vibration), bands at 2918 cm^{-1} and 2850 cm^{-1} (saturated carbon chain $-CH_2$ symmetrical and asymmetrical stretching vibration), 1744 cm^{-1} (-C=O stretching vibration), 1463 cm^{-1} and 1378 cm^{-1} (bending vibration of $-CH_2$ and $-CH_3$, respectively), 1223, 1160 and 1095 cm^{-1} (-C-O stretching vibrations) and the band at 722 cm^{-1} (cis –CH=CH– out of plane bending vibrations) (Lerma-García et al., 2010). The absence of the -OH bands in triglyceride and biodiesel spectra indicates the lack of, corresponding to OH group, indicates the lack of mono and diglycerides as well as unreacted glycerol and methanol in the oils and biodiesel (Rafati et al., 2019).
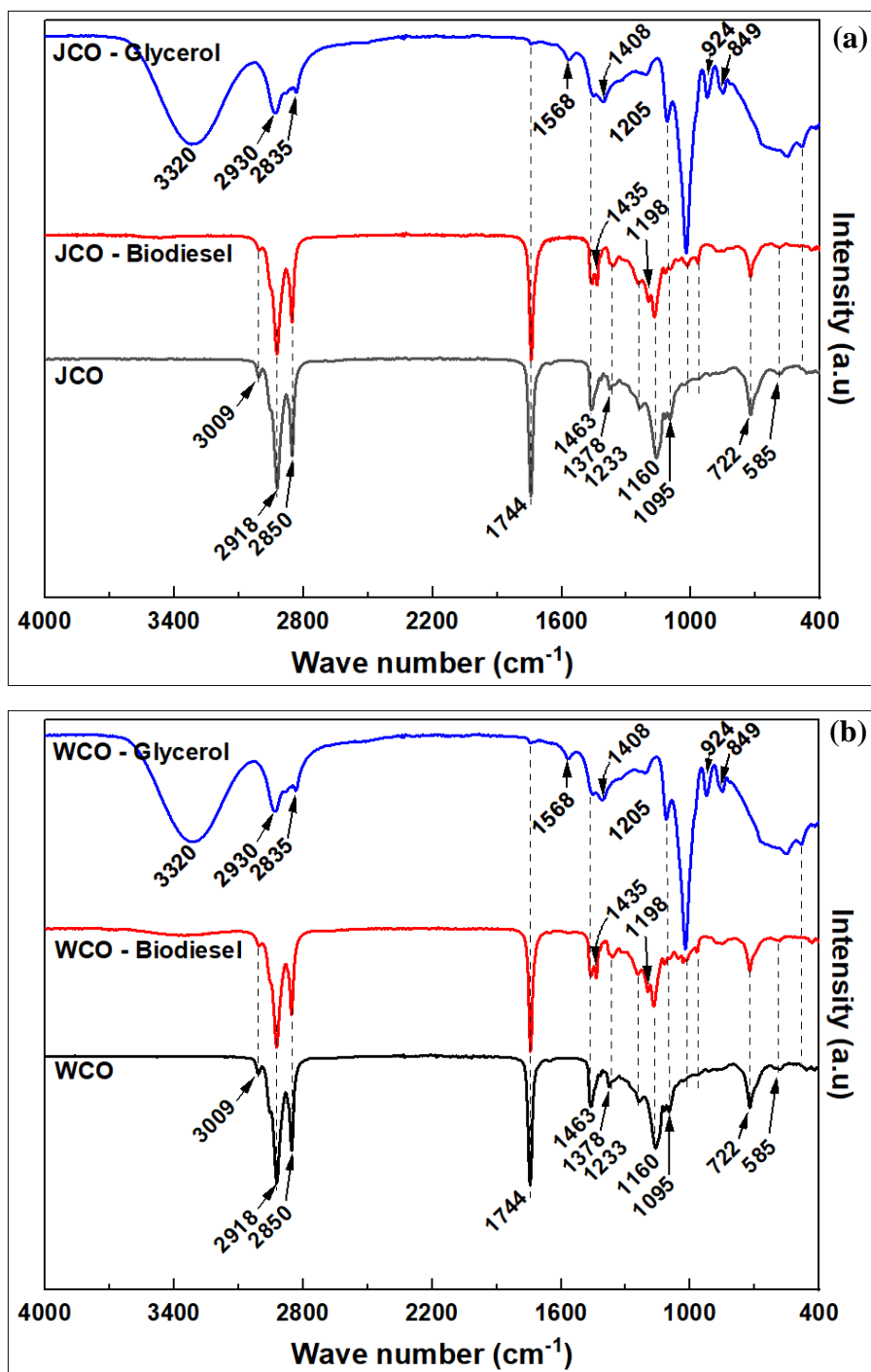
Figure 4.46; FTIR analysis of oils and the derived biodiesel and glycerol product; (a). JCO, and (b). WCO.

To investigate the thermal properties and to check the organic purity of the oils, TGA analysis were performed on JCO and WCO. Figure 4.47 shows the TGA analysis curves for JCO and WCO.
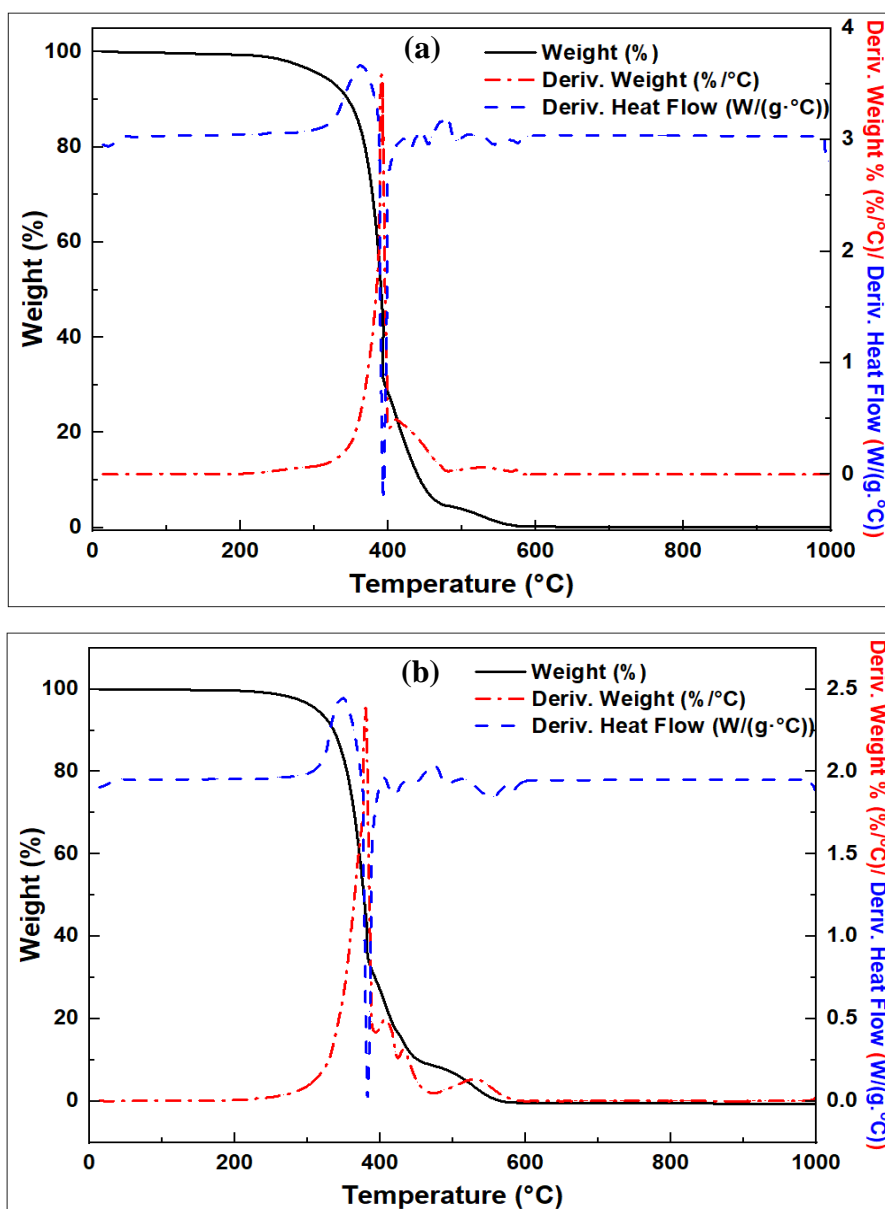
Figure 4.47; TGA analysis of oils; (a). JCO, and (b). WCO.

Three stages of wight loss for the oils due to carbonization and subsequent burning off of the carbon was observed in in both cases. The 100 % weight loss for both JCO and WCO implies that inorganic impurities in WCO were successfully removed during its cleaning and that both oils were purely organic without inorganic components. The individual fatty acid constituents (FAME content) of JCO and WCO, which were identified in their respective GC chromatographs in Figure 4.43(b & c), were calculated using the formula;

$$FAME = [i.s] \times A_{p(ME)} \times RF_{ME}/A_{p(i.s)} \tag{11}$$

Where; FAME = Fatty acid methyl ester content of individual fatty acid

$A_{p(ME)}$ = Peak area of the individual methyl ester in the sample

RF_{ME} = Response factor of the respective reference standard, calculated in

Table 4.18

The calculated fatty acid composition of JCO and WCO are summarized in Table 4.22. The FAME composition of JCO oil and WCO are different with the major contents of JCO being methyl linoleate and methyl oleate while those of WCO were methyl palmitate and methyl oleate. However, the composition of individual oils was consistent with those reported in literature, (Abbaszadeh-Mayvan et al., 2018; Ewunie et al., 2021; Singh et al., 2021).

Table 4.22; Summary of individual FAME constituents of the JCO and WCO.

FAME	Composition (%)	
	Jatropha curcas	Waste cooking
Methyl palmitate (C16:0Me)	13.7	41.7
Methyl stearate (C18:0Me)	6.3	5.1
Methyl oleate (C18:1Me)	37.2	38.7
Methyl linoleate (C18:2Me)	41.2	8.8
Others	1.6	5.7
Total	**100**	**100**

4.7.4 FAME Yields from batch transesterification using optimal conditions

Batch transesterification reactions of JCO and WCO using optimum conditions obtained in section 4.7.2, that is; methanol:oil molar ratio of 10:1, catalyst loading of 8 %, reaction temperature of 70 °C and reaction time of 5 h was performed with various developed catalysts. The total FAME yield (%) from individual batch reaction was calculated using the formula in equation (6). The FAMEs yield from various batch transesterification reactions are summarized in Table 4.23.

Table 4.23; Summary of biodiesel yields obtained using optimum transesterification conditions with various prepared catalysts.

Catalyst			FAME Yield (%)	
Code	Type	Oil Type	1st	2nd
KOH – JCO	Homogeneous - KOH	JCO	91.56 ± 1.10	
KOH – WCO	Homogeneous - KOH	WCO	89.21 ± 0.53	
Act/Kaolin	Kaolin	JCO	13.40 ± 0.25	
Act/MK	Metakaolinite	JCO	11.96 ± 0.05	
Act/F-MK	Fused-metakaolinite	JCO	15.47 ± 0.21	
Act/Zeolite 3A	Molecular sieve Na-A	JCO	34.81 ± 2.64	
Act/Zeolite 13X	Molecular sieve 13-X	JCO	75.03 ± 0.77	
Act/Zeolite Y	Commercial Na-Y	JCO	46.08 ± 0.17	
Act/SA-MK-48h	Na-A	JCO	32.36 ± 0.31	
*SX-a-FM-48h	Na-X	JCO	16.78 ± 0.35	
Act/SX-a-FM-48h	Na-X	JCO	83.63 ± 0.89	80.12 ± 1.04
Act/SX-a-FM-48h	Na-X	WCO	79.25 ± 1.35	
Act/SX-a-FM-96h	Na-X	JCO	82.66 ± 0.21	
Act/SX-a-FM-168h	Na-X	JCO	79.07 ± 0.26	
Act/SX-b-FM-48h	Na-X	JCO	20.04 ± 0.21	
Act/SX-c-FM-48h	Na-X	JCO	87.41 ± 0.05	86.54 ± 0.43
Act/SX-c-FM-48h	Na-X	WCO	89.98 ± 0.51	
Act/FSY-c-FM-48h	Na-X	JCO	55.04 ± 0.33	
Act/MSX-a-FM/FF-48h	Na-X	JCO	79.12 ± 1.20	77.40 ± 0.06
Act/MSX-a-FM/FF-48h	Na-X	WCO	83.45 ± 0.79	
Act/MSX-b-FM/FF-48h	Na-X	JCO	77.51 ± 0.99	
Act/MSX-c-FM/FF-10h	Na-X	JCO	79.12 ± 1.20	
Act/MSX-c-FM/FF-48h	Na-X	JCO	93.94 ± 0.25	91.37 ± 0.62
Act/MSX-c-FM/FF-48h	Na-X	WCO	91.07 ± 1.21	
Act/MSX-c-FM/FF-72h	Na-X	JCO	87.84 ± 2.67	
Act/MSY-a-FM/PF-48h	Na-Y	JCO	18.34 ± 0.05	
Act/MSY-b-FM/PF-48h	Na-Y	JCO	19.73 ± 0.02	
Act/MSY-c-FM/PF-48h	Na-Y	JCO	20.05 ± 0.24	18.86 ± 0.54
Act/SZ1-c-FVA-10h	Na-X	JCO	92.82 ± 1.92	89.08 ± 0.85
Act/SZ1-c-FVA-48h	Na-X	JCO	82.02 ± 0.60	
Act/SZ2-c-FVA-48h	Na-P & Na-X	JCO	42.43 ± 0.16	
Act/SZ3-c-FVA-48h	Na-HS	JCO	70.05 ± 0.23	
Act/KoVo-c-FM-48h	Na-P & Na-X	JCO	54.43 ± 0.86	
Act/Nat-SA-10%A	Clinoptilolite	JCO	95.54 ± 1.54	
Act/Nat-SA-10%A	Clinoptilolite	WCO	92.62 ± 0.95	

 * SX-a-FM-48h: Zeolite was used as synthesized without modification

The catalytic conversion of oils using homogeneous KOH catalyst was performed to act as a bench mark for the subsequent heterogenous catalysis. The FAMEs yield under homogeneous transesterification was high at 91.56 and 89.21 % for the conversion of JCO and WCO, respectively (Table 4.23). The catalytic conversion of oils using raw kaolin, MK and F-MK , without converting them to zeolites, as well as using unmodified zeolites (*SX-a-FM-48h) are very low at 13.40 %, 11.96 %, 15.47 % and 16.78 %, respectively, see Table 4.23. Their conversions to zeolite products before use is therefore justified. The performance of both JCO and WCO in terms of their conversions to biodiesel was fairly the same.

The Na occluded natural zeolite clinoptilolite and zeolite-X generally performed better than other zeolite types. In addition, zeolites synthesized via wet mixing of kaolin with NaOH before dry fusion recorded better FAME yields (see -c- coded zeolites in Table 4.23) compared to other zeolites obtained via other kaolin pre-treatment methods. The performance of the synthesized zeolite types was in the order; natural clinoptilolite, Na-X, hydroxysodalite (Na-HS), Na-Y, Na-P & Na-X mixture and lastly Na-A. Among the synthetic zeolites, Na-X related zeolite (MSX-c-FM/FF-48h) recorded the highest yield at 93.94 % while Na-A related zeolite (SA-MK-48h) recorded the least yield at 32.36 %. The highest yields for each zeolite type were however higher than their commercial zeolite analogues.

Although the choice of kaolin pre-treatment method with NaOH before fusion directly impacted on the surface properties, such impact was not observed in terms of zeolite transesterification performances. For example, wet mixing followed by dry fusion of kaolin resulted in zeolites MSX-c-FM/FF-48h, SX-c-FM-48h and SZ1-c-FVA-48h which showed very high surface area and pore properties as were observed in Table 4.8, 4.10 and 4.13. The same was however not duplicated by the zeolite FSY-c-FM-48h (Na-Y) which recorded just 55.04 % conversion. In addition, SZ3-c-FVA-48h (Na-HS) which showed very low surface area and pore properties in Table 4.13 recorded fairly good biodiesel conversion at 70.05 %.

The performance of zeolites does not therefore depend on the surface area and porosity of zeolites but rather on the alumina content of the zeolite catalyst. Hydrophilic catalysts with high Al/Si content performed better than the hydrophobic catalysts with high SiO_2/Al_2O_3 content. This might be because the higher the Al in the zeolite structure the higher the Na ions occluded in the structure, and thus the higher the active catalytic sites for the zeolite. The surface area and porosity analysis of the modified zeolite in Table 4.17 also showed significant reduction of surface area and porosity, yet their catalytic conversions to biodiesel was high. The high conversion would only imply that most of catalytic activity of the zeolite catalysts are taking place on the surface of the catalyst and not on the blocked pore structure.

Other properties of the derived biodiesel in comparison with the European Norm (EN-14214:2008, 2009) are shown in Table 4.24.

Table 4.24; Properties of JCO and the derived biodiesel in comparison with the EN-14214 standard.

Property	*Jatropha curcas* oil	Biodiesel	EU biodiesel specifications (EN-14214:2008, 2009)
Ester content (wt. %)	93.9	-	96.5
Density (g/ml)	0.91	0.86	0.86-0.90
Kinematic viscosity (mm^2/s)	39.63	3.05	3.5-5.0
Iodine value (g I$_2$/100g)	105.01	101.00	≤ 120
Acid value (mg KOH/g)	4.86	0.50	≤ 0.50
Saponification value (mg KOH/g)	175.00	n.d[*]	-
Linolenic acid methyl ester (wt. %)		≤ 1.6	12.0

[*]n.d = not done

There is a significant decrease in important properties of viscosity and acid value of the transesterification product to values within biodiesel specifications. The properties tested for the JCO are also consistent with the properties which have been reported in literature (Kibuge et al., 2015; Singh et al., 2021). Except for the ester (FAME) content, all the other tested

parameters were within the biodiesel specifications. This shows that zeolites derived from less expensive natural clay minerals and volcanic ash are promising catalysts for the transesterification of non-edible plant oils with high free fatty acids such as JCO and WCO. The low ester content of synthesized biodiesel (93.94 %) in the present study, with reference to biodiesel specification in Table 4.24, might be an indication of more catalyst load (wt. %) required for the complete conversion within the shortest reaction time. This is can also be seen by the steep catalyst loading curve in the mean data and S/N ratio plots in Figure 4.44. It may also signify the need to fine tune the zeolites further to increase their catalytic surface area where transesterification reactions are taking place.

4.7.4.1 Regeneration of zeolite catalysts

Regeneration study for the selected zeolite catalysts was performed by washing the zeolite catalysts used in the transesterification of JCO with heptane six times. The washed catalyst was dried at 100 °C for 12 h before calcining at 500 °C at similar conditions described above. Such a catalyst when tested showed very small loss in activity in the second reuse of the catalysts, see Table 4.23. The zeolite catalysts obtained in this study are therefore suitable for use in multiple catalytic transesterification activity for the JCO.

CHAPTER 5

SUMMARIES, CONCLUSIONS AND RECOMMENDATIONS

5.1   Summaries

The clay material consists of SiO_2 at 56.74 %, Al_2O_3 at 30.34 % and trace oxides of Na, Ti, Fe, Cu and K. The SiO_2 is in the form of kaolinite mineral at 35.71 % and quartz phase at 21.03 %. All the kaolin bands and peaks except those for quartz phase were eliminated by heating the clay at high temperature of 750 °C. The quartz phase was however, eliminated by fusing clay with NaOH where new FTIR bands and XRD peaks were formed in the lower wave numbers and higher 2 θ values, respectively. Raw clay is thermally stable up to 400 °C with subsequent exothermic weight loss of 10.49 % at 500 °C occurring in a single step during dehydroxylation reaction. In contrast, the dried wet mix of clay with NaOH had multiple steps of weight loss. The kaolin material exhibits a type II adsorption isotherm with a type H3 hysteresis and porosity at 14.8 Å.

Raw volcanic ash (KVA) consists of CaO at 47.09 %, in the form of calcite polymorph, and SiO_2 at 18.38 %. A total of 33 % of its weight is lost on ignition (LOI). Other oxides of Al, Ti, Fe, K, Cu and Ca are also present in trace amounts. Calcite is, however, eliminated by washing the KVA with 10 % HCl, resulting in > 99 % amorphous silica and traces of quartz phase. Raw volcanic ash is thermally stable up to 620 °C where a total of 33 % of weight loss (LOI) occurs between 620-815 °C with the integral peak at 790 °C. On the other hand, only 3 % weight loss, due to small quantity of absorbed water occur for the acid-washed volcanic ash.

In the synthesis of zeolites in protocol 1, FAU and LTA zeolites of high crystallinity are synthesized from kaolin material. For gels of the same chemical composition and under identical synthesis conditions, the resulting zeolite type depended on the pre-treatment method, namely MK or F-MK, which was applied to kaolin material prior to the hydrothermal

crystallization step. Both zeolites Na-A and Na-X were obtained separately within 8 h of crystallization in the MK and F-MK methods respectively. The hydrothermal crystallization time required for the preparation of FAU zeolites from kaolin was significantly reduced when the fusion route was followed. At lower SiO_2/Al_2O_3 of the synthesis hydrogel, i.e., when kaolin was used without additional silica, apart from the drop in crystallinity to less than 70 % after 120 h for the Na-A obtained in MK method, no phase change was observed even after 168 h of reaction. On the other hand, HS impurity was formed beyond 48 h of reaction in the F-MK method. At elevated SiO_2/Al_2O_3 of the synthesis hydrogel, i.e., when additional fumed silica was used, a mixture of zeolite products (Na-X, Na–P, analcime) were obtained in the MK method, while Na-Y was the dominant phase in the product obtained in the F-MK method.

Besides, zeolites obtained through F-MK hydrogels in protocol 1 showed high surface area, micropore surface area, micropore volume and pore size. The Na-Y (FSY-a-FM-48h) zeolite obtained from modified F-MK hydrogels had the highest BET surface area, micropore surface area and micropore volume at 599 m^2/g, 445 m^2/g and 0.18 cm^3/g, respectively. On the other hand, the zeolites obtained through MK hydrogels had very low sorption properties. Increasing the crystallization time from 48 h to 120 h for the Na-Y zeolite in the modified hydrogel of protocol 1b led to a decrease in the surface area and the pore volume from 599 to 473 m^2/g and 0.18 to 0.15 cm^3/g respectively. However, the zeolite median pore width remained constant at 0.99 nm.

In the synthesis of faujasite zeolites in protocol 2, the resulting zeolite structure not only depended on the hydrogel composition and the synthesis conditions but also on the fusion conditions, i.e., the amount of NaOH used in the fusion step. Two sets of products were obtained depending on the protocol used in the pre-treatment of the kaolin material. For hydrogels with the same concentrations of starting materials, partial fusion of the kaolin,

involving limited quantities of NaOH led to the formation of zeolite Na-Y, while full fusion led to the formation of zeolite Na-X. The resulting zeolite type depended on the nature of the silica and alumina components of the synthesis hydrogel. Various pre-treatment procedures on kaolin did not affect the zeolite Na-Y products obtained in the partial fusion protocol. The influence of pre-treatment procedures on kaolin before fusion step on the nature of zeolite products was however observed in the full fusion protocol. Wet mixing followed by wet fusion results in undesired reactions that lead to the undesirable formation of hydroxysodalites as impurities in Na-X and Na-Y products. Dry mixing, on the other hand, results in a non-uniform mixture leading to the formation of zeolite Na-X alongside zeolite Na-A as an impurity. The best pre-treatment method was wet mixing of kaolin followed by removal of the solvent via drying before the fusion step, which resulted in high quality Na-X and Na-Y zeolites with textural properties comparable to those of commercially available zeolite. Both NaOH concentration in the fusion step and crystallization time did not affect the SiO_2/Al_2O_3 molar ratio of the resulting products. The ratio was however affected by the mode of kaolin pre-treatment with NaOH.

Except for the wet fusion product in the full fusion method, all protocol 2 products exhibited a reversible type I isotherm for microporous adsorbents. The wet fusion products, in both partial fusion and full fusion protocols, had the least specific surface area, micropore surface area and pore volume. On the other hand, the products obtained in wet mixing of kaolin with NaOH before dry fusion in the full fusion protocol had the highest specific surface area, micropore surface area and pore volume which are comparable with those of their commercial analogues.

In the synthesis of faujasite zeolites using calcined acid-washed volcanic ash and sodium aluminate as a starting material in protocol 3, the resulting product depended on the SiO_2 and Na_2O content of the synthesis hydrogel. Low silica hydrogel resulted in either pure Na-X or

162

pure hydroxysodalite while high SiO_2 content resulted in a mixture of Na-X and Na-P zeolites. For the low SiO_2 hydrogel, low Na_2O content in the hydrogel resulted in pure hydroxysodalite while high Na_2O content in the hydrogel resulted in pure Na-X zeolite. The silicon and aluminium oxide composition of the products is not dictated by the synthesis hydrogel composition but rather by the resulting products types. In addition, the conversion of the raw materials to hydroxysodalite is enhanced with increased crystallization time, leading to a corresponding improvement in the product properties.

Except for the Na-X and Na-P zeolite mixture obtained from a hydrogel prepared using acid-washed volcanic ash and fused-metakaolinite, all other products in protocol 3 exhibited a reversible type I isotherms. The Na-X and Na-P zeolite mixture (i.e., SZ2-c-FVA-48h and KoVo-c-FM-48h) had the least specific surface area and micropore volume. On the other hand, pure Na-X product (i.e., SZ1-c-FVA-48h) had the highest specific surface area, micropore surface area and pore volume which are comparable with those of commercial molecular sieve 13X. All zeolite products synthesized in protocol 3 were also thermally stable at least up to 800 °C. A single step weight loss was observed for the Na-X zeolite of SZ1-c-FVA-48h and hydroxysodalite of SZ3-c-FVA-48h products, accompanied with up to 23 % and 11 % weight loss, respectively. On the other hand, a multi-step weight loss, accompanied with 18 % weight loss, was observed for the SZ2-c-FVA-48h and KaVo-c-FM-48h products.

In the analysis of natural zeolites, both raw and acid-washed natural zeolites were confirmed by the FTIR and XRD analysis to be of clinoptilolite (HEU) type. The clinoptilolite zeolites exhibited high crystallinity alongside some unidentified phases. The raw natural zeolite had a high SiO_2/Al_2O_3 molar ratio of 10 which was further increased to 12 by washing the raw clinoptilolite zeolite with 10 % HCl solution. Four steps of weight loss were observed for the Nat-SA-Pristine zeolite. On the other hand, three steps of weight loss were observed for the

Nat-SA-10%A zeolite. Approximately 10 % of weight loss was observed in both cases. In addition, the decomposition of clinoptilolite zeolites and structural changes took place at temperature between 900-1000 °C.

In the modification of zeolites, apart from the reduction in XRD intensities for the modified zeolite, the FTIR, XRD and SEM analysis showed that there was no change in functional groups, crystallinity as well as crystallite structures of zeolites impregnated with sodium acetate. It however, resulted in the reduction in intensity of the zeolites peaks. Zeolite crystallinity was maintained even after its first use in the transesterification reactions. Analysis of chemical composition of the modified zeolites also showed that Na ions were successfully incorporated into the modified zeolite structure. Modification of zeolites however, resulted in significant reduction in BET and micropore surface area from 473.34 and 428.80 m^2/g to 38.92 and 0.58 m^2/g, respectively. A two-step weight loss was also observed in the TGA analysis of the modified zeolites. Besides, a significant reduction in weight loss, due to absorbed water, was observed for the modified zeolites.

In the transesterification of JCO and WCO to biodiesel, Using the Taguchi $L_{16}(4^4)$ experimental design approach, the optimum conditions for the transesterification reaction of JC oil were found to be 10/1 as the mole ratio of methanol/oil, 8 % by mass as catalyst loading, 70 °C as the reaction temperature and 5 hours as the reaction time. Besides, based on ANOVA the contribution from the catalyst loading was more significant at 93.79 %, other factors, namely; reaction time, methanol to oil molar ratio and reaction temperature had very low significance in the reaction at 2.14 %, 1.43 % and 1.10 % respectively. The best separation of FAME components of GLC-10 reference standard was achieved from the optimized GC-FID conditions. In addition, varying response factors were obtained for the different FAME components of GLC-10 reference standard. The FAME composition of JCO oil and WCO are different. The major contents of JCO were methyl linoleate and methyl oleate while those of

164

WCO were methyl palmitate and methyl oleate. The catalytic conversion of oils using raw kaolin, MK and F-MK materials, without converting them to zeolites, as well as using unmodified zeolites are very low at low at 13.40 %, 11.96 %, 15.47 % and 16.78 %, respectively.

The Na occluded natural zeolite clinoptilolite and zeolite-X performed slightly better than other zeolite types. The yields for each zeolite type were higher than their commercial zeolites analogues. In addition, zeolites Na-X performed better than other zeolite types. Zeolites synthesized via wet mixing of kaolin with NaOH before dry fusion recorded better FAME yields compared to other synthesized zeolites. The performance of the synthesized zeolite types was in the order; natural clinoptilolite, Na-X, Na-HS, Na-Y, Na-P & Na-X mixture and lastly Na-A.

5.2   Conclusions

Analysis of materials used in this study have shown that the clay material was of kaolin type but having high quartz levels at 21.03 %. Raw Kenyan volcanic ash, on the other hand, consist of silica (SiO_2) and calcite ($CaCO_3$) at 18.38 and 47.08 %, respectively. The volcanic ash can be used as pure silica when calcite is removed by simple treatment of the raw volcanic ash with 10% HCl acid solution.

The findings from the study have shown that a variety of quality and pure zeolite products can be obtained from the abundant and inexpensive natural aluminosilicate resources such as kaolin and volcanic ash by choice of either the fusion or metakaolinization routes and by selecting the right synthesis hydrogel composition with no change in hydrothermal synthesis conditions.

Various pre-treatment conditions have also been studied and the best pre-treatment method was found to be the one where wet mixing of kaolin followed by removal of the water solvent via drying at 100 °C before the fusion step is performed. This operation results in production of quality Na-X, Na-Y/ Na-HS zeolites having properties comparable to those of commercially available zeolites. This study has therefore identified synthesis protocols that enable use of sustainable and less expensive kaolin and volcanic ash as a raw material for the production of pure and high-quality zeolite materials.

Functionalization of zeolites via wet Na^+ ion impregnation using CH_3COONa with subsequent activation by heat at 500 °C did not destroy the zeolite crystallite structures, instead, it resulted into significant increase in Na_2O content of modified zeolite. In addition, functionalization was found to be important because it resulted into zeolites with high catalytic activities.

Transesterification parameters using kaolin and volcanic ash derived zeolite catalysts were successfully optimized via Taguchi method. The best conditions for the transesterification reaction of the oils were found to be 10/1 as the mole ratio of methanol/oil, 8 % by mass as catalyst loading, 70 °C as the reaction temperature and 5 hours as the reaction time. Besides, the catalyst loading was the most significant factor affecting the transesterification process at 93.79 %.

Under optimized conditions, both modified natural and synthetic zeolites exhibited high catalytic performance; natural zeolite clinoptilolite and synthetic zeolite Na-X showed FAME conversions of 95.54 and 93.94 %, respectively. The FAME yields were higher than those of commercial zeolites equivalents (for example, 93.94% for Act/MSX-c-FM/FF-48h (Na-X) against 75.03 % for molecular sieve 13X), unmodified zeolites and raw materials.

5.3 Recommendations

The importance of performing metakaolinization versus fused-metakaolinization as well as the crucial role of NaOH content in the fusion of kaolin in the zeolite synthesis has been shown. Zeolites derived from clay and volcanic ash as alternative sources of aluminosilicates are therefore promising catalysts for the biodiesel synthesis from non-edible plant oils.

The use of kaolin clay and volcanic ash as sustainable aluminosilicates for the synthesis of zeolites is recommend. This is because high quality zeolites are obtained from abundant and less expensive natural aluminosilicate resources such as kaolin and volcanic ash. A variety of quality zeolites are achievable via the method of fusion or metakaolinization routes using natural kaolin or volcanic ash materials. MK method is recommended for the production of zeolite Na-A, while fusion method is recommended for FAU zeolites.

Efficient pre-treatment method allows for the complete conversion of kaolin into suitable ingredients before the hydrothermal crystallization step. Pre-treatment by wet mixing of kaolin or volcanic ash with NaOH before dry fusing the mixture and subsequent hydrothermal crystallization is recommended because it results into pure zeolite Na-X, Na-Y or Na-HS with high surface and pore properties comparable to commercial zeolites.

Modification of zeolites via wet Na^+ ion impregnation and activation by heat at 500 °C is recommended as it retains zeolite crystallites and functional groups while giving high catalytic conversion of oils to biodiesel. In addition, among the zeolites used, zeolites Na-X and natural zeolite clinoptilolite are more suitable catalysts and are therefore recommended for use in the transesterification reactions because they lead to high FAME conversion.

A study to determine the sustainability and cost of producing biodiesel from renewable biomass sources and catalyzed by zeolites obtained from natural materials is recommended. The data will inform on viability of starting business of biodiesel production.

5.4   Suggestions for future research

The wet mixing followed by dry fusion method of kaolin pretreatment in the zeolites synthesis should be investigated further using other sources of kaolin and other types of natural aluminosilicates and the results compared to what have been reported.

More work should be done on zeolites synthesis using purely a mixture of kaolin and volcanic ash as sources of aluminosilicates (without additional materials). This will lead to zeolites being formed purely from natural materials.

Other cation other than Na^+ ion should be investigated in the modification of developed zeolites in order to compare their resulting catalytic activities with the reported data.

Further optimization of catalyst loading should be carried out because it was the most significant factor in the transesterification process.
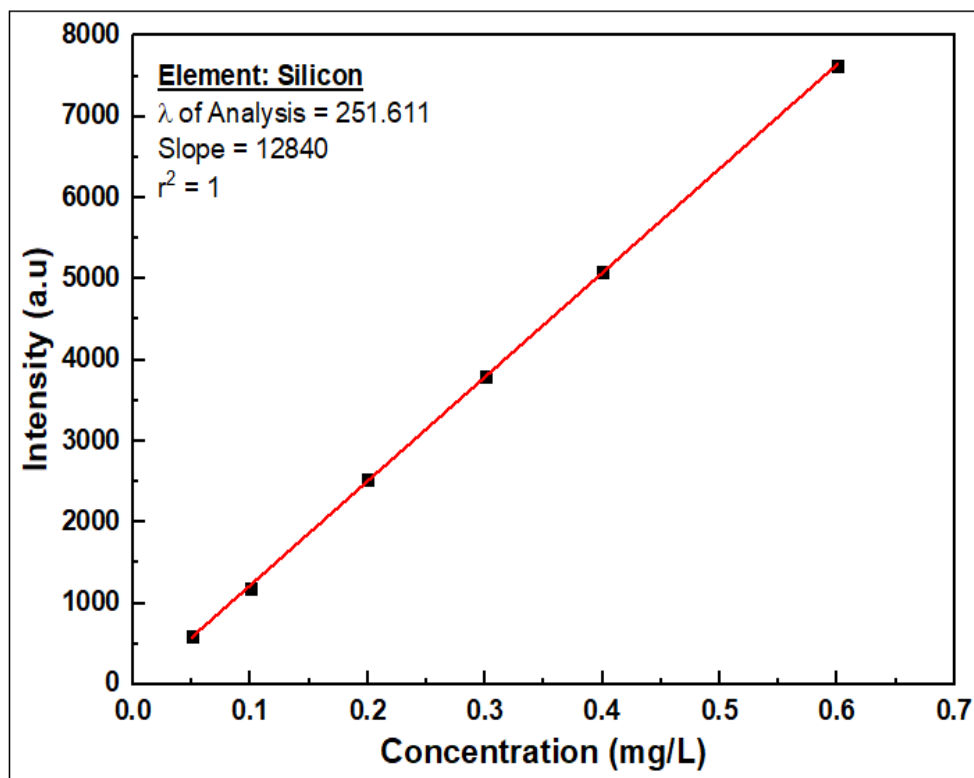
Appendix 1; ICP-OES Calibration curve for analysis of silicon (Si) elemental
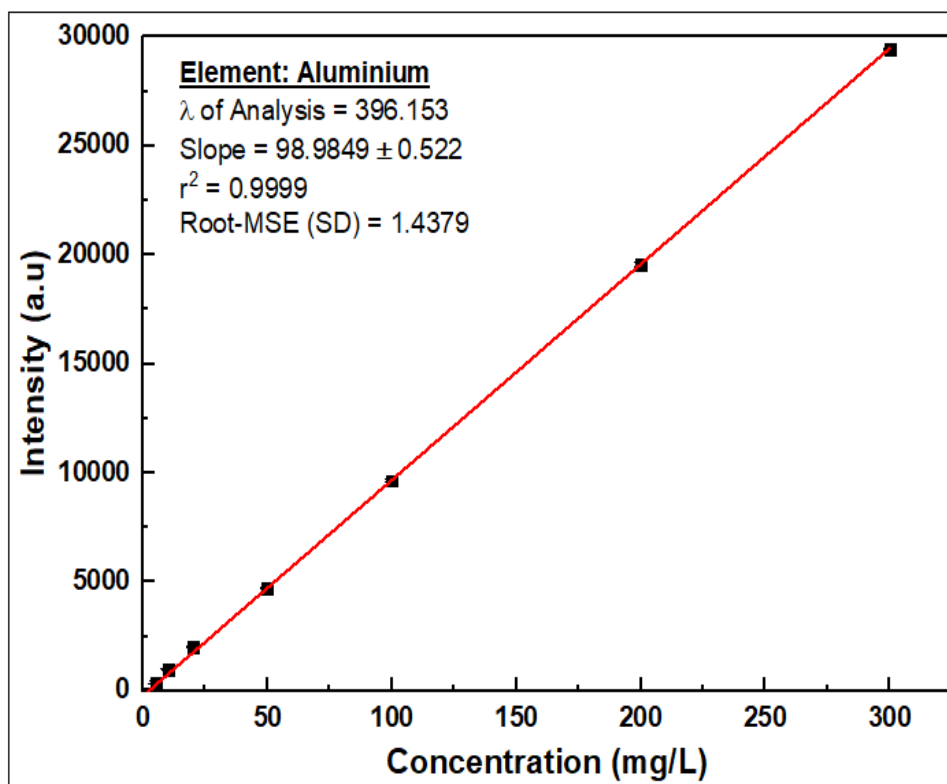
Appendix 2; ICP-OES Calibration curve for analysis of aluminium (Al) elemental
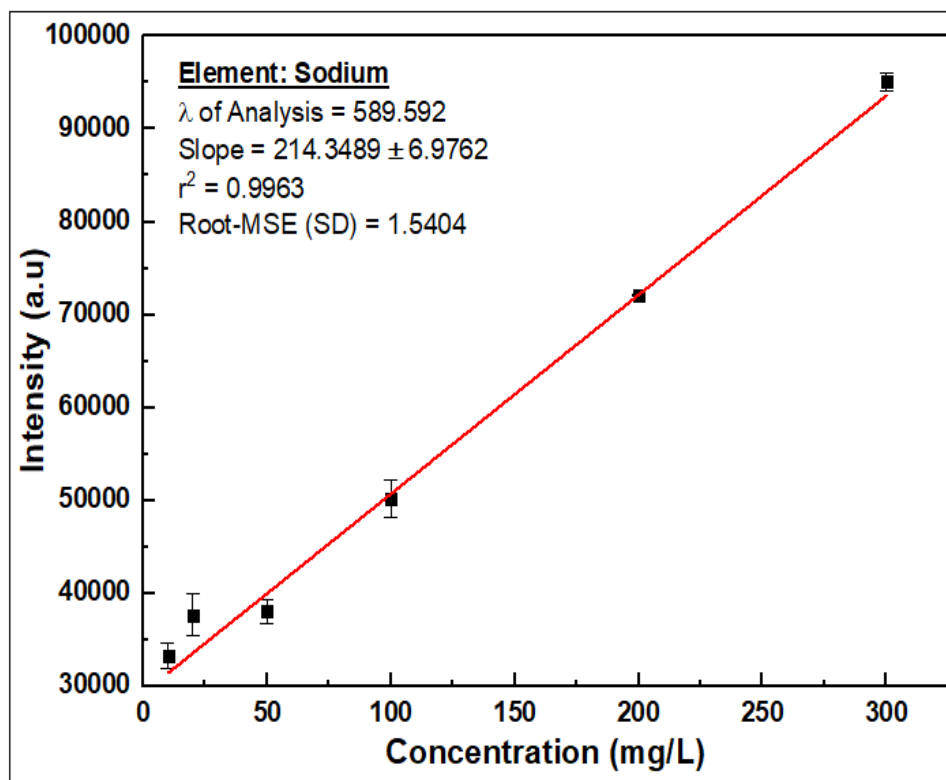
Appendix 3; ICP-OES Calibration curve for analysis of sodium (Na) elemental
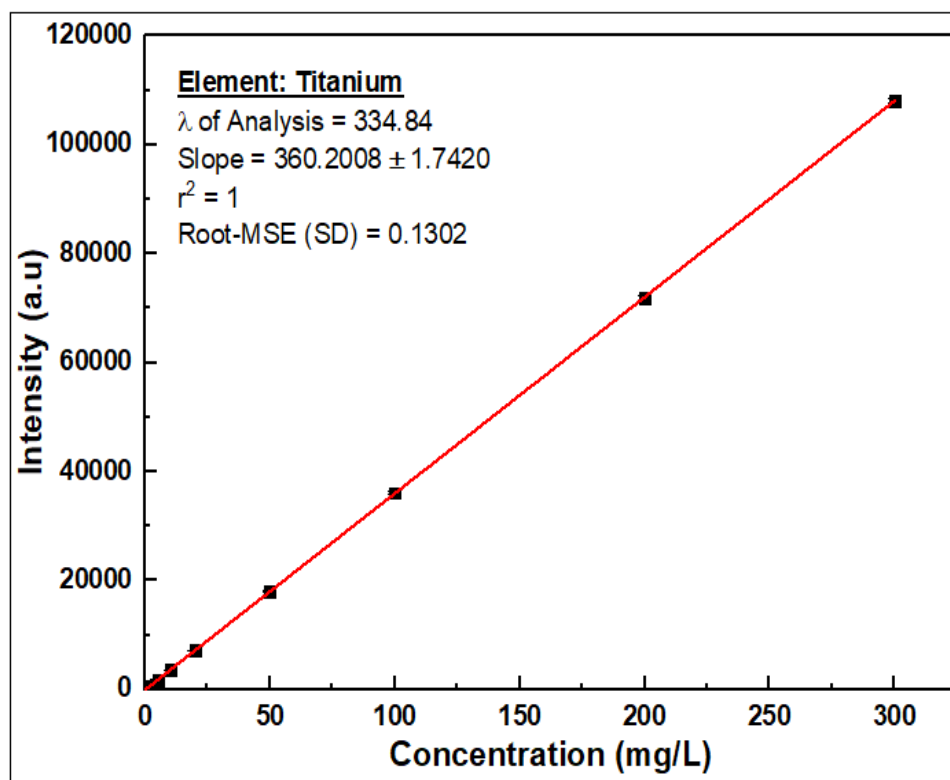
Appendix 4; ICP-OES Calibration curve for analysis of titanium (Ti) elemental
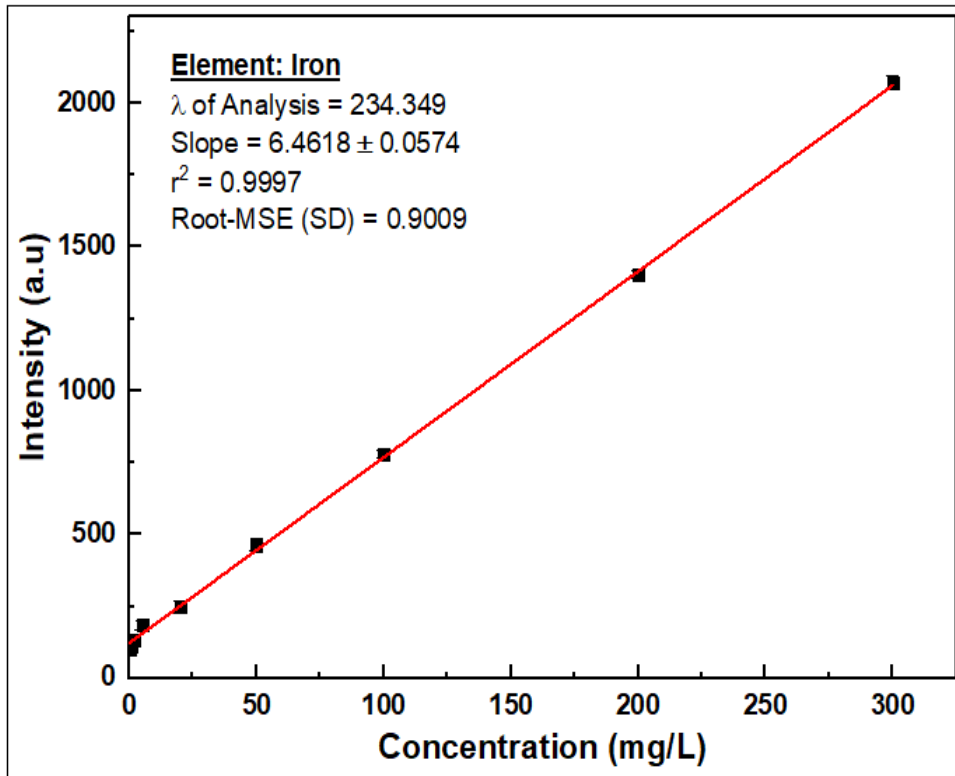
Appendix 5; ICP-OES Calibration curve for analysis of iron (Fe) elemental
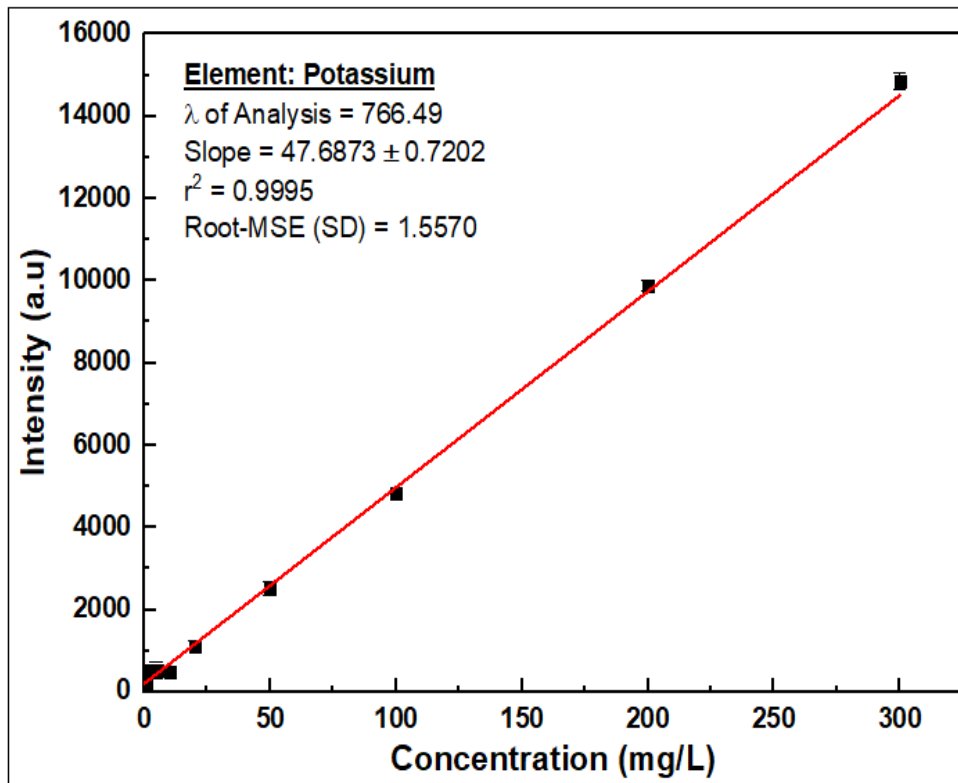
Appendix 6; ICP-OES Calibration curve for analysis of potassium (K) elemental
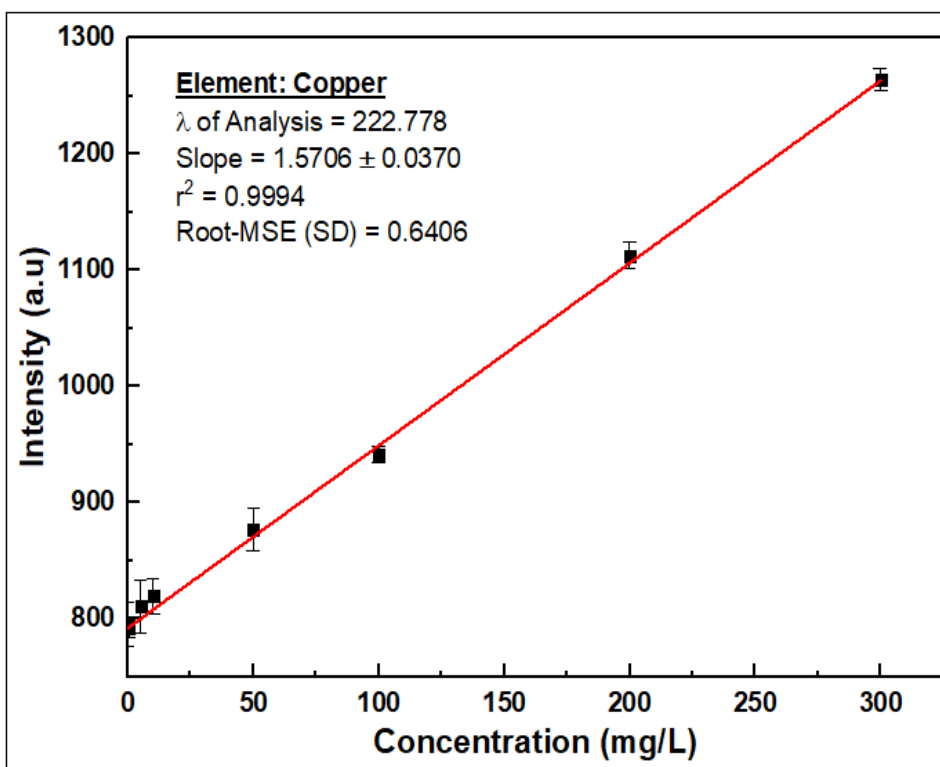
Appendix 7; ICP-OES Calibration curve for analysis of copper (Cu)elemental
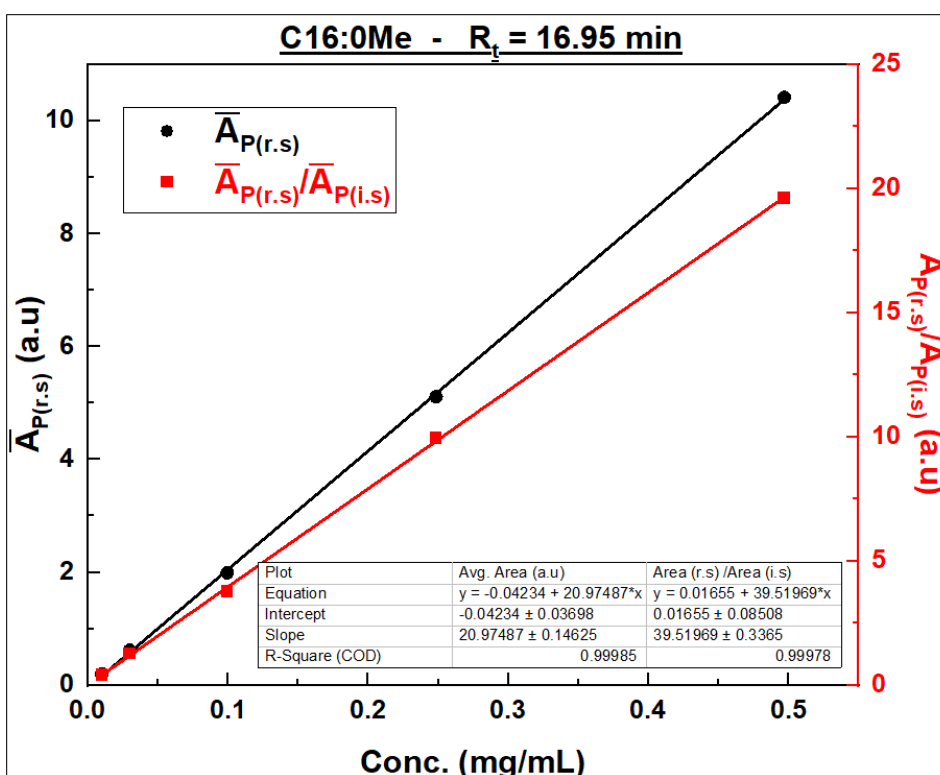
Appendix 8; Plots of the average peak area of methyl palmitate (C16:0Me) FAME in GLC-10 reference standard ($\bar{A}_{p(r.s)}$) and the ratio of its average peak area to average peak area of methyl nonadecanoate (C19:0Me) internal standard ($\bar{A}_{p(r.s)}/\bar{A}_{p(i.s)}$) at different concentration levels.

172
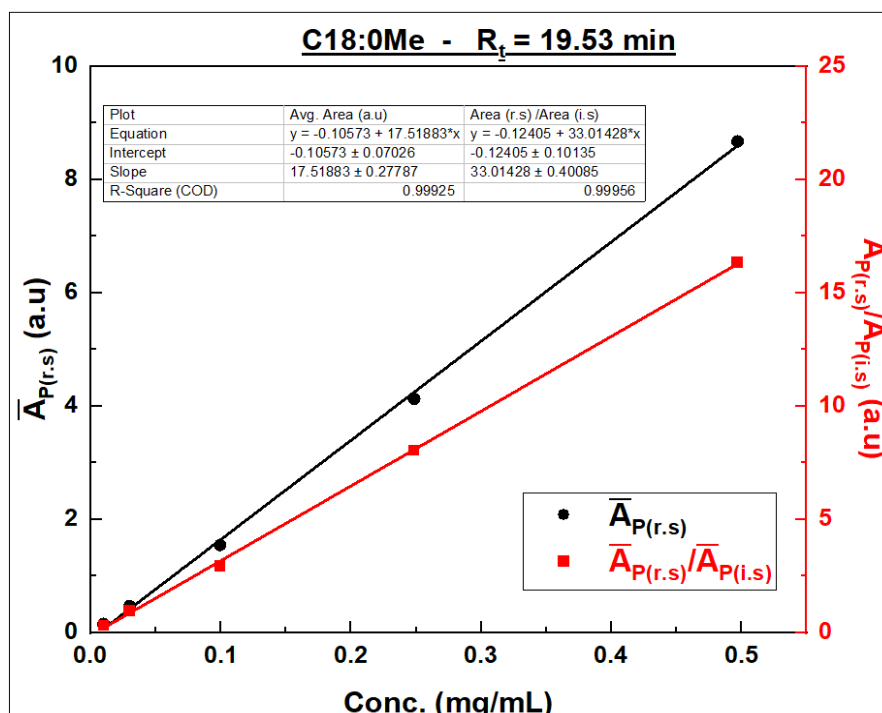
Appendix 9; Plots of the average peak area of methyl stearate (C18:0Me) FAME in GLC-10 reference standard ($\bar{A}_{p(r.s)}$) and the ratio of its average peak area to average peak area of methyl nonadecanoate (C19:0Me) internal standard ($\bar{A}_{p(r.s)}/\bar{A}_{p(i.s)}$) at different concentration levels.
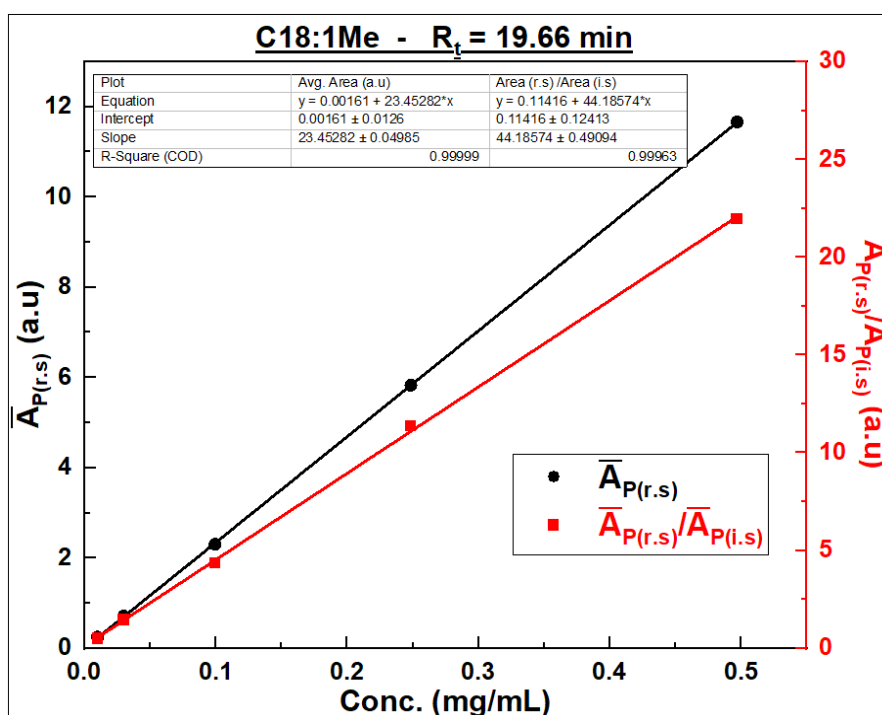
Appendix 10; Plots of the average peak area of methyl oleate (C18:1Me) FAME in GLC-10 reference standard ($\bar{A}_{p(r.s)}$) and the ratio of its average peak area to average peak area of methyl nonadecanoate (C19:0Me) internal standard ($\bar{A}_{p(r.s)}/\bar{A}_{p(i.s)}$) at different concentration levels.
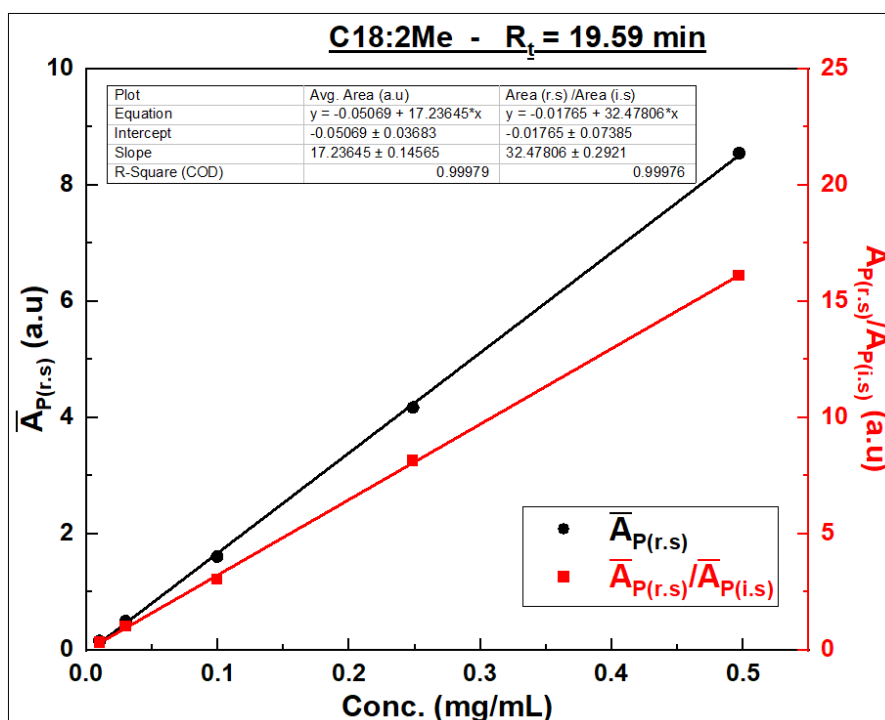
Appendix 11; Plot of the average peak area of methyl linoleate (C18:2Me) FAME in GLC-10 reference standard ($\bar{A}_{p(r.s)}$) and the ratio of its average peak area to average peak area of methyl nonadecanoate (C19:0Me) internal standard ($\bar{A}_{p(r.s)}/\bar{A}_{p(i.s)}$) at different concentration levels.
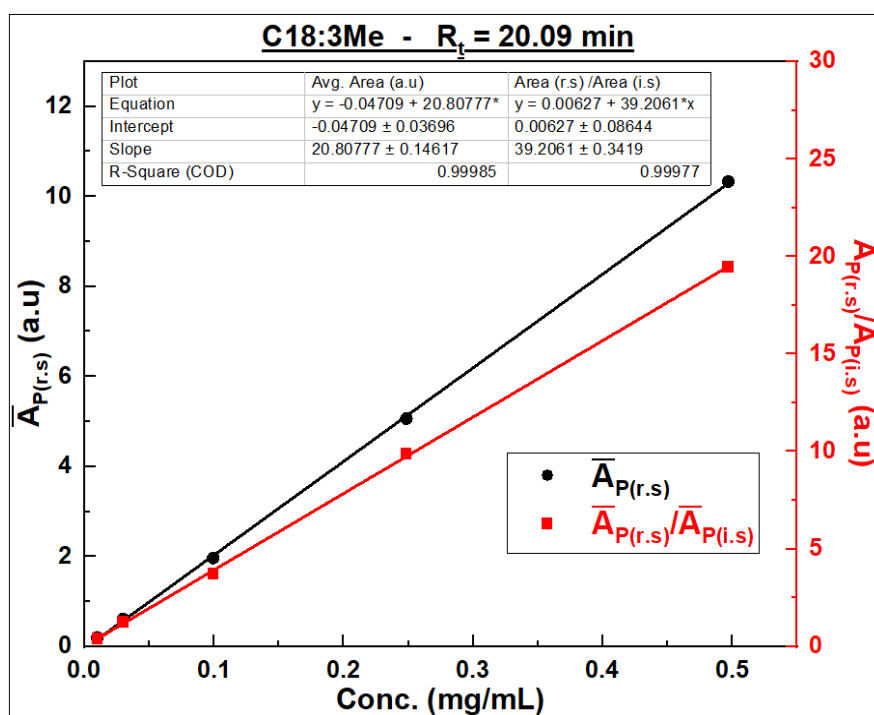
Appendix 12; Plots of the average peak area of methyl linolenate (C18:3Me) FAME in GLC-10 reference standard ($\bar{A}_{p(r.s)}$) and the ratio of its average peak area to average peak area of methyl nonadecanoate (C19:0Me) internal standard ($\bar{A}_{p(r.s)}/\bar{A}_{p(i.s)}$) at different concentration levels.

REFERENCES

Abbaszadeh-Mayvan, A., Ghobadian, B., Najafi, G., & Yusaf, T. (2018). Intensification of Continuous Biodiesel Production from Waste Cooking Oils Using Shockwave Power Reactor: Process Evaluation and Optimization through Response Surface Methodology (RSM). *Energies*, *11*(10), 2845. https://www.mdpi.com/1996-1073/11/10/2845

Abdullahi, T., Harun, Z., & Othman, M. H. D. (2017). A review on sustainable synthesis of zeolite from kaolinite resources via hydrothermal process. *Advanced Powder Technology*, *28*(8), 1827-1840. https://doi.org/10.1016/j.apt.2017.04.028

Aboul-Fotouh, S. M. K., Ali, L. I., Naghmash, M. A., & Aboul-Gheit, N. A. K. (2017). Effect of the Si/Al ratio of HZSM-5 zeolite on the production of dimethyl ether before and after ultrasonication. *Journal of Fuel Chemistry and Technology*, *45*(5), 581-588. https://doi.org/10.1016/S1872-5813(17)30030-0

Abukhadra, M. R., & Sayed, M. A. (2018). K+ trapped kaolinite (Kaol/K+) as low cost and eco-friendly basic heterogeneous catalyst in the transesterification of commercial waste cooking oil into biodiesel. *Energy Conversion and Management*, *177*, 468-476. https://doi.org/10.1016/j.enconman.2018.09.083

Achten, W. M. J., Verchot, L., Franken, Y. J., Mathijs, E., Singh, V. P., Aerts, R., & Muys, B. (2008). Jatropha bio-diesel production and use. *Biomass and Bioenergy*, *32*(12), 1063-1084. http://dx.doi.org/10.1016/j.biombioe.2008.03.003

Agus, B., Hari, P. D., Achmad, R., & Kusno, B. (2014). HZSM-5 Catalyst for Cracking Palm Oil to Biodiesel: A Comparative Study with and without Pt and Pd Impregnation. *Scientific Study and Research*, *15*(1), 81-90.

Alderton, D. (2021). Zeolites☆. In D. Alderton & S. A. Elias (Eds.), *Encyclopedia of Geology (Second Edition)* (pp. 313-325). Academic Press. https://doi.org/10.1016/B978-0-08-102908-4.00041-2

Alegría, A., & Cuellar, J. (2015). Esterification of oleic acid for biodiesel production catalyzed by 4-dodecylbenzenesulfonic acid. *Applied Catalysis B: Environmental*, *179*, 530-541. http://dx.doi.org/10.1016/j.apcatb.2015.05.057

Anderson, D., Balapangu, S., Fleischer, H. N. A., Viade, R. A., Krampa, F. D., Kanyong, P., Awandare, G. A., & Tiburu, E. K. (2017). Investigating the Influence of Temperature on the Kaolinite-Base Synthesis of Zeolite and Urease Immobilization for the Potential Fabrication of Electrochemical Urea Biosensors. *Sensors*, *17*(8), 1831. https://doi.org/10.3390/s17081831

Anil, D. K., Sarvaya, R. M., & Rehman, A. (2011). Characterization of Processed Jatropha Oil for use as Engine Fuel. *Current World Environment*, *6*(1), 101-107. http://dx.doi.org/10.12944/CWE.6.1.14

Antonova, Z. A., Krouk, V. S., Pilyuk, Y. E., Maksimuk, Y. V., Karpushenkava, L. S., & Krivova, M. G. (2015). Exergy analysis of canola-based biodiesel production in Belarus. *Fuel Processing Technology*, *138*, 397-403. http://dx.doi.org/10.1016/j.fuproc.2015.05.005

Aragaw, T. A., & Ayalew, A. A. (2018). Removal of water hardness using zeolite synthesized from Ethiopian kaolin by hydrothermal method. *Water Practice and Technology*, *14*(1), 145-159. https://doi.org/10.2166/wpt.2018.116

Aransiola, E. F., Ojumu, T. V., Oyekola, O. O., Madzimbamuto, T. F., & Ikhu-Omoregbe, D. I. O. (2014). A review of current technology for biodiesel production: State of the art. *Biomass and Bioenergy*, *61*, 276-297. https://doi.org/10.1016/j.biombioe.2013.11.014

Ayele, L., Pérez-Pariente, J., Chebude, Y., & Díaz, I. (2016). Conventional versus alkali fusion synthesis of zeolite A from low grade kaolin. *Applied Clay Science*, *132-133*, 485-490. https://doi.org/10.1016/j.clay.2016.07.019

Bacariza, M. C., Graça, I., Lopes, J. M., & Henriques, C. (2018). Enhanced activity of CO2 hydrogenation to CH4 over Ni based zeolites through the optimization of the Si/Al ratio. *Microporous and Mesoporous Materials*, *267*, 9-19. https://doi.org/10.1016/j.micromeso.2018.03.010

Baerlocher, C., & McCusker, L. B. (2017). *Database of Zeolite Structures*. Retrieved March, 13th 2020 from, Structure Commission of the International Zeolite Association (IZA-SC). http://www.iza-structure.org/databases/

Baerlocher, C., McCusker, L. B., Olson, D. H., Meier, W. M., & Association, I. Z. (2007). *Atlas of zeolite framework types* (6th ed.). Elsevier. https://doi.org/10.1016/B978-0-444-53064-6.X5186-X

Bahgaat, A., Mohamed, M., Abdel Karim, A., Melegy, A., & Hassan, H. (2020). Synthesis and Characterization of Zeolite-Y from natural clay of Wadi Hagul, Egypt. *Egyptian Journal of Chemistry*, *63*(10), 3791-3800. https://doi.org/10.21608/ejchem.2020.23195.2378

Baroi, C., Mahto, S., Niu, C., & Dalai, A. K. (2014). Biofuel production from green seed canola oil using zeolites. *Applied Catalysis A: General*, *469*(0), 18-32. http://dx.doi.org/10.1016/j.apcata.2013.09.034

Barrer, R. M. (1948). Synthesis of a zeolitic mineral with chabazite-like sorptive properties. *Journal of the Chemical Society (Resumed)*(0), 127-132. https://doi.org/10.1039/JR9480000127

Belaabed, R., Elabed, S., Addaou, A., Laajab, A., Rodríguez, M. A., & Lahsini, A. (2016). Synthesis of LTA zeolite for bacterial adhesion. *Boletín de la Sociedad Española de Cerámica y Vidrio*, *55*(4), 152-158. https://doi.org/10.1016/j.bsecv.2016.05.001

Belviso, C., Cavalcante, F., Lettino, A., & Fiore, S. (2013). A and X-type zeolites synthesised from kaolinite at low temperature. *Applied Clay Science*, *80-81*, 162-168. https://doi.org/10.1016/j.clay.2013.02.003

Berger, C., Gläser, R., Rakoczy, R. A., & Weitkamp, J. (2005). The synthesis of large crystals of zeolite Y re-visited. *Microporous and Mesoporous Materials*, *83*(1), 333-344. https://doi.org/10.1016/j.micromeso.2005.04.009

Bessa, R., Costa, L., Oliveira, C., Bohn, F., do Nascimento, R., Sasaki, J., & Loiola, A. (2017). Kaolin-based magnetic zeolites A and P as water softeners. *Microporous and Mesoporous Materials*, *245*. https://doi.org/10.1016/j.micromeso.2017.03.004

Bi-Zeng, Z., Anne, W. M., Tsun-Kong, S., A., P. J., J., D. R., Ramana, R. K. V., N., R. K., & Stanley, C. T. (2003). Zeolite-Confined Nano-RuO2: A Green, Selective, and Efficient Catalyst for Aerobic Alcohol Oxidation. *Journal of the American Chemical Society*, *125*(8), 2195-2199. https://doi.org/10.1021/ja0282691

Bortolatto, L. B., Boca Santa, R. A. A., Moreira, J. C., Machado, D. B., Martins, M. A. P. M., Fiori, M. A., Kuhnen, N. C., & Riella, H. G. (2017). Synthesis and characterization of Y zeolites from alternative silicon and aluminium sources. *Microporous and Mesoporous Materials*, *248*, 214-221. https://doi.org/10.1016/j.micromeso.2017.04.030

BP Energy Outlook. (2018). https://www.bp.com/energyoutlook

BP Statistical Review of World Energy. (2019). https://www.bp.com/statisticalreview

Brask, J., Cowan, D., & Nielsen, P. (2015). Applications of enzymes in industrial biodiesel production. In P. Grunwald (Ed.), *Industrial biocatalysis* (pp. 417-447). CRC Press.

Breck, D. W. (1974). *Zeolite Molecular Sieves: Structure, Chemistry, and Use*. Wiley & Sons.

Bronić, J., Palčić, A., Subotić, B., Itani, L., & Valtchev, V. (2012). Influence of alkalinity of the starting system on size and morphology of the zeolite A crystals. *Materials Chemistry and Physics*, *132*(2), 973-976. https://doi.org/10.1016/j.matchemphys.2011.12.043

Bukalo, N. N., Ekosse, G.-I. E., Odiyo, J. O., & Ogola, J. S. (2017). Fourier Transform Infrared Spectroscopy of Clay Size Fraction of Cretaceous-Tertiary Kaolins in the Douala Sub-Basin, Cameroon. *Open Geosciences*, *9*(1). https://doi.org/10.1515/geo-2017-0031

Cao, J., Wang, P., Shen, J., & Sun, Q. (2020). Core-shell Fe3O4@zeolite NaA as an Adsorbent for Cu2+. *Materials*, *13*(21), 5047. https://www.mdpi.com/1996-1944/13/21/5047

Carrero, A., Vicente, G., Rodríguez, R., Linares, M., & del Peso, G. L. (2011). Hierarchical zeolites as catalysts for biodiesel production from Nannochloropsis microalga oil. *Catalysis Today*, *167*(1), 148-153. http://dx.doi.org/10.1016/j.cattod.2010.11.058

Castro, P. R. D. S. D., Maia, A. Á. B., & Angélica, R. S. (2019). Study of the Thermal Stability of Faujasite Zeolite Synthesized from Kaolin Waste from the Amazon. *Materials Research*, *22*(5). https://doi.org/10.1590/1980-5373-mr-2019-0321

Cataldo, E., Salvi, L., Paoli, F., Fucile, M., Masciandaro, G., Manzi, D., Masini, C. M., & Mattii, G. B. (2021). Application of Zeolites in Agriculture and Other Potential Uses: A Review. *Agronomy*, *11*(8), 1547. https://www.mdpi.com/2073-4395/11/8/1547

Chandrasekhar, S., & Pramada, P. N. (2004). Kaolin-based zeolite Y, a precursor for cordierite ceramics. *Applied Clay Science*, *27*(3), 187-198. https://doi.org/10.1016/j.clay.2004.07.001

Chellappan, S., Nair, V., V, S., & K, A. (2018). Experimental validation of biochar based green Bronsted acid catalysts for simultaneous esterification and transesterification in biodiesel

production. *Bioresource Technology Reports*, *2*, 38-44. https://doi.org/10.1016/j.biteb.2018.04.002

Chen, G., Shan, R., Li, S., & Shi, J. (2015). A biomimetic silicification approach to synthesize CaO–SiO2 catalyst for the transesterification of palm oil into biodiesel. *Fuel*, *153*, 48-55. http://dx.doi.org/10.1016/j.fuel.2015.02.109

Cheng, L. S., & Yang, R. T. (1994). Improved Horvath—Kawazoe equations including spherical pore models for calculating micropore size distribution. *Chemical Engineering Science*, *49*(16), 2599-2609. https://doi.org/10.1016/0009-2509(94)E0054-T

Cheng, Y., Lu, M., Li, J., Su, X., Pan, S., Jiao, C., & Feng, M. (2012). Synthesis of MCM-22 zeolite using rice husk as a silica source under varying-temperature conditions. *Journal of Colloid and Interface Science*, *369*(1), 388-394. https://doi.org/10.1016/j.jcis.2011.12.024

Chhabra, M., Sharma, A., & Dwivedi, G. (2017). Performance evaluation of diesel engine using rice bran biodiesel. *Egyptian Journal of Petroleum*, *26*(2), 511-518. https://doi.org/10.1016/j.ejpe.2016.07.002

Chhetri, A. B., Watts, K. C., & Islam, M. R. (2008). Waste Cooking Oil as an Alternate Feedstock for Biodiesel Production. *Energies*, *1*(1), 3-18. https://doi.org/10.3390/en1010003

Choe, E., & Min, D. B. (2007). Chemistry of Deep-Fat Frying Oils. *Journal of Food Science*, *72*(5), R77-R86. https://doi.org/10.1111/j.1750-3841.2007.00352.x

Christidis, G. E., & Papantoni, H. (2008). Synthesis of FAU Type Zeolite Y from Natural Raw Materials: Hydrothermal SiO2-Sinter and Perlite Glass. *The Open Mineralogy Journal*, *2*(1), 1-5. https://doi.org/10.2174/1874456700802010001

Chung, K.-H., & Park, B.-G. (2009). Esterification of oleic acid in soybean oil on zeolite catalysts with different acidity. *Journal of Industrial and Engineering Chemistry*, *15*(3), 388-392. https://doi.org/10.1016/j.jiec.2008.11.012

Cirujano, F. G., Corma, A., & Llabrés i Xamena, F. X. (2015). Zirconium-containing metal organic frameworks as solid acid catalysts for the esterification of free fatty acids: Synthesis of biodiesel and other compounds of interest. *Catalysis Today*, *257, Part 2*, 213-220. http://dx.doi.org/10.1016/j.cattod.2014.08.015

Climent, M. J., Corma, A., & Iborra, S. (2010). Zeolites as Catalysts for the Synthesis of Fine Chemicals. In *Zeolites and Catalysis* (pp. 775-826). https://doi.org/10.1002/9783527630295.ch25

Colella, C., & Gualtieri, A. F. (2007). Cronstedt's zeolite. *Microporous and Mesoporous Materials*, *105*(3), 213-221. https://doi.org/10.1016/j.micromeso.2007.04.056

Colella, C., & Wise, W. S. (2014). The IZA Handbook of Natural Zeolites: A tool of knowledge on the most important family of porous minerals. *Microporous and Mesoporous Materials*, *189*, 4-10. https://doi.org/10.1016/j.micromeso.2013.08.028

Covarrubias, C., García, R., Arriagada, R., Yánez, J., & Garland, M. T. (2006). Cr(III) exchange on zeolites obtained from kaolin and natural mordenite. *Microporous and Mesoporous Materials*, *88*(1), 220-231. https://doi.org/10.1016/j.micromeso.2005.09.007

CrystalMaker®: A crystal and molecular structures program for Mac and Windows. *CrystalMaker Software Ltd, Oxford, England*. https://www.crystalmaker.com

Đặng, T.-H., Chen, B.-H., & Lee, D.-J. (2017). Optimization of biodiesel production from transesterification of triolein using zeolite LTA catalysts synthesized from kaolin clay. *Journal of the Taiwan Institute of Chemical Engineers*, *79*, 14-22. https://doi.org/10.1016/j.jtice.2017.03.009

De Souza, V. C., Villarroel-Rocha, J., De Araújo, M. J. G., Sapag, K., & Pergher, S. B. C. (2018). Basic Treatment in Natural Clinoptilolite for Improvement of Physicochemical Properties. *Minerals*, *8*(12), 595. https://www.mdpi.com/2075-163X/8/12/595

Dhawane, S. H., Kumar, T., & Halder, G. (2016). Biodiesel synthesis from Hevea brasiliensis oil employing carbon supported heterogeneous catalyst: Optimization by Taguchi method. *Renewable Energy*, *89*, 506-514. https://doi.org/10.1016/j.renene.2015.12.027

Djeffal, N., Benbouzid, M., Boukoussa, B., Sekkiou, H., & Bengueddach, A. (2017). CO_2 adsorption properties of ion-exchanged zeolite Y prepared from natural clays. *Materials Research Express*, *4*(3), 035504. https://doi.org/10.1088/2053-1591/aa6465

Djomgoue, P., & Njopwouo, D. (2013). FT-IR Spectroscopy Applied for Surface Clays Characterization. *Journal of Surface Engineered Materials and Advanced Technology*, *03*(04), 275-282. https://doi.org/10.4236/jsemat.2013.34037

Doyle, A. M., Albayati, T. M., Abbas, A. S., & Alismaeel, Z. T. (2016). Biodiesel production by esterification of oleic acid over zeolite Y prepared from kaolin. *Renewable Energy*, *97*, 19-23. https://doi.org/10.1016/j.renene.2016.05.067

Duvarcı, Ö. Ç., Akdeniz, Y., Özmıhçı, F., Ülkü, S., Balköse, D., & Çiftçioğlu, M. (2007). Thermal behaviour of a zeolitic tuff. *Ceramics International*, *33*(5), 795-801. https://doi.org/10.1016/j.ceramint.2006.01.003

Dziedzicka, A., Sulikowski, B., & Ruggiero-Mikołajczyk, M. (2016). Catalytic and physicochemical properties of modified natural clinoptilolite. *Catalysis Today*, *259*, 50-58. https://doi.org/10.1016/j.cattod.2015.04.039

Eevera, T., & Pazhanichamy, K. (2013). Cotton Seed Oil: A Feasible Oil Source for Biodiesel Production. *Energy Sources, Part A,*, *35*, 1118-1128. https://doi.org/10.1080/15567036.2010.514648

El-Mekkawi, D. M., Ibrahim, F. A., & Selim, M. M. (2016). Removal of methylene blue from water using zeolites prepared from Egyptian kaolins collected from different sources. *Journal of Environmental Chemical Engineering*, *4*(2), 1417-1422. https://doi.org/10.1016/j.jece.2016.01.007

El-Mekkawi, D. M., & Selim, M. M. (2012). Effect of metal loading processes on the stability and thermal transformation of Co2+- and Cu2+-zeolite Y prepared from Egyptian kaolin. *Materials Characterization*, *69*, 37-44. https://doi.org/10.1016/j.matchar.2012.04.001

EN-14214:2008. (2009). Automotive fuels - Fatty Acid Methyl Esters (FAME) for diesel engines - requirements and test methods.

Esaifan, M., Warr, L. N., Grathoff, G., Meyer, T., Schafmeister, M.-T., Kruth, A., & Testrich, H. (2019). Synthesis of Hydroxy-Sodalite/Cancrinite Zeolites from Calcite-Bearing Kaolin for the Removal of Heavy Metal Ions in Aqueous Media. *Minerals*, *9*(8), 484. https://doi.org/10.3390/min9080484

Ewunie, G. A., Lekang, O. I., Morken, J., & Yigezu, Z. D. (2021). Characterizing the potential and suitability of Ethiopian variety *Jatropha curcas* for biodiesel production: Variation in yield and physicochemical properties of oil across different growing areas. *Energy Reports*, *7*, 439-452. https://doi.org/10.1016/j.egyr.2021.01.007

Fadhil, A. B., Aziz, A. M., & Al-Tamer, M. H. (2016). Biodiesel production from Silybum marianum L. seed oil with high FFA content using sulfonated carbon catalyst for esterification and base catalyst for transesterification. *Energy Conversion and Management*, *108*, 255-265. http://dx.doi.org/10.1016/j.enconman.2015.11.013

Fan, X., Wang, X., & Chen, F. (2011). Biodiesel Production from Crude Cottonseed Oil: An Optimization Process Using Response Surface Methodology. *The Open Fuels & Energy Science Journal*, *4*, 1-8. https://doi.org/10.2174/1876973X01104010001

Fatimatul, M., Laila Khamsatul, M., Triwikantoro, & Zaenal, A. (2019). Synthesis and Characterization of Precipitated $CaCO_3$ from Ankerite Prepared by Bubbling Method. *KnE Engineering*, *4*(2). https://doi.org/10.18502/keg.v1i2.4435

Favvas, E. P., Tsanaktsidis, C. G., Sapalidis, A. A., Tzilantonis, G. T., Papageorgiou, S. K., & Mitropoulos, A. C. (2016). Clinoptilolite, a natural zeolite material: Structural characterization and performance evaluation on its dehydration properties of hydrocarbon-based fuels. *Microporous and Mesoporous Materials*, *225*, 385-391. https://doi.org/10.1016/j.micromeso.2016.01.021

Foroughi, M., Salem, A., & Salem, S. (2021). Characterization of phase transformation from low grade kaolin to zeolite LTA in fusion technique: Focus on quartz melting and crystallization in presence of NaAlO2. *Materials Chemistry and Physics*, *258*, 123892. https://doi.org/10.1016/j.matchemphys.2020.123892

García-Soto, A. R., Rodríguez-Niño, G., & Trujillo, C. A. (2013). Zeolite LTA synthesis: Optimising synthesis conditions by using the modified sequential simplex method. *Ingeniería e Investigación*, *33*, 22-27. http://www.scielo.org.co/scielo.php?script=sci_arttext&pid=S0120-56092013000300005&nrm=iso

García, A., López, C. M., García, L. V., Casanova, J., & Goldwasser, M. R. (2016). Improvements in the synthesis of zeolites with low Si/Al ratio from Venezuelan sodium silicate for an environmentally friendly process. *Ingeniería e Investigación*, *36*, 62-69. http://www.scielo.org.co/scielo.php?script=sci_arttext&pid=S0120-56092016000100008&nrm=iso

Garshasbi, V., Jahangiri, M., & Anbia, M. (2017). Equilibrium CO2 adsorption on zeolite 13X prepared from natural clays. *Applied Surface Science*, *393*, 225-233. https://doi.org/10.1016/j.apsusc.2016.09.161

Georgiev, D., Bogdanov, B., Angelova, K., Markovska, I., & Hristov, Y. (2009, 4th - 5th June 2009). *Synthetic Zeolites - Structure, Clasification, Current Trends in Zeolite Synthesis Review* International Science conference - Stara Zagora, Bulgaria,

Gomes, R., Bhanja, P., & Bhaumik, A. (2016). Sulfonated porous organic polymer as a highly efficient catalyst for the synthesis of biodiesel at room temperature. *Journal of Molecular Catalysis A: Chemical*, *411*, 110-116. http://dx.doi.org/10.1016/j.molcata.2015.10.016

Gougazeh, M., & Buhl, J. C. (2014). Synthesis and characterization of zeolite A by hydrothermal transformation of natural Jordanian kaolin. *Journal of the Association of Arab Universities for Basic and Applied Sciences*, *15*, 35-42. https://doi.org/10.1016/j.jaubas.2013.03.007

Greer, H., Wheatley, P. S., Ashbrook, S. E., Morris, R. E., & Zhou, W. (2009). Early Stage Reversed Crystal Growth of Zeolite A and Its Phase Transformation to Sodalite. *Journal of the American Chemical Society*, *131*(49), 17986-17992. https://doi.org/10.1021/ja907475z

Guesmi, H., & Massiani, P. (2011). A combined EXAFS and DFT study of the Ni2+ environment in dehydrated Ni/NaX. *Catalysis Today*, *177*(1), 25-30. https://doi.org/10.1016/j.cattod.2011.04.047

Hanlie, H., Wang, C., Zeng, K., Zhang, K., Yin, K., & Li, Z. (2012). *Clay Mineralogy of the Zhada Sediments: Evidence for Climatic and Tectonic Evolution Since ∼9 Ma in Zhada, Southwestern Tibet* (Vol. 60). https://doi.org/10.1346/CCMN.2012.0600302

Heller-Kallai, L., & Lapides, I. (2007). Reactions of kaolinites and metakaolinites with NaOH—comparison of different samples (Part 1). *Applied Clay Science*, *35*(1), 99-107. https://doi.org/10.1016/j.clay.2006.06.006

Helwani, Z., Aziz, N., Kim, J., & Othman, M. R. (2016). Improving the yield of *Jatropha curcas's* FAME through sol–gel derived meso-porous hydrotalcites. *Renewable Energy*, *86*, 68-74. http://dx.doi.org/10.1016/j.renene.2015.07.094

Hu, T., Gao, W., Liu, X., Zhang, Y., & Meng, C. (2017). Synthesis of zeolites Na-A and Na-X from tablet compressed and calcinated coal fly ash. *Royal Society open science*, *4*(10), 170921-170921. https://doi.org/10.1098/rsos.170921

Huggett, J. M. (2005). Clay minerals. *Encyclopedia of Geology*, (pp.358-365). https://doi.org/10.1016/B0-12-369396-9/00273-2

Imandiani, S., Indira, C., Johan, A., & Budiyono. (2018). Utilization of Natural Zeolite from Ponorogo and Purworejo for Naphthol Substance Adsorption. *E3S Web of Conferences*, *31*, 05002. https://doi.org/10.1051/e3sconf/20183105002

Jaya, N., Selvan, B. K., & Vennison, S. J. (2015). Synthesis of biodiesel from pongamia oil using heterogeneous ion-exchange resin catalyst. *Ecotoxicology and Environmental Safety*, *121*, 3-9. http://dx.doi.org/10.1016/j.ecoenv.2015.07.035

Johnson, E. B. G., & Arshad, S. E. (2014). Hydrothermally synthesized zeolites based on kaolinite: A review. *Applied Clay Science*, *97-98*, 215-221. https://doi.org/10.1016/j.clay.2014.06.005

Johnson, M., O'Connor, D., Barnes, P., Catlow, C. R. A., Owens, S. L., Sankar, G., Bell, R., Teat, S. J., & Stephenson, R. (2003). Cation Exchange, Dehydration, and Calcination in Clinoptilolite: In Situ X-ray Diffraction and Computer Modeling. *The Journal of Physical Chemistry B*, *107*(4), 942-951. https://doi.org/10.1021/jp021672+

Joshi, H. C., Toler, J., & Walker, T. (2008). Optimization of Cottonseed Oil Ethanolysis to Produce Biodiesel High in Gossypol Content. *Journal of the American Oil Chemists' Society*, *85*(4), 357-363. https://doi.org/10.1007/s11746-008-1200-7

Kakati, J.P, & Gogoi, T. K. (2016). Biodiesel production from Kutkura (Meyna spinosa Roxb. Ex.) fruit seed oil: Its characterization and engine performance evaluation with 10% and 20% blends. *Energy Conversion and Management*, *121* 152-161. https://doi.org/10.1016/j.enconman.2016.05.019

Kamba, S. A., Ismail, M., Tengku Ibrahim, T. A., & Zakaria, Z. A. B. (2013). Synthesis and Characterisation of Calcium Carbonate Aragonite Nanocrystals from Cockle Shell Powder (*Anadara granosa*). *Journal of Nanomaterials*, *2013*, 398357. https://doi.org/10.1155/2013/398357

Kamzolova, S., Fatykhova, A., Dedyukhina, E., Anastassiadis, S., Golovchenko, N., & Morgunov, I. (2011). Citric Acid Production by Yeast Grown on Glycerol-Containing Waste from Biodiesel Industry. *Food Technol Biotechnol*, *49*, 65 - 74.

Karuppasamya, K., Thaheer, S. A. A., & Basha, A. C. (2013). Biosynthesis and Characterization of Biodiesel from Cottonseed Oil Using Pseudomonas fluorescences Lipase and the Performance of its Blend (B20) in diesel Engine. *Chem. Biochem. Eng.*, *27*(2), 157-166.

Kay, K. H., & Yasir, S. M. (2012). Biodiesel Production from Low Quality Crude Jatropha Oil Using Heterogeneous Catalyst. *APCBEE Procedia*, *3*, 23-27. http://dx.doi.org/10.1016/j.apcbee.2012.06.040

Kazemimoghadam, M. (2016). Comparision of Kaolin and chemical source for preparation of Nano pore NaA Zeolite membranes. *Journal of Water Environmental Nanotechnology*, *1*(1), 45-53.

Khan, G. M. A., Arafat, S. M. Y., Reza, M. N., Razzaque, S. M. A., & Alam, M. S. (2010). Linde Type-A zeolite synthesis and effect of crystallization on its surface acidity. *Indian Journal of Chemical Technology*, *17*(4), 303-308.

Kibuge, R. M., Kariuki, S. T., & Njue, M. R. (2015). Influence of fuel properties on the burning characteristics of sour plum (Ximenia americana L.) seed oil compared with *Jatropha curcas* L. seed oil. *Renewable Energy*, *78*, 128-131. https://doi.org/10.1016/j.renene.2014.12.030

Kosanović, C., Havancsák, K., Subotić, B., Svetličić, V., Radić, T. M., Cziráki, Á., Huhn, G., Buljan, I., & Smrečki, V. (2011). Study of the mechanism of formation of nano-crystalline

zeolite X in heterogeneous system. *Microporous and Mesoporous Materials*, *142*(1), 139-146. https://doi.org/10.1016/j.micromeso.2010.11.027

Kovo, A. S., Hernandez, O., & Holmes, S. M. (2009). Synthesis and characterization of zeolite Y and ZSM-5 from Nigerian Ahoko Kaolin using a novel, lower temperature, metakaolinization technique. *Journal of Materials Chemistry*, *19*(34), 6207-6212. https://doi.org/10.1039/b907554b

Kraljević Pavelić, S., Simović Medica, J., Gumbarević, D., Filošević, A., Pržulj, N., & Pavelić, K. (2018). Critical Review on Zeolite Clinoptilolite Safety and Medical Applications in vivo [Review]. *Frontiers in Pharmacology*, *9*(1350). https://doi.org/10.3389/fphar.2018.01350

Król, M. (2020). Natural vs. Synthetic Zeolites. *Crystals*, *10*(7), 622. https://www.mdpi.com/2073-4352/10/7/622

Król, M., Mozgawa, W., Jastrzębski, W., & Barczyk, K. (2012). Application of IR spectra in the studies of zeolites from D4R and D6R structural groups. *Microporous and Mesoporous Materials*, *156*, 181-188. https://doi.org/10.1016/j.micromeso.2012.02.040

Kumar, N., Mohapatra, S. K., Ragit, S. S., Kundu, K., & Karmakar, R. (2017). Optimization of safflower oil transesterification using the Taguchi approach. *Petroleum Science*, *14*(4), 798-805. https://doi.org/10.1007/s12182-017-0183-0

Kumar, R., & Das, N. (2018). Survey and selection of *Jatropha curcas* L. germplasm: Assessment of genetic variability and divergence studies on the seed traits and oil content. *Industrial Crops and Products*, *118*, 125-130. https://doi.org/10.1016/j.indcrop.2018.03.032

Kumar, S. R., Sureshkumar, K., & Velraj, R. (2015). Optimization of biodiesel production from Manilkara zapota (L.) seed oil using Taguchi method. *Fuel*, *140*, 90-96. https://doi.org/10.1016/j.fuel.2014.09.103

Lapides, I., & Heller-Kallai, L. (2007). Reactions of metakaolinite with NaOH and colloidal silica — Comparison of different samples (part 2). *Applied Clay Science*, *35*(1), 94-98. https://doi.org/10.1016/j.clay.2006.06.007

Legodi, M. A., de Waal, D., Potgieter, J. H., & Potgieter, S. S. (2001). Rapid determination of CaCO3 in mixtures utilising FT—IR spectroscopy. *Minerals Engineering*, *14*(9), 1107-1111. https://doi.org/10.1016/S0892-6875(01)00116-9

Lelieveld, J., Klingmüller, K., Pozzer, A., Burnett, R. T., Haines, A., & Ramanathan, V. (2019). Effects of fossil fuel and total anthropogenic emission removal on public health and climate. *Proceedings of the National Academy of Sciences*, *116*(15), 7192-7197. https://doi.org/10.1073/pnas.1819989116

Lerma-García, M. J., Ramis-Ramos, G., Herrero-Martínez, J. M., & Simó-Alfonso, E. F. (2010). Authentication of extra virgin olive oils by Fourier-transform infrared spectroscopy. *Food Chemistry*, *118*(1), 78-83. https://doi.org/10.1016/j.foodchem.2009.04.092

Li, N., Li, T., Liu, H., Yue, Y., & Bao, X. (2017). A novel approach to synthesize in-situ crystallized zeolite/kaolin composites with high zeolite content. *Applied Clay Science*, *144*, 150-156. https://doi.org/10.1016/j.clay.2017.05.010

Li, Y., Li, L., & Yu, J. (2017). Applications of Zeolites in Sustainable Chemistry. *Chem*, *3*(6), 928-949. https://doi.org/10.1016/j.chempr.2017.10.009

Li, Y., Ma, L., Liu, H., & He, D. (2014). Influence of H-ZSM 5 on the activity of Ru catalysts and product selectivity during the hydrogenolysis of glycerol. *Applied Catalysis A: General*, *469*(0), 45-51. http://dx.doi.org/10.1016/j.apcata.2013.09.028

Lima, R. C., Bieseki, L., Melguizo, P. V., & Pergher, S. B. C. (2019). Zeolite Synthesis: General Aspects. In *Environmentally Friendly Zeolites: Synthesis and Source Materials* (pp. 21-63). Springer International Publishing. https://doi.org/10.1007/978-3-030-19970-8_2

Logar, N. Z., Tušar, N. N., Ristić, A., Mali, G., Mazaj, M., & Kaučič, V. (2009). Chapter 5 - Functionalisation and Structure Characterisation of Porous Silicates and Aluminophosphates. In V. Valtchev, S. Mintova, & M. Tsapatsis (Eds.), *Ordered Porous Solids* (pp. 101-126). Elsevier. https://doi.org/10.1016/B978-0-444-53189-6.00005-6

Lotero, E., Liu, Y., Lopez, D. E., Suwannakarn, K., Bruce, D. A., & Goodwin, J. G. (2005). Synthesis of Biodiesel via Acid Catalysis. *Industrial & Engineering Chemistry Research*, *44*(14), 5353-5363. https://doi.org/10.1021/ie049157g

Lutz, W. (2014). Zeolite Y: Synthesis, Modification, and Properties; A Case Revisited. *Advances in Materials Science and Engineering*, *2014*, 20, Article 724248. https://doi.org/10.1155/2014/724248

Ma, Y., Yan, C., Alshameri, A., Qiu, X., Zhou, C., & li, D. (2014). Synthesis and characterization of 13X zeolite from low-grade natural kaolin. *Advanced Powder Technology*, *25*(2), 495-499. https://doi.org/10.1016/j.apt.2013.08.002

Maia, A. A. B., Angélica, R. S., & Neves, R. F. (2011). Use of industrial kaolin waste from the Brazilian Amazon region for synthesis of zeolite A. *Clay Minerals*, *46*(1), 127-136. https://doi.org/10.1180/claymin.2011.046.1.127

Maia, A. Á. B., Dias, R. N., Angélica, R. S., & Neves, R. F. (2019). Influence of an aging step on the synthesis of zeolite NaA from Brazilian Amazon kaolin waste. *Journal of Materials Research and Technology*, *8*(3), 2924-2929. https://doi.org/10.1016/j.jmrt.2019.02.021

Makgabutlane, B., Nthunya, L. N., Nxumalo, E. N., Musyoka, N. M., & Mhlanga, S. D. (2020). Microwave Irradiation-Assisted Synthesis of Zeolites from Coal Fly Ash: An Optimization Study for a Sustainable and Efficient Production Process. *ACS Omega*, *5*(39), 25000-25008. https://doi.org/10.1021/acsomega.0c00931

Manadee, S., Sophiphun, O., Osakoo, N., Supamathanon, N., Kidkhunthod, P., Chanlek, N., Wittayakun, J., & Prayoonpokarach, S. (2017). Identification of potassium phase in catalysts supported on zeolite NaX and performance in transesterification of Jatropha seed oil. *Fuel Processing Technology*, *156*, 62-67. https://doi.org/10.1016/j.fuproc.2016.09.023

Marantos, I., Christidis, G. E., & Ulmanu, M. (2012). Zeolite formation and deposits. *Handbook of Natural Zeolites*, 28-51. https://doi.org/10.2174/978160805261511201010028

Margeta, K., Logar, N. Z., Šiljeg, M., & Farkaš, A. (2013). Natural Zeolites in Water Treatment - How Effective is Their Use, Water Treatment. In W. E. (Ed.) (Ed.). InTech, 2013. http://dx.doi.org/10.5772/50738

Martínez, S. L., Romero, R., Natividad, R., & González, J. (2014). Optimization of biodiesel production from sunflower oil by transesterification using Na2O/NaX and methanol. *Catalysis Today*, *220-222*, 12-20. https://doi.org/10.1016/j.cattod.2013.08.022

Marwaha, A., Rosha, P., Mohapatra, S. K., Mahla, S. K., & Dhir, A. (2018). Waste materials as potential catalysts for biodiesel production: Current state and future scope. *Fuel Processing Technology*, *181*, 175-186. https://doi.org/10.1016/j.fuproc.2018.09.011

Maryam, H., Ghasem, N., Maedeh, M., & Mahmood, R. (2014). Preparation, Characterization and Application of Zeolite-based Catalyst for Production of Biodiesel from Waste Cooking Oil. *Journal of Scientific and Industrial Research (JSIR)*, *73*, 129-133. Feb-2014

McCarthy, P., Rasul, M. G., & Moazzem, S. (2011). Comparison of the performance and emissions of different biodiesel blends against petroleum diesel. *International Journal of Low-Carbon Technologies*, *6*(4), 255-260. https://doi.org/10.1093/ijlct/ctr012

Meloni, D., Perra, D., Monaci, R., Cutrufello, M. G., Rombi, E., & Ferino, I. (2016). Transesterification of *Jatropha curcas* oil and soybean oil on Al-SBA-15 catalysts. *Applied Catalysis B: Environmental*, *184*, 163-173. http://dx.doi.org/10.1016/j.apcatb.2015.11.038

Mentus, S., Mojović, Z., & Radmilović, V. (2009). The use of NaX zeolite as a template to obtain a mono-atomic pt dispersion by impregnation with Pt(II) acetylacetonate/acetone solution. *Journal of the Serbian Chemical Society*, *74*(10), 1113-1123. https://doi.org/10.2298/JSC0910113M

Mezni, M., Hamzaoui, A., Hamdi, N., & Srasra, E. (2011). Synthesis of zeolites from the low-grade Tunisian natural illite by two different methods. *Applied Clay Science*, *52*(3), 209-218. https://doi.org/10.1016/j.clay.2011.02.017

Michot, A., Smith, D. S., Degot, S., & Lecomte, G. L. (2011). Effect of dehydroxylation on the specific heat of simple clay mixtures. *Journal of the European Ceramic Society*, *31*(8), 1377-1382. https://doi.org/10.1016/j.jeurceramsoc.2011.01.007

Millini, R., & Bellussi, G. (2017). Chapter 1 Zeolite Science and Perspectives. In *Zeolites in Catalysis: Properties and Applications* (pp. 1-36). The Royal Society of Chemistry. https://doi.org/10.1039/9781788010610-00001

Milton, R. M. (1989). Molecular Sieve Science and Technology. In *Zeolite Synthesis* (Vol. 398, pp. 1-10). American Chemical Society. https://doi.org/10.1021/bk-1989-0398.ch001

Mizik, T., & Gyarmati, G. (2021). Economic and Sustainability of Biodiesel Production—A Systematic Literature Review. *Clean Technologies*, *3*(1), 19-36. https://doi.org/10.3390/cleantechnol3010002

Mohsin, R., Majid, Z. A., Shihnan, A. H., Nasri, N. S., & Sharer, Z. (2014). Effect of biodiesel blends on engine performance and exhaust emission for diesel dual fuel engine. *Energy Conversion and Management*, *88*, 821-828. https://doi.org/10.1016/j.enconman.2014.09.027

Moneim, M. A., & Ahmed, E. A. (2015). Synthesis of Faujasite from Egyptian Clays: Characterizations and Removal of Heavy Metals. *Geomaterials*, *5*, 68-76. http://dx.doi.org/10.4236/gm.2015.52007

Mozgawa, W. (2001). The relation between structure and vibrational spectra of natural zeolites. *Journal of Molecular Structure*, *596*(1), 129-137. https://doi.org/10.1016/S0022-2860(01)00741-4

Mozgawa, W., Jastrzębski, W., & Handke, M. (2005). Vibrational spectra of D4R and D6R structural units. *Journal of Molecular Structure*, *744-747*, 663-670. https://doi.org/10.1016/j.molstruc.2004.12.051

Mozgawa, W., Krol, M., & Barczyk, K. (2011). FT-IR studies of zeolites from different structural groups. *Chemik*, *55*(7), 667-674.

Mozgawa, W., Sitarz, M., & Rokita, M. (1999). Spectroscopic studies of different aluminosilicate structures. *Journal of Molecular Structure*, *511-512*, 251-257. https://doi.org/10.1016/S0022-2860(99)00165-9

Musyoka, N. M., Missengue, R., Kusisakana, M., & Petrik, L. F. (2014). Conversion of South African clays into high quality zeolites. *Applied Clay Science*, *97-98*, 182-186. https://doi.org/10.1016/j.clay.2014.05.026

Nakao, M., Hasegawa, G., Yasuhara, T., & Ishihara, Y. (2015). Degradation of *Jatropha curcas* phorbol esters derived from Jatropha oil cake and their tumor-promoting activity. *Ecotoxicology and Environmental Safety*, *114*, 357-364. https://doi.org/10.1016/j.ecoenv.2014.07.009

Naskar, M. K., Kundu, D., & Chatterjee, M. (2011). Coral-like hydroxy sodalite particles from rice husk ash as silica source. *Materials Letters*, *65*(23), 3408-3410. https://doi.org/10.1016/j.matlet.2011.07.084

Nastro, A., & Aiello, R. (1989). Synthesis and Characterization of Zeolite Zsm–5 from Alkali–Tpa Systems. In T. Inui (Ed.), *Studies in Surface Science and Catalysis* (Vol. 44, pp. 227-236). Elsevier. https://doi.org/10.1016/S0167-2991(09)61297-0

Negm, N. A., Sayed, G. H., Yehia, F. Z., Habib, O. I., & Mohamed, E. A. (2017). Biodiesel production from one-step heterogeneous catalyzed process of Castor oil and Jatropha oil using novel sulphonated phenyl silane montmorillonite catalyst. *Journal of Molecular Liquids*, *234* 157-163. https://doi.org/10.1016/j.molliq.2017.03.043

Neha, P., Chintan, B., Pallavi, D., & Neha, T. (2013). Use of Sunflower and Cottonseed Oil to prepare Biodiesel by catalyst assisted Transesterification. *Research Journal of Chemical Sciences*, *3*(3), 42-47.

NREL. (2019). *Alternative Fuels Data Center*. National Renewable Energy Laboratory. https://afdc.energy.gov/fuels/biodiesel_production.html

Nyakairu, G. W. A., Koeberl, C., & Kurzweil, H. (2001). The Buwambo kaolin deposit in central Uganda: Mineralogical and chemical composition. *Geochemical Journal*, *35*, 245-256. https://doi.org/10.2343/geochemj.35.245

OECD. (2011). *Green Growth Studies: Energy*. OECD Publishing, Paris. https://doi.org/10.1787/22229523

OECD/FAO. (2019). *Share of vegetable oil used for biodiesel production*. OECD Publishing, Paris. https://doi.org/10.1787/b1d59ace-en

OECD/FAO. (2020). *OECD-FAO Agricultural Outlook 2020-2029*. https://doi.org/10.1787/agr-data-en

Okoronkwo, M. U., Galadima, A., & Leke, L. (2012). Advances in Biodiesel synthesis: from past to present. *Elixir Appl. Chem.*, *43* 6924-6945.

Olson, D. H. (1995). The crystal structure of dehydrated NaX. *Zeolites*, *15*(5), 439-443. https://doi.org/10.1016/0144-2449(95)00029-6

Olubunmi, B. E., Karmakar, B., Aderemi, O. M., G, A. U., Auta, M., & Halder, G. (2020). Parametric optimization by Taguchi L9 approach towards biodiesel production from restaurant waste oil using Fe-supported anthill catalyst. *Journal of Environmental Chemical Engineering*, *8*(5), 104288. https://doi.org/10.1016/j.jece.2020.104288

Park, M., Choi, C. L., Lim, W. T., Kim, M. C., Choi, J., & Heo, N. H. (2000). Molten-salt method for the synthesis of zeolitic materials: I. Zeolite formation in alkaline molten-salt system. *Microporous and Mesoporous Materials*, *37*(1), 81-89. https://doi.org/10.1016/S1387-1811(99)00196-1

Patil, P. D., & Deng, S. (2009). Transesterification of Camelina Sativa Oil Using Heterogeneous Metal Oxide Catalysts. *Energy & Fuels*, *23*(9), 4619-4624. https://doi.org/10.1021/ef900362y

Patil, P. D., Gude, V. G., Reddy, H. K., Muppaneni, T., & Deng, S. (2012). Biodiesel Production from Waste Cooking Oil Using Sulfuric Acid and Microwave Irradiation Processe. *Journal of Environmental Protection*, *3*(1), 107-113. https://doi.org/10.4236/jep.2012.31013

Peña, R., Romero, R., Martínez, S. L., Natividad, R., & Ramírez, A. (2013). Characterization of KNO_3/NaX catalyst for sunflower oil transesterification. *Fuel*, *110*, 63-69. https://doi.org/10.1016/j.fuel.2012.07.072

Peng, D.X. (2015). Exhaust emission characteristics of various types of biofuels. *Advances in Mechanical Engineering*, *7*(7), 1687814015593036. https://doi.org/10.1177/1687814015593036

Perego, C., & Bosetti, A. (2010). Biomass to fuels: the challenges of zeolite and mesoporous materials. 16th International Zeolite Conference joint with the 7th International Mesostructured Materials Symposium (IZC-IMMS 2010), Sorrento, Italy.

Pereira, P., Ferreira, B., Oliveira, N., Nassar, E., Ciuffi, K., Vicente, M., Trujillano, R., Rives, V., Gil, A., Korili, S., & De Faria, E. (2018). Synthesis of Zeolite A from Metakaolin and Its Application in the Adsorption of Cationic Dyes. *Applied Sciences*, *8*(4), 608. https://doi.org/10.3390/app8040608

Perraki, T., & Orfanoudaki, A. (2004). Mineralogical study of zeolites from Pentalofos area, Thrace, Greece. *Applied Clay Science*, *25*(1-2), 9-16. https://doi.org/10.1016/s0169-1317(03)00156-x

Prinsen, P., Luque, R., & González-Arellano, C. (2018). Zeolite catalyzed palmitic acid esterification. *Microporous and Mesoporous Materials*, *262*, 133-139. https://doi.org/10.1016/j.micromeso.2017.11.029

Qiu, T., Guo, X., Yang, J., Zhou, L., Li, L., Wang, H., & Niu, Y. (2016). The synthesis of biodiesel from coconut oil using novel Brønsted acidic ionic liquid as green catalyst. *Chemical Engineering Journal*, *296*, 71-78. http://dx.doi.org/10.1016/j.cej.2016.03.096

Rabo, J. A., & Schoonover, M. W. (2001). Early discoveries in zeolite chemistry and catalysis at Union Carbide, and follow-up in industrial catalysis. *Applied Catalysis A: General*, *222*(1), 261-275. https://doi.org/10.1016/S0926-860X(01)00840-7

Rafati, A., Tahvildari, K., & Nozari, M. (2019). Production of biodiesel by electrolysis method from waste cooking oil using heterogeneous MgO-NaOH nano catalyst. *Energy Sources, Part A: Recovery, Utilization, and Environmental Effects*, *41*(9), 1062-1074. https://doi.org/10.1080/15567036.2018.1539139

Ramos, M. J., Casas, A., Rodríguez, L., Romero, R., & Pérez, Á. (2008). Transesterification of sunflower oil over zeolites using different metal loading: A case of leaching and agglomeration studies. *Applied Catalysis A: General*, *346*(1), 79-85. https://doi.org/10.1016/j.apcata.2008.05.008

Reddy, M. S., Sharma, N., & Agarwal, A. K. (2016). Effect of straight vegetable oil blends and biodiesel blends on wear of mechanical fuel injection equipment of a constant speed diesel engine. *Renewable Energy*, *99*, 1008-1018. https://doi.org/10.1016/j.renene.2016.07.072

Ríos, C. A., Williams, C. D., & Castellanos, O. M. (2012). Crystallization of low silica Na-A and NA-X zeolites from transformation of kaolin and obsedian by alkaline fusion. *Ingenieria y Competitividad*, *14*(2), 125-137.

Ríos, C. A., Williams, C. D., & Fullen, M. A. (2009). Nucleation and growth history of zeolite LTA synthesized from kaolinite by two different methods. *Applied Clay Science*, *42*(3), 446-454. https://doi.org/10.1016/j.clay.2008.05.006

Rios, C. A., Williams, C. D., & Maple, M. J. (2007). Synthesis of Zeolites and Types by Hydrothermal Transformation of Kaolinite and Metakaolinite. *BISTUA*, *5*(1), 15-26.

Rodriguez-Blanco, J. D., Shaw, S., & Benning, L. G. (2011). The kinetics and mechanisms of amorphous calcium carbonate (ACC) crystallization to calcite, viavaterite. *Nanoscale*, *3*(1), 265-271. http://dx.doi.org/10.1039/C0NR00589D

Rodríguez-Guerrero, J. K., Rubens, M. F., & Rosa, P. T. V. (2013). Production of biodiesel from castor oil using sub and supercritical ethanol: Effect of sodium hydroxide on the ethyl ester production. *The Journal of Supercritical Fluids*, *83*, 124-132. http://dx.doi.org/10.1016/j.supflu.2013.08.016

Roschat, W., Siritanon, T., Yoosuk, B., & Promarak, V. (2016). Biodiesel production from palm oil using hydrated lime-derived CaO as a low-cost basic heterogeneous catalyst. *Energy Conversion and Management*, *108*, 459-467. http://dx.doi.org/10.1016/j.enconman.2015.11.036

Ruren, X., Wenqin, P., Jihong, Y., Qisheng, H., & Jiesheng, C. (2008). Chemistry of Zeolites and Related Porous Materials: Synthesis and Structure. In (pp. 696). Singapore: Markono Print Media Pte Ltd.

Saikia, B. J., & Parthasarathy, G. (2010). Fourier Transform Infrared Spectroscopic Characterization of Kaolinite from Assam and Meghalaya, Northeastern India. *Journal of Modern Physics*, *01*(04), 206-210. http://dx.doi.org/10.4236/jmp.2010.14031

Sang, S. Y., Chang, F. X., Liu, Z. M., He, C. Q., He, Y. L., & Xu, L. (2004). Difference of ZSM-5 zeolites synthesized with various templates. *Catalysis Today*, *93-95*, 729-734. http://dx.doi.org/10.1016/j.cattod.2004.06.091

Şanli, H., Canakci, M., & Alptekin, E. (2011). *Characterization of Waste Frying Oils Obtained from Different Facilities* (Vol. 57). http://dx.doi.org/10.3384/ecp11057479

Santana, H. S., Tortola, D. S., Reis, É. M., Silva Jr, J. L., & Taranto, O. P. (2016). Transesterification reaction of sunflower oil and ethanol for biodiesel synthesis in microchannel reactor: Experimental and simulation studies. *Chemical Engineering Journal*, *302*, 752-762. http://dx.doi.org/10.1016/j.cej.2016.05.122

SathyaSelvabala, V., Selvaraj, D. K., Kalimuthu, J., Periyaraman, P. M., & Subramanian, S. (2011). Two-step biodiesel production from Calophyllum inophyllum oil: Optimization of modified β-zeolite catalyzed pre-treatment. *Bioresource Technology*, *102*(2), 1066-1072. https://doi.org/10.1016/j.biortech.2010.08.052

Schulze, D. G. (2005). CLAY MINERALS. In D. Hillel (Ed.), *Encyclopedia of Soils in the Environment* (pp. 246-254). Elsevier. https://doi.org/10.1016/B0-12-348530-4/00189-2

Schwanke, A., & Pergher, S. (2018). Lamellar MWW-Type Zeolites: Toward Elegant Nanoporous Materials. *Applied Sciences*, *8*(9), 1636. https://www.mdpi.com/2076-3417/8/9/1636

Sen, D., Kim, C. W., Heo, N. H., & Seff, K. (2014). Using CuCl vapor to ion exchange copper into zeolite Na–Y. Single crystal structure of $|Cu_{30}Na_{30}Cl_9|[Si_{121}Al_{71}O_{384}]$–FAU containing $Cu_{16}Cl_7^{21+}$, Cu_4Cl^{7+}, Cu_3Cl^{2+}, and Cu^{2+}. *Microporous and Mesoporous Materials 185*, 16-25. https://doi.org/10.1016/j.micromeso.2013.09.014

Senoussi, H., Osmani, H., Courtois, C., & Bourahli, M. E. H. (2016). Mineralogical and chemical characterization of DD3 kaolin from the east of Algeria. *Boletín de la Sociedad Española de Cerámica y Vidrio*, *55*(3), 121-126. https://doi.org/10.1016/j.bsecv.2015.12.001

Shambhu, V. B., Bhattacharya, T. K., Nayak, L. K., & Das, S. (2013). Studies on Characterization of Raw Jatropha Oil and its Biodiesels with Relevance of Diesel. *International Journal of Emerging Technology and Advanced Engineering*, *3*(4), 48-54.

Sharma, P., Song, J.-S., Han, M., & Cho, C.-H. (2016). GIS-NaP1 zeolite microspheres as potential water adsorption material: Influence of initial silica concentration on adsorptive and physical/topological properties. *Scientific Reports*, *6*, 22734. https://doi.org/10.1038/srep22734

Shirani Lapari, S., Ramli, Z., & Triwahyono, S. (2015). Effect of Different Templates on the Synthesis of Mesoporous Sodalite. *Journal of Chemistry*, *2015*, 272613. https://doi.org/10.1155/2015/272613

Shu, Q., Zhang, Q., Xu, G., Nawaz, Z., Wang, D., & Wang, J. (2009). Synthesis of biodiesel from cottonseed oil and methanol using a carbon-based solid acid catalyst. *Fuel Processing Technology 90* 1002-1008.

Silitonga, A. S., Masjuki, H. H., Mahlia, T. M. I., Ong, H. C., Atabani, A. E., & Chong, W. T. (2013). A global comparative review of biodiesel production from *jatropha curcas* using different homogeneous acid and alkaline catalysts: Study of physical and chemical properties. *Renewable and Sustainable Energy Reviews*, *24*, 514-533. https://doi.org/10.1016/j.rser.2013.03.044

Singh, D., Sharma, D., Soni, S. L., Inda, C. S., Sharma, S., Sharma, P. K., & Jhalani, A. (2021). A comprehensive review of physicochemical properties, production process, performance and emissions characteristics of 2nd generation biodiesel feedstock: *Jatropha curcas*. *Fuel*, *285*, 119110. https://doi.org/10.1016/j.fuel.2020.119110

Singh, D., Sharma, D., Soni, S. L., Sharma, S., Kumar Sharma, P., & Jhalani, A. (2020). A review on feedstocks, production processes, and yield for different generations of biodiesel. *Fuel*, *262*, 116553. https://doi.org/10.1016/j.fuel.2019.116553

Singh, M., Vinodh Kumar, S., Waghmare, S. A., & Sabale, P. D. (2016). Aragonite–vaterite–calcite: Polymorphs of CaCO3 in 7th century CE lime plasters of Alampur group of temples, India. *Construction and Building Materials*, *112*, 386-397. https://doi.org/10.1016/j.conbuildmat.2016.02.191

Singh, R. K., & Padhi, S. (2009). Characterization of Jatropha oil for the preparation of biodiesel. *Natural Product Radiance*, *8*(2), 127-132.

Sinha, P., Islam, M. A., Negi, M. S., & Tripathi, S. B. (2015). Changes in oil content and fatty acid composition in *Jatropha curcas* during seed development. *Industrial Crops and Products*, *77*, 508-510. https://doi.org/10.1016/j.indcrop.2015.09.025

Sousa-Aguiar, E. F. (2016). Chapter 6 - Y Zeolites as a Major Component of FCC Catalysts: Main Challenges in the Modification Thereof. In B. F. Sels & L. M. Kustov (Eds.), *Zeolites and Zeolite-Like Materials* (pp. 265-282). Elsevier. https://doi.org/10.1016/B978-0-444-63506-8.00007-0

Su, C.-H. (2013). Recoverable and reusable hydrochloric acid used as a homogeneous catalyst for biodiesel production. *Applied Energy*, *104*, 503-509. http://dx.doi.org/10.1016/j.apenergy.2012.11.026

Sun, K., Lu, J., Ma, L., Han, Y., Fu, Z., & Ding, J. (2015). A comparative study on the catalytic performance of different types of zeolites for biodiesel production. *Fuel*, *158*, 848-854. http://dx.doi.org/10.1016/j.fuel.2015.06.048

Supamathanon, N., Wittayakun, J., & Prayoonpokarach, S. (2011). Properties of Jatropha seed oil from Northeastern Thailand and its transesterification catalyzed by potassium supported on NaY zeolite. *Journal of Industrial and Engineering Chemistry*, *17*(2), 182-185. https://doi.org/10.1016/j.jiec.2011.02.004

Suppes, G. J., Dasari, M. A., Doskocil, E. J., Mankidy, P. J., & Goff, M. J. (2004). Transesterification of soybean oil with zeolite and metal catalysts. *Applied Catalysis A: General*, *257*(2), 213-223. http://dx.doi.org/10.1016/j.apcata.2003.07.010

Taborda, F., Willhammar, T., Wang, Z., Montes, C., & Zou, X. (2011). Synthesis and characterization of pure silica zeolite beta obtained by an aging–drying method. *Microporous and Mesoporous Materials*, *143*(1), 196-205. http://dx.doi.org/10.1016/j.micromeso.2011.02.030

Tan, Y. H., Abdullah, M. O., & Nolasco-Hipolito, C. (2015). The potential of waste cooking oil-based biodiesel using heterogeneous catalyst derived from various calcined eggshells coupled with an emulsification technique: A review on the emission reduction and engine performance. *Renewable and Sustainable Energy Reviews*, *47*, 589-603. http://dx.doi.org/10.1016/j.rser.2015.03.048

Tchadjie, L. N., & Ekolu, S. O. (2018). Enhancing the reactivity of aluminosilicate materials toward geopolymer synthesis. *Journal of Materials Science*, *53*(7), 4709-4733. https://doi.org/10.1007/s10853-017-1907-7

Thangaraj, B., Solomon, P. R., Muniyandi, B., Ranganathan, S., & Lin, L. (2019). Catalysis in biodiesel production—a review. *Clean Energy*, *3*(1), 2-23. https://doi.org/10.1093/ce/zky020

Thangarasu, V., M, A. V., & Ramanathan, A. (2021). Artificial neural network approach for parametric investigation of biodiesel synthesis using biocatalyst and engine characteristics of diesel engine fuelled with Aegle Marmelos Correa biodiesel. *Energy*, *230*, 120738. https://doi.org/10.1016/j.energy.2021.120738

Thommes, M., Kaneko, K., Neimark, A. V., Olivier, J. P., Rodriguez-Reinoso, F., Rouquerol, J., & Sing, K. S. W. (2015). Physisorption of gases, with special reference to the evaluation of surface area and pore size distribution (IUPAC Technical Report). *Pure and Applied Chemistry*, *87*(9-10), 1051-1069. https://doi.org/10.1515/pac-2014-1117

Tounsi, H., Mseddi, S., & Djemel, S. (2009). Preparation and characterization of Na-LTA zeolite from Tunisian sand and aluminum scrap. *Physics Procedia*, *2*(3), 1065-1074. https://doi.org/10.1016/j.phpro.2009.11.064

Tsoutsos, T., Tournaki, S., Gkouskos, Z., Paraíba, O., Giglio, F., García, P. Q., Braga, J., Adrianos, H., & Filice, M. (2019). Quality Characteristics of Biodiesel Produced from Used Cooking Oil in Southern Europe. *ChemEngineering*, *3*(1), 19. https://doi.org/10.3390/chemengineering3010019

Ursini, O., Lilla, E., & Montanari, R. (2006). The investigation on cationic exchange capacity of zeolites: The use as selective ion trappers in the electrokinetic soil technique. *Journal of Hazardous materials*, *137*(2), 1079-1088. https://doi.org/10.1016/j.jhazmat.2006.03.070

U.S. Energy Information Administration (2022). *Short-Term Energy Outlook* https://www.eia.gov/outlooks/steo/

Vaculikova, L., Plevova, E., Vallova, S., & Koutnik, I. (2011). Characterization and Differentiation of Kaolinites from Selected Czech Deposits Using Infrared Spectroscopy and Differential Thermal Analysis. *Acta Geodyn. Geomater*, *8*(161), 59-67.

Van Wychen, S., Ramirez, K., & Laurens, L. M. L. (2016). *Determination of Total Lipids as Fatty Acid Methyl Esters (FAME) by in situ Transesterification: Laboratory Analytical Procedure (LAP)*. https://dx.doi.org/10.2172/1118085

Vieira, S. S., Magriotis, Z. M., Graça, I., Fernandes, A., Ribeiro, M. F., Lopes, J. M. F. M., Coelho, S. M., Santos, N. A. V., & Saczk, A. A. (2017). Production of biodiesel using HZSM-5 zeolites modified with citric acid and SO_4^{2-}/La_2O_3. *Catalysis Today*, *279*, 267-273. https://doi.org/10.1016/j.cattod.2016.04.014

Volli, V., & Purkait, M. K. (2015). Selective preparation of zeolite X and A from flyash and its use as catalyst for biodiesel production. *Journal of Hazardous materials*, *297*, 101-111. http://dx.doi.org/10.1016/j.jhazmat.2015.04.066

Wang, P., Sun, Q., Zhang, Y., & Cao, J. (2019). Synthesis of Zeolite 4A from Kaolin and Its Adsorption Equilibrium of Carbon Dioxide. *Materials (Basel, Switzerland)*, *12*(9), 1536. https://doi.org/10.3390/ma12091536

Warzybok, M., Chverenhuk, A., & Warchoł, J. (2015). Acetone Adsorption on Synthesized Zeolite from Natural Clay Material. *Czasopismo Inżynierii Lądowej, Środowiska i Architektury*, *z. 62, nr 3/I*, 485-495.

Warzybok, M., & Warchoł, J. (2018). Synthesis of kaolin-based zeolite Y and its application for adsorption of two carbonyl compound gases. *Czasopismo Inżynierii Lądowej, Środowiska i Architektury*, *z. 65, nr 1*, 13-26. https://doi.org/10.7862/rb.2018.2

Weitkamp, J., & Puppe, L. (1999). *Catalysis and zeolites: fundamentals and applications*. Springer Science & Business Media. https://doi.org/10.1007/978-3-662-03764-5

Wu, H., Zhang, J., Wei, Q., Zheng, J., & Zhang, J. (2013). Transesterification of soybean oil to biodiesel using zeolite supported CaO as strong base catalysts. *Fuel Processing Technology*, *109*, 13-18. http://dx.doi.org/10.1016/j.fuproc.2012.09.032

Yahaya, M. S., Wan, M. A., Wan, D., & Abdul Aziza, A. R. (2014). Activity of solid acid catalysts for biodiesel production: A critical review. *Applied Catalysis A: General*, *470*, 140-161. http://dx.doi.org/10.1016/j.apcata.2013.10.052

Yang, J., Li, D., & Fang, Y. (2017). Synthesis of Nanoscale CaO-Al_2O_3-SiO_2-H_2O and Na_2O-Al_2O_3-SiO_2-H_2O Using the Hydrothermal Method and Their Characterization. *Materials 10*, 695-712. https://doi.org/10.3390/ma10070695

Ye, S., Sun, J., Yi, X., Wang, Y., & Zhang, Q. (2017). Interaction between the exchanged Mn^{2+} and Yb^{3+} ions confined in zeolite-Y and their luminescence behaviours. *Scientific Reports*, *7*(1), 46219. https://doi.org/10.1038/srep46219

Yeong, S. P., Chan, Y. S., Law, M. C., & Ling, J. K. U. (2022). Improving cold flow properties of palm fatty acid distillate biodiesel through vacuum distillation. *Journal of Bioresources and Bioproducts*, *7*(1), 43-51. https://doi.org/10.1016/j.jobab.2021.09.002

Yilmaz, B., Muller, U., Feyen, M., Maurer, S., Zhang, H., Meng, X., Xiao, F.-S., Bao, X., Zhang, W., Imai, H., Yokoi, T., Tatsumi, T., Gies, H., De Baerdemaeker, T., & De Vos, D.

(2013). A new catalyst platform: zeolite Beta from template-free synthesis. *Catalysis Science & Technology*, *3*(10), 2580-2586. https://doi.org/10.1039/C3CY00073G

Zamechek, W. (2001). Chapter 10 - Determination of the elemental compositor of zeolitic materials. In H. Robson & K. P. Lillerud (Eds.), *Verified Syntheses of Zeolitic Materials* (pp. 51-53). Elsevier Science. https://doi.org/10.1016/B978-044450703-7/50108-3

Zayed, A. M., Selim, A. Q., Mohamed, E. A., Abdel Wahed, M. S. M., Seliem, M. K., & Sillanpää, M. (2017). Adsorption characteristics of Na-A zeolites synthesized from Egyptian kaolinite for manganese in aqueous solutions: Response surface modeling and optimization. *Applied Clay Science*, *140*, 17-24. https://doi.org/10.1016/j.clay.2017.01.027

Zhang, K., Zhang, H., Xu, G., Xiang, S., Xu, D., Liu, S., & Li, H. (2001). Alkylation of phenol with tert-butyl alcohol catalyzed by large pore zeolites. *Applied Catalysis A: General*, *207*(1–2), 183-190. http://dx.doi.org/10.1016/S0926-860X(00)00663-3

Zhang, X., Tang, D., Zhang, M., & Yang, R. (2013). Synthesis of NaX zeolite: Influence of crystallization time, temperature and batch molar ratio SiO_2/Al_2O_3 on the particulate properties of zeolite crystals. *Powder Technology*, *235*, 322-328. https://doi.org/10.1016/j.powtec.2012.10.046

Zhang, Y., Leng, Z., Zou, F., Wang, L., Chen, S. S., & Tsang, D. C. W. (2018). Synthesis of zeolite A using sewage sludge ash for application in warm mix asphalt. *Journal of Cleaner Production*, *172*, 686-695. https://doi.org/10.1016/j.jclepro.2017.10.005

Zhou, H. M., Qiao, X. C., & Yu, J. G. (2013). Influences of quartz and muscovite on the formation of mullite from kaolinite. *Applied Clay Science*, *80-81*, 176-181. https://doi.org/10.1016/j.clay.2013.04.004

Zhou, Q., Zhang, H., Chang, F., Li, H., Pan, H., Xue, W., Hu, D.-Y., & Yang, S. (2015). Nano La2O3 as a heterogeneous catalyst for biodiesel synthesis by transesterification of *Jatropha curcas L.* oil. *Journal of Industrial and Engineering Chemistry*, *31*, 385-392. http://dx.doi.org/10.1016/j.jiec.2015.07.013

Zhu, J., Zhu, Y., Zhu, L., Rigutto, M., van der Made, A., Yang, C., Pan, S., Wang, L., Zhu, L., Jin, Y., Sun, Q., Wu, Q., Meng, X., Zhang, D., Han, Y., Li, J., Chu, Y., Zheng, A., Qiu, S., Zheng, X., & Xiao, F.-S. (2014). Highly Mesoporous Single-Crystalline Zeolite Beta

Synthesized Using a Nonsurfactant Cationic Polymer as a Dual-Function Template. *Journal of the American Chemical Society*, *136*(6), 2503-2510. https://doi.org/10.1021/ja411117y

Zhu, P., Meier, S., Saravanamurugan, S., & Riisager, A. (2021). Modification of commercial Y zeolites by alkaline-treatment for improved performance in the isomerization of glucose to fructose. *Molecular Catalysis*, *510*, 111686. https://doi.org/10.1016/j.mcat.2021.111686

Zou, J., Guo, C., Wei, C., Li, F., & Jiang, Y. (2016). Synthesis of Pure Na–X and Na–P Zeolite from Acid-Extracting Residues of CFB Fly Ash by a Single-Step Hydrothermal Method. *MATERIALS TRANSACTIONS*, *57*(5), 726-731. https://doi.org/10.2320/matertrans.M2015463